공학박사 학위논문

Isostructural Charge-Transfer Crystals via Molecular Isometric Donor-Acceptor Pairs: Unraveling the Optoelectrical Properties-Structure Relationships of Luminescent Semiconductors

등구조형 전하 전이 결정을 통한 형광성 반도체 물질의 광전자 기능성-구조 상관관계에 관한 연구

2020 년 8 월

서울대학교 대학원

재료공학부

오 상 윤

Isostructural Charge-Transfer Crystals via Molecular Isometric Donor-Acceptor Pairs: Unraveling the Optoelectrical Properties-Structure Relationships of Luminescent Semiconductors

A THESIS SUBMITTED IN PARTIAL FULFILLMENT OF
THE REQUIREMENTS FOR THE DEGREE OF
DOCTOR OF PHILOSOPHY
IN ENGINEERING AT THE GRADUATE SCHOOL OF
SEOUL NATIONAL UNIVERSITY

August 2020

By
Sangyoon Oh

Supervisor
Prof. Soo Young Park

Isostructural Charge-Transfer Crystals via Molecular Isometric Donor-Acceptor Pairs: Unraveling the Optoelectrical Properties-Structure Relationships of Luminescent Semiconductors

등구조형 전하 전이 결정을 통한 형광성 반도체 물질의 광전자 기능성-구조 상관관계에 관한 연구

지도 교수 박 수 영

이 논문을 공학박사 학위논문으로 제출함

2020 년 7 월

서울대학교 대학원

재료공학부

오 상 윤

오상윤의 공학박사 학위논문을 인준함

2020 년 7 월

위 원 장 _____ (인)

부위원장 _____ (인)

위 원 _____ (인)

위 원 _____ (인)

위 원 _____ (인)

Abstract

Isostructural Charge-Transfer Crystals via Molecular Isometric Donor-Acceptor Pairs: Unraveling the Optoelectrical Properties-Structure Relationships of Luminescent Semiconductors

Sangyoon Oh

Department of Materials Science and Engineering

The Graduate School

Seoul National University

During the past few decades, π-conjugated molecule based crystals have drawn much interest due to their potential optoelectronic functions/ device applications. Here, systemic understanding on structure-property relationships is crucial for the design of materials with desirable properties. However, it is still a challenge to predict various optoelectrical properties of organic crystals because their properties are not only a function of the molecular structure, but are also sensitively affected by the intermolecular arrangement in the crystal. In this regard, crystal systems having similarities in crystal packing/arrangement – *i.e.*, isostructural systems – allows to study optoelectrical response by varying the molecular structure while keeping the intermolecular arrangement in constant. Among the π-conjugated organic crystals, charge-transfer (CT) crystals constituted of electron donor (D) and electron acceptor (A) pairs are receiving increasing attention these days due to their unique electrical transport and emission properties distinct from their D and A molecules. However, arbitrary molecular design of CT complexes limits our

understanding on optoelectrical property-structure relationships of CT complexes.

In this work, I focus on two distyrylbenzene (DSB) type electron donors (D) and two dicyano-distyrylbenzene (DCS) type electron acceptors (A) which share an isometric molecular structure each other. Remarkably, based on strong self-assembling ability of DSB and DCS, cocrystals of all possible four D:A (1:1) pairs form CT crystals with bright solid-state luminescence with a systemic color variation from red to green, controlled by the frontier molecular orbitals. It was found that isometric D-A interactions in the mixed-stack isostructural CT crystals can generate highly increased oscillator strength within the slipped stack intermolecular arrangement via favorable configuration interaction, effective suppression of the non-radiative processes, and also triplet harvesting via reverse intersystem crossing. Based on the synergy of these effects, our mixed stack CT crystal in this work marks the record high PL quantum yields of 83 %. Notably, four different CT pairs made of isometric D and A molecules all showed the isomorphic/ quasi-isostructural intra-stack (π-stack) crystal, enabling us to find the sole effect of electronic CT interaction on their photophysical properties by decoupling the complicated morphological effect.

By virtue of the high miscibility of isometric molecules in the crystal, all D:A pairs were thermodynamically stable even at crystalline solid solution states. Similar with D:A 1:1 cocrystals, the four crystalline solid solutions (D:A 1:99 ~ 10:90) were quasi-isostructural each other by virtue of the isometric molecular structure. However, different from 1:1 CT cocrystal, crystalline solid solution showed 2D-type morphology like the host (acceptor). Isometric D and A molecules result in the densely packed substitutional doped CT complexes in the host, all crystalline solution showed overall CT emissions with the high energy transfer (ET) efficiency

up to 80%. Furthermore, the doped CT complexes in the host crystal were structurally/ electrically non-destructive even in heavily doped condition (20 %). Interestingly, CT complexes in the host activated organic photo-transistor (OPT) behavior with moderate photo-responsivity (~500 AW^{-1}) and few tens of threshold voltage shift (ΔV_{TH}). Therefore, OPT performances were systemically correlated the with various physical parameters within the isostructural crystalline solutions; ET %, D:A energetical offsets, electrical transport ability of the crystalline solid solutions.

Meanwhile, microscale pattern fabrication using lithographic techniques is indispensable for practical application of organic devices, yet patterning method fully compatible with organic materials is rare by the physical softness of organic materials. In this regard, I developed the fully organic compatible new soft-lithographic method call ‘patterned taping’, and further the CT crystals are micro-patterned onto the acceptor and/or donor crystals through combination of top-down and bottom-up method: patterned taping as former and vapor-driven self-assembly (VDSA) as latter. The patterned taping method utilizes the patterned pressure-sensitive tape which subtractive/ additive patterns the target film through the strong adhesion force of pressure-sensitive tape. Therefore, the method was applicable to various kind of targeted thin film, and also it was morphologically/ electrically non-evasive even to organic materials. In addition, patterned taping demonstrated various advantageous features for high-efficiency patterning; sub-micron resolution, the low-cost, simple procedure, and high scalability. Through the patterned taping method, the micro-patterned donor and/or acceptor thin films were generated on the acceptor and/or donor crystal, and then the templated grown CT crystals are fabricated by solvent vapor exposure. Interestingly, they showed peculiar optical

response under rotation of polarizer, and thus the origin of this behavior was unambiguously revealed through crystallographic approaches, optical investigation, and quantum chemical calculations. Furthermore, the nucleation and growth mechanism of templated growing CT crystals was fully investigated based on morphological/ thermo-dynamical studies.

In this dissertation, I mainly focus on developing isostructural systems of CT crystal to challenge the D-A structure-property correlation under identical morphology condition and thus to understand the underlying nature of various optoelectrical features of the CT complex. For this, four quasi-isostructural 1:1 CT cocrystals as well as four quasi-isostructural crystalline solid solutions based on two isometric donors and two isometric acceptors. Supported by photo-physical approach, crystallographic investigation, and quantum chemical calculations, isostructural crystal systems enabled the extensive investigation on the sole effect of various physical parameters on optoelectrical properties of CT crystals. Furthermore, as the possible practical applications, micro-patterned templated grown CT crystals were successfully fabricated by virtue of strong self-assembling properties of CT crystals and organic compatible soft-lithographic technique.

Key words: Charge-transfer (CT) crystal, Molecular isometric donor (D)- acceptor (A), Structure-property relationship, isostructural 1:1 CT cocrystal, isostructural crystalline solid solution, Novel soft-lithographic technique.

Student number: 2013-20609

Contents

List of Tables

List of Schemes

List of Figures

Chapter 1. Introduction

1.1. Optoelectrical properties of π-conjugated organic functional crystals

π-conjugated organic molecules with semiconducting and/or luminescent properties have drawn much interest due to their potential for optoelectronic applications including organic light emitting diodes (OLED)[1, 2], organic field-effect transistors (OFET)[3], organic light emitting transistors (OLET)[4, 5] and organic lasers[6]. To date, systematic studies on (electrical) transport-structure relationship and (luminescent) emission-structure relationship are conducted for the targeted design of molecular materials with desirable optoelectronic properties[7, 8]. Especially, organic crystals are particularly interesting for investigating structure-property relationships because the analysis can be based on the known crystal structure.

1.1.1 Electrical properties of organic crystals

Electrical transport in organic solids is basically relying on charge hopping mechanism between adjacent molecules, and systemic understanding based on this intrinsic mechanism have been studied so far [7]. To investigate the electrical properties of organic solid, field-effect transistor (FET) is usually fabricated because FET is widely used in the complementary integrate circuit[9] and active matrix[10]. In a classical model of charge transport in organic solid, it is known that charge transport is closely related with the parameters of transfer integral and reorganization energy[11]: transfer integral is electronic coupling which is related with the π-orbital overlap between adjacent molecules, and reorganization energy is

related with the energy difference between the charge molecule and neutral molecule. Charge transfer (transport) rate also can be correlated theoretically as following equation[12]:

$$k_{et} = (4\pi^2/h) \cdot t^2 \cdot (4\pi\lambda RT)^{-0.5} \cdot \exp(-\lambda/4RT)$$

k_{et} is charge transfer rate, h is Planck constant, t is transfer integral, λ is reorganization energy, R is distance between molecular centers, and T is temperature, and thus maximized t and minimized λ warrants the efficient charge transfer in organic semiconductors. For this, large orbital overlap t as well as high molecular rigidity and long conjugation length is favorble for better semiconducting ability. In this regard, organic crystals have advantageous features than amorphous organic materials in terms of charge transfer hopping mechanism (**Figure 1-1**)[10] because of rather small distance between adjecent molecules (better orbital overlap) and molecular rigidity by virtue of densely packed structure in crystals (small λ). However, not all crystal system is good semiconductor because subtle change on molecular arrangements largely affects the electronic coupling (**Figure 1-2**)[7, 13]: The molecular orbitals have valley and summit, thereby electronic coupling is largely varied by molecular displacnements (**Figure 1-2c-d**), and electronic coupling also affected by tilt angle of adjacent molecules (**Figure 1-2b**). Therefore, molecular arragement in the crystal have considerable effects on electrical transport ability of semiconductors.

In addition to such electrical properties described by charge hopping model above, the real electrical properties are also related to the various extrinsic factors of devices such as (i) defects at organic semiconductor and interfaces[7]; (ii) morphology of crystal[14]; and (iii) injection barrier between eletrode and organic

layer[15]. As for the first extrinsic factor; defects in semiconducutor, organic crystalline materials basically have less defects than amophous materials and thus higher electrical mobility with crystals [12]. In the organic FET (OFET) structure, 2D-like morphology of crystals usually have rather small effect of interfacial defect by their smooth interfaces [14]. It should be noted the macroscopic mophology of crystal is also functioned by molecular structure because the mophology is macroscopic extension of molecular arrangments between adjacent molecules[14], for example, 2D-like crystals have rather strong intermolecular interaction at in-plane directions while small at in out-of-plane direction, thereby lamination transfer was easily attempted by adhesive tape [16]. The third one is related with the electronic states of the organic semiconductors: injection barrier is related with the energy gap between source (S) electrode work function (WF) and frontier molecular orbitals (FMO); lowest unoccupied molecular orbital (LUMO) for electron transport at n-type semiconductors and highest occupied molecular orbnital (HOMO) for hole transport at p-type semiconductors. Indeed one can choice electrode element with proper WF for semicondcutor FMO, however, metals with high WF is suitable for practical device appliations because metals with low WF is less stable than high WF metals [17], *e.g.*, silver/gold/platinum have high WF at 4.25/5.1/5.65 eV respectively. Similarly, semiconductors with shallow FMO is unstable especially LUMO higher than -4.0 eV [12]. In this regard, researchers tried to shift-down the electronic levels of organic semiconductors for better injection through stable metals, and thus electron withdrawing groups (EWG) was introduced for n-type semiconductors, *e.g.*, LUMO of perfluoropentacene is 1.6 eV lower than that of pentacene [18]. In fact, the real situation of FMOs is more complex because the FMOs are also interelated with the molecular arrangement in the solid

state (**Figure 1-3**) [12] depending on molecular arrangements by the different energy splitting aspects[7].

As a result, the electrical properties of organic semicondcutors is the result of complex interelation of various factors such as electronic coupling and electronic levels. Indeed, in spite of these complex situation on electrical properties of organic crystals, extensive studies have been made on the conductivity of π-conjugated organic crystals; thus, transport-structure relationships in them is already well-established providing molecular design guidelines for high performance organic semiconductors [7, 12, 14, 19]. However, for more proper assessment on the transport-structure relationship, it is desirable to rule out one of the factors into constant for the systemic assignment on the electrical properties, *e.g.*, (i) crystalline polymorphs have the same molecular structure and different intermolecular arrangement, and (ii) isostructural crystals have different molecular structure and the same intermolecular arrangement.

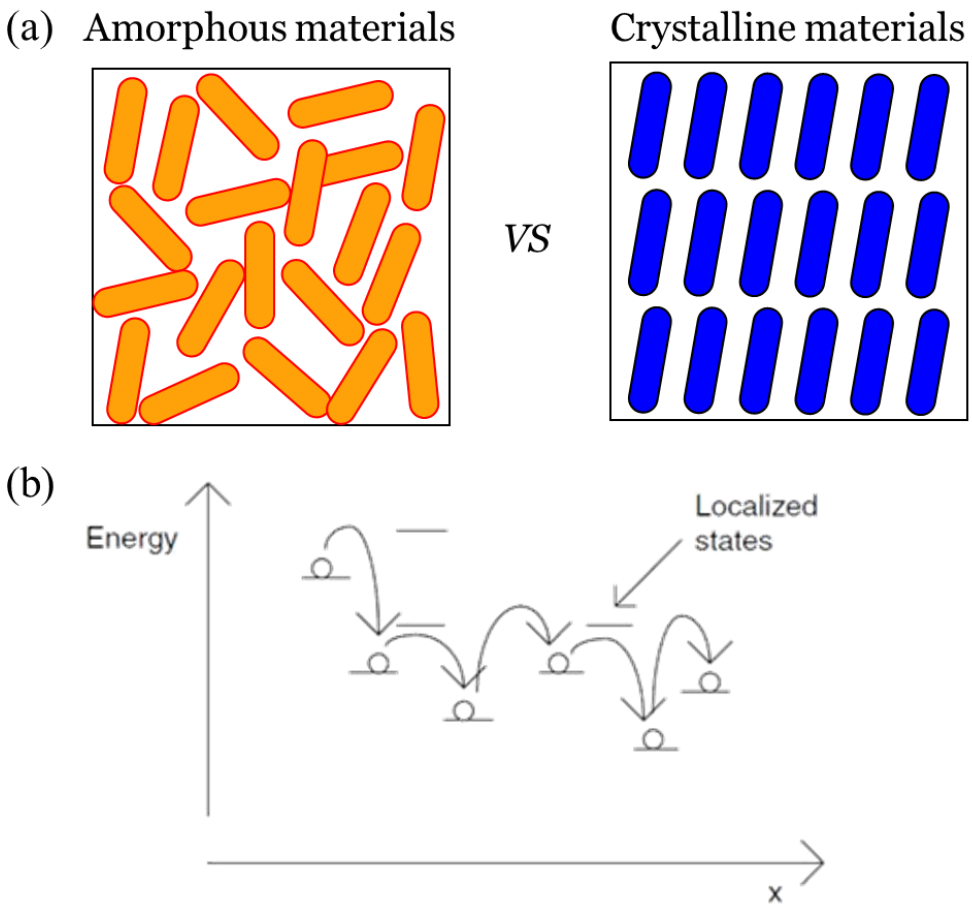

Figure 1-1. Molecular arrangement and charge hopping mechanism of organic solid. (a) Amorphous vs crystalline organic materials, and (b) charge transfer hopping mechanism of organic semiconductors[10].

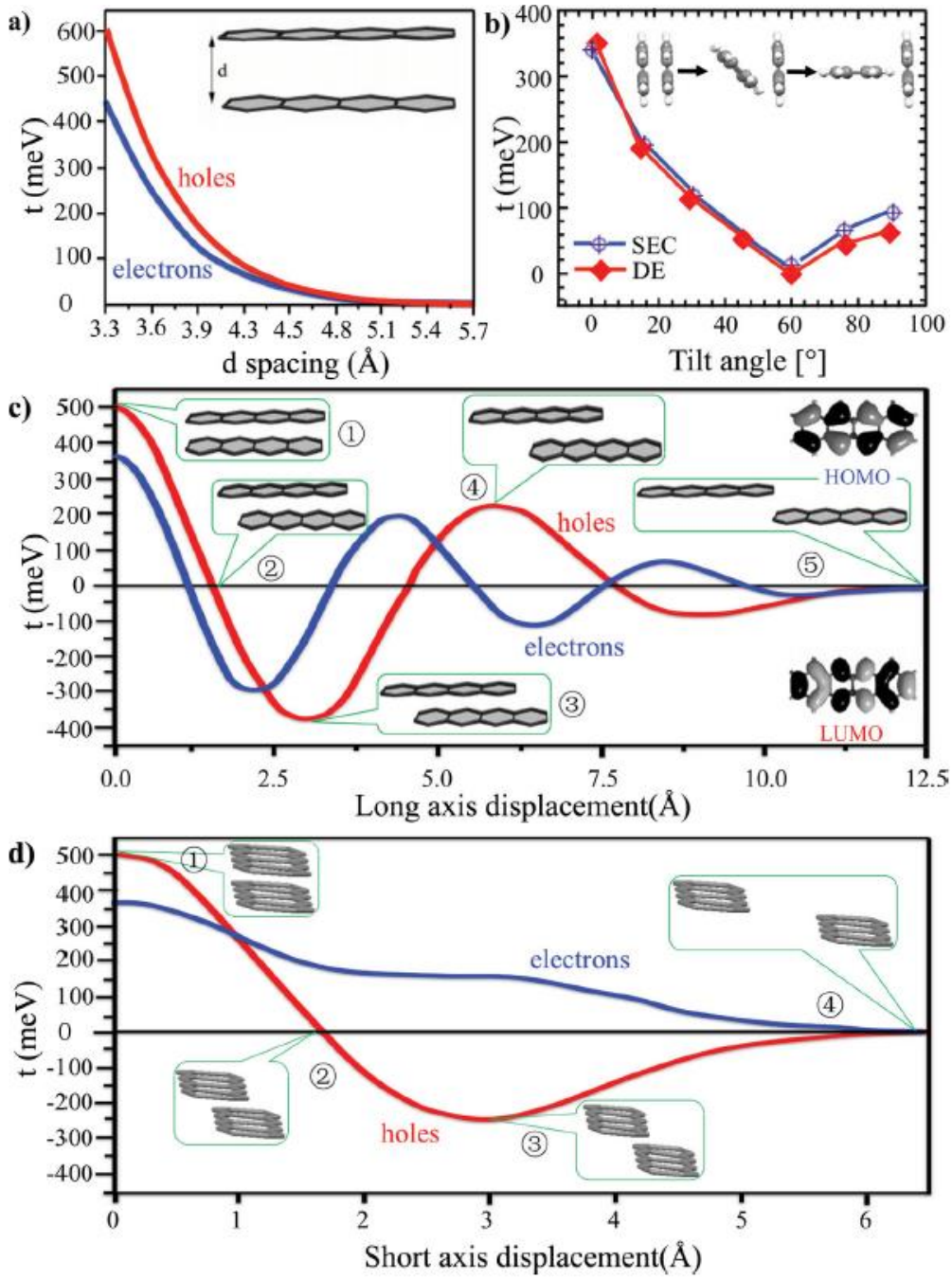

Figure 1-2. Electronic coupling depending on molecular arrangement[7, 13]. Electronic coupling depending on (a) molecular distance, (b) tilting angle, (c) long axis displacement, and (d) short axis displacement.

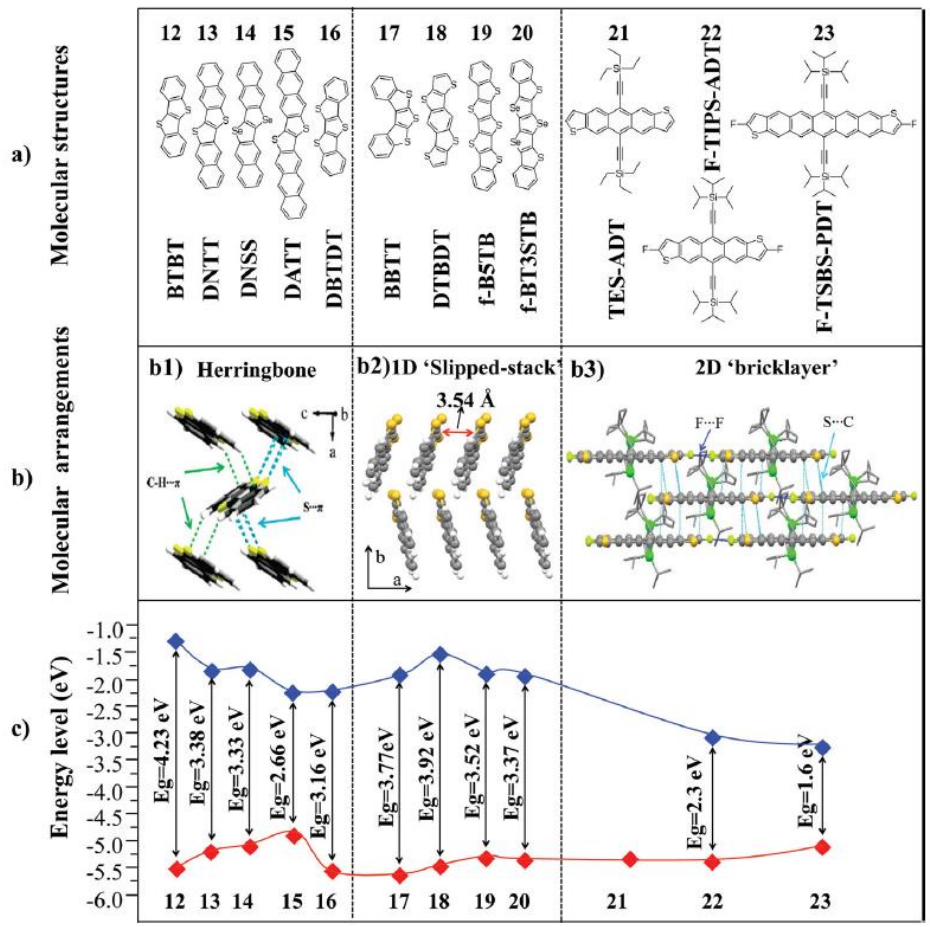

Figure 1-3. Molecular arrangement and electronic levels of heteroacenes. (a) Molecular structure of heteroacenes, (b) molecular arrangements, and (c) electronic levels [12].

1.1.2 Optical properties of organic crystals

Various optical responses take place when matter meets light. By light absorption, the excitons are generated, and the final stop of excitons are all headed to the ground state. However, there are various pathways the excited exciton can experience before reaching to the ground state; thermal relaxation (TR), internal conversion (IC), and intersystem crossing (ISC) as the non-radiative transitions; and fluorescence (FL) and phosphorescence (PH) as the radiative transitions (**Figure 1-4**). Each processes requires specific conditions to be take placed in organic optoelectronic materials; IC happens through conical intersection (CI) between two states[20, 21], ISC requires special conditions such as heavy atom effects to induce sufficient mixing between singlet and triplet states[22], and FL requires symmetry allowed (dipole allowed) S_1 respectively[8]. In fact, various optical processes are involved in many optoelectrical devices: Organic solar cells require the broad range of light absorption as well as strong absorption to efficient exploitation of light energy, organic light emitting devices including light emitting diodes (LED) and light emitting transistors (LET) should have high photoluminescence (PL) quantum yield via efficient radiative process. Therefore, it is necessary to understand/control these optical process particularly in the solid-state to make organic optoelectronic device with desirable traits. In this regard, as state earlier, organic crystals have analytical merits compared to the amorphous systems which is hard to predict the properties due to their somewhat randomly oriented nature. To date, the theoretical origin of solid state luminescence enhancement (SLE)[20] was investigated by systematically correlating the luminescent properties of organic crystals and various intermolecular factors such as J-/H-aggregation[20, 23], excitonic/ excimeric coupling [6, 8, 24], and also crystal size

effect[6, 8, 25].

Classical Kasha's conrotatory movement model of dimer in point dipole approximation (PDA) depicts that pitch angle is critical for luminescent properties (Kasha's magic angle = 54.7°) of the organic dimer or organic condensed solid system[26, 27]. However, this theory can be only applied in a loosely packed solid-states where intermolecular separation is larger than the length of the transition dipole moment (TDM) of the luminophore [8]. Therefore, more suitable modeling describing the luminescent properties of dense molecular aggregates such as crystals of which many of them have (very) close intermolecular distance lower than their TDMs. In this regard, the quantum chemical calculations were extensively introduced to predict/ study the emission-structure relationships of condensed organic materials[6, 8, 23]. From the quantum chemically estimated electronic energy levels in dimer of **Figure 1-5**, energy of monomer is splitted in the dimer, and the H-type aggregation and J-type aggregation can be understood with this model: The H-type is result in large excitonic coupling and the J-type result in small excitonic coupling.

The type of coupling is greatly affected by the X-slip of rod type molecule such as DSB type molecules, and roughly over the 50% of x-slips the J-aggregation is formed. In the H-aggregation, due to the TDMs of lowest excited transition are canceled out each other, the radiative deactivation in excited state is forbidden. Therefore, it results in blue shift of the main peak of absorption in solid against the solution absorption spectra, and the radiative rate is decreased against the solution. In fact, in the optically dense system such as crystal cannot be measured the absorption spectrum due to their severe scattering. With the photo luminescent

excitation spectra (PLE) the scattering effect can be excluded by the nature of PLE measurement, however PLE also suffered from inner filter effect in optically dense sample. Therefore, in the crystal system, it is more reasonable to compare the radiative rate of solution and solid state[6]. In J-aggregation case, the trends go opposite, and the absorption spectrum is red-shifted and the radiative rate is increased against the solution state. The J-/H-aggregation is not terms of the quantum yield but it is related with the radiative rate of the solid state.

In this context, the effect 'aggregation induced quenching' is somewhat ambiguous and not reflecting the underlying fundamentals of solid-state luminescence. By the 'aggregation' the PL quantum yield is quenching is not always true, but it can be applied only in the nanoparticle or vacuum deposited microcrystalline grains of which non-radiative rate is very high due to the large interfacial quenching sites[25]. However, in the monolithic crystal, the non-radiative rate is very low due to the low trap density inside of the crystal, and low surface/volume ratio which can minimize the exciton quenching mechanism at the surface (**Figure 1-6**). Therefore, in spite of the low radiative rate in H-aggregation, the radiative rate can competitive with the low non-radiative rate of the crystal. Regarding the PL quantum yield formula which are related with the ratio of radiative/ non-radiative term, H-aggregation can have large PL quantum yield also in the solid-state, for the equation see below:

$$\Phi_{PL} = k_r \cdot \tau_F = \frac{k_r}{k_r + k_{nr}}$$

Φ_{PL} is PL quantum yield, kr is radiative rate, τ_F is lifetime decay, and k_{nr} is non-radiative rate. The rate parameters can be extracted by the Φ_{PL} and τ_F which can be

measured by photo-physical measurements.

Evidently the perfect side-by-side stack of the dimer fully quenching the radiative transition by their dipole-forbidden nature, but most of the molecular dimer in solid-state has at least small x-slip or y-slip. In fact, displacement (x-/y-slip) can make radiative transition allowed in conjunction with Herzberg-Teller coupling which is prevalent behavior in organic material: vibronic coupling with energetically nearby allowed states can open a pathway to radiative transition[20]. From the dimer model, H-aggregation has the energetically intimate allowed state, and the large displacement the lesser excitonic coupling thereby less energy splitting. In this regard, H-aggregation with large displacement is more favorable to have larger radiative rates which already has been confirmed by the numerous organic luminophores. Like the displacements, the large torsion angle between the rings can affect the amount of excitonic coupling[24, 28], and finally yields weaker H-aggregation which has rather small excitonic coupling like in herringbone stacking case[36]. The excimeric features of the emission can be distinct by the Stokes shift and the shape of the emission spectrum. Other than excitonic emission, excimeric emissions have red shifted large Stokes shifted emission with broad structureless spectrum. This is because the emission is not decayed from the monomer S_1 state, but the excited state is coupled with the ground state with many breathing modes by vibronically coupled character.

To correlate the high PL quantum yield of the solid-states, radiative rate and non-radiative rate should be considered, and one can gain many information regarding both rates by carefully investigated with the structural data (X-ray) and photo-physical/optical measurements. Still, the PL quantum yield is important factor for

evaluating external quantum efficiency of the light emitting devices, not only for strategy for molecular design but also the geometry of solid-state should be counted also.

In terms of non-radiative rate, especially the red and NIR emitter has large internal conversion (IC) rate due to their small optical bandgap. With the small optical bandgap, based on the Energy gap law, the vibronic modes of ground state and vibronic modes of excited state can be coupled easily due to the closely located energy level *i.e.* vibronically coupled S_1 and S_0 state. Therefore, they tend to have low PL quantum yield by the facilitated non-radiative deactivation pathway. The molecules cannot move freely in the condensed state, and thus the solid-state can have smaller IC rate due to the lower population on the vibronic modes in higher energies. Full-mirror image of absorption and emission spectra indicates that excited state and ground state have equivalent geometry without large geometrical change and planar structure of both states and also the low population of the vibronic modes with lower chance of vibronically coupling between excited state and ground state[29]; for example, in case of the rigid planar molecule tends to have small IC, and it can be confirmed by the full-mirror image and small Stokes shift of the spectral data[30].

Other important parameter evaluating luminophore especially for light emitting devices is Commission Internationale de I'Eclairage (CIE) coordinate in color space. The CIE value is obtained by the overlap of RGB photopic spectrum of human eyes. In 1957, national television standard committee designated the standard primary R, G, B colors. NTSC primary red was (0.67, 0.33), green was (0.21, 0.71) and blue was (0.14, 0.08) respectively (**Figure 1-7**). Ratio between the

triangle in the color gamut composed of primary RGB of the device and that of triangle of NTSC standard is percent of NTSC. If the percent of NTSC is larger, then the emitting device will represent the many colors in natural true color.

Consequently, various optical features especially emission of organic solids are also functioned by electronic nature and also intermolecular arrangement in the crystals. Therefore, like the transport-structure relationship, polymorphs and/or isostructural system can endow unambiguous insight on the emission-transport relationship of the organic crystals.

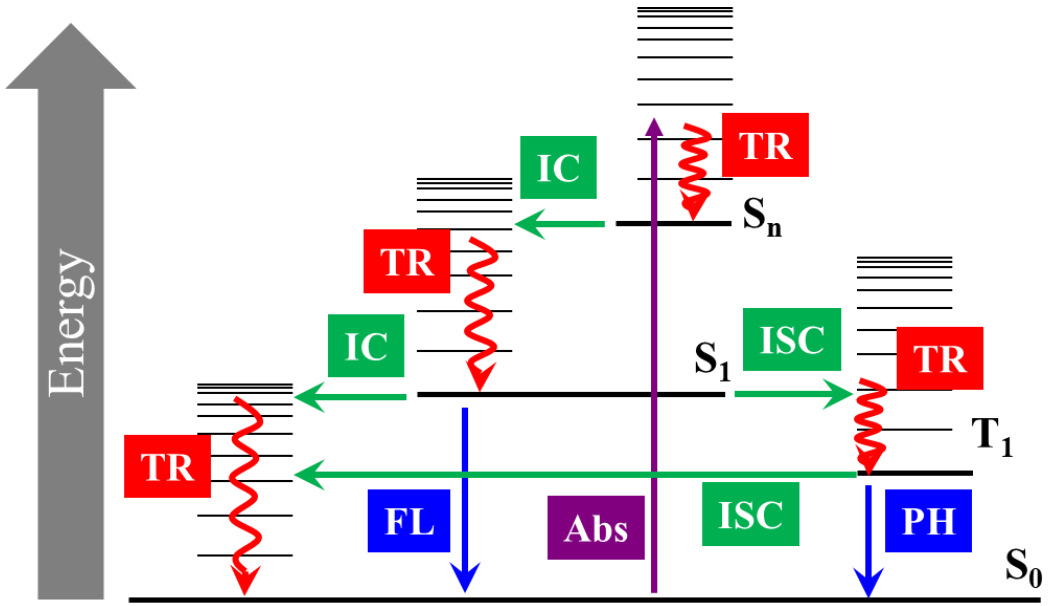

S_0 = electronic ground state (singlet)
S_1 = 1st singlet excited state
T_1 = 1st triplet excited state
S_n = Higher singlet excited state

Abs = Absorption
FL = Fluorescence
PH = Phosphorescence
IC = Internal conversion
ISC = Intersystem crossing

Figure 1-4. Jablonski diagram

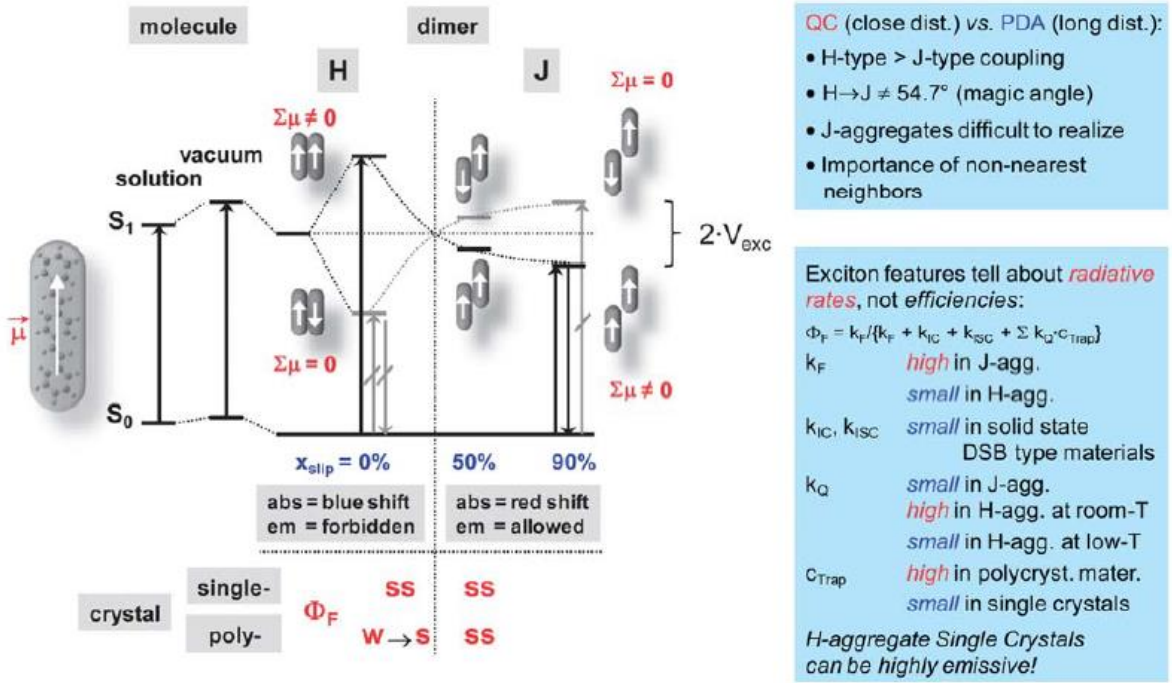

Figure 1-5. Excitonic coupling of dimer in solid-state by quantum chemical calculation and their estimated photo-physical properties [8]

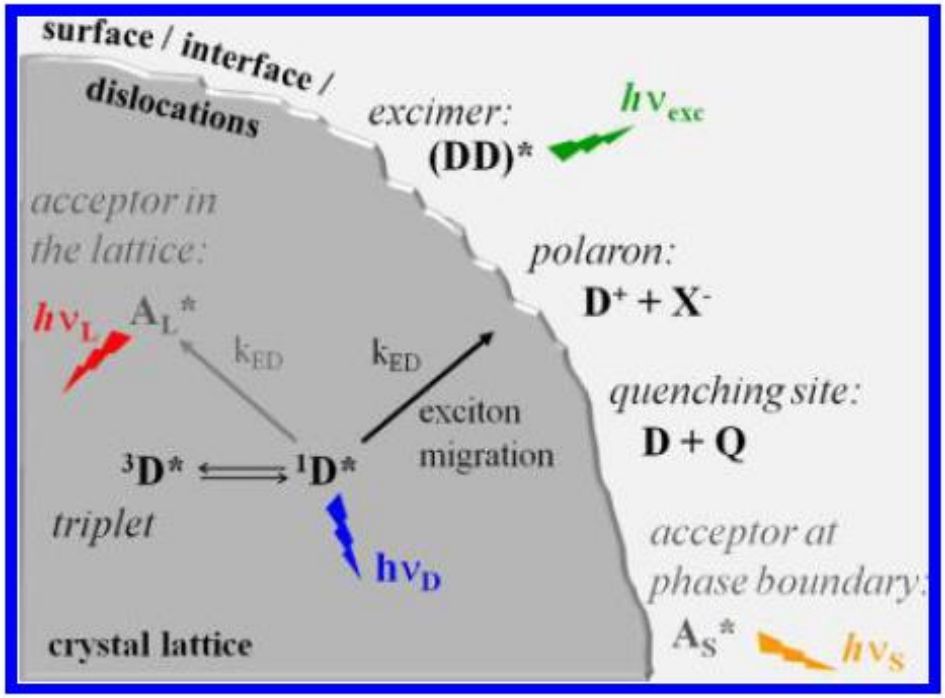

Figure 1-6. Exciton quenching pathways at the surface/interface[25]

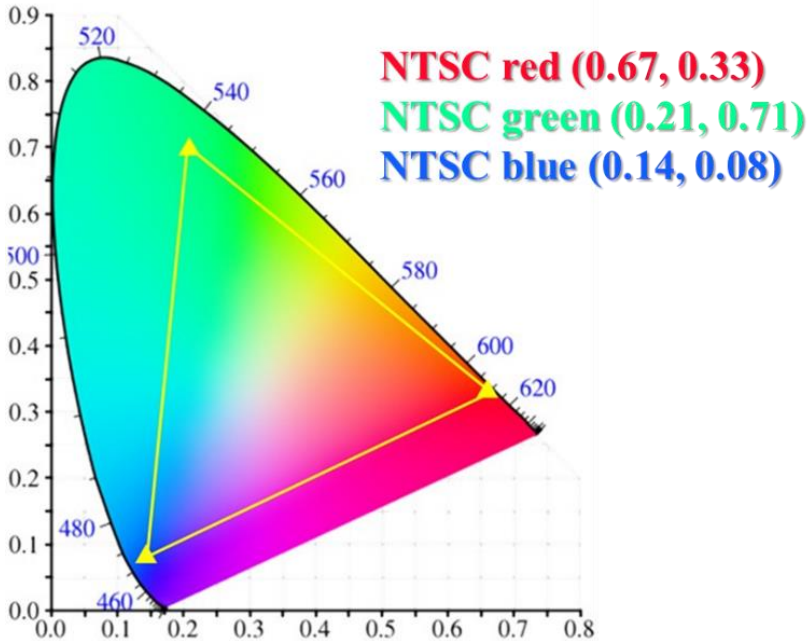

Figure 1-7. CIE color gamut and NTSC standard RGB color.

1.2. Crystal structural engineering to understand structure-property relationships

The molecular arrangements in the crystal indeed determined by the summation of intermolecular secondary interactions which stabilize the lattice energy of crystals. Therefore, delicate design of molecules is required to attain the wanted molecular arrangements[14] because the synthons in the molecules can provoke various intermolecular forces (**Figure 1-8**)[31]. Especially, among the secondary interactions, dispersion intermolecular force is most influential force, and it is also related with the molecular shape and size [31] (**Figure 1-9**)[32, 33]. The origin of interdigitation beween alkyl chains (**Figure 1-8 # 15**) is also mediated by dispersion forces. The other secondary interaction between molecules are electrostatic interaction, polarization interaction, exchange-repulsion (*vide infra*). Electrostatic interaction and polarization interaction is dipole related intermolecular interaction: Electrostatic interaction is dipole – dipole interaction which can be promoted by strong EWGs [31], and polarization energy is dipole – induced dipole interaction which can be estimated by induced electric field by the charge distribution of the other molecules [34]. Exchange-repulsion force' theoretical base is Pauli-exclusion principle[35], and this resulsion force become larger higher π-orbital overlab.

As stated earlier, organic crystal system has analytical merits to reveal structure-property relationship of organic functional materials powered by crystallographic measurements and quantum chemical computational calculation. However, optoelectrical properties are determined by various factors including molecular arrangements and electronic nature of organic crystals, and therefore, crystal structure engineering – prediction/ control the molecular arrangement – is desirable

to understand structure-property relationships of organic crystals. In this regard, studies to fabricate isostructural crystal – crystal systems have similarities in crystal packing/arrangement at least in one direction mediated by robust intermolecular interaction[36, 37] – can enable to reveal structure-property relations of organic functional crystals by the engineered molecular arrangement in the crystals. Similar term with isostructural crystals is isomorphic crystals – crystal system with similar external factors such as unit cell dimensions and same space group.[37, 38] There are fully isostructural crystals based on similar molecular structures, *e.g.*, digitoxigenin, (21S)-methyldigitoxigenin, and 3-epi-digitoxigenin have almost the same molecular arrangement in the unit lattice (**Figure 1-10**)[38], and also there is isomorphic crystals at **Figure 1-11**[39, 40]. These kind of isostructural/ isomorphic crystal system can be fabricated by the molecules having similarity, *i.e.*, isometric molecules[38]. There are number of moiety candidates to design isometric molecules, for example, chlorine (Cl) and methyl (Me) are in similar size (19, 24 $Å^3$ respectively [41]), for more example, see **Figure 1-10**. In fact, definition of isostructural crystals can be extended by introducing the concept 1-dimensional (1D) isostructural crystals and 2-dimensional (2D) isostructural crystals (*vide infra*). 1D isostructural crystals have similar crystal structure in one direction, *e.g.*, polymorphs of 6-hydroxypyridazin-3(2H)-one is 1D isostructural crystal: both polymorphs have same hydrogen bonded features side-by-side direction, while generated the same structured while molecular arrangement in π-stacking direction and inter-stack direction is different (**Figure 1-12a**) [36]. 2D isostructural crystals have similar molecular arrangement in the layer with different interlayer stacking, *e.g.*, polymorphs of 2,3,5,6-tetrachloroterephthalonitrile and 1,2,3,4,5,6-hexamethylbenzene cocrystal is 2D isostructural crystal by their displacements

between layers (**Figure 1-12b**)[36, 42].

In some cases, isometric molecules themselves are replaceable each other in the bi-component crystal system; they can interchange the position of each other. In these cases, crystallographic solution cannot resolve the exact position of each isometric molecules, *i.e.*, statistical disorder. Same behavior observed at cocrystal of isometric molecules (**Figure 1-13**); (E)-2-(4-bromobenzylidene)-5-(4-methylbenzyl)cyclopentan-1-one (**Me-Br**) and (E)-2-(4-bromobenzylidene)-5-(4-chlorobenzyl)cyclopentan-1-one (**Cl-Br**)[39, 43]. Due to the different conformation of each crystal, **Me-Br** showed 2+2 dimerization while **Cl-Br** has not shown any sign of photo-reaction: At the single-component crystal of **Me-Br**, conformation of dimer is rather planar, and thus double bond of each molecules is stay in close distance (4.5 Å) (**Figure 1-13a**), meanwhile, the **Cl-Br** dimer has some torsion thereby double bond is comparably far away each other (6.0 Å) (**Figure 1-13b**). The cocrystals of **Me-Br** and **Cl-Br** (**Figure 1-13c**) showed statistical disorder at Me/ Cl site, where occupation factor was 7:3 respectively. Interestingly, the cocrystal followed the conformation of **Me-Br** regardless of presence of **Cl-Br**, and the cocrystal also showed 2+2 dimerization by the favorable conformation to undergo photo-reaction with rather close distance between double bonds (5.1 Å). The statistical disorder is due to similar molecular structure of the molecules, and this kind of statistical disorder can be found other isometric molecules[44]. Other than the cocrystal system which have fixed stoichiometry, Isometric molecules often afford to generate crystalline solid solution system of which stoichiometry is variable [45]. In fact, crystalline solid solution includes not only the all homogeneous multi-component crystal but also statistically disordered multi-component crystals

(**Figure 1-14**) [45]. Crystalline solid solutions are roughly classified to substitutional crystalline solid solutions and interstitial crystalline solid solution, and there is solid solution which is not crystalline such as dispersed guest in the amorphous host.

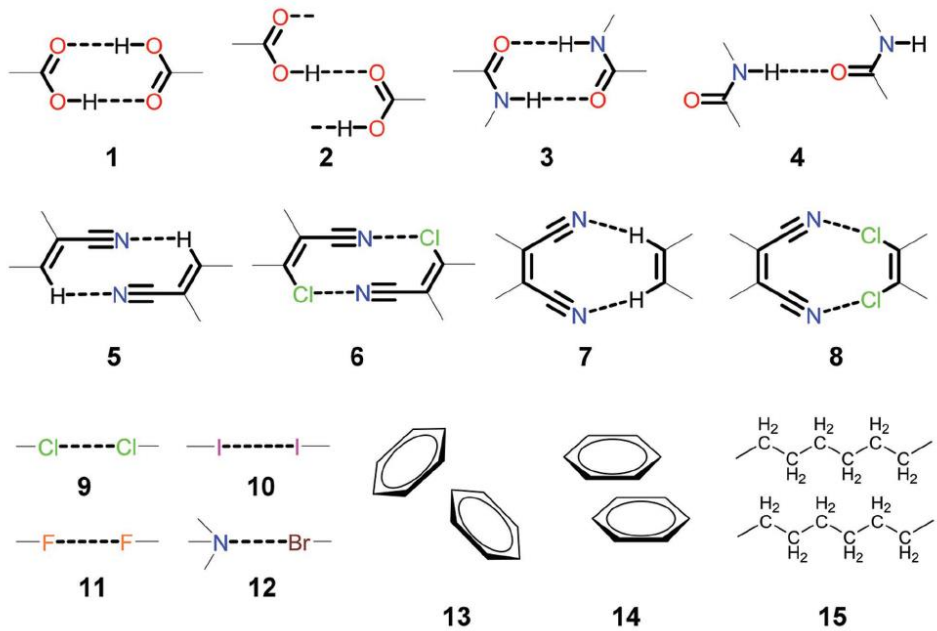

Figure 1-8. Supramolecular synthons in organic molecules[31].

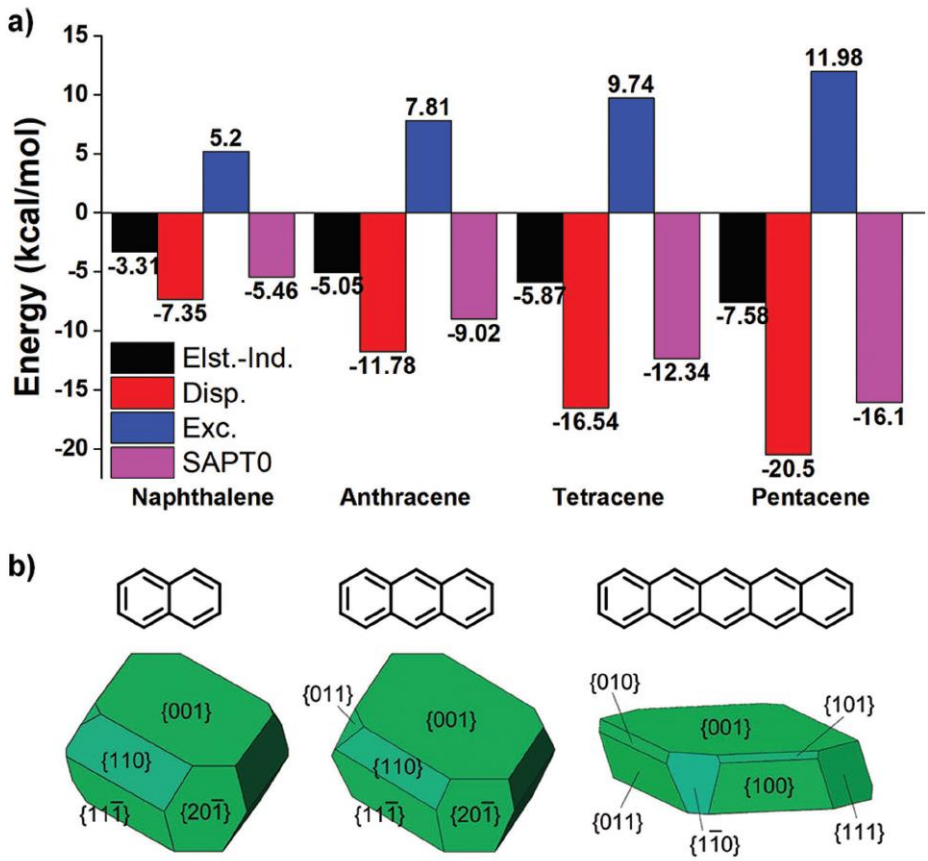

Figure 1-9. Intermolecular interaction in organic crystals. (a) Estimated various intermolecular interactions by SAPT0[33] and (b) their molecular structure and estimated crystalline morphology[35]

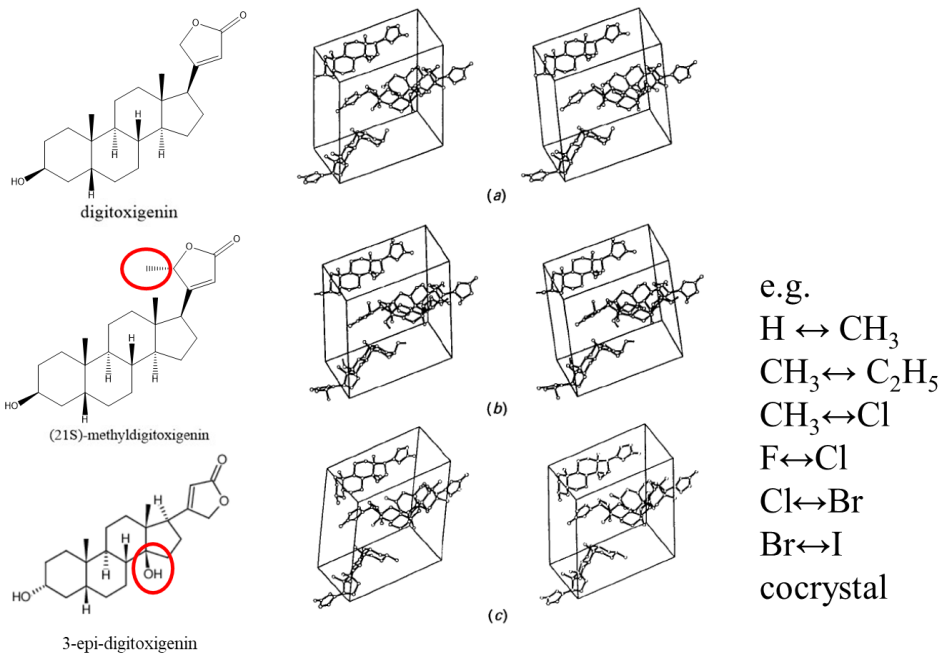

Figure 1-10. Isostructural crystals by isometric molecules and moiety candidates of isometric molecules.[38] Red circles depicts the similar sized moieties in the molecules.

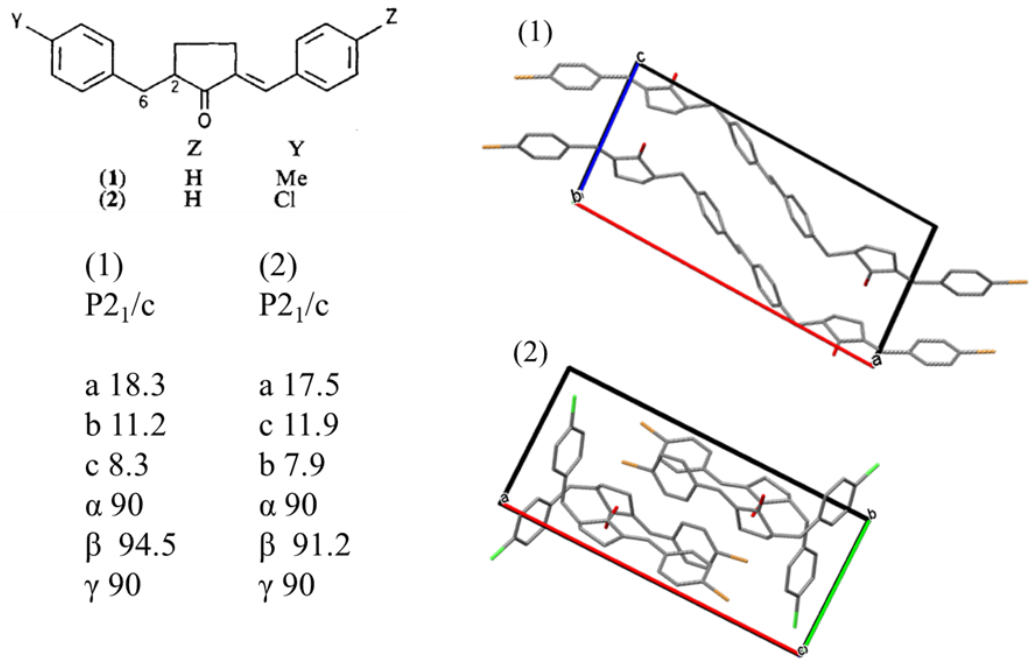

Figure 1-11. Isomorphic crystals by isometric molecules

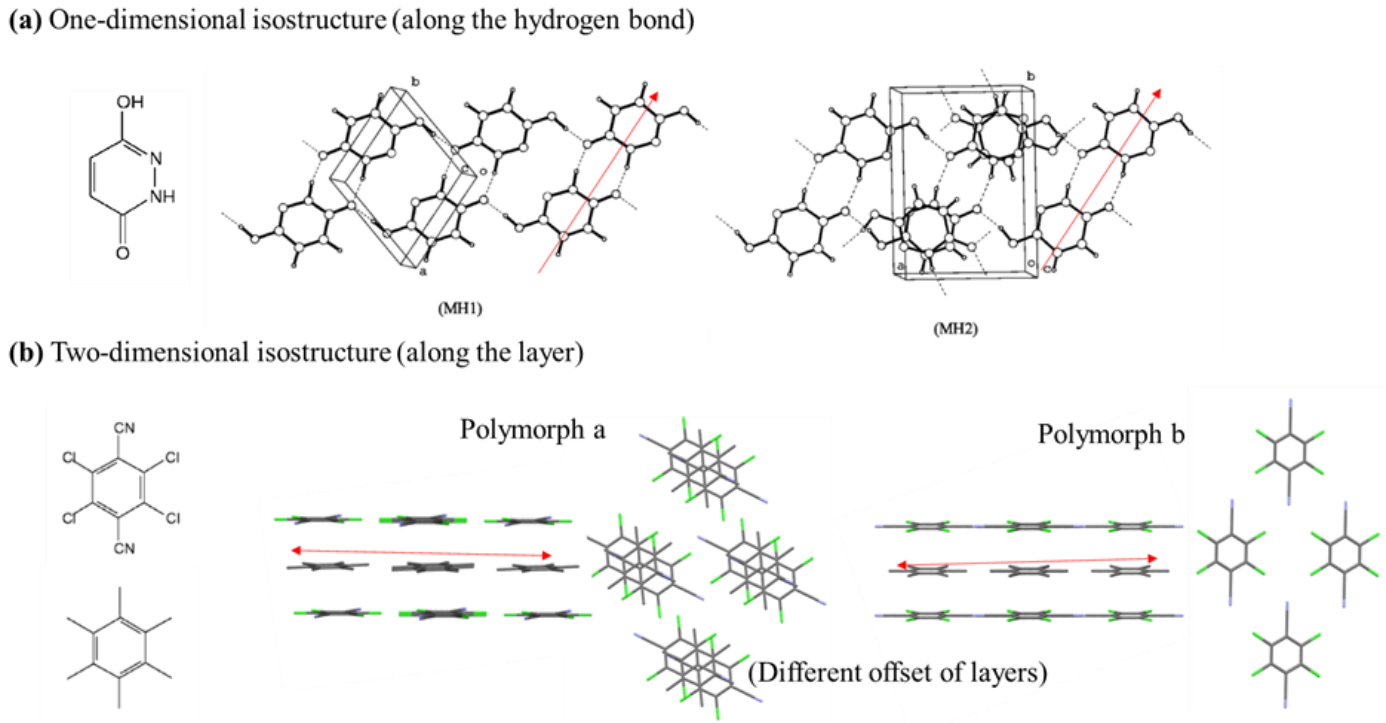

Figure 1-12. Example of 1D/2D isostructural crystals (a) 1D isostructural crystals[36]; polymorphs are isostructural along the direction of hydrogen bonds and (b) 2D isostructural crystals; polymorphs are isostructural along the layer. [36, 42]

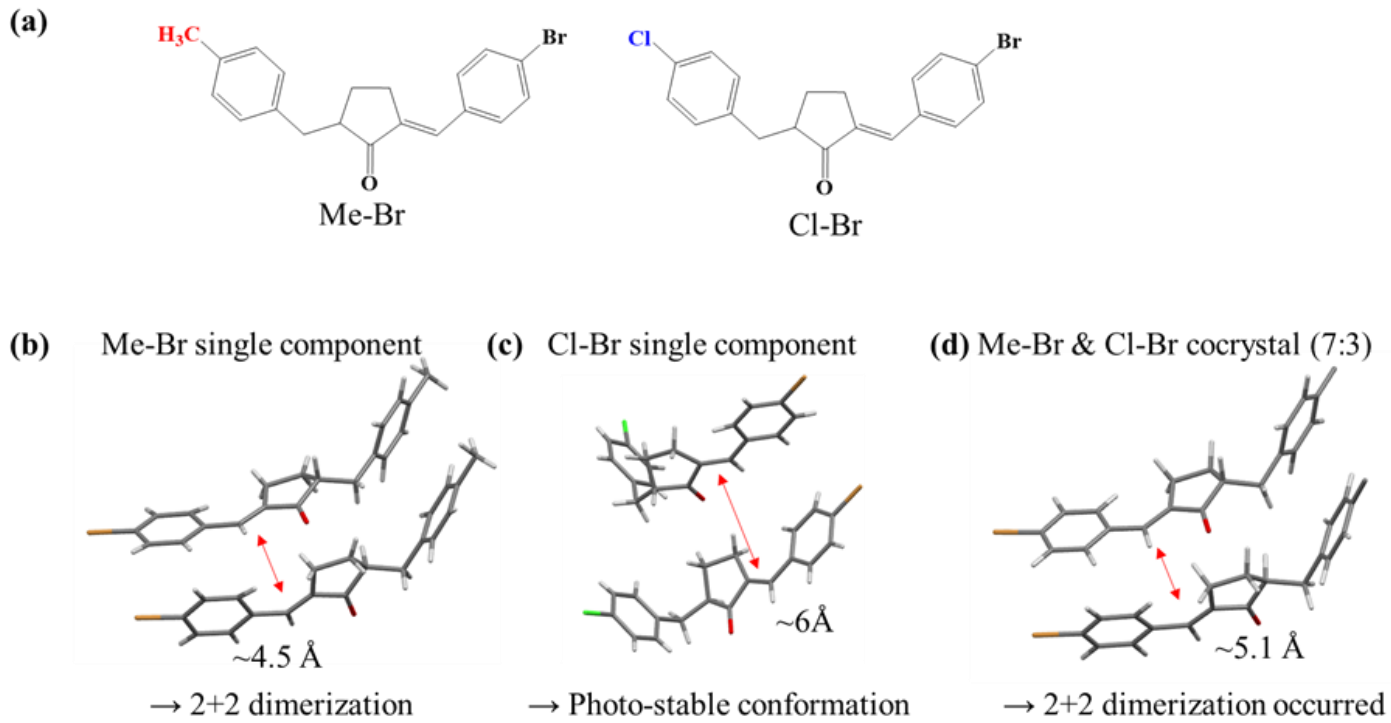

Figure 1-13. Example of statistical disorder at the cocrystal of isometric molecules[39, 43]

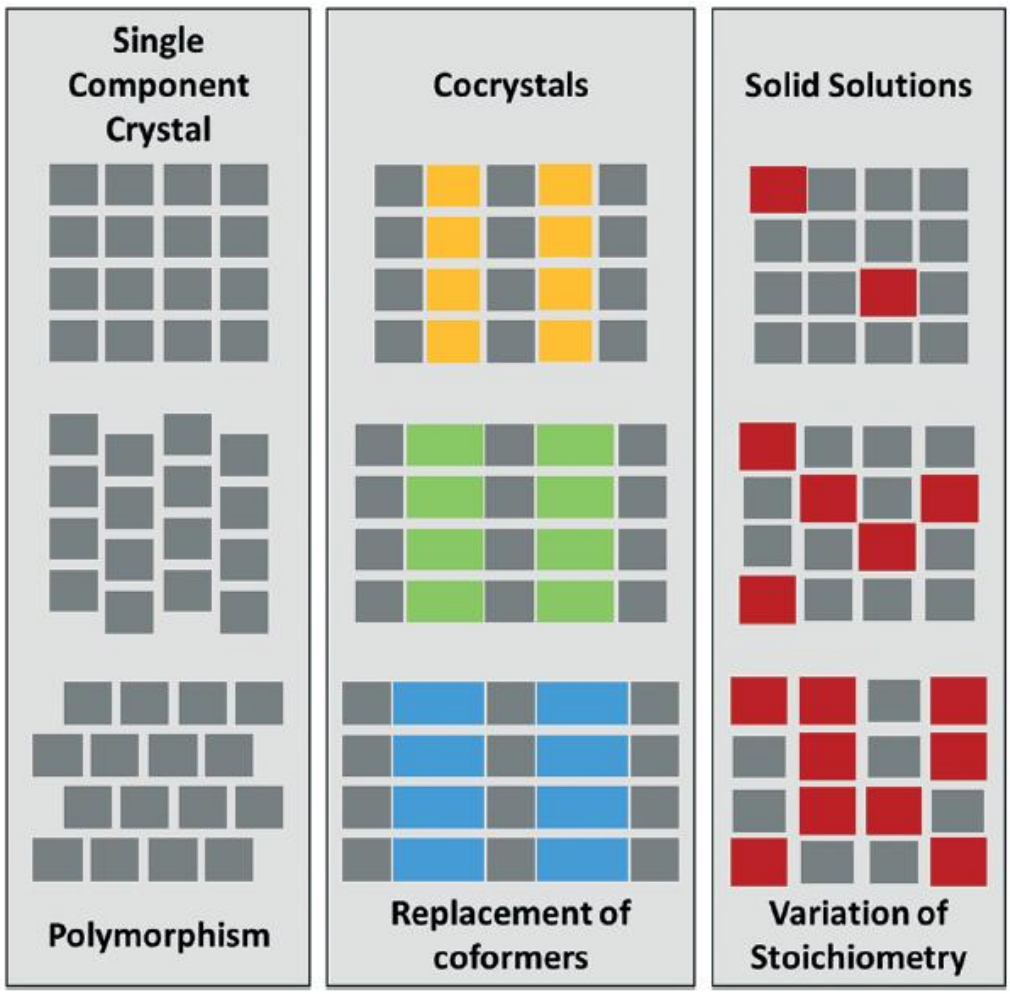

Figure 1-14. Schematics of single component crystals, cocrystals, and crystalline solid solutions[45]

1.3. Charge-transfer cocrystals and their optoelectrical properties.

The interaction between donor (D) and acceptor (A) have driven much interests in academic society, because they can endow useful functional distinct from the individual donor and acceptors; *e.g.,* exciton dissociation at charge-transfer (CT) state of solar cell[46], exciplex thermally activated delayed fluorescence (TADF) of light emitting devices [47, 48], and CT doping effect in transistors[49]. Among the D-A complexes in organic chemistry, the ground CT complex, they already transferred the charge each other in the ground state[50], which is different from the exciplex systems which is the result of interaction between excited state of donor (D*) and ground state of acceptor (A) and vice versa: A* and D [48].

FMOs of CT complex are localized to each D and A: CT complex' HOMO is localized to donor and LUMO is localized to acceptor, therefore CT complex have similar energy level with donor HOMO and acceptor LUMO (**Figure 1-15**)[51]. In conjunction with the interaction between charged molecules, CT complexes have high crystallinity to generate D:A cocrystals, and the CT cocrystals can be classified as their stacking nature of D-A molecules; segregated stack and mixed stack (**Figure 1-15**): In the segregated stacked CT cocrystals, donors and acceptors are formed separated column respectively, and each donors and acceptors in column stacked along π-stack direction, while the mixed stacked CT cocrystals has periodic sequence of D and A in the same column. Various molecular D and A for CT complexes are reported (**Figure 1-16**), and in fact, most of the CT complexes are confined to 7,7,8,8-Tetracyanoquinodimethane (TCNQ) derivatives[52, 53], and the design rule for CT co-crystals are not full determined yet and somewhat remain ambiguous [51, 52].

Straight forward method to assign on the CT complex formation is spectroscopic approach (*vide infra*). The simplest way is to investigate absorption spectrum, because other than exciplex case, they already formed CT between D and A in the ground state, so they have red-shifted CT band in the absorption spectrum[54, 55]. If the CT complex has luminescent character, red-shifted onsets of PLE than each counterpart can assign ground CT band without the effect of scattering of UV/Vis measurement. Also, the electron paramagnetic resonance (ESR) signal can be used: The CT co-crystals exhibit the resonance signals and the calculated value of g should be close to free electron value of 2.0023[52]. In addition, the lifetime became longer and the luminescence spectrum is red-shifted than that of donor and acceptor by the D:A interactions. There are other ways to assign the formation of CT complex; electrical density of olefin bonds (C=C) or C≡N bonds of TCNQ molecule in the CT complex is different without interaction [50, 52]. This can be can be detected by Raman or IR spectroscopy because the IR is relying on the dependence of oscillator strength of the charge-transfer band, and the Raman is relying on specific stretching mode of moieties. Other method to validate the CT interaction is to use the X-ray crystallography [56]: The bond length tends to be changed by CT interaction. However, assignment methods based on IR/Raman and bond-length is limited to TCNQ based molecules, and thus spectroscopic measurement can be the most reliable method for general assignment on CT complex formation.

CT cocrystals have shown various unique electrical/ optical properties distinct from D and A molecules including conductivity [57], ambipolar semiconductivity[54], optical wave guide[58], and room temperature phosphorescence (RTP) [59]. Other than

the electrical properties numerous functions can be expected with ground CT complex such as ferroelectricity[60] and stimuli-responsivity[61]. Classically, the electrical properties have been extensively researched from the first discovery on the pure organic conductor at 1973 [57]: CT complex of tetrathiafulvene (TTF) as donor and TCNQ as acceptor showed conductivity ~10^4 ohm^{-1} cm^{-1} at 6.6 K. Segregated stack CT cocrystals shows better electrical properties empirically (**Figure 1-17**)[50]. In addition, depending on the degree of charge transfer (DCT) of CT cocrystals, they can be semiconductor to superconductor[51]; the segregated CT cocrystals with DCT range around 0.5~0.75 showed superconducting behavior otherwise charges are too localized to transport at two extremes of DCT range which result in semiconducting behavior (**Figure 1-17)**. There are many ways to estimate DCT values; the change of specific bond length of TCNQ by crystallographic measurement[56], change of infrared (IR) and Raman peaks of TCNQ [50, 52], energy offset between D and A [56], electronic coupling of D and A [62], and summation of Mulliken charges [63]. On the other hand, the luminescent properties of CT cocrystals has been recently [58, 59, 64], therefore little is known for emission-structure properties on CT cocrystals[4]. In fact, this is attributed from the low oscillator strength (*f*) of emissive CT states by their small overlap between the ground and luminescent excited states [65]. In spite of this drawback of CT cocrystals as luminophores, there have been reports on high luminescent crystals of which PL quantum yields over 30 % with mixed stacked CT complexes of which quantum yield is in fact rare cases in CT complexes (**Figure 1-18**)[4, 54, 66, 67]. The understanding on the origin of high-efficient luminescent of CT cocrystals is still premature state, and therefore, systemic approach to unravel emission-structure relationship is desirable. It should be noted that side-stepped from the

TCNQ based CT complex, CT cocrystals of the isometric molecules of distyrylbenzene (DSB) based donors and acceptors showed all high luminescent character over 30 % [4, 54] which indicates isometric distyrylbenzene (DSB) based donors and acceptors can be the nice candidate for high luminescence CT cocrystals.

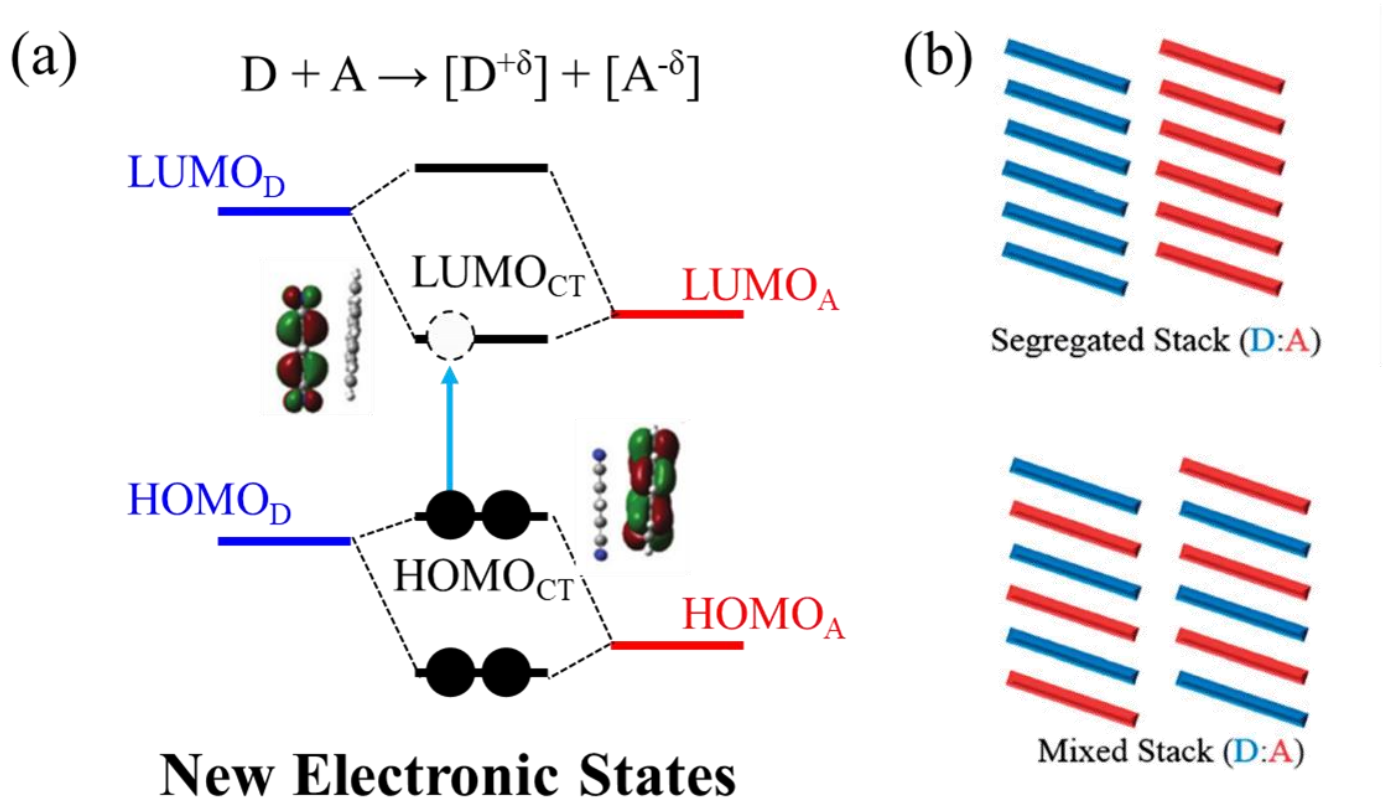

Figure 1-15. Electronic energy level and molecular stacking of organic CT complex. (a) Electronic energy level of CT complex and that of constituting donor and acceptor, and (b) Two kind of stacking modes of CT cocrystals; mixed stack and segregated stack arrangements[51].

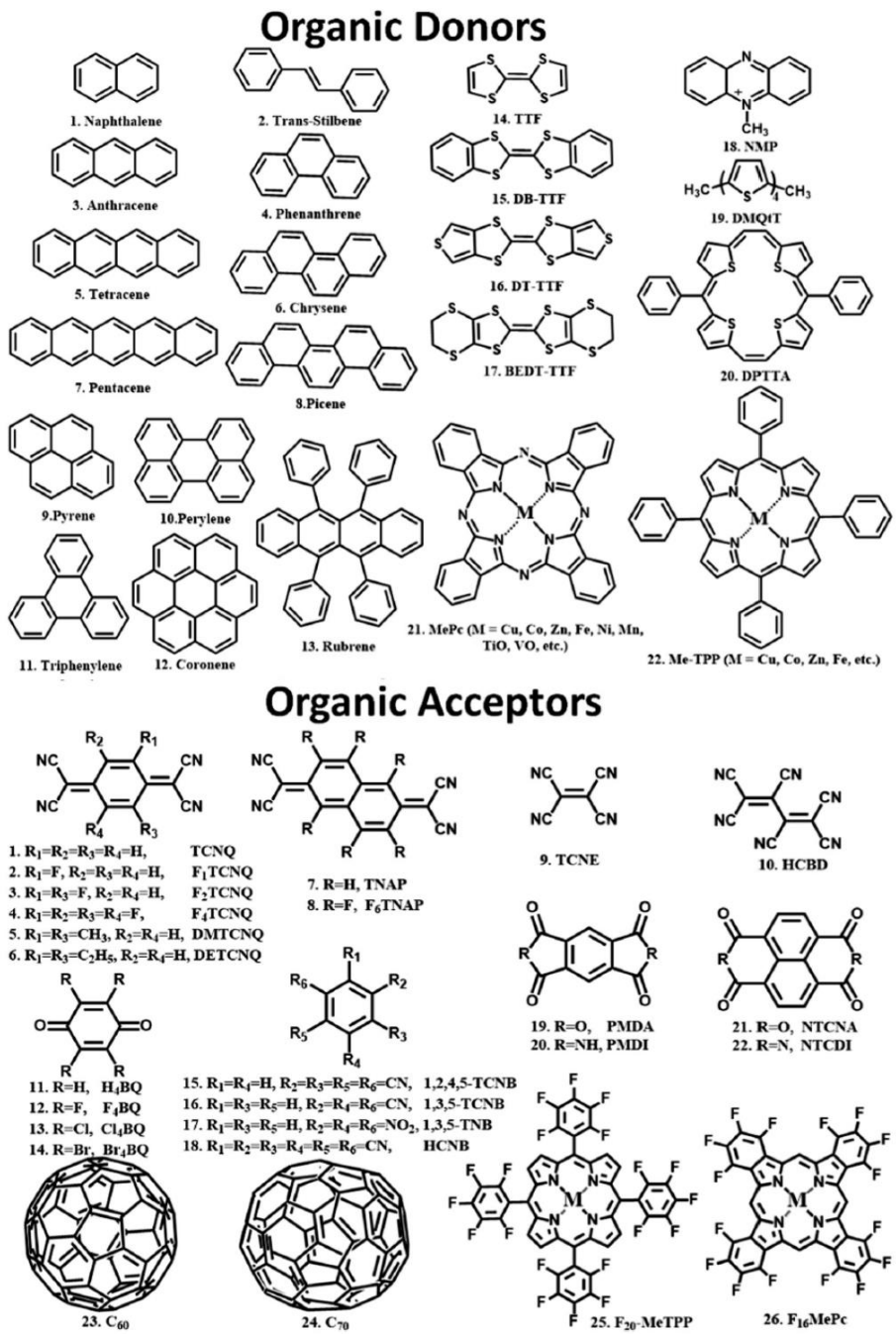

Figure 1-16. Organic donors and acceptors for CT complexes[50]

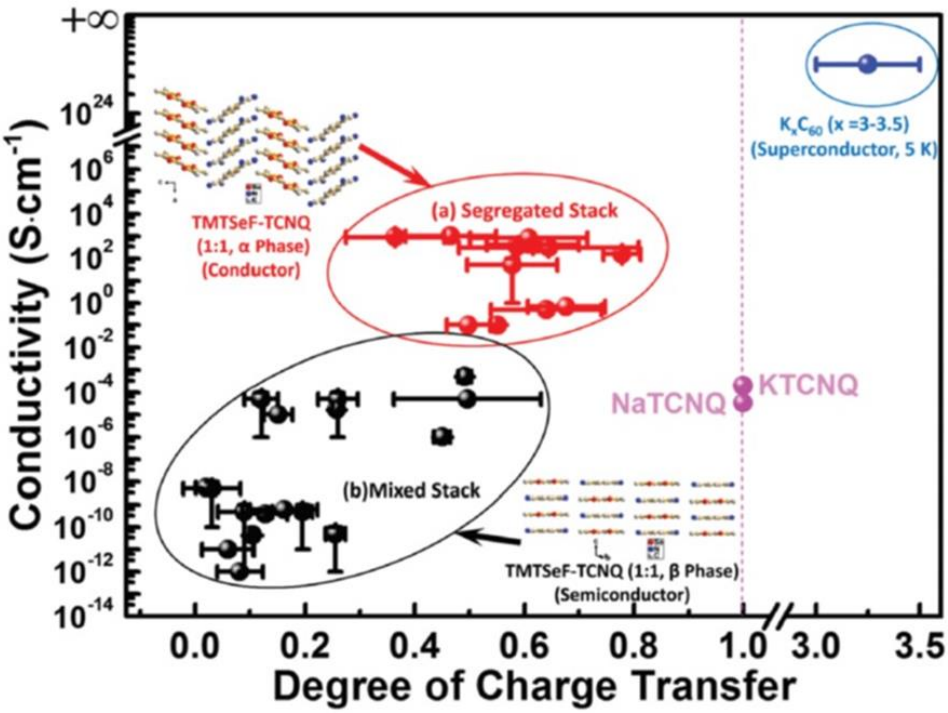

Figure 1-17. DCT and conductivity of CT complexes[50]

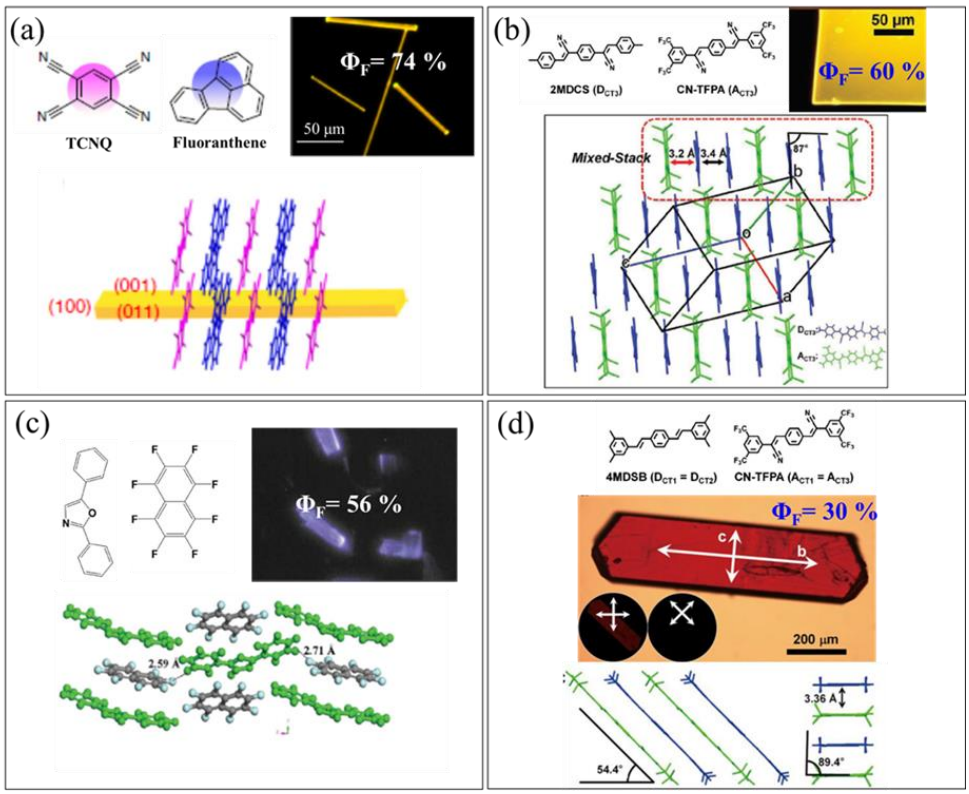

Figure 1-18. High luminescent CT complexes′ molecular structure, OM image under UV light, PL quantum yield (PLQY), and crystal structure (a) TCNQ and Fluoranthene based CT cocrystal with state-of-the art 74 % of PLQY [66], (b) DCS derivatives based CT cocrystal with 60 % of PLQY [4], (c) Diphenyloxazole and perfluoronaphthalene based CT cocrystal with 56 % of PLQY[67], and (d) DCS and DSB derivative based CT cocrystal with 30 % PLQY[54]. All of them are mixed stack CT cocrystals.

1.4. Micro-/ Nano-fabrication methods for organic materials

Micro-/ nano-fabrication is essential process for the practical device applications[68, 69]; *e.g.*, transistor array of active matrix[70], OLED pixels[71]. In this regard, patterning techniques closely related with the price of the commercial electronic goods, and thus good patterning techniques have scalability, high-throughput, cost-effectiveness as well as affordable high resolution patterns [72] of which traits in necessity are mainly focused by conventional photo-lithography techniques. However, the harsh patterning condition of photo-lithography can sacrifice the functionality of organic materials which are susceptible to outer stimuli by rather week secondary interaction between the constituting molecules. Therefore, organic compatible patterning which can replace the high efficiency of conventional photo-lithography is indispensable. Lithography techniques can be roughly classified in 3 parts: bottom-up, top-down and bottom-up & top-down hybrid approaches (**Figure 1-19**)[72, 73]. Bottom-up methods are based on physical or chemical self-assembly of materials such as polymer wrinkling and nucleation and growth of crystals [73]. Most of the patterning methods can be classified as top-down methods including photo-lithography techniques, direct writing methods, and soft-lithographic molding and printing methods (**Figure 1-19**).

Bottom-up methods can easily access to nano-scale fabrication, but they have limited application to self-assembling materials. Physical methods of bottom-up methods utilize self-assembly of substrate and forms winkles by physical pressure or heating, and chemical method utilize the self-assembly of target materials including self-relief grating (SRG) and self-assembly of block copolymer.

Top-down methods subtract the unwanted pattern from the pre-deposited film or

transfer and/or write the wanted patterns to the other substrate [74]. Representative patterning methods via solution process are described as follows (*vide infra*). Inkjet printing is direct writing technique which can apply to various substrates with only small amount of solvent with scalability[75]. Dip-pen nanolithography is also direct writing method which utilizes sharp probe of scanning probe microscopy. Inked tip of the probe draw the fine pattern with nanoscale resolution. In order to obtain accurate with high quality pattern, we must consider liquid-tip interaction and liquid-surface interaction carefully, so selecting appropriate combination of solution and substrate is important[72]. Micromolding in capillaries (MIMIC) employ pre-patterned soft stamp such as poly-(dimethylsiloxane) (PDMS). Because the MIMIC introduced the soft-elastomeric stamp PDMS, it is also classified as soft-lithography[76] (**Figure 1-19**). Capillary forces drive solution into gap between soft elastomeric stamp and substrate [68]. It should be noted the method based on solution process can be only applied to soluble materials, and always have a risk to solution expansion into adjacent patterns; *e.g.,* rather accurate and high resolution pattern hard to achieve via inkjet printing of which resolution limit is typically ~20 μm [75].

Representative top-down method without using solvent is nano-imprint lithography (NIL)[68]: Patterns on the template can be transferred by mechanical deformation. There are two types of NIL, one is thermal nano-imprint lithography (T-NIL) and the another one is photo-nano-imprint lithography (P-NIL). T-NIL processes under elevated temperature, above of T_g in the case of polymer, for efficient mechanical deformation of organic layers. P-NIL employ photo-curable resist, resist poured at patterned template, and radiate resist for patterned structure. Advantages of NIL are inexpensive setup, reusable template, high resolution and

high through-put, but organic layer can be damaged by elevated temperature and irradiations. There are also solvent-free soft-lithographic methods which introduce soft elastomeric stamp; heat and/or pressure was applied to ensure the adhesion with the target substrate and micro-patterned elastomeric stamp[77, 78]. These outer stimuli can lead to oxidation by heat[79-80] as well as pressure deformation[81].

In this regard, lithography methods with milder condition is required to realize the fully organic compatible patterning method. By virtue of the viscoelastic nature of elastomeric stamp, delamination speed of elastomeric stamp can kinetically control the adhesion energy: the fast delamination speed instaneously increases the young′s modulus by reinforced elasticity of elastomeric mold, and slow delamination speed lays down the attached film at the elastomeric stamp [82, 83]. Also as the adhesive stamp, commercialized pressure-sensitives tape can be utilized by virtue of their strong adhesion ability[84, 85]. The adhesion energy itself is hard to be diffused into adjacent patterns, and thus it is very compatible with stimuli-sensitive organic functional materials. However, many of the adhesion force lithographic methods confined their application to pre-determined patterns, *i.e.*, deterministic transfer (**Figure 1-20**)[70] which means additional patterning procedure other than adhesion lithography is required at adhesion lithography. We can also expect retained performance of organic functional material via vacuum deposition through fine metal mask (FMM) patterning method, unfortunately, their resolution limit are confined to 20 μm [86, 87].

Therefore, to overcome limitations of current patterning methods, it is highly desirable to develop patterning method for organic functional materials which

satisfy the following criteria; (i) solvent-free dry approach, (ii) non-evasive method such as adhesion lithography, (iii) high resolution (< 20 μm), and (iv) high-efficiency including scalability, cost-effectiveness, and high speed.

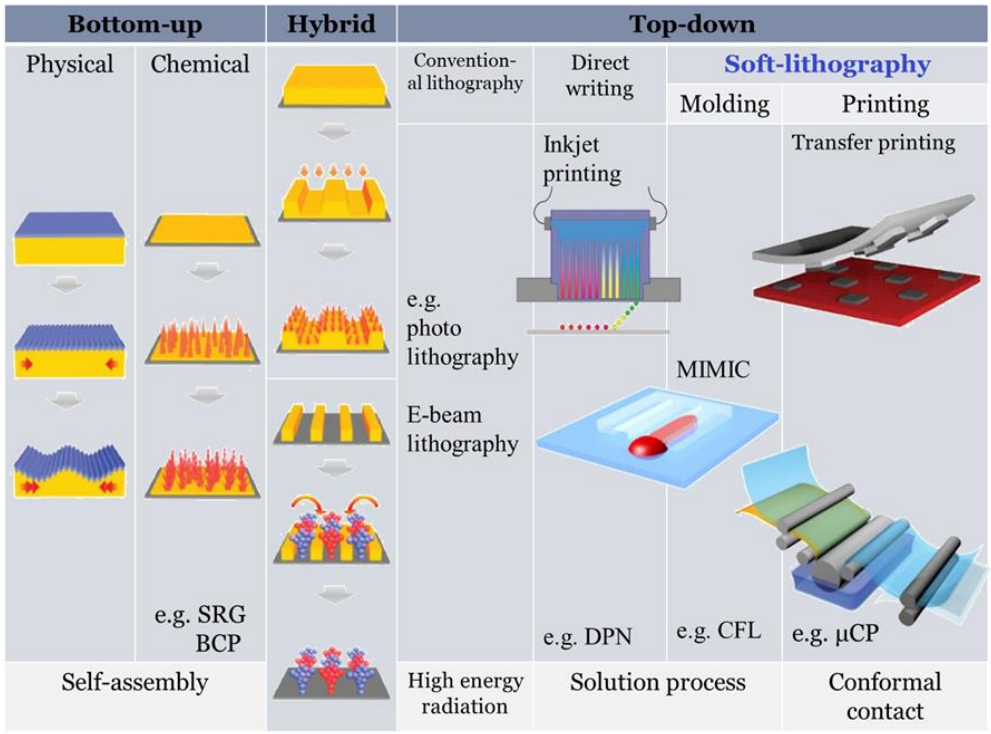

Figure 1-19. Rough classification of lithographic methods[73]

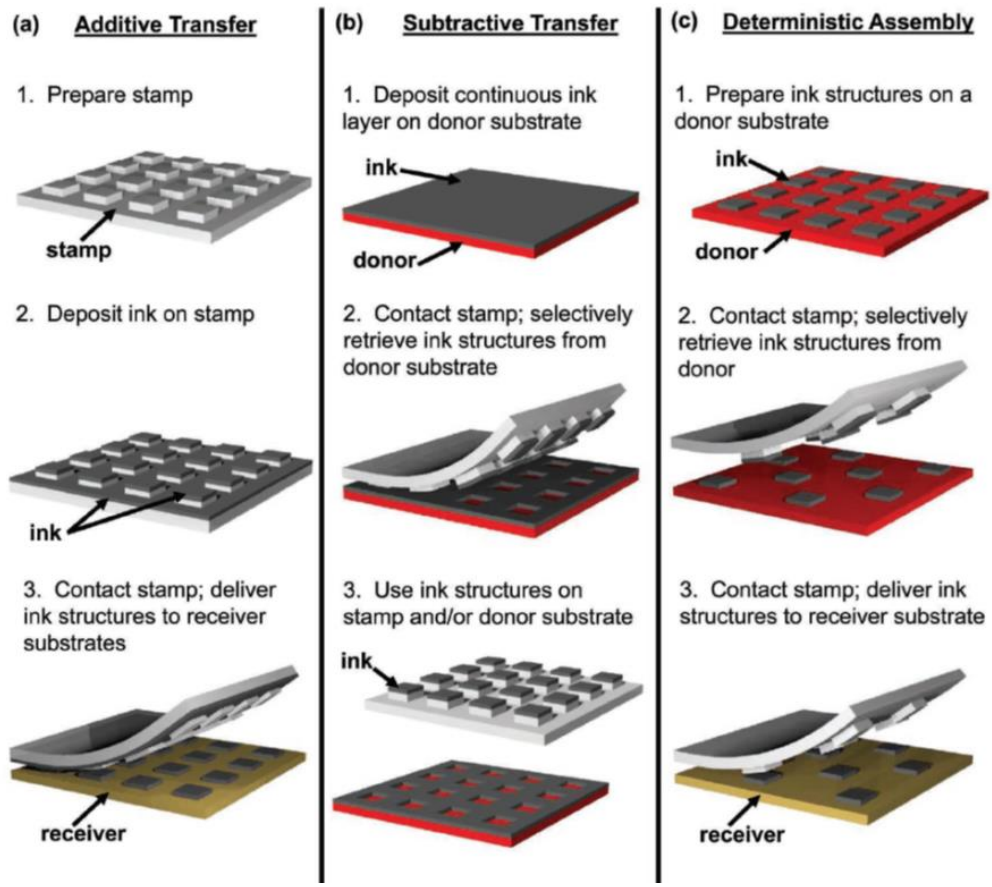

Figure 1-20. Dry pattern transferring methods via soft elastomeric stamp. (a) additive transfer, (b) subtractive transfer, and (c) deterministic transfer.

1.5. Contents of thesis

In this dissertation, I propose the quasi-isostructural CT crystals to unravel the optoelectrical property-structure relationships of CT complexes. Inspired by earlier reported isometric DSB donor (D1) and DCS acceptor (A1) molecules for 1:1 CT cocrystal[54], I designed additional isometric DSB donor (D2) and DCS acceptor (D2) to generate isostructural CT crystals. I have found CT complexes are successfully make for all four pairs with quasi-isostructural crystal structure. Interestingly, the CT complex of isometric molecules have demonstrated unique photo-physical/ optoelectrical/ crystallographic features distinct from individual donor and acceptor counterpart. Therefore, the origin of CT crystals' unique behaviors were unambiguously revealed by keeping the molecular arrangement factor in constant.

In Chapter 2, I presented the isometric design of D-A molecules to unravel the emission-structure relationship of charge transfer (CT) cocrystals. Up to date, photophysical processes of CT crystals particularly the emission-structure relationship in CT crystals remain ambiguous due to the common weak luminescence and arbitrary molecular designs of reported CT crystals so far. However, my elongated isometric D and A molecules designed to produce the extremely strong CT emission (record high PL quantum yields up to 83 %) in a predictive way. Because the four different D:A (1:1) CT pairs reproducibly all showed the quasi-isostructural intra-stack crystal structure, I could finally have correlated the electronic CT interaction and their photophysical properties by excluding the complicated morphological effect.

In Chapter 3, the quasi-isostructural crystalline solid solutions of four isometric

D-A pairs are presented. It was found that the D-A isometric molecular structure of crystalline solid solution have brought various unique scientifically/ technically important features than the other D:A systems such as bilayer and mixture: (i) densely packed structure warranted the high energy transfer (ET) efficiency up to 80% and thus giving CT emission at entire 2D acceptor crystals, (ii) substitutional doped CT complexes were structurally/ electrically non-destructive to host crystal even in heavily doped condition (20 %), and (iii) pairs of quasi-isostructural crystalline solid solutions ruled out the morphological factors and gave virtually ideal platform to unveil the structure-property relations of CT complex. Based on these systemic merits, I also found CT complexes in the host activated organic photo-transistor (OPT) behavior: The OPT device showed moderate photo-responsivity (~500 AW^{-1}) with few tens of threshold voltage shift (ΔV_{TH}). Furthermore, I could systemically correlated the OPT performances with the ET %, D:A energetical offsets, and electrical transport ability of the isostructural crystalline solid solutions system.

In Chapter 4, I presented a high-efficient soft-lithographic method for universal thin film patterning called patterned taping which indeed fully compatible with organic devices, and applied this method to CT crystal patterning. In fact, bilayers of the D and A layer showed novel stimuli-responsive behaviors: CT crystals are templated growth on the host crystal by solvent vapor exposure, orthogonal response of emission lights under polarizer rotation. Therefore, combining the patterned taping method and this stimuli-sensitive system, micro-patterned CT crystals are templated grown on the host crystal. To the end, the further morphological/ thermo-dynamical study unambiguously revealed the nucleation

and growth mechanism of CT cocrystals templated by host crystals, and also origin of novel optical behavior of templated grown CT on host crystal was fully revealed through the crystallographic information and optical investigations.

1.5. References

1. Ding R.; Feng J.; Dong F. X.; Zhou W.; Liu Y.; Zhang X. L.; Wang X. P.; Fang H. H.; Xu B.; Li X. B.; Wang H. Y.; Hotta S., Sun H. B. *Adv. Funct. Mater.,* **2017**, *27*.

2. Liu J.; Zhang H.; Dong H.; Meng L.; Jiang L.; Jiang L.; Wang Y.; Yu J.; Sun Y.; Hu W., Heeger A. J. *Nat. Commun.,* **2015**, *6*, 10032.

3. Briseno A. L.; Mannsfeld S. C.; Ling M. M.; Liu S.; Tseng R. J.; Reese C.; Roberts M. E.; Yang Y.; Wudl F., Bao Z. *Nature,* **2006**, *444*, 913-917.

4. Park S. K.; Kim J. H.; Ohto T.; Yamada R.; Jones A. O. F.; Whang D. R.; Cho I.; Oh S.; Hong S. H.; Kwon J. E.; Kim J. H.; Olivier Y.; Fischer R.; Resel R.; Gierschner J.; Tada H., Park S. Y. *Adv. Mater.,* **2017**, *29*, 1701346.

5. Li J.; Zhou K.; Liu J.; Zhen Y.; Liu L.; Zhang J.; Dong H.; Zhang X.; Jiang L., Hu W. *J. Am. Chem. Soc.,* **2017**, *139*, 17261-17264.

6. Gierschner J.; Varghese S., Park S. Y. *Adv. Opt. Mater.,* **2016**, *4*, 348-364.

7. Coropceanu V.; Cornil J.; da Silva Filho D. A.; Olivier Y.; Silbey R., Bredas J. L. *Chem Rev,* **2007**, *107*, 926-952.

8. Gierschner J., Park S. Y. *J. Mater. Chem. C,* **2013**, *1*, 5818-5832.

9. Ren Y.; Yang X. Y.; Zhou L.; Mao J. Y.; Han S. T., Zhou Y. *Adv. Funct. Mater.,* **2019**, *29*.

10. Li W., Kwok H. Conduction Mechanisms in Organic Semiconductors. In: Bhushan B (ed). *Encyclopedia of Nanotechnology*. Springer Netherlands: Dordrecht, 2012, pp 493-500.

11. Bredas J. L.; Beljonne D.; Coropceanu V., Cornil J. *Chem Rev,* **2004**, *104*, 4971-5004.

12. Dong H.; Fu X.; Liu J.; Wang Z., Hu W. *Adv. Mater.,* **2013**, *25*, 6158-6183.

13. Wang L.; Nan G.; Yang X.; Peng Q.; Li Q., Shuai Z. *Chem Soc Rev,* **2010**, *39*, 423-434.

14. Park S. K.; Kim J. H., Park S. Y. *Advanced Materials,* **2018**, *30*, 1704759.

15. Paterson A. F.; Singh S.; Fallon K. J.; Hodsden T.; Han Y.; Schroeder B. C.; Bronstein H.; Heeney M.; McCulloch I., Anthopoulos T. D. *Adv Mater,* **2018**, e1801079.

16. Oh S.; Park S. K.; Kim J. H.; Cho I.; Kim H.-J., Park S. Y. *ACS Nano,* **2016**, *10*, 3478-3485.

17. Uijttewaal M. A.; de Wijs G. A.; de Groot R. A.; Coehoorn R.; van Elsbergen V., Weijtens C. H. L. *Chemistry of Materials,* **2005**, *17*, 3879-3882.

18. Zhang F. Y.; Feng Y. W.; Song X. Y., Bu Y. X. *Physical Chemistry Chemical Physics,* **2016**, *18*, 16179-16187.

19. Wang C.; Dong H.; Hu W.; Liu Y., Zhu D. *Chem. Rev.,* **2012**, *112*, 2208-2267.

20. Shi J.; Aguilar Suarez L. E.; Yoon S.-J.; Varghese S.; Serpa C.; Park S. Y.; Lüer L.; Roca-Sanjuán D.; Milián-Medina B., Gierschner J. *J. Phys. Chem. C,* **2017**, *121*, 23166-23183.

21. Shi J. Q.; Izquierdo M. A.; Oh S.; Park S. Y.; Milian-Medina B.; Roca-Sanjuan D., Gierschner J. *Org. Chem. Front.,* **2019**, *6*, 1948-1954.

22. Dias F. B.; Penfold T. J., Monkman A. P. *Methods Appl Fluoresc,* **2017**, *5*, 012001.

23. An B.-K.; Gierschner J., Park S. Y. *Acc. Chem. Res.,* **2012**, *45*, 544-554.

24. Yoon S. J.; Varghese S.; Park S. K.; Wannemacher R.; Gierschner J., Park S. Y. *Adv. Opt. Mater.,* **2013**, *1*, 232-237.

25. Gierschner J.; Lüer L.; Milián-Medina B.; Oelkrug D., Egelhaaf H.-J. *J. Phys. Chem. Lett.,* **2013**, *4*, 2686-2697.

26. Kasha M.; Rawls H. R., Ashraf El-Bayoumi M. *Pure and Applied Chemistry,* **1965**, *11*, 371-392.

27. Kasha M. *Reviews of Modern Physics,* **1959**, *31*, 162-169.

28. Varghese S.; Park S. K.; Casado S.; Fischer R. C.; Resel R.; Milian-Medina B.; Wannemacher R.; Park S. Y., Gierschner J. *J. Phys. Chem. Lett.*, **2013**, *4*, 1597-1602.

29. Gierschner J.; Mack H. G.; Luer L., Oelkrug D. *J. Chem. Phys.*, **2002**, *116*, 8596-8609.

30. Oh S.; Kim J. H.; Park S. K.; Ryoo C. H., Park S. Y. *Adv. Opt. Mater.*, **2019**, *7*, 1901274.

31. Desiraju G. R. *Angew Chem Int Ed Engl*, **1995**, *34*, 2311-2327.

32. Massaro F. R.; Moret M.; Bruno M., Aquilano D. *Cryst Growth Des*, **2012**, *12*, 982-989.

33. Sutton C.; Marshall M. S.; Sherrill C. D.; Risko C., Brédas J.-L. *Journal of the American Chemical Society*, **2015**, *137*, 8775-8782.

34. Mackenzie C. F.; Spackman P. R.; Jayatilaka D., Spackman M. A. *IUCrJ*, **2017**, *4*, 575-587.

35. Sutton C.; Risko C., Bredas J. L. *Chemistry of Materials*, **2016**, *28*, 3-16.

36. Fabian L., Kalman A. *Acta Crystallogr B*, **2004**, *60*, 547-558.

37. Anthony A.; Jaskolski M.; Nangia A., Desiraju G. R. *Chemical Communications*, **1998**, 2537-2538.

38. Kalman A.; Parkanyi L., Argay G. *Acta Crystallographica Section B-Structural Science Crystal Engineering and Materials*, **1993**, *49*, 1039-1049.

39. Theocharis C. R.; Jones W.; Motevalli M., Hursthouse M. B. *J Cryst Spectrosc*, **1982**, *12*, 377-389.

40. Jones W.; Theocharis C. R.; Thomas J. M., Desiraju G. R. *J Chem Soc Chem Comm*, **1983**, 1443-1444.

41. Desiraju G. R., Sarma J. A. R. P. *P Indian as-Chem Sci*, **1986**, *96*, 599-605.

42. Britton D. *Acta Crystallogr B,* **2002**, *58*, 553-563.

43. Theocharis C. R.; Desiraju G. R., Jones W. *Journal of the American Chemical Society,* **1984**, *106*, 3606-3609.

44. Polito M.; D'Oria E.; Maini L.; Karamertzanis P. G.; Grepioni F.; Braga D., Price S. L. *Crystengcomm,* **2008**, *10*, 1848-1854.

45. Lusi M. *Crystengcomm,* **2018**, *20*, 7042-7052.

46. Yang Y.; Chen W.; Dou L. T.; Chang W. H.; Duan H. S.; Bob B.; Li G., Yang Y. *Nat Photonics,* **2015**, *9*, 190-198.

47. Kim K. H.; Yoo S. J., Kim J. J. *Chemistry of Materials,* **2016**, *28*, 1936-1941.

48. Sarma M., Wong K. T. *ACS Appl Mater Interfaces,* **2018**, *10*, 19279-19304.

49. Salzmann I.; Heimel G.; Oehzelt M.; Winkler S., Koch N. *Acc. Chem. Res.,* **2016**, *49*, 370-378.

50. Jiang H.; Hu P.; Ye J.; Zhang K. K. K.; Long Y.; Hu W. P., Kloc C. *J. Mater. Chem. C,* **2018**, *6*.

51. Goetz K. P.; Vermeulen D.; Payne M. E.; Kloc C.; McNeil L. E., Jurchescu O. D. *J. Mater. Chem. C,* **2014**, *2*, 3065-3076.

52. Sun L.; Zhu W.; Yang F.; Li B.; Ren X.; Zhang X., Hu W. *Phys. Chem. Chem. Phys.,* **2018**, *20*, 6009-6023.

53. Zhang Q.; Huang Y.; Wang Z., Chen Z. *Angew. Chem. Int. Ed.,* **2019**.

54. Park S. K.; Varghese S.; Kim J. H.; Yoon S. J.; Kwon O. K.; An B. K.; Gierschner J., Park S. Y. *J. Am. Chem. Soc.,* **2013**, *135*, 4757-4764.

55. Wykes M.; Park S. K.; Bhattacharyya S.; Varghese S.; Kwon J. E.; Whang D. R.; Cho I.; Wannemacher R.; Luer L.; Park S. Y., Gierschner J. *J. Phys. Chem. Lett.,* **2015**, *6*, 3682-3687.

56. Zhu L.; Kim E.-G.; Yi Y., Brédas J.-L. *Chem. Mater.*, **2011**, *23*, 5149-5159.

57. Ferraris J.; Walatka V.; Perlstei.Jh, Cowan D. O. *J. Am. Chem. Soc.*, **1973**, *95*, 948-949.

58. Zhuo M. P.; Tao Y. C.; Wang X. D.; Wu Y.; Chen S.; Liao L. S., Jiang L. *Angew. Chem. Int. Ed.*, **2018**, *57*, 11300-11304.

59. Ono T.; Taema A.; Goto A., Hisaeda Y. *chem. Eur. J.*, **2018**, *24*, 17487-17496.

60. Tayi A. S.; Shveyd A. K.; Sue A. C.; Szarko J. M.; Rolczynski B. S.; Cao D.; Kennedy T. J.; Sarjeant A. A.; Stern C. L.; Paxton W. F.; Wu W.; Dey S. K.; Fahrenbach A. C.; Guest J. R.; Mohseni H.; Chen L. X.; Wang K. L.; Stoddart J. F., Stupp S. I. *Nature*, **2012**, *488*, 485-489.

61. Park S. K.; Cho I.; Gierschner J.; Kim J. H.; Kim J. H.; Kwon J. E.; Kwon O. K.; Whang D. R.; Park J. H.; An B. K., Park S. Y. *Angew. Chem. Int. Ed.*, **2016**, *55*, 203-207.

62. Behera R. K.; Goud N. R.; Matzger A. J.; Brédas J.-L., Coropceanu V. *J. Phys. Chem. C*, **2017**, *121*, 23633-23641.

63. Zhu W.; Zheng R.; Zhen Y.; Yu Z.; Dong H.; Fu H.; Shi Q., Hu W. *J. Am. Chem. Soc.*, **2015**, *137*, 11038-11046.

64. Chu M.; Qiu B.; Zhang W.; Zhou Z.; Yang X.; Yan Y.; Yao J.; Li Y. J., Zhao Y. S. *ACS Appl. Mater. Interfaces*, **2018**, *10*, 42740-42746.

65. Tao Y.; Yuan K.; Chen T.; Xu P.; Li H.; Chen R.; Zheng C.; Zhang L., Huang W. *Adv Mater*, **2014**, *26*, 7931-7958.

66. Ye X.; Liu Y.; Guo Q.; Han Q.; Ge C.; Cui S.; Zhang L., Tao X. *Nat Commun*, **2019**, *10*, 761.

67. Yan D. P.; Yang H. J.; Meng Q. Y.; Lin H. Y., Wei M. *Adv. Funct. Mater.*, **2014**, *24*, 587-594.

68. Wen Y.; Liu Y.; Guo Y.; Yu G., Hu W. *Chem Rev*, **2011**, *111*, 3358-3406.

69. Persano L.; Camposeo A., Pisignano D. *Journal of Materials Chemistry C*,

2013, *1*, 7663-7680.

70. Carlson A.; Bowen A. M.; Huang Y.; Nuzzo R. G., Rogers J. A. *Adv. Mater,* **2012**, *24*, 5284-5318.

71. Muller C. D.; Falcou A.; Reckefuss N.; Rojahn M.; Wiederhirn V.; Rudati P.; Frohne H.; Nuyken O.; Becker H., Meerholz K. *Nature,* **2003**, *421*, 829-833.

72. Gates B. D.; Xu Q.; Stewart M.; Ryan D.; Willson C. G., Whitesides G. M. *Chem Rev,* **2005**, *105*, 1171-1196.

73. Bae W. G.; Kim H. N.; Kim D.; Park S. H.; Jeong H. E., Suh K. Y. *Adv Mater,* **2014**, *26*, 675-700.

74. Carlson A.; Bowen A. M.; Huang Y.; Nuzzo R. G., Rogers J. A. *Adv Mater,* **2012**, *24*, 5284-5318.

75. Lessing J.; Glavan A. C.; Walker S. B.; Keplinger C.; Lewis J. A., Whitesides G. M. *Advanced Materials,* **2014**, *26*, 4677-4682.

76. Qin D.; Xia Y., Whitesides G. M. *Nat Protoc,* **2010**, *5*, 491-502.

77. Park S. Y.; Kwon T., Lee H. H. *Advanced Materials,* **2006**, *18*, 1861-1864.

78. Kim K. H.; Bong K. W., Lee H. H. *Applied Physics Letters,* **2007**, *90*, 093505.

79. Katz H. E.; Lovinger A. J.; Johnson J.; Kloc C.; Siegrist T.; Li W.; Lin Y. Y., Dodabalapur A. *Nature,* **2000**, *404*, 478-481.

80. Jung Y.; Baeg K. J.; Kim D. Y.; Someya T., Park S. Y. *Synthetic Metals,* **2009**, *159*, 2117-2121.

81. Wang Z.; Zhang J.; Xing R.; Yuan J.; Yan D., Han Y. *J Am Chem Soc,* **2003**, *125*, 15278-15279.

82. Meitl M. A.; Zhu Z. T.; Kumar V.; Lee K. J.; Feng X.; Huang Y. Y.; Adesida I.; Nuzzo R. G., Rogers J. A. *Nature Materials,* **2006**, *5*, 33-38.

83. Yu J., Bulovic V. *Applied Physics Letters,* **2007**, *91*, 043102.

84. Liu S. H.; Becerril H. A.; LeMieux M. C.; Wang W. C. M.; Oh J. H., Bao Z. N. *Advanced Materials,* **2009**, *21*, 1266-1270.

85. Kim B. J.; Lee D.; Lee J., Yang S. *Journal of Micromechanics and Microengineering,* **2015**, *25*, 017003.

86. Kwon J. H., Lampande R. *OLED Manufacturing Process for Mobile Application*, 2018.

87. Cantatore E. *Applications of Organic and Printed Electronics: A Technology-Enabled Revolution*, 2013.

Chapter 2. Unraveling the Origin of High Efficiency Photoluminescence in Mixed-Stack Isostructural Crystals of Organic Charge-Transfer Complex: Fine-Tuning of Isometric Donor-Acceptor Pairs

2.1. Introduction

During the past few decades, π-conjugated organic molecules with semiconducting and/or luminescent properties have drawn much interest due to their potential for optoelectronic applications including organic light emitting diodes (OLED)[1, 2], organic field-effect transistors (OFET)[3], organic light emitting transistors (OLET)[4, 5] and organic lasers[6]. To this end, systematic studies on (electrical) transport-structure relationship and (luminescent) emission-structure relationship have been conducted for the targeted design of molecular materials with desirable optoelectronic properties[7, 8]. In this regard, organic crystals have necessarily been employed for the unambiguous structure-property relationships because the analysis has to be based on the known crystal structure; furthermore, the small surface-to-volume ratio in the crystal ensures that the properties are determined by the bulk.[8, 9, 10, 11] Based on such analytical merits of organic crystals and also their practical application potentials, extensive studies on the conductivity of π-conjugated organic crystals have been conducted; thus, transport-structure relationships in them is already established providing molecular design guidelines for high performance organic semiconductors [7, 11, 12, 13]. On the other hand, studies on the emission-structure relationship of luminescent π-conjugated organic crystals are lagging behind to the large extent. Only recently, we were able to report a systematic study on emission-structure relationship by using the extensive library of luminescent distyrylbenzene crystals which show moderate to high emission

efficiencies also with known crystal structures.[6, 8] Subsequently, the theoretical origin of solid state luminescence enhancement (SLE)[9] was investigated by systematically correlating the luminescent properties of organic crystals and various intermolecular factors such as J-/H-aggregation[9, 14], excitonic/ excimeric coupling [6, 8, 15], and also crystal size effect[6, 8, 10].

Among crystals of π-conjugated organic compounds, charge-transfer (CT) crystals constituted of electron donor (D) and electron acceptor (A) pairs are receiving increasing attention these days due to their unique transport and emission properties including conducting properties[16], ambipolar semiconductivity[17], ferroelectricity[18], electrically generated light emission,[4] stimuli-responsive emission[19], optical wave guides[20], room temperature phosphorescence (RTP)[21], and thermally activated delayed fluorescence (TADF)[22]. Theories for the charge transport properties of CT crystals have also been successfully developed to explain their unique electrical properties. [23, 24, 25]. On the other hand, only a handful of highly luminescent CT crystals among most of the weak luminescent CT crystals have been reported to date (**Table 2-1**) and thus little is known of their emission-structure properties[4, 26]. It is generally considered that the negligible oscillator strength (*f*) of emissive CT state due to the spatially separated frontier molecular orbitals (FMOs) in D and A molecules should result in weak luminescence[27]. It is also noted from **Table 2-1** that the mixed stack CT crystals are relatively more fluorescent than the segregated stack CT crystals [28, 29]. Apart from such fractional information, it is highly demanded to establish general emission-structure relationship for luminescent CT organic crystals, which however is extremely challenging, since the emission properties are not only determined by the molecular structures of the D and A pair, but also by the crystalline polymorphism

through different excitonic/electronic couplings in the crystal [8, 30, 31, 32, 33, 34]. Therefore, to explore the pure electronic effects of D-A pairs on the luminescent properties of CT crystal, it is necessary to warrant the isostructural crystal system while varying the D-A molecular structure to rule out the morphology effect in advance. It should be noted that isostructural crystals have similarities in crystal packing/arrangement at least in one direction mediated by robust intermolecular interaction[35, 36], while isomorphic crystals have similar external factors such as unit cell dimensions[36, 37].

In this work, we focus on developing isostructural systems of mixed-stack CT complexes to challenge the D-A structure-property correlation under identical morphology condition and thus to unveil the pure electronic mechanism of CT emission. To this end, we decided to employ a distyrylbenzene (DSB) type donor and a dicyanodistyrylbenzene (DCS) type acceptor, which form a dense, mixed-stack 1:1 D:A crystal by their isometric molecular structures[17]. The isometric concept combines *similarity* (same size and small structural differences between D and A) and *complementarity* (strong differences in the electronic nature) to generate densely packed, highly luminescent isostructural CT crystals. It should be noted, despite a pronounced CT character, bright red fluorescence (Φ_F = 0.30) of the single crystals was observed[26]. Our previous observation on this isometric CT pair (D1 and A1) has inspired us to extend the isometric D-A pairing concept to the series of isostructural crystal generation of the present work by adding additional isometric molecules D2 and A2 to fabricate four different potentially isostructural CT crystals as shown in **Figure 2-1**. To unveil the mechanism of CT emission from these isostructural crystals, single crystal X-ray analysis, photophysical measurements and time-dependent density functional theory (TD-DFT)

calculations are comprehensively carried out in this work. Importantly, the relationship between electronic nature of the D/A molecules and its effect on the CT luminescence of the crystals are clearly established by decoupling the morphological effect employing this isostructural system for the first time.

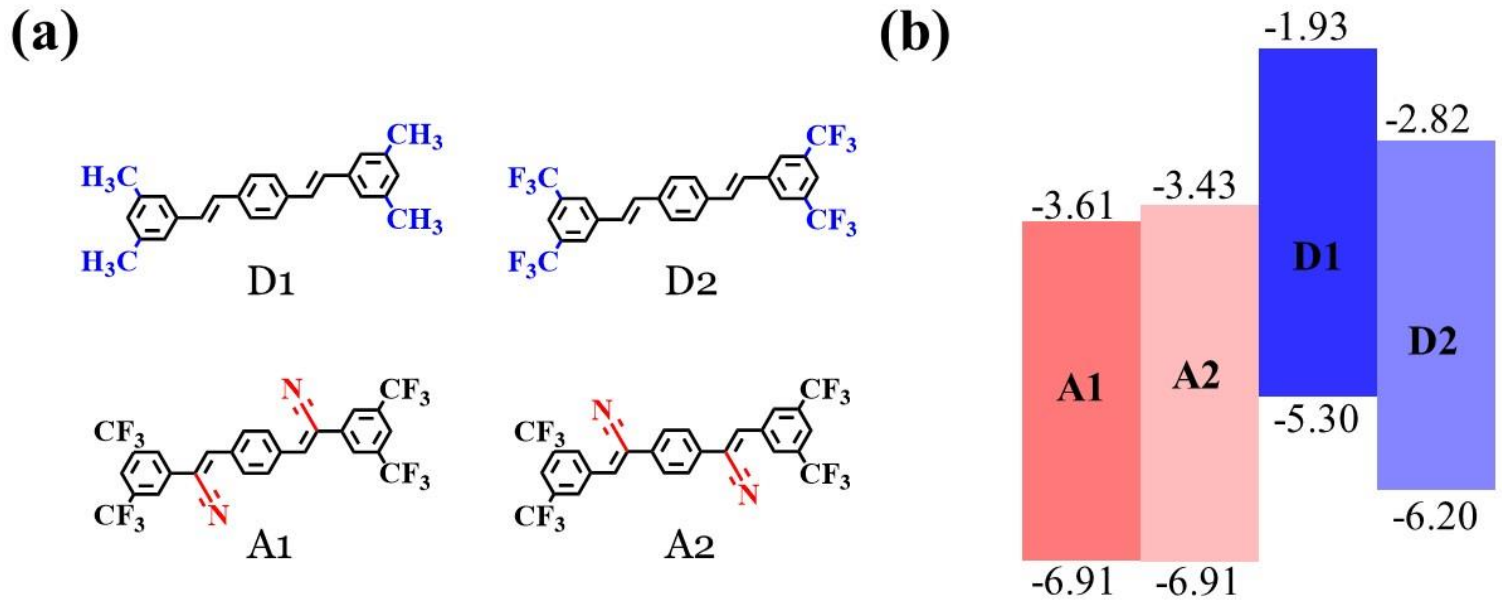

Figure 2-1. D:A CT co-crystals under study. (a) Design concept of the two donors (D1, D2) and two acceptors (A1, A2). (b) DFT-calculated HOMO and LUMO energy levels (B3LYP/ 6-311G*)

#	Pair	PLQY [%]	Stack
1	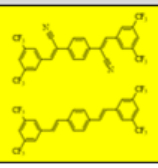	83	MS
2	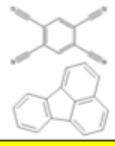	74	MS
3	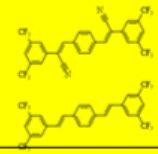	69	MS
4	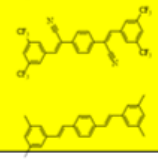	63	MS
5	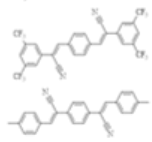	60	MS
6	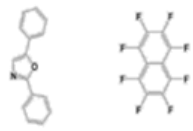	56	MS
7	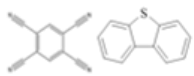	47	MS
8	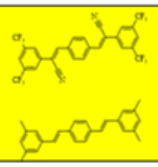	30	MS

#	Pair	PLQY [%]	Stack
17	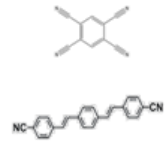	13	SS
18	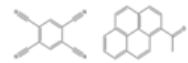	12	MS
19	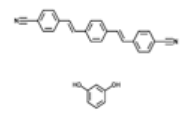	12	SS
20	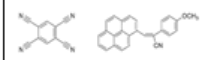	11	MS
21	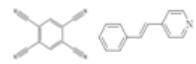	10	MS
22	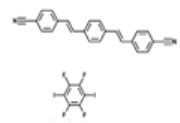	9	MS
23	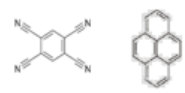	9	MS
24	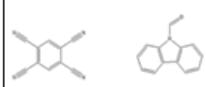	7	MS

Continued...

#	Pair	PLQY [%]	Stack
9	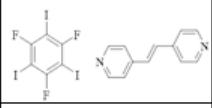	26	SS
10	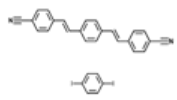	26	MS
11	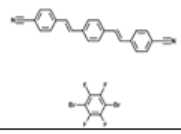	26	MS
12	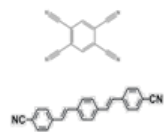	26	MS
13	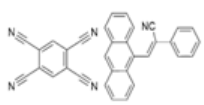	21	MS
14	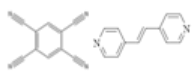	19	MS
15	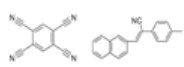	14	MS
16	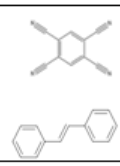	14	MS

#	Pair	PLQY [%]	Stack
25	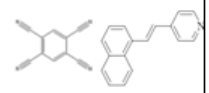	7	MS
26	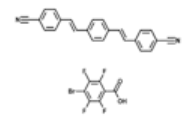	6	MS
27	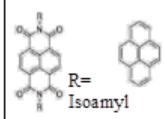 R= Isoamyl	4	MS
28	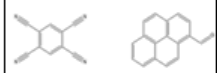	4	MS
29	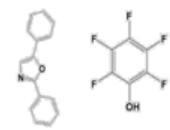	3	MS
30	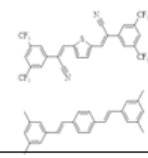	3	MS
31	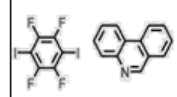	1	SS
32	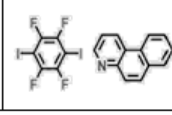	1	MS

Table 2-1. Summary of luminescent CT crystal survey
Yellow highlight : CT crystal covering in this work, Red letter: Segregated stacked (SS) CT crystals, Black letter: Mixed stacked (MS) CT crystals

2.2. Experimental

Material

In every experiment, sublimed grade of donors and acceptors were used. Synthesis and assignment of 4M-DSB (D1) and β-CN-TFPA (A1) were described elsewhere.[17] The reagents were purchased from Sigma Aldrich Chemical Co. (Darmstadt), Tokyo Chemical Industry Co. (Tokyo), and Alfa Aesar Co. (Massachusetts). Synthesis and assignment of 4CF3-DSB (D2) and α-CN-TFPA (A2) can be found at **Figure 2-2**.

Tetraethyl (1,4-phenylenebis(methylene))bis(phosphonate) 1,4-bis(bromomethyl)benzene (8.0 g, 30 mmol) and triethyl phosphate (25.2 g, 151 mmol) were added to toluene 70ml solution, and the mixture was stirred under reflux in 115 ˚C for 3 hr. After cooling, the mixture was poured into water and extracted with dichloromethane. The solvent was evaporated in 80 ˚C vacuum. Column chromatography using dichloromethane and sequent re-precipitation with n-hexane/dichloromethane co-solvent yield the white powder product (9.3 g, 81%). ^{1}H NMR ($CDCl_3$) δ [ppm]: 7.25 (s, 4H, Ar-H), 4.01 (m, 8H, OCH_2), 3.13 (d, 4H, $ArCH_2$), 1.67 (s, 4H, PCH_2), 1.24 (m, 12H, CH_3)

4CF$_3$-DSB (D2) tetraethyl (1,4-phenylenebis(methylene))bis(phosphonate) (5 g, 13.2 mmol) and 3,5-bis(trifluoromethyl)benzaldehyde (6.4g, 26.4 mmol) was added to tetrahydrofuran 100 ml solvent. Then the tert-potassium butoxide powder (3.71 g, 33 mmol) was added to solution and stirred at 25 ˚C for 1 hr. With the crude solution, column chromatography of tetrahydrofuran solvent was done, and sequent re-crystallization yield 4CF$_3$-DSB powder (3.5 g, 48 %). The product was assigned with NMR and EA after sublimation. ^{1}H NMR (THF) δ [ppm]: 8.17 (s,

4H, Ar-H), 7.87 (s, 2H, Ar-H), 7.67 (s, 4H, Ar-H), 7.47 (d, 4H, Vinyl-H)

Calculated elemental analysis result for $C_{26}H_{14}F_{12}$: C, 56.31: H, 2.55: F, 41.15. Found: C, 58.39: H, 2.42.

α-CN-TFPA (A2) 2,2'-(1,4-phenylene)diacetonitrile (10.8 g, 44.6 mmol) and 3,5-bis(trifluoromethyl)benzaldehyde (3.5 g, 22.3 mmol) was solvated in tert-butyl alcohol 250 ml. The Tetrabutylammoniumhydroxide (TBAH) in MeOH 1M solution was added (4.46 ml, 4.46 mmol) to the mixture solvent and stirred at 50 ˚C for 1 hr. Column chromatography with tetrahydrofuran solvent yielded product (6g, 45%). The product was assigned with NMR and EA after sublimation. ^{1}H NMR ($CDCl_3$) δ [ppm]: 8.35 (s, 4H, Ar-H), 7.98 (s, 2H, Ar-H), 7.85 (s, 4H, Ar-H), 7.70 (s, 2H, Vinyl-H). Calculated elemental analysis result for $C_{28}H_{12}F_{12}N_2$: C, 55.62: H, 2.00: F, 37.74: N, 4.64. Found: C, 55.55: H, 2.02: N, 4.67. Characterization of the synthesized materials were done after careful purification through sublimation.

Sample preparation

For the NC suspension, 0.2 ml of THF solution (5×10^{-4} M) was added to the vigorously stirring 9.8 ml of water. After 30 min of stirring, 10 ml of NC suspension (THF:H_2O = 2:98, 1×10^{-5} M) was obtained, and formation of the NC suspension was verified by the occurrence of the Tyndal effect. For the micro crystal formation via drop-casting (DC) method, the silicon/silicon oxide(Si/SiO_2) substrates were subsequently rinsed under sonication of water, acetone, and isopropyl alcohol (IPA), and then treated by ozone plasma. After that, the 1×10^{-2} M of THF solution was dropped onto the prepared substrates and dried under ambient conditions. For the vacuum deposited (VD) film, the Si/SiO_2 substrates were cleaned with the same method, and the material was vacuum deposited under high

vacuum condition (1×10^{-6} Torr). For the bhe bulk single crystal (SC) samples of CT-O, CT-Y', and CT-G, saturated solutions were obtained with a good solvent (e.g., THF, benzene, dichloromethane; DCM), and seeding was provoked by slowly diffusing the poor solvent (methanol) into the solution. The CT-Y SC samples were obtained through physical vapor transport (PVT) under inert argon (Ar) gas flowing condition.

Sample characterization

UV/Vis absorption spectra were obtained from a UV-1650 PC spectrometer (Shimadzu) equipped with halogen lamp and deuterium lamp. The PL and PLE spectra were measured from QM-40 (Photon Technology International) of which light source and detection method is high power continuous Xenon arc lamp and photon counting/analog method respectively. The fluorescence quantum yields Φ_F were obtained in the same setup, using an integrating sphere accessory. Fluorescence lifetimes and TRES were obtained from Fluo Time 200 (PicoQuant GmbH) by the time-correlated single photon counting (TCSPC) technique. The excitation source was 375 nm laser diode (LDH-P-C-375) of pulse width (FWHM) <40 ps controlled by PDL800-D diode laser driver at a repetition rate of 80MHz. The decay time was fitted through FluoFit Pro software. The temperature dependency of the samples was measured via a liquid N_2 Cryostat. The out of plane XRD data was taken by the D8 advanced X-ray diffractometer (Bruker Miller) of which irradiation source is Cu Ka1with 3 degree/min scanning speed, and the d-spacing of the same was extracted from the out-of-plane XRD data using Bragg's equation: $n\lambda = 2d\sin\theta$. The GIXD data was obtained by PLS-II 9A U-SAXS beamline of the Pohang Acceleration Laboratory in Korea. The optical microscope images were taken by Leica DMLP polarizing optical microscope.

For the X-ray diffraction analysis of structural characterization of CT-Y (CT-Yb) and CT-Y'(CT-Ya), data collections were performed at the XRD1 X-ray diffraction beamline of the Elettra Synchrotron, Trieste (Italy).[38] Crystals were dipped in NHV oil (Jena Bioscience, Jena, Germany), mounted on kapton loops (MiTeGen, Ithaca, USA) and flash cooled in liquid nitrogen. Complete datasets were collected at 100 K (nitrogen stream supplied through an Oxford Cryostream 700 - Oxford Cryosystems Ltd., Oxford, United Kingdom) through the rotating crystal method. Unit cell parameters have been checked on data collected at 298 K: despite diffraction limits are much poorer the same lattice parameters are found at both temperatures, for each crystal form (CT-Y, CT-Y'), suggesting that no phase transition happens upon cooling. Data were acquired using a monochromatic wavelength of 0.700 Å, on Pilatus 2M hybrid-pixel area detectors (DECTRIS Ltd., Baden-Daettwil, Switzerland). The diffraction data were indexed and integrated using XDS.[39] For the triclinic CT-Y crystal form two different datasets have been merged using CCP4-Aimless code.[40, 41] All the structures were solved by the dual space algorithm implemented in SHELXT.[42] Fourier analysis and refinement were performed by the full-matrix least-squares methods based on F^2 implemented in SHELXL (Version 2018/3)[43]. The Coot program was used for modeling.[44] Anisotropic thermal motion refinement have been used for all atoms. Hydrogen atoms were included at calculated positions with isotropic $U_{factors} = 1.2 \cdot U_{eq}$ (U_{eq} being the equivalent isotropic thermal factor of the bonded non hydrogen atom). Geometric (DFIX, DANG, FLAT) and thermal (SIMU) restrains have been used for poorly defined/disordered fragments. Both CT-Y, CT-Y' solid phases can be described using a single molecular unit. The asymmetric units (ASU – **Figure 2-3**) contain one full CN-TFPA in the CT-Y triclinic form and half bis-

(trifluoromethyl)phenyl)acrylonitrile (CN-TFPA) fragment in the monoclinic crystal form of CT-Y'.

For single crystal X-ray diffractometry of CT-O and CT-G, a single crystal was selected, mounted on a glass rod on a copper pin, and placed in the cold N_2 stream provided by an Oxford Cryosystems cryometer (T=100 K). XRD data collection was performed on a Bruker APEX II diffractometer with use of Mo Kα radiation (λ= 0.71073 Å) from an IμS microsource and a CCD area detector. Empirical absorption corrections were applied using SADABS.[45, 46] All the structures were solved by the dual space algorithm implemented in SHELXT.[42] Fourier analysis and refinement were performed by the full-matrix least-squares methods based on F^2 implemented in SHELXL (Version 2018/3)[43]. The space group assignments and structural solutions were evaluated using PLATON.[47, 48] All non-hydrogen atoms were refined anisotropically. All other hydrogen atoms were placed in calculated positions corresponding to standard bond lengths and angles using riding models. All CF_3 groups in the solid state structure of CTG are disordered and were modelled using SIMU and ISOR constraints.

Quantum-chemical calculations

The geometries of the molecules in vacuum were optimized imposing Ci symmetry by DFT using the B3LYP functional and 6-311G* basis set as defined in the Gaussian09 program package.[49] To calculate the characteristics of free dimer pairs for the different co-crystals, nearest-neighbor pairs from the X-ray analysis were replaced by DFT-optimized molecules, however imposing the torsional angles found in the X-ray analysis. Vertical $S_0 \rightarrow S_n$ transition energies were then obtained by single point TD-DFT calculations.

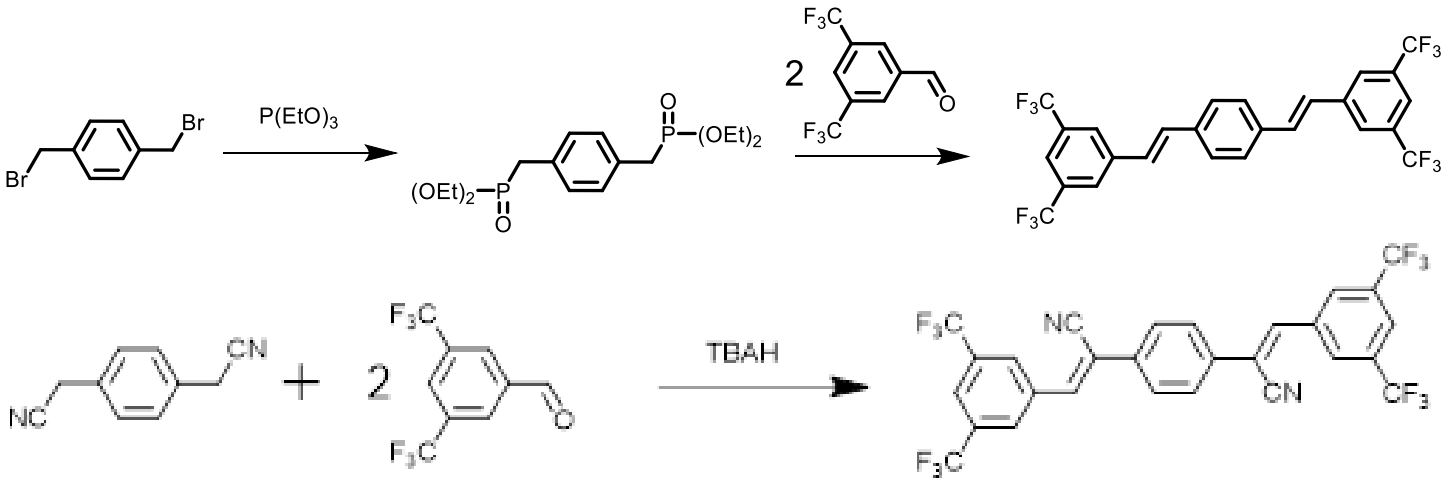

Figure 2-2. Material synthesis and assignment

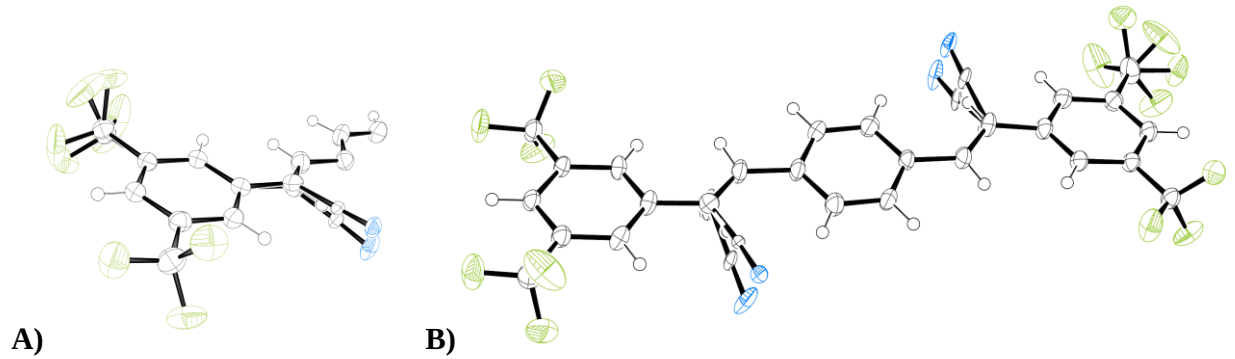

Figure 2-3. Ellipsoids representation of ASU contents (50% probability) for A) CT-Y' (CT-Ya) and B) CT-Y (CT-Yb).

2.3. Result and discussion

2.3.1. Molecular Design and Co-Crystal Formation

The original CT D-A pair comprised a DSB-based donor (4M-DSB, D1) and a DCS-based acceptor (β-CN-TFPA, A1; **Figure 2-1**), which formed a tightly packed luminescent crystal by virtue of their isometric D-A molecular structures.[4, 17] Within our isometric CT concept, the structural and dimensional differences between D and A were kept to a minimum, whereas the variation of electronic factors was intended to be maximized. For this, both D1 and A1 carry CR_3 groups in the meta-positions of the terminal rings, however being R = H for D1 and R = F for A1. The substitution of H by F secures a strong energetic stabilization of the frontier molecular orbitals (FMOs) by the high electronegativity of the F atom,[50] while the substituent size is very similar (atomic radii of H and F are 42 and 53 pm, respectively).[51] Stabilization of the FMOs in A1 is further enhanced by cyano (CN) substitution in the outer (β) position of the vinylene unit, where the steric demand of CN is moderate.[32] In doing so, the strong intermolecular FMO interaction between D1 and A1 gave rise to the CT absorption rendering the intense red color,[17] and the non-zero oscillator strength of the emitting state by favorable configuration interaction together with the highly suppressed non-radiative decay secured strong CT luminescence.[26]

For the generation of isostructural CT crystals in this work, we synthesized an additional donor ($4CF_3$-DSB, D2) and an acceptor (α-CN-TFPA, A2, **Figure 2-1a** and **Figure 2-2**), which also share isometric features with D1 and A1. Briefly, D2 differs from D1 that it carries meta-CF_3 instead of CH_3 groups, and A2 differs from A1 that CN substitution is carried out in the inner (α) position instead of β. For the

co-crystallization, solutions of D and A (1×10^{-2} M, tetrahydrofuran; THF) were mixed in all four possible D:A combinations in a 1:1 ratio, and each mixed solution was simply drop-cast onto SiO_2 substrates (**Figure 2a-d**). We emphasize at this point that isostructural stacking is expected for all isometric D-A pairs not only due to the molecules' isometric structure but also to their elongated shapes. The rod-like shape roughly guides the stacking direction in the crystal, as the long axes of the rods tend to lie in parallel due to intermolecular dispersion forces.[11] In addition, other electrostatic interactions through the secondary bonding of C≡N and C-F local dipoles and Coulombic interaction between D-A should further contribute to the precise control of intermolecular orientations. Indeed, all four D:A combinations made needle-shaped highly luminescent crystals which showed virtually identical crystal structures particularly in intra-stack direction (*vide infra*).

According to the DFT calculation of D and A molecules, meta-CF_3 in D2 instead of CH_3 groups in D1 significantly stabilizes the FMO energies (**Figure 2-1**). In case of A2 with CN substitution in the inner (α) position, the lowest unoccupied MO (LUMO) is destabilized while the highest occupied MO (HOMO) remains unchanged compared to those of A1 with β CN group, see **Figure 2-1b**. The photoluminescence (PL) color range of the CT crystals is (**Figure 2a-d**) from red (CT-R; D1:A1) via orange (CT-O; D1:A2) and yellow (CT-Y; D2:A1) to green (CT-G; D2:A2). This correlates well with the qualitative ordering of CT energy gaps simply thought as the energy gaps between the HOMO of the respective donor and the LUMO of the acceptor, obtained from DFT calculations (**Figure 2-1b**). We emphasize, however, that a quantitative understanding of photophysical processes requires a proper ‘state description’ for the electronic transition, which depends on

the exact intermolecular arrangement in the crystals, specifically mixed vs. segregated stacking[19] and regular vs. irregular arrangements in the stacks, as well as separation and slips between neighboring molecules.[9] Therefore, crystal structure analysis is a crucial and inevitable step for a detailed understanding of the luminescence properties.

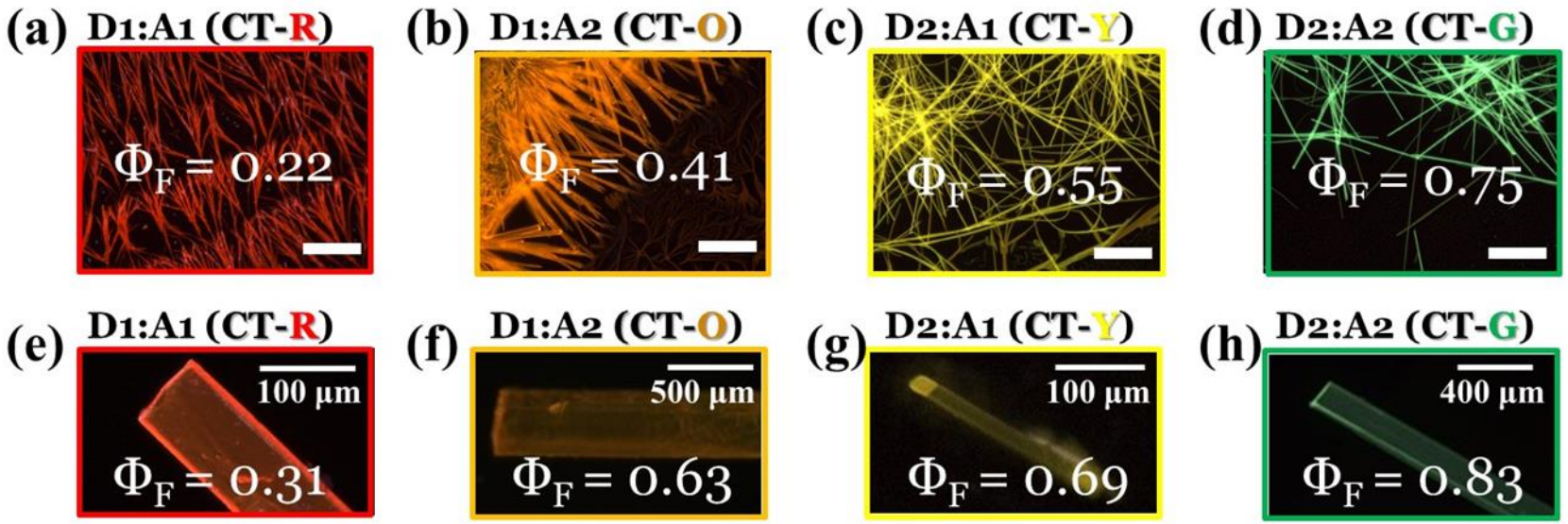

Figure 2-4. Crystal morphology and PL quantum yield of CT crystals.
(a-d) Drop-casted crystal images of each CT crystals: (a) CT-R, (b) CT-O, (c) CT-Y, and (d) CT-G respectively (scale bar = 50 μm). (e-h) Single crystal images of each CT crystals: (a) CT-R, (b) CT-O, (c) CT-Y, and (d) CT-G respectively.

CT pair	CT-R	CT-O	CT-Y	CT-G
Composition	D1:A1	D1:A2	D2:A1	D2:A2
a (Å)	15.0774(8)	8.3506(7)	**4.899(1)***	8.3614(8)
b (Å)	**9.3896(6)**	**9.4033(8)**	14.671(3)	29.069(3)
c (Å)	16.7012(9)	14.9954(13)	16.958(3)	**9.6245(14)**
α (˚)	90.00	104.616(4)	104.02(3)	90
β (˚)	112.131(3)	97.473(4)	91.19(3)	100.0840(5)
γ (˚)	90.00	101.085(4)	96.08(3)	90
Cell volume	2190.2	1098.2	1174.5	2297.5
Volume per molecule	1095.1	1098.2	1174.5	1148.8
Z	2	1	1	2
D-A distance (Å)	**3.31**	**3.38**	**3.40**	**3.46**
Counter pitch angle (˚)	**46.7**	**46.3**	**45.9**	**46.2**
Counter role angle (˚)	**89.4**	**91.0**	**87.7**	**89.4**

Table 2-2. Crystal information of 4 CT co-crystals in lattice parameters (a, b, c, α, β, γ) of 4 CT co-crystals, cell volume, volume per molecule, Z value, and intra-stack direction (marked in bold) of each CT co-crystals. * asterisked value should be doubled due to the same position of D2 and A1, *see manuscript.*

2.3.2. Isostructural Mixed Stack Arrangement in the CT crystals

All four D:A compounds formed quality CT single crystals for X-ray diffraction analysis. The crystal structure of CT-R (D1:A1) was solved earlier to the smallest R-value (reliability factor) of 5 %,[17] giving completely alternating 1:1 mixed, slightly slipped π-stacks of D1 and A1 in a 1D fashion (**Figure 2-5** and **Table 2-2**), while neighboring stacks are oriented perpendicular to each other. This is one way to ensure electroneutrality of the static dipoles formed by the D/A pairs, while the alternative arrangement is parallel stacks, generated through translation.[19] The latter inter-stack situation is in fact found in the CT-O (D1:A2), CT-Y (D2:A1), and CT-G (D2:A2) crystal structures (**Figure 2-5**). Within the stack of CT-O, a regular 1:1 alternating D1:A2 arrangement could be resolved, with only small conformational disorders in the individual D1 and A2 units to give a reasonably small R value of 5%. On the other hand, the CT-Y and CT-G crystals with smaller CT strength compared to CT-R and CT-O showed reduced tendency of D-A alternation thus revealing statistic disorder of D-A sequence along the intra-stack in the single crystal structure analysis. It is to be noted however that such CT crystal even with statistic disorder showed sharp diffraction spots because the D and A units are isometric. CT-Y crystal refinement based only on the A1 showed statistic disorder of –CN; the final occupancy factor of 50% on –CN of A1 with 50% on C-H of D2 considerably reduced the R value down to 8%, which implies intra-stack disorder is quite substantial showing almost the same occurrence probability of alternating D2-A1 sequence and non-alternating sequences. To double check such disorder model of CT-Y, crystal structure analysis of a separate crystal grown by a different method (CT-Y') was made, which again confirmed the disordered model

with a small R value of 7%. In the literature, such kind of statistical disorder behavior has previously been reported for the specific cocrystal systems comprising the isometric molecular structures with different substituents[52, 53, 54], *e.g.* chloro and methyl ortho-benzoic acids[55]. Therefore, the statistical disorder in the isometric CT-Y cocrystal system is unambiguously attributed to the relatively weak CT interaction between D2 and A1. Similarly, the CT-G crystal showed a substantial level of statistical disorder with 67% of alternating sequence (D2-A2) and 33% of the other reverse alternating sequence (A2-D2) finally giving R value of 6 %. In spite of such statistic disorder in CT-G, it is to be noted that the overall stoichiometry of D2 and A2 in the crystal is maintained at 1:1. For the detailed refinement process of CT-Y and CT-G, see SI. Due to the isometric molecular structures of D1, D2, A1, and A2, the molecules arranged in all CT crystals occupied virtually the same volume of around 1100 $Å^3$ **(Table 2-2)** enabling the formation of 1-D isostructural crystals in the mixed stacking direction. It is shown that the D and A molecules are effectively planarized in all the crystals, due to the 'twist elasticity' of the DCS motif.[33] In these isostructural CT crystals, however, it is well correlated that the formation of D-A alternating sequence is driven by the strength of D-A interaction resulting in completely alternating D-A sequences in CT-R and CT-O but in substantial statistic disorder in CT-Y and CT-G (*vide supra*). The order of D-A interaction can also be indicated by the gradually increasing trend of D-A intermolecular distance with decreasing CT strength: CT-R: 3.31 Å, CT-O: 3.38 Å, CT-Y: 3.40, CT-G: 3.46 Å (**Table 2-2**).

Therefore, despite the apparently different inter-stack arrangements, the four CT crystals showed virtually identical intra-stack arrangements within the 1D π-stacks (**Figure 2-5a-h** and **Table 2-2**). This is seen in the rather similar D-A inter-plane

distances (*vide supra*) with fine-tuning by the CT strength, and nearly identical intermolecular slips, expressed by counter pitch angles (47˚, 46˚, 46˚, 46˚) and counter roll angles (89˚, 91˚, 88˚, 89˚), see **Table 2-2**, **Figure 2-5** and **Figure 2-6~9**. Also the long axis and short axis of each isometric molecules are all close to identical (18 Å, 5 Å, respectively), and cell dimension parallel to π-stack (intra-stack) is similar (9.4, 9.4, 4.9*, 9.6 Å; the asterisked CT-Y value should be doubled due to the same position of D2 and A1 by statistical disorder), see **Table 2-2**. Therefore, we can state that these CT crystals are 'isomorphic in the π-stack direction'. It should be noted that the slipped stack arrangement of D and A molecules along the isomorphic π-stack is one of the essential factors to ensure bright luminescent features of CT crystal as will be discussed later. Furthermore, the nearest-neighbor arrangements within the π-stacks are quasi-isostructural in that the D and A molecules are isometric (*vide infra*). This is an important asset, as D-A interactions mainly exist in intra-stack direction, and this D-A interaction indeed determines the overall optical properties of CT crystals, while interactions between neighboring stacks are of minor importance (**Figure 2-5i-l**)[4, 26]. Therefore, the isostructural intra-stack arrangement in the four crystals allows us to attribute the optical and photophysical properties essentially to the different electronic properties of D and A by providing the same supramolecular arrangement; this allows for a detailed comparative electronic analysis of the resulting excited state features and fates in the following section.

The extended rod-shaped isometric molecular structure of our DSB:DCS type D-A molecules presumably promotes the formation of such unique isomorphic and

isostructural 1D CT stack, which is less evident in the conventional CT pairs of TCNQ and TTF derivatives[28, 56] with their short, plate-like molecular shapes. This may partially explain why the mechanism of CT formation in TCNQ:TTF systems, and the prediction on which pair would form actually a CT system, are not fully understood yet [28].

In this regard, the new prototype DSB:DCS type crystal series in this work can provide insight to targeted molecular design of CT crystals. For comparison, the intermolecular interaction energies (E_I) of the TCNQ based and DSB:DCS based CT crystals were calculated. Due to the larger molecular size and the isometric D:A design in the latter, much larger E_I were obtained; [11] for instance, CT-R showed a total E_I of -87.1 kJ/mol between D and A, while the conventional TCNQ-DBTTF pair[57] showed only -45.8 kJ/mol (**Figure 2-10, Table S2**; the degree of CT was not considered in the calculation). The stronger E_I in DSB:DCS pairs is seen as the main reason for the very small D-A intermolecular distances (~3.4 Å) and planarized molecular geometries (**Figure 2-5**).

By virtue of the controlled intra-stack molecular orientation with strong intermolecular forces between DSB type donors and DCS type acceptors, co-crystalline systems were not only obtained as single crystals but also as nanocrystal suspensions through simple re-precipitation (*vide infra*) as well as by vacuum-co-deposited thin films (**Figure 2-11**). The D-A co-evaporated thin films could be assigned to have the same crystal structure with the corresponding single crystals based on the out-of-plane XRD results (**Figure 2-12**). The GIXD pattern does not show any traces of pure donor (or pure acceptor) crystals (**Figure 2-11**). Therefore, all D:A combinations form crystals even under vacuum deposition conditions, rather than forming separate aggregates of donors or acceptors.

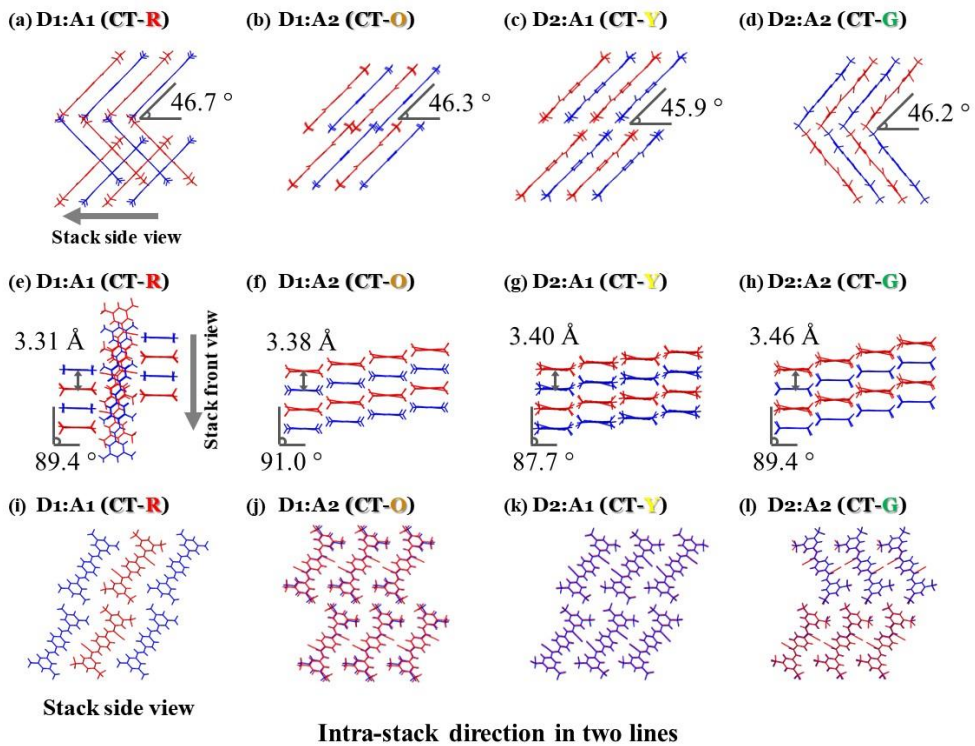

Figure 2-5. Crystal structure of the CT crystals.
(a-h) Intra-stack (D = blue, A = red) of each CT crystals with counter pitch angle, counter-roll angle and intermolecular distances: (a,e) CT-R, (b,f) CT-O, (c,g) CT-Y, and (d,h) CT-G respectively. (i-l) Inter-stack of each CT crystals: (i) CT-R, (j) CT-O, (k) CT-Y, and (l) CT-G respectively (intra-stack direction was depicted in the figures). CT-Y and CT-G showed statistic disorder of D and A within the molecular stacks**.**

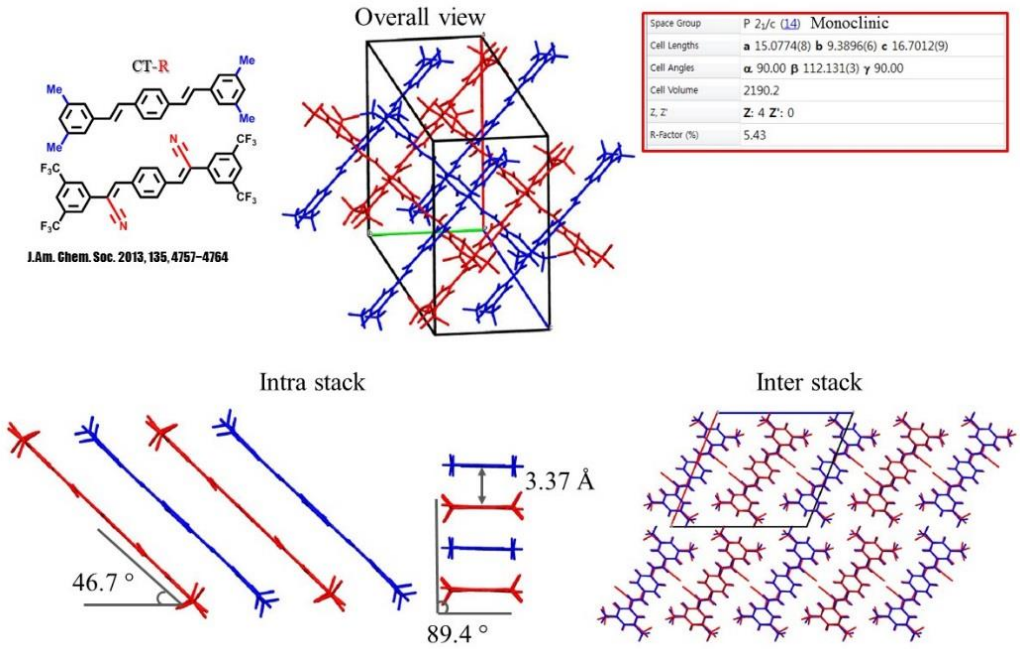

Figure 2-6. Crystal structure of CT-R (D1-A1)

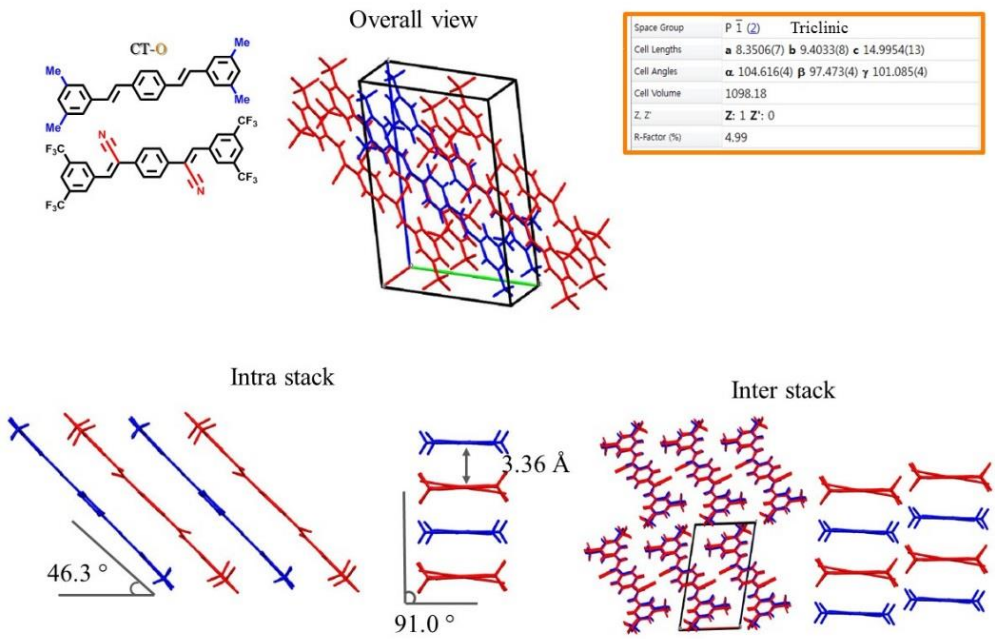

Figure 2-7. Crystal structure of CT-O (D1-A2)

CT-Y

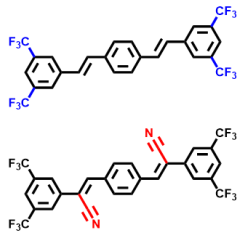

Space Group	P $\bar{1}$ (2)
Cell Lengths	**a** 4.899(1) **b** 14.671(3) **c** 16.958(3)
Cell Angles	**α** 104.02(3) **β** 91.19(3) **γ** 96.08(3)
Cell Volume	1174.5
Z, Z'	**Z**: 1 **Z'**: 0
R-Factor (%)	8.06

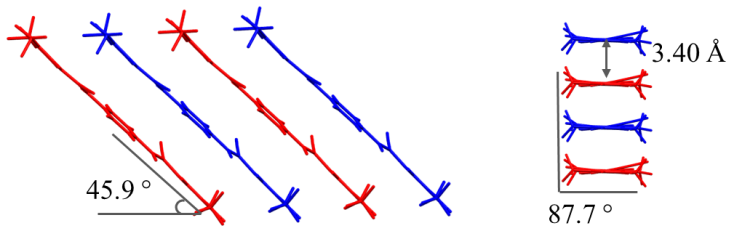

CT-Y'

CT pair	CT-Y'
Composition	D2:A1
a (Å)	**4.880(1)***
b (Å)	28.207(6)
c (Å)	8.756(2)
α (°)	90
β (°)	104.81(3)
γ (°)	90
Cell volume	1165.2
Volume per molecule	1165.2
Z	1
D-A distance (Å)	**3.44**
Counter pitch angle (°)	**52.1**
Counter role angle (°)	**90.8**

Space Group	P $2_1/c$ (14)
Cell Lengths	**a** 4.880(1) **b** 28.207(6) **c** 8.756(2)
Cell Angles	**α** 90 **β** 104.81(3) **γ** 90
Cell Volume	1165.22
Z, Z'	**Z**: 1 **Z'**: 0
R-Factor (%)	7.25

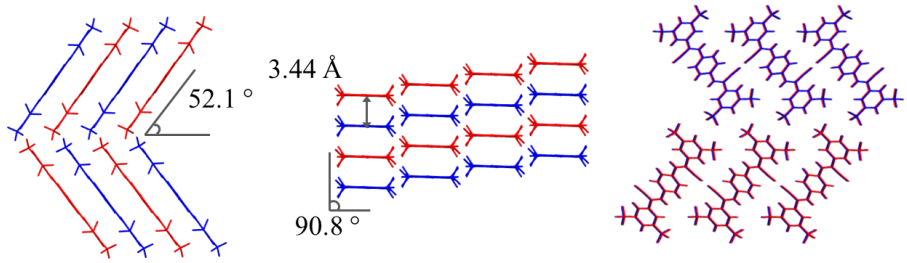

Figure 2-8. Crystal structure of CT-Y (up) and CT-Y' (down) (D2-A1)

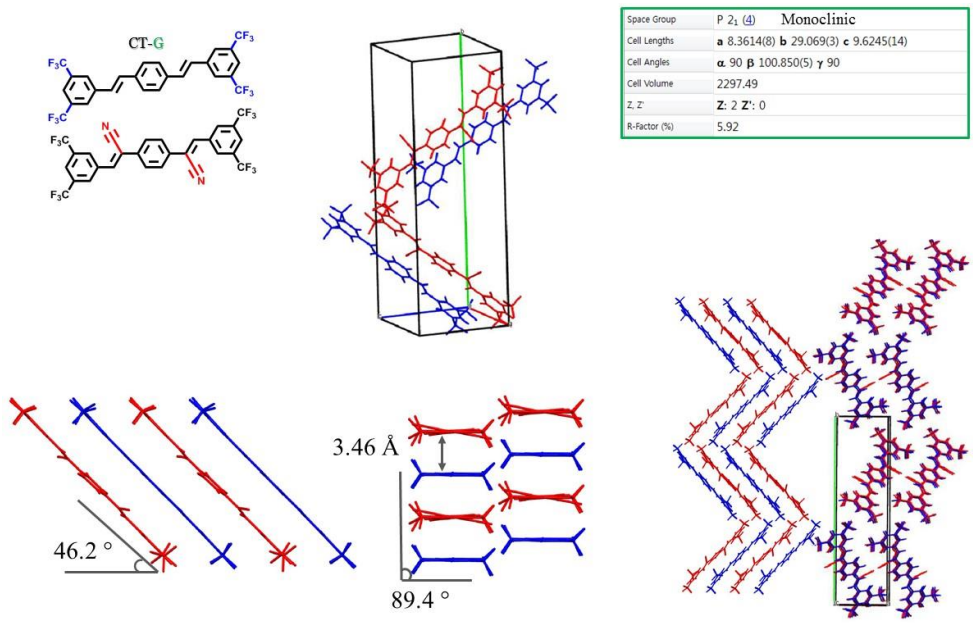

Figure 2-9. Crystal structure of CT-G (D2-A2)

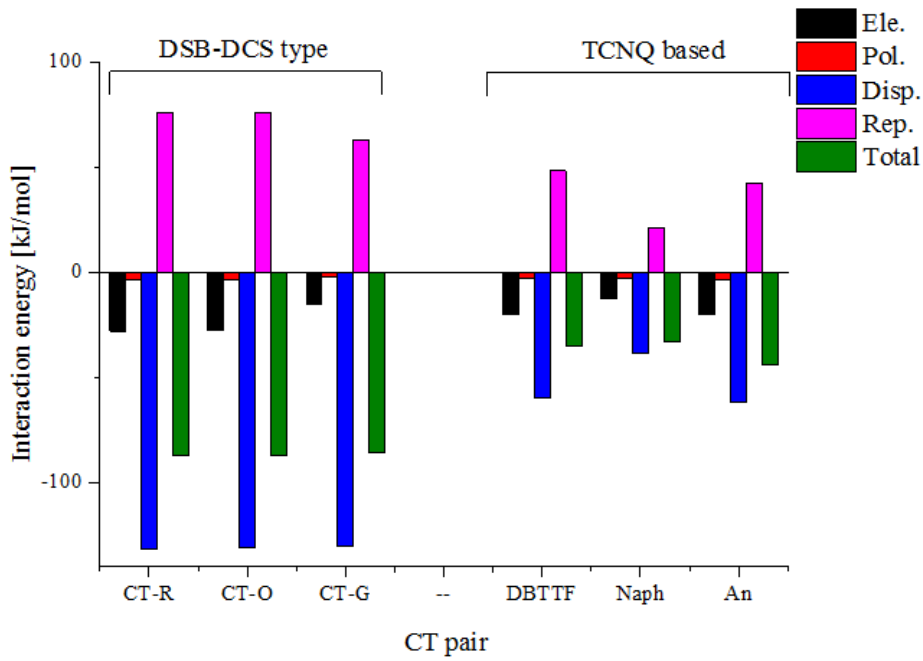

Figure 2-10. Interaction energy of DSB-DCS CT complexes and TCNQ based CT complexes. All the CT pairs are mixed stack, and it was calculated from D-A interaction in intra-stack direction. Crystal Explorer (B3LYP/6-31G(d,p))

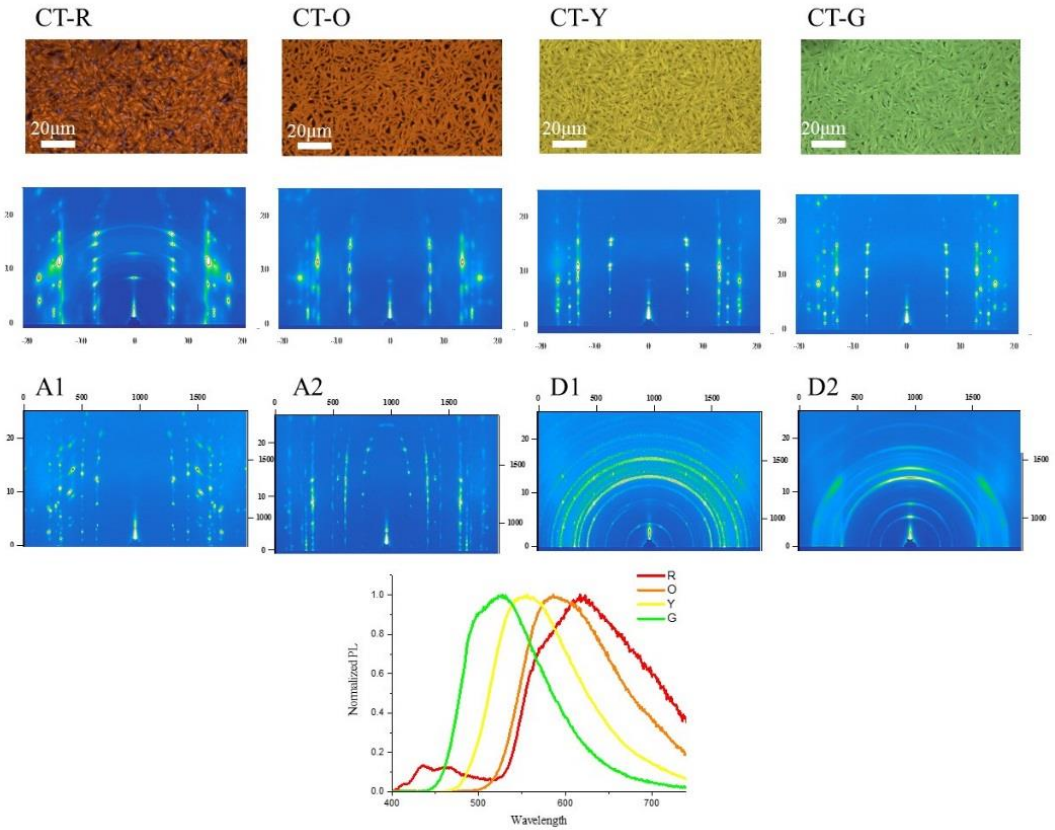

Figure 2-11. Vacuum deposited film (GIXD)

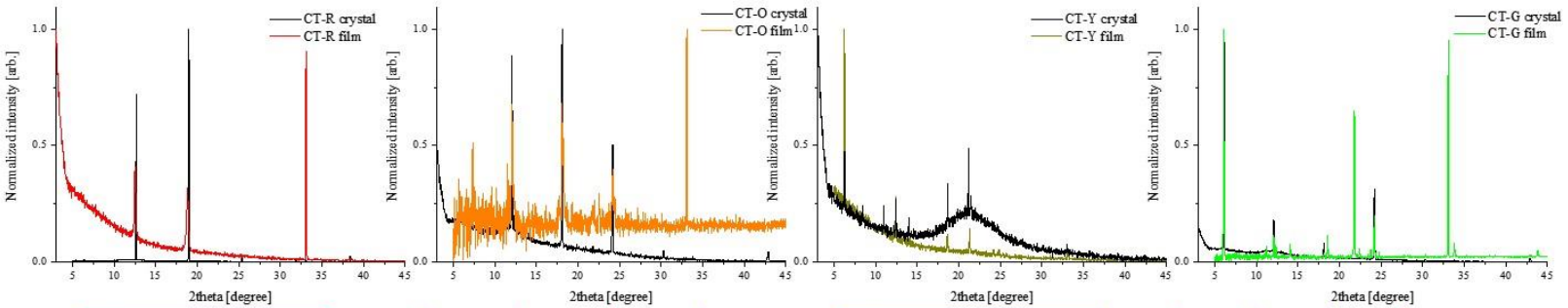

CT -R		001	002	003	004	005
VD film	2theta [deg.]	-	12.51	18.82	-	33.07
	λ [Å]	-	14.14	14.14	-	13.53
SC	2theta [deg.]		12.66	18.98	25.39	31.83
	λ [Å]		13.98	14.02	14.02	14.05
SC (Cal.)	2theta [deg.]		12.66	19.04		
	λ [Å]		13.97	13.97		

CT -O		001	002	003	004	005
VD film	2theta [deg.]	-	12.04	18.04	24.18	-
	λ [Å]	-	14.68	14.74	14.71	-
SC	2theta [deg.]	5.96	12.06	18.07	24.16	30.27
	λ [Å]	14.83	14.66	14.71	14.72	14.75
SC (Cal.)	2theta [deg.]	6.20	12.42	18.66	24.98	
	λ [Å]	14.24	14.24	14.25	14.25	

CT-Y		001	002	003	004	005
VD film	2theta [deg.]	6.23	12.40	18.61	-	-
	λ [Å]	14.18	14.27	14.29	-	-
SC	2theta [deg.]	6.25	12.42	18.67	-	-
	λ [Å]	14.13	14.24	14.25	-	-
SC (Cal.)	2theta [deg.]	6.24	12.51	18.79		
	λ [Å]	14.15	14.14	14.15		

CT-G		001	002	003	004	005
VD film	2theta [deg.]	6.07	12.08	18.55	24.18	-
	λ [Å]	14.54	14.64	14.34	14.71	-
SC	2theta [deg.]	6.09	12.08	18.11	24.20	-
	λ [Å]	14.49	14.64	14.68	14.70	-
SC (Cal.)	2theta [deg.]*	6.08	12.17	-	24.48	
	λ [Å]	14.52	14.53	-	14.53	

Figure 2-12. Out-of-plane XRD of VD film and SC

CT Pair	CT-R	CT-O	CT-Y	CT-G
$\Phi_{PL,DC}$	0.22	0.41	0.55	0.75
$\Phi_{PL,SC}$	0.31	0.63	0.69	0.83
λ_{PL} [nm]	613	572	542	500
λ_{PL} [eV]	2.02	2.17	2.29	2.48
τ_F [ns]	22.4	61.0	123.5	157.7
τ_1 [ns]	10	27	42	47
τ_2 [ns]	70	190	250	320
I_1% [%]	79	79	61	59
I_2% [%]	21	21	39	41
k_r*10^7 [s^{-1}]	1.7	1.2	0.8	1.0
$k_{nr}*10^7$ [s^{-1}]	5.9	1.7	0.7	0.3
f / eV	0.05/1.70	0.03/ 1.85	0.03/ 2.19	0.04/ 2.34

Table 2-3. Summarized optical/photo-physical characteristics of CT crystals $\Phi_{PL,DC}$: PL quantum yield of drop-casted crystal, $\Phi_{PL,SC}$: PL quantum yield of single crystal. τ_F: intensity weighted lifetime, I_i % [%]: Fractional intensity, k_r: radiative rate, k_{nr}: non-radiative rate of drop-casted crystals , f: Oscillator strength and energy level of S_1 state calculated by TD-DFT (B3LYP/ 6-311G*)

2.3.3. CT State Formation and Resulting PL properties

As shown in **Figure 2-4**, we observe a continuous PL color shift among the four crystals, which corresponds qualitatively to the energy difference $\Delta E(LUMO_A\text{-}HOMO_D)$, suggesting D-A CT states as the origin of the PL. In order to verify whether the crystals feature the properties of CT complexes or not, comparative ultra-violet/visible (UV/Vis) absorption as well as PL emission and excitation (PLE) measurements were performed (**Figure 2-13**). Due to the high optical density of the single crystals, absorption spectra generally suffer from shadowing effects, and also the PL and PLE spectra from inner filter effects.[10] Therefore, we prepared nano-crystal (NC) suspensions ($THF:H_2O$ = 2:98, 1×10^{-5} M) of the pure donor and acceptor compounds (**Figure 2-14**) and also of their 1:1 mixtures (**Figure 2-13a-d**). The PL spectra of the nano-crystals agree well in their spectral positions with those of the single crystals. Importantly, they are red-shifted compared to those of the single donor and acceptor counterparts, which clearly indicates the presence of D-A CT interactions in all four crystals.[39] In addition, the absorption spectra of the crystals show bands at the low energy side compared to those of the pure compounds. In order to exclude the effect of light scattering by the nano-crystals as a possible source of these low-energy bands,[9] PLE spectra were measured, where light scattering is not present, and only absorption bands which give rise to emission are monitored. The PLE spectra essentially follow the absorption spectra, excluding light scattering, and unambiguously assigning them to the real absorption caused by CT states (**Figure 2-15**). Taking these results together, CT interactions were clearly identified in all four crystals.[17, 26] Despite the CT character of the emitting state of crystals, drop-cast (DC) crystals showed very bright emission with high PL quantum yield of 0.22, 0.41, 0.55, 0.75 for CT-R, CT-

O, CT-Y, CT-G, respectively (**Figure 2-4a-d**). These are remarkably high values as drop-cast samples tend to show PL quenching due to the prevailing exciton trapping because of their polycrystalline nature.[10] Bulk single crystals (SCs) of CT complexes exhibited even higher PL quantum yields: 0.31[17], 0.63, 0.69, 0.83 for CT-R, CT-O, CT-Y, CT-G respectively (**Figure 2-4e-h**). It should be noted that these values mark the highest ever PL quantum yield reported so far for CT complexes (see **Table 2-1** for comparison). Therefore, it is exciting and challenging to unravel the origin of high efficiency CT emission in these isostructural D-A crystals.

High Φ_F in organic solids requires the predominance of the radiative over non-radiative decay channels; from experiment, the respective rates (k_r, k_{nr}) can be extracted through the PL lifetime τ_F via $k_r = \Phi_F/\tau_F$ and $k_{nr} = (1-\Phi_F)/\tau_F$, where τ_F is the intensity-weighted average lifetime. In fact, the PL decay of all crystals showed two decay components in the 10-47 ns (τ_1) and 70-320 ns (τ_2) ranges (**Figure 2-13e**, **Table 2-3**). It is clearly noted however that both τ_1 and τ_2 gradually increase with decreasing CT strength, i.e. CT-R < CT-O < CT-Y < CT-G. Nevertheless, both emission components originate from the same excited state as evidenced by the time-resolved emission spectra (TRES; see **Figure 2-16**), thus suggesting the presence of reverse intersystem crossing (RISC; *vide infra*). Based on the isomorphous crystal nature and their evolution with D-A CT strength shown in the previous section, the exceptionally high Φ_F values and the monotonic variation of PL lifetime in these co-crystals are most likely attributed to a combination of following five factors:[26] (i) dense packing which reduces k_{nr} (**Table 2-3**) through the restricted access to the conical intersection,[58] known as a main nonradiative

deactivation pathway in DCS molecules,[9, 59, 60] (ii) suppression of PL trapping by the high structural integrity of the crystals which is especially important for the (CT) single crystals, [8, 9, 10] (iii) non-negligible oscillator strength and thus a moderate radiative rate k_r of the emitting CT state through (iii-1) configuration interaction [26], (iii-2) tight intermolecular slip stacking for appropriate CT exciton formation[6, 8] and aggregated-type Herzberg teller (AHT) coupling[9], and (iii-3) triplet harvesting via ISC/RISC which further promotes the radiative pathway.[61]

The non-zero oscillator strength of the CT emitting state indeed observed in the low energy bands of the absorption spectra (**Figure 2-13a**) and in the experimental k_r values (**Table 2-3**) was theoretically supported by TD-DFT calculations. The calculations were done on D:A dimer pairs, as the CT states are strongly localized,[23] to give oscillator strengths *f* for the S_1 state of 0.03-0.05 for all four D-A combinations (see **Table 2-4**; for a detailed analysis on CT-R, see Ref.[26]). The non-negligible *f*, which is the apparent driving force for the high Φ_F, is due to significant admixing of other one-electron configurations to the dominant HOMO→LUMO transition. This alters the simple MO picture of **Figure 2-1** to give highest occupied and lowest unoccupied natural transition orbitals (HONTO, LUNTO) with a non-zero differential overlap, and thus non-negligible *f*, which results from the tightly stacked isometric D-A molecules; for details, see **Figure 2-17** in the SI.

Interestingly, the very substantial CT character of S_1 gives rise to an energetically close-lying triplet state T_1; this generally promotes ISC, and RISC by thermal activation. RISC is the apparent reason for the observed delayed fluorescence component (revealed as τ_2) from the S_1 state seen in experiment (**Fig. 2-13e** and **Table 2-3**), which however shows only moderate contributions as the fractional

intensities (~20 % for CT-R and CT-O and ~40 % for CT-Y and CT-G, **Table 2-3**) compared to the other molecularly designed TADF cases (50~80 %) [62, 63]. This is associated with the short lifetime of the delayed component in the sub-microsecond range (**Table 2-3**) when compared to prototypical TADF molecules.[64, 65] This is in fact a result of a delicate electronic situation found for energies and characteristics of the relevant singlet and triplet states in the co-crystals. As delayed fluorescence contributes however only moderately but systematically to the overall PL, we will analyze this complex situation in full detail in a forthcoming paper through comprehensive transient (low-temperature) PL investigations, combined with in-depth TD-DFT studies, including spin-orbit coupling (SOC) calculations to estimate ISC/RISC. For now, we just summarize the main features: according to our studies, the four co-crystals fall in two groups. Thermal activation of the fluorescence is experimentally observed for CT-Y and CT-G, while no such effect is observed for CT-R and CT-O, see **Fig. 2-18**. This is essentially due to considerable singlet-triplet gaps ΔE_{ST} for the former, while for the latter S_1 and T_1 are almost degenerate. It is interesting to note that the former group features statistic disorder in D-A sequence, while the latter group shows perfect D-A alternation. Understanding the effect of the CT strength and sequential heterogeneity on the singlet and triplet energy levels and relevant ISC/RISC should be the important subject of forthcoming paper. Despite such favorable TADF potential, the ISC rates for CT-R and CT-O are very low due to small SOC compared to prototypical TADF molecules. For this reason, the delayed fluorescence components are relatively small, and the very high Φ_F of the designed isometric and isostructural co-crystals is dominantly controlled by the prompt emission process, which are less influenced by temperature variations.

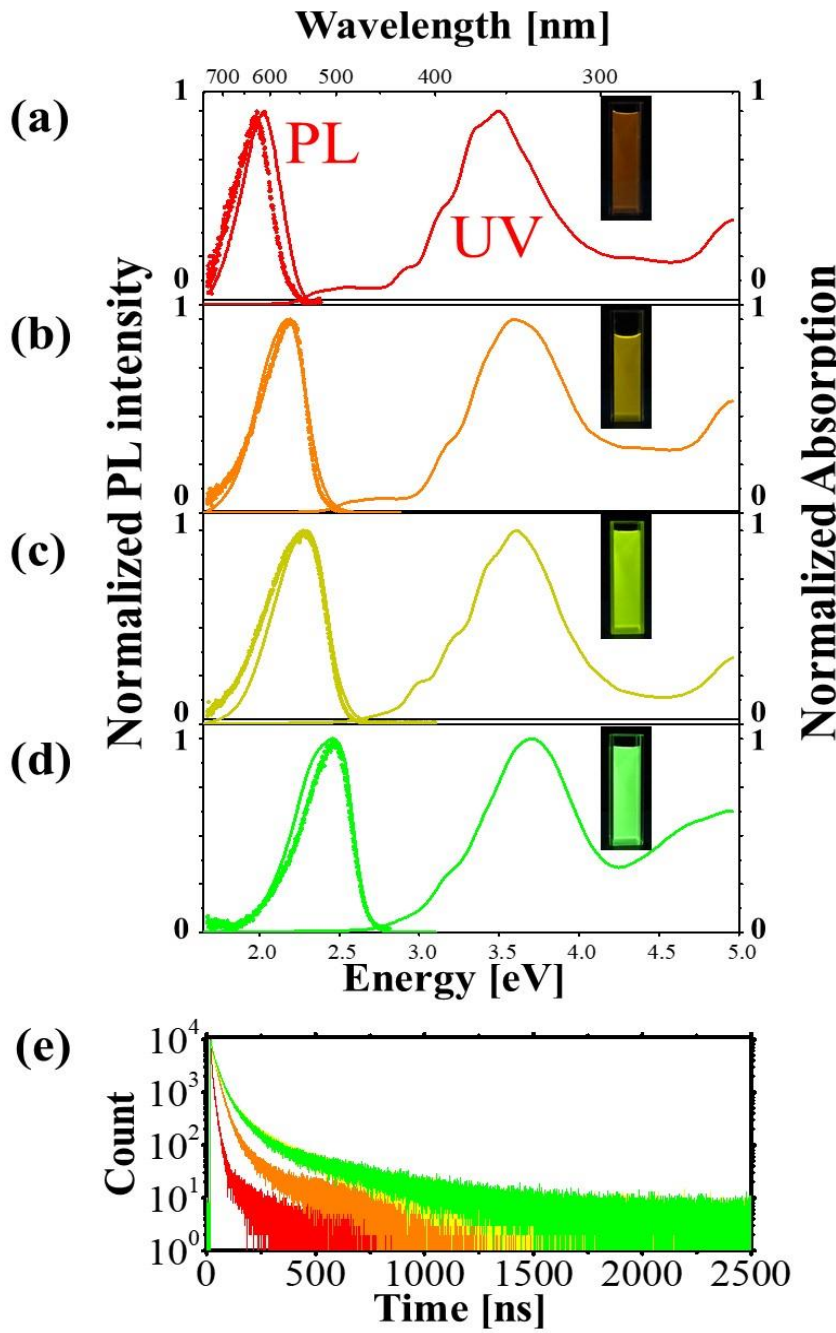

Figure 2-13. Optical properties of CT nano crystals (NCs) and single crystals (SCs). (a-d) UV spectra of CT NCs and PL spectra of CT NCs (solid line) and SCs (dot), insets: Image of CT NC suspension (THF : H_2O = 2:98, 1×10^{-5} M) under UV light) (e) PL decay profiles.

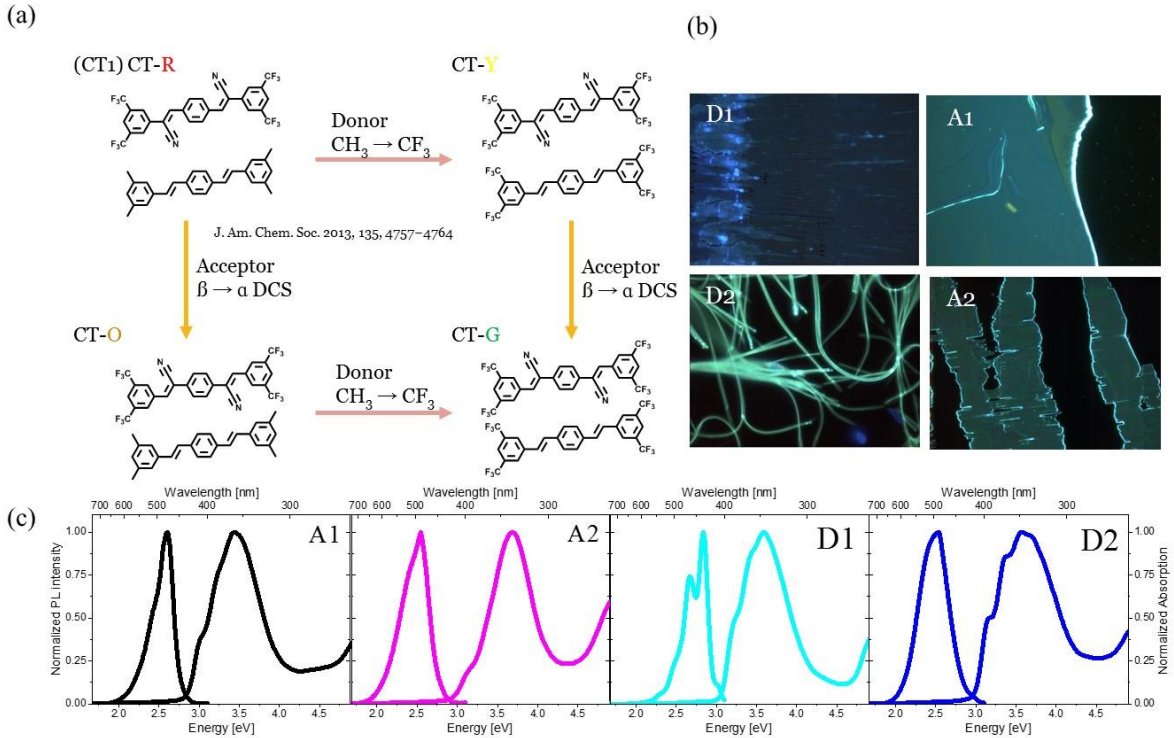

Figure 2-14. Material design of each donors and acceptors and their crystal
(a) Design of donors and acceptors
(b) Crystal morphology and luminescent image of each donors and acceptors

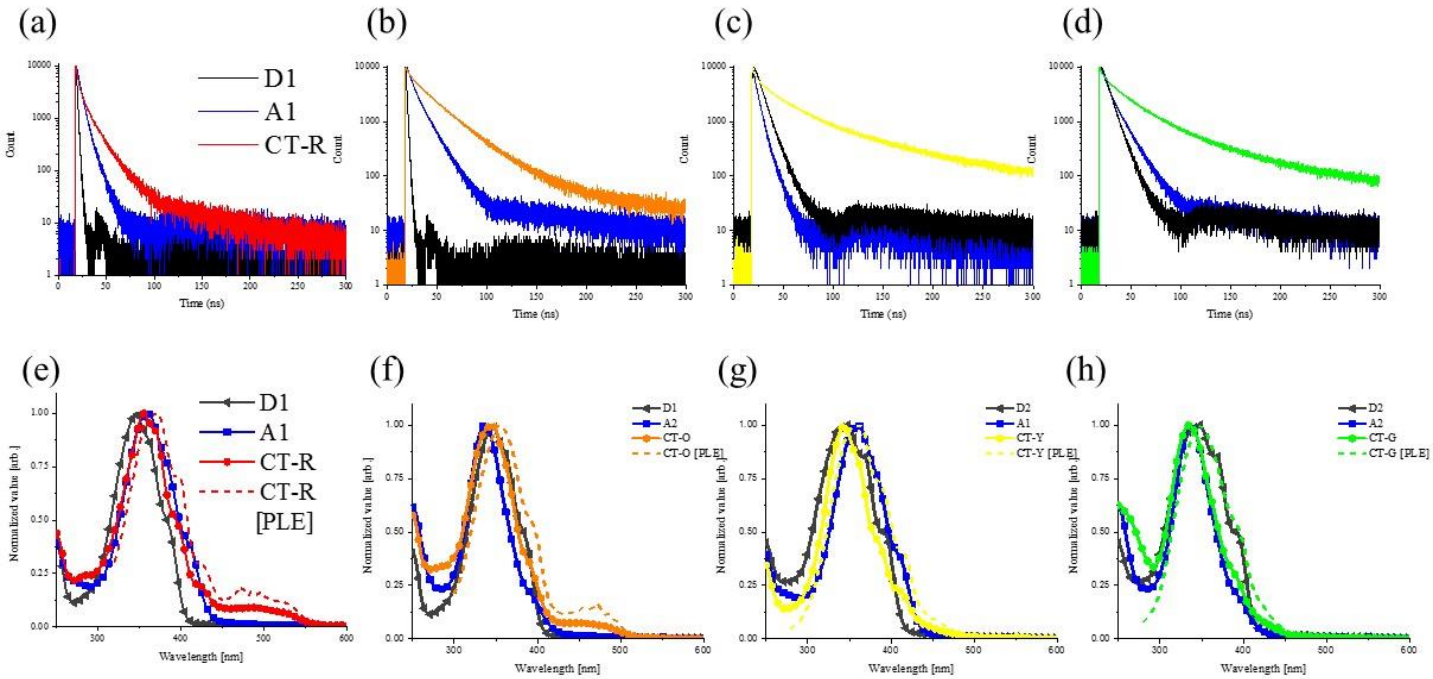

Figure 2-15. Optical properties of CT nano crystals (NCs)
(a-d) PL decay profiles of each CT pairs and corresponding donor-acceptor counterparts. (e-h) UV/Vis absorption spectra and PLE spectra of each CT pairs and UV/Vis absorption spectra of corresponding donor-acceptor counterpart.

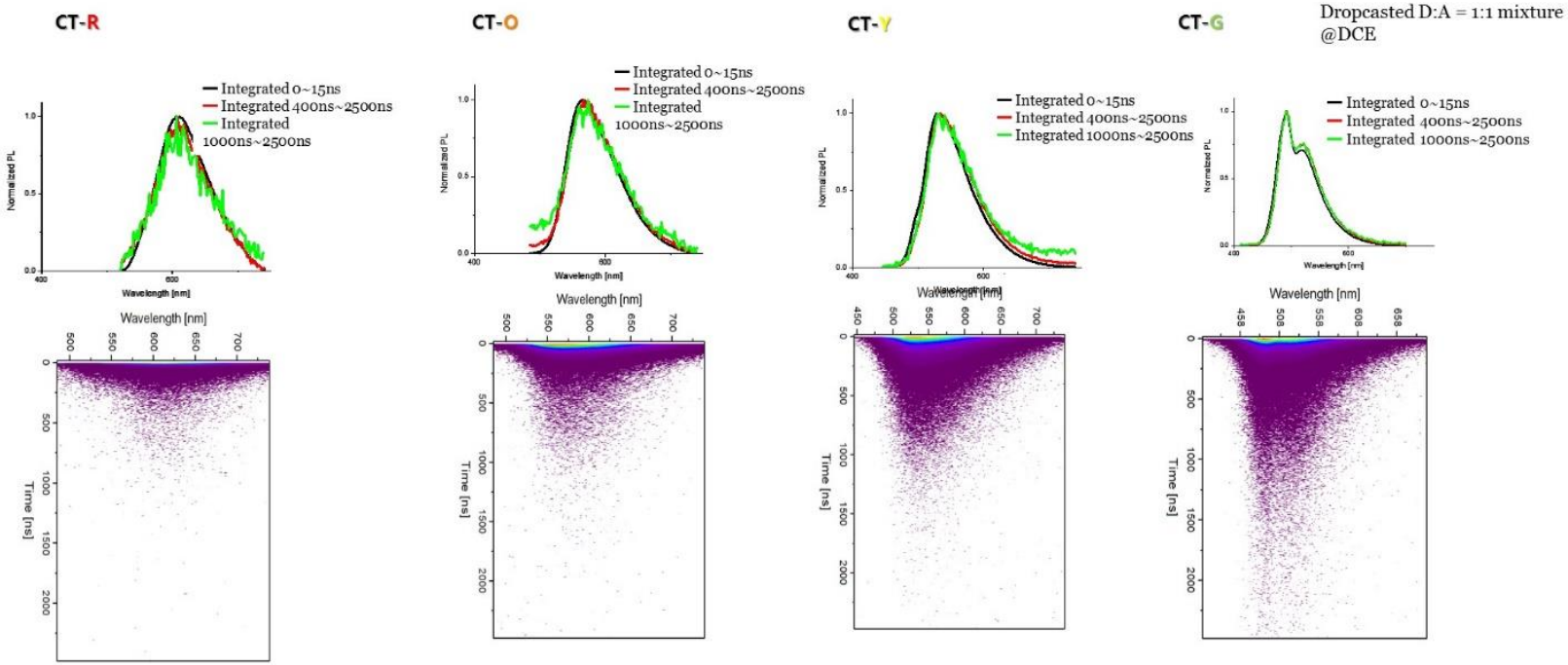

Figure 2-16. TRES of CT co-crystals

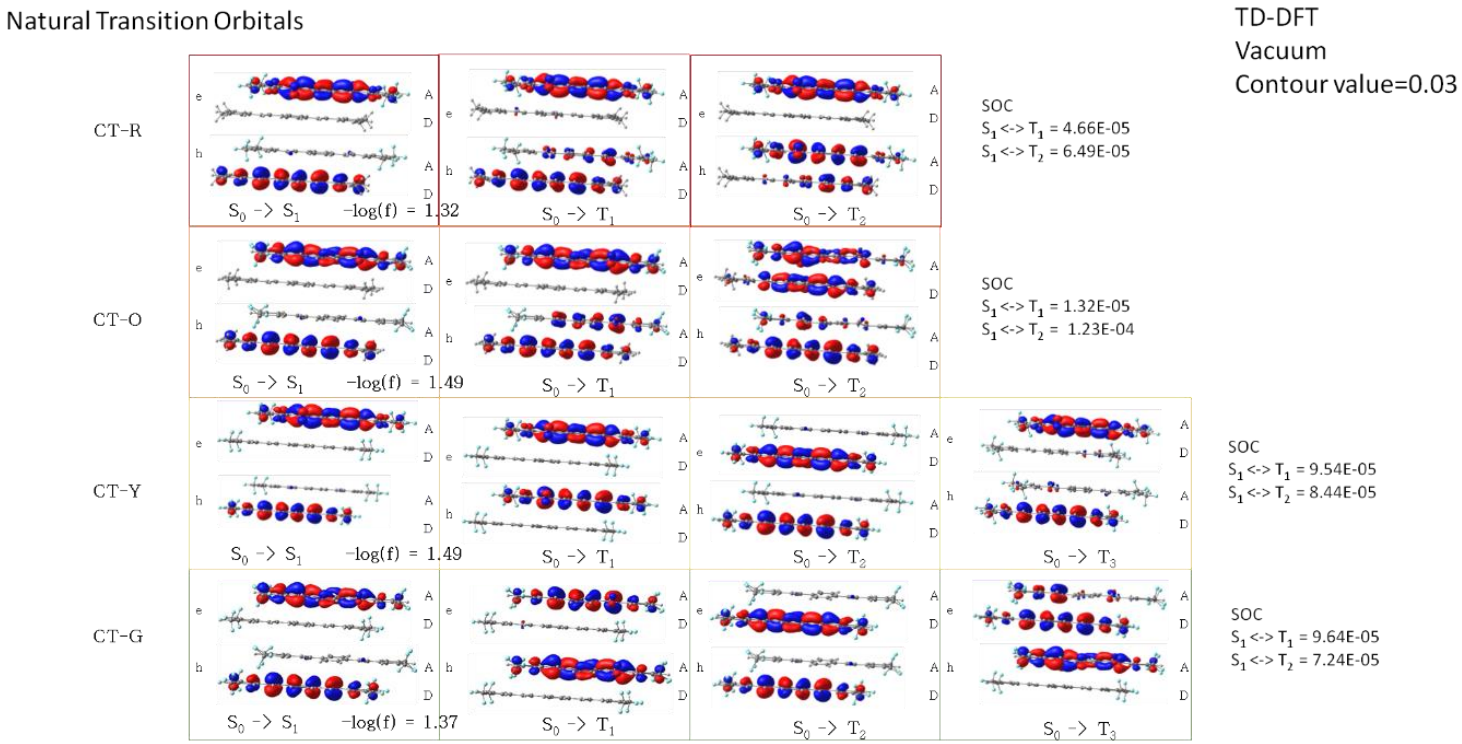

B3LYP/6-311G(d)//B3LYP/6-311G(d)

Figure 2-17. Highest occupied and lowest unoccupied natural transition orbitals (HONTO, LUNTO) of dimer in cocrystals

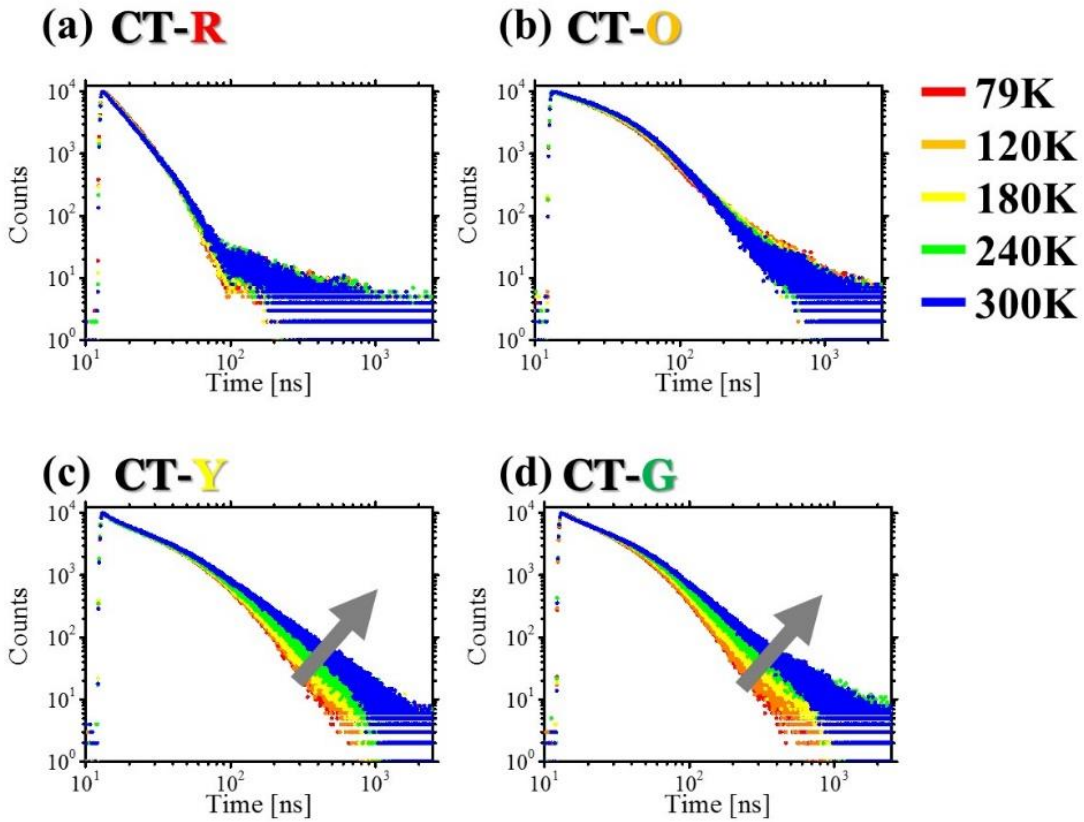

Figure 2-18. Photo-physical investigation of CT complexes and TADF behavior of CT-Y and CT-G. (a-d) Luminescent lifetime decay with thermal energy variation for CT-R, CT-O, CT-Y, CT-G respectively

	R			O			Y			G		
	E	*f*	CI	E	*f*	CI	E	*f*	CI	E	*f*	CI
S_1	1.70	0.05	H→L	1.85	0.03	H→L, …	2.19	0.03	H→L	2.34	0.04	H→L, …
S_m	3.13 [7]	2.35	MC	3.16 [7]	1.69	MC	3.17 [3]	2.54	H→L+1,…	3.18 [4]	2.06	MC
T_1	1.60		H→L (H-2→L)	1.75		H→L H-3→L	1.74		H-1→L H→L…	1.87		H-1→L
T_2	1.78		H-2→L H-1→L..	1.90		H→L+2, …	1.91		H→L+1 …	1.93		H→L+1, …
T_3				1.94		H→L+2, …	2.16		H→L…	2.26		H→L, …
$\Delta E(S_1\text{-}S_m)$	1.43			1.31			0.98			0.84		
$\Delta E(S_1\text{-}T_1)$	0.10			0.10			0.45			0.47		

Table 2-4. Estimated energy levels, oscillator strength, and configuration interaction of each CT co-crystals based on crystal structure. (TD)DFT b3lyp/6-311g*

2.4. Conclusion

Four different mixed stack CT co-crystals comprising isometric D-A pairs with different degree of charge transfer (CT) interaction were designed and synthesized. Attributed to the isometric and elongated nature of D and A molecules which essentially share the same chemical structure of molecular skeleton, four CT crystals were isostructural with virtually isomorphic mixed stack D-A interaction. With increasing CT strength, however, D-A distance in the crystal was gradually reduced and a systematic red-shift of CT emission was observed. CT-G, CT-Y, CT-O, CT-R were in the order of CT strength which showed impressively high PL quantum yields of 0.83, 0.69, 0.63, and 0.31, respectively. Based on the comprehensive structure-property correlation, such an unexpectedly high CT emission was attributed to the combination of increased oscillator strength of emitting charge-transfer (CT) state by configuration interaction, and restricted nonradiative processes by dense packing and structural integrity. The pronounced CT character gave rise to small singlet-triplet gaps which partially contributed to the delayed radiative deactivation by reverse inter-system crossings as well.

2.5. References

1. Ding R.; Feng J.; Dong F. X.; Zhou W.; Liu Y.; Zhang X. L.; Wang X. P.; Fang H. H.; Xu B.; Li X. B.; Wang H. Y.; Hotta S., Sun H. B. *Adv. Funct. Mater.*, **2017**, *27*.

2. Liu J.; Zhang H.; Dong H.; Meng L.; Jiang L.; Jiang L.; Wang Y.; Yu J.; Sun Y.; Hu W., Heeger A. J. *Nat. Commun.*, **2015**, *6*, 10032.

3. Briseno A. L.; Mannsfeld S. C.; Ling M. M.; Liu S.; Tseng R. J.; Reese C.; Roberts M. E.; Yang Y.; Wudl F., Bao Z. *Nature*, **2006**, *444*, 913-917.

4. Park S. K.; Kim J. H.; Ohto T.; Yamada R.; Jones A. O. F.; Whang D. R.; Cho I.; Oh S.; Hong S. H.; Kwon J. E.; Kim J. H.; Olivier Y.; Fischer R.; Resel R.; Gierschner J.; Tada H., Park S. Y. *Adv. Mater.*, **2017**, *29*, 1701346.

5. Li J.; Zhou K.; Liu J.; Zhen Y.; Liu L.; Zhang J.; Dong H.; Zhang X.; Jiang L., Hu W. *J. Am. Chem. Soc.*, **2017**, *139*, 17261-17264.

6. Gierschner J.; Varghese S., Park S. Y. *Adv. Opt. Mater.*, **2016**, *4*, 348-364.

7. Coropceanu V.; Cornil J.; da Silva Filho D. A.; Olivier Y.; Silbey R., Bredas J. L. *Chem Rev*, **2007**, *107*, 926-952.

8. Gierschner J., Park S. Y. *J. Mater. Chem. C*, **2013**, *1*, 5818-5832.

9. Shi J.; Aguilar Suarez L. E.; Yoon S.-J.; Varghese S.; Serpa C.; Park S. Y.; Lüer L.; Roca-Sanjuán D.; Milián-Medina B., Gierschner J. *J. Phys. Chem. C*, **2017**, *121*, 23166-23183.

10. Gierschner J.; Lüer L.; Milián-Medina B.; Oelkrug D., Egelhaaf H.-J. *J. Phys. Chem. Lett.*, **2013**, *4*, 2686-2697.

11. Park S. K.; Kim J. H., Park S. Y. *Advanced Materials*, **2018**, *30*, 1704759.

12. Wang C.; Dong H.; Hu W.; Liu Y., Zhu D. *Chem. Rev.*, **2012**, *112*, 2208-2267.

13. Dong H.; Fu X.; Liu J.; Wang Z., Hu W. *Adv. Mater.*, **2013**, *25*, 6158-6183.

14. An B.-K.; Gierschner J., Park S. Y. *Acc. Chem. Res.*, **2012**, *45*, 544-554.

15. Yoon S. J.; Varghese S.; Park S. K.; Wannemacher R.; Gierschner J., Park S. Y. *Adv. Opt. Mater.*, **2013**, *1*, 232-237.

16. Ferraris J.; Walatka V.; Perlstei.Jh, Cowan D. O. *J. Am. Chem. Soc.*, **1973**, *95*, 948-949.

17. Park S. K.; Varghese S.; Kim J. H.; Yoon S. J.; Kwon O. K.; An B. K.; Gierschner J., Park S. Y. *J. Am. Chem. Soc.*, **2013**, *135*, 4757-4764.

18. Tayi A. S.; Shveyd A. K.; Sue A. C.; Szarko J. M.; Rolczynski B. S.; Cao D.; Kennedy T. J.; Sarjeant A. A.; Stern C. L.; Paxton W. F.; Wu W.; Dey S. K.; Fahrenbach A. C.; Guest J. R.; Mohseni H.; Chen L. X.; Wang K. L.; Stoddart J. F., Stupp S. I. *Nature*, **2012**, *488*, 485-489.

19. Park S. K.; Cho I.; Gierschner J.; Kim J. H.; Kim J. H.; Kwon J. E.; Kwon O. K.; Whang D. R.; Park J. H.; An B. K., Park S. Y. *Angew. Chem. Int. Ed.*, **2016**, *55*, 203-207.

20. Zhuo M. P.; Tao Y. C.; Wang X. D.; Wu Y.; Chen S.; Liao L. S., Jiang L. *Angew. Chem. Int. Ed.*, **2018**, *57*, 11300-11304.

21. Ono T.; Taema A.; Goto A., Hisaeda Y. *chem. Eur. J.*, **2018**, *24*, 17487-17496.

22. Sun L.; Hua W.; Liu Y.; Tian G.; Chen M.; Chen M.; Yang F.; Wang S.; Zhang X.; Luo Y., Hu W. *Angew. Chem. Int. Ed.*, **2019**.

23. Zhu L.; Yi Y.; Li Y.; Kim E. G.; Coropceanu V., Bredas J. L. *J Am Chem Soc*, **2012**, *134*, 2340-2347.

24. Zhu L.; Kim E.-G.; Yi Y., Brédas J.-L. *Chem. Mater.*, **2011**, *23*, 5149-5159.

25. Behera R. K.; Goud N. R.; Matzger A. J.; Brédas J.-L., Coropceanu V. *J. Phys. Chem. C*, **2017**, *121*, 23633-23641.

26. Wykes M.; Park S. K.; Bhattacharyya S.; Varghese S.; Kwon J. E.; Whang D. R.; Cho I.; Wannemacher R.; Luer L.; Park S. Y., Gierschner J. *J. Phys. Chem. Lett.*, **2015**, *6*, 3682-3687.

27. Tao Y.; Yuan K.; Chen T.; Xu P.; Li H.; Chen R.; Zheng C.; Zhang L., Huang W. *Adv Mater,* **2014**, *26*, 7931-7958.

28. Sun L.; Zhu W.; Yang F.; Li B.; Ren X.; Zhang X., Hu W. *Phys. Chem. Chem. Phys.,* **2018**, *20*, 6009-6023.

29. Zhang Q.; Huang Y.; Wang Z., Chen Z. *Angew. Chem. Int. Ed.,* **2019**.

30. Aliaga-Gosalvez M. J.; Demitri N.; Dohr M.; Roldao J. C.; Park S. K.; Oh S.; Varghese S.; Park S. Y.; Olivier Y.; Milián-Medina B.; Resel R., Gierschner J. *Adv. Opt. Mater.,* **2019**, *7*, 1900749.

31. Yoon S. J.; Chung J. W.; Gierschner J.; Kim K. S.; Choi M. G.; Kim D., Park S. Y. *J. Am. Chem. Soc.,* **2010**, *132*, 13675-13683.

32. Varghese S.; Park S. K.; Casado S.; Resel R.; Wannemacher R.; Luer L.; Park S. Y., Gierschner J. *Adv. Funct. Mater.,* **2016**, *26*, 2349-2356.

33. Shi J.; Yoon S.-J.; Viani L.; Park S. Y.; Milián-Medina B., Gierschner J. *Adv. Opt. Mater.,* **2017**, *5*, 1700340.

34. Majumdar P.; Tharammal F.; Gierschner J., Varghese S. *Chemphyschem,* **2020**, *21*.

35. Fabian L., Kalman A. *Acta Crystallogr B,* **2004**, *60*, 547-558.

36. Anthony A.; Jaskolski M.; Nangia A., Desiraju G. R. *Chemical Communications,* **1998**, 2537-2538.

37. Kalman A.; Parkanyi L., Argay G. *Acta Crystallographica Section B-Structural Science Crystal Engineering and Materials,* **1993**, *49*, 1039-1049.

38. Lausi A.; Polentarutti M.; Onesti S.; Plaisier J. R.; Busetto E.; Bais G.; Barba L.; Cassetta A.; Campi G.; Lamba D.; Pifferi A.; Mande S. C.; Sarma D. D.; Sharma S. M., Paolucci G. *The European Physical Journal Plus,* **2015**, *130*, 1-8.

39. Kabsch W. *Acta Crystallogr D Biol Crystallogr,* **2010**, *66*, 125-132.

40. Winn M. D.; Ballard C. C.; Cowtan K. D.; Dodson E. J.; Emsley P.; Evans

P. R.; Keegan R. M.; Krissinel E. B.; Leslie A. G.; McCoy A.; McNicholas S. J.; Murshudov G. N.; Pannu N. S.; Potterton E. A.; Powell H. R.; Read R. J.; Vagin A., Wilson K. S. *Acta Crystallogr D Biol Crystallogr,* **2011**, *67*, 235-242.

41. Evans P. R., Murshudov G. N. *Acta Crystallogr D Biol Crystallogr,* **2013**, *69*, 1204-1214.

42. Sheldrick G. M. *Acta Crystallogr A Found Adv,* **2015**, *71*, 3-8.

43. Sheldrick G. M. *Acta Crystallogr C Struct Chem,* **2015**, *71*, 3-8.

44. Emsley P.; Lohkamp B.; Scott W. G., Cowtan K. *Acta Crystallogr D Biol Crystallogr,* **2010**, *66*, 486-501.

45. Blessing R. H. *Acta Crystallogr A,* **1995**, *51 (Pt 1)*, 33-38.

46. Sheldrick G. SADABS, Version 2.10. University of Göttingen, Germany; 2003.

47. Spek A. L. *Journal of Applied Crystallography,* **2003**, *36*, 7-13.

48. Spek A. L. *Acta Crystallogr D Biol Crystallogr,* **2009**, *65*, 148-155.

49. Frisch M. J. T., G. W.; Schlegel, H. B.; Scuseria, G. E.; Robb, M. A.; Cheeseman, J. R.; Scalmani, G.; Barone, V.; Mennucci, B.; Petersson, G. A.; et al. Gaussian 09, revision D.01. *Gaussian 09, revision D.01*. revision D.01 ed. Wallingford, CT, : Gaussian, Inc.; 2009.

50. Milian-Medina B., Gierschner J. *J. Phys. Chem. Lett.*, **2017**, *8*, 91-101.

51. Clementi E.; Raimondi D. L., Reinhardt W. P. *J. Chem. Phys.*, **1967**, *47*, 1300-1307.

52. Theocharis C. R.; Jones W.; Motevalli M., Hursthouse M. B. *J Cryst Spectrosc,* **1982**, *12*, 377-389.

53. Theocharis C. R.; Desiraju G. R., Jones W. *Journal of the American Chemical Society,* **1984**, *106*, 3606-3609.

54. Jones W.; Theocharis C. R.; Thomas J. M., Desiraju G. R. *J Chem Soc Chem Comm*, **1983**, 1443-1444.

55. Polito M.; D'Oria E.; Maini L.; Karamertzanis P. G.; Grepioni F.; Braga D., Price S. L. *Crystengcomm*, **2008**, *10*, 1848-1854.

56. Jiang H.; Hu P.; Ye J.; Zhang K. K. K.; Long Y.; Hu W. P., Kloc C. *J. Mater. Chem. C*, **2018**, *6*.

57. Emge T. J.; Wiygul F. M.; Chappell J. S.; Bloch A. N.; Ferraris J. P.; Cowan D. O., Kistenmacher T. J. *Molecular Crystals and Liquid Crystals*, **2007**, *87*, 137-161.

58. Crespo-Otero R.; Li Q., Blancafort L. *Chem Asian J*, **2019**, *14*, 700-714.

59. Shi J.; Izquierdo M. A.; Oh S.; Park S. Y.; Milián-Medina B.; Roca-Sanjuán D., Gierschner J. *Org Chem Front*, **2019**, *6*, 1948-1954.

60. Izquierdo M. A.; Shi J. Q.; Oh S.; Park S. Y.; Milian-Medina B.; Gierschner J., Roca-Sanjuan D. *Phys. Chem. Chem. Phys.*, **2019**, *21*, 22429-22439.

61. Goushi K.; Yoshida K.; Sato K., Adachi C. *Nat Photonics*, **2012**, *6*, 253.

62. Zhang Q. S.; Li B.; Huang S. P.; Nomura H.; Tanaka H., Adachi C. *Nat. Photonics*, **2014**, *8*, 326-332.

63. Park I. S.; Matsuo K.; Aizawa N., Yasuda T. *Adv. Funct. Mater.*, **2018**, *28*.

64. Song Y.; Kim Y.; Noh Y.; Singh V. K.; Behera S. K.; Abudulimu A.; Chung K.; Wannemacher R.; Gierschner J.; Luer L., Kwon M. S. *Macromolecules*, **2019**, *52*, 5538-5545.

65. Nguyen T. B.; Nakanotani H.; Hatakeyama T., Adachi C. *Adv. mater.*, **2020**.

Chapter 3. Organic 2D-type Quasi-Isostructural Crystalline Solid Solution with Partial Charge-Transfer (CT) Doping based on Isometric Donor and Acceptor Molecules for Organic Photo-Transistor (OPT) Application

3.1. Introduction

CT states generated by D:A interface have played a crucial role in the various optoelectrical devices; *e.g.*, exciton dissociation at heterojunction of organic solar cells (OSC) [1, 2, 3], thermally activated fluorescence (TADF) of exciplex in organic light-emitting diodes (OLED) [4, 5, 6], and charge-transfer (CT) doping in organic field-effect transistors (OFET) [7, 8, 9]. However, it is still challenging to control/ predict the molecular orientation at the D:A interface to understand the various optoelectrical responses function. Furthermore, low morphological compatibility of D and A limits the electrical transport [10, 11, 12] and confines the doping ratio in various organic optoelectrical devices [13, 14, 15]. Regarding these scientific/ technical challenges on D:A system, our isostructural crystal system via isometric molecules can provide virtually ideal platform to investigate optoelectrical property-structure relationship of CT states as well as can provide non-destructive D:A bi-component system even in the heavily doped conditions. By virtue of the high miscibility of isometric molecules in the crystal, I found all four D:A pairs were thermodynamically stable at crystalline solid solution states in majority of acceptor composition (D:A = guest: host). Crystalline solid solution followed the 2D-like morphology of acceptor host, and the guest and host molecules generated CT complex which are substitutional doped in the host. In addition, isometric guest and host molecular structure have brought various distinct scientifically/ technically

important features to crystalline solid solution: (i) densely packed structure warranted the high energy transfer (ET) efficiency up to 80% and thus giving CT emission at entire 2D crystals (ii) structurally/ electrically non-destructive doped features even in heavily doped condition (20 %) in some case, and (iii) pairs of quasi-isostructural crystalline solid solutions which rules out the morphological factors.

Recently the organic photo-transistor (OPT) devices have gained many interests in organic optoelectronic society [10, 16, 17, 18] due to the increasing demands on image sensors[17, 19] and also comparable benefits of the organic transistor as an image sensor such as high on/off ratio and high gain [20, 21]. Similar to other organic devices, CT state at the interface of D-A also play a central role in OPT devices: CT state at D-A interface dissociates the excitons into free electrons and holes by the built-in-potential [10, 20], and the generated minor carrier trapped in the device eventually result in electric signal amplification through threshold voltage shift (ΔV_{TH}) of the transistor device [22, 23, 24]. To the end, based on these systemic merits we demonstrated organic photo-transistor (OPT) device without any supplementary layers other than the crystalline solid solution. The OPT device showed moderate photo-responsivity (~500 AW^{-1}) with few tens of threshold voltage shift (ΔV_{TH}). Based on the engineered crystal structure by isometric molecular pairs, we systemically correlated the OPT performances and the ET %, D:A energetical offsets, electrical transport of the crystalline solid solutions.

3.2. Experimental

Characterization of CT doped plate crystals

The synthesis and purification of the host and guest molecules were described in detail at the previous paper [25]. The reagents were purchased from Sigma Aldrich Chemical Co. (Darmstadt), Tokyo Chemical Industry Co. (Tokyo), and Alfa Aesar Co. (Massachusetts). All of the final products were characterized after sublimation purification. For the optical/ photophysical property investigation of CT doped plate crystals, QM-40 was used for PL spectra measurement, and the luminescent lifetime were measured through Fluotime 200. Out of plane XRD data was taken through D8 advanced X-ray diffractometer (Bruker Miller). The d-spacing from out-of-plane XRD peaks were extracted using Bragg's equation: $n\lambda = 2d\sin\theta$.

Energy transfer efficiency (η) was obtained through the lifetime according to following equation: $1-(\tau_{F,\ CT}/\tau_{F,\ Host})$. $\tau_{F,\ CT}$ is the amplitude weighted lifetime detected from pure CT emissive region, and $\tau_{F,\ Host}$ is the amplitude weighted lifetime detected from pure host emissive region.

OPT device fabrication and characterization.

The silicon/silicon oxide (Si/SiO_2) substrates (SiO_2 thickness: 300 Å) were sonicated in deionized water, acetone, and isopropyl alcohol (IPA) sequent for 10 min, then the substrates were ozone treated for 30 min. The host and guest molecules were fully solvated in the dichloromethane (DCM) solvent, and the 6 ml of solution was filled in the 20 ml vial. The washed substrate was leaned against the inner wall of the vial with the solution and dried in the room temperature condition. The drying speed can be controlled by slightly open the vial cap from the vial. Via slow evaporation of the solvent, the large plate crystal can be formed

over the substrate surface. The source/drain (S/D) electrode, Al 50 nm was thermally deposited on the plate crystal through the patterned shadow mask in the high vacuum condition ($1 \cdot 10^{-6}$ torr).

The electrical properties of the fabricated devices were measured by Keithley 4200 connected to three probe-station for contacting source, drain, and gate respectively. From the following equation, FET mobility in saturation region and V_{TH} was extracted:

$$I_D = \frac{WC_i}{2L} \mu (V_G - V_{TH})^2$$

I_D is the drain current, W/L is the channel width and length respectively, C_i is the capacitance of dielectric layer, μ is the mobility of the device in the saturation region, V_G/ V_{TH} are the gate voltage and threshold voltage respectively. For the static measurement of the OPT, the halogen lamp ($P = 1.24 \cdot 10^{-5}$ W/cm^2) was used and for the dynamic response measurement and light intensity dependent measurement, the UV light (497 nm) controlled by the Keithley 2400 was introduced. Responsivity (R) was measured by the equation as follows: (I_{Light} - I_{Dark})/ P_{light} ($A \cdot W^{-1}$).

3.3. Result and discussion

3.3.1. Molecular substitutional doped CT crystals

The molecular structure of two hosts (H1, H2) and guests (G1, G2) is shown at **Figure 3-1a-b** respectively. Small amount of guest molecules (1~10 %) and host molecules dissolved in dichloromethane (DCM) solvent, and the solution was slowly evaporated to make co-crystals (**Figure 3-2**). Through this simple 1-step solvent evaporation, all of the resultant co-crystals showed the plate type morphology like the host crystals (**Figure 3-1c-h**, **Figure 3-3**), and the sharp out-of-plane X-ray diffraction (XRD) peaks of them (**Figure 3-4a-e**) indicate the high crystallinity of the co-crystals. Other than the corresponding host emission (**Figure 3-4f-i**, blue line), every guest doped host crystals (**Figure 3-1c-d, f-g**) showed the red-shifted photo luminescent (PL) emission which is corresponding with that of 1:1 CT co-crystals of the same D:A pair [25]; Red (R) emission of G1 doped H1 (G1:H1) co-crystals (**Figure 3-4f**), yellow (Y) emission of G2:H1 co-crystals (**Figure 3-1g**), orange (O) emission of G1:H2 co-crystals (**Figure 3-1h**), and green (G) emission of G2:H2 co-crystals (**Figure 3-1i**). Furthermore, the red-shifted emission by doping showed longer lifetime decay than that of corresponding host emission (**Figure 3-5**). Therefore, it is apparent that the guests and hosts generated CT complexes in the host crystal matrixes, which now the fabricated co-crystals can be called ‘CT doped co-crystals’.

The CT complexes doped in the host crystals seem to have negligible effect on the original crystal structure and morphology by virtue of the isometric molecular structure of guests and hosts (*vide infra*). Every out-of-plane XRD peaks of non-doped host crystals (**Figure 3-4a-d**, blue line) was coincided with that of CT doped

co-crystals (**Figure 3-4a-d**, colored) for every CT doped co-crystals in various doping concentrations (0.5~20%, **Figure 3-4a-d**, **Figure 3-6**) even in 20% doped condition at R (G1:H1) co-crystal case (**Figure 3-4a**). Also, the deviation of d-spacing values (**Figure 3-4e**) between CT doped co-crystals and corresponding host crystal was minor (~0.1 Å, **Table 3-1)**. In addition, it was found the XRD results well-correlated with the real step height of (co-)crystals (**Figure 3-7**) which was assigned by the atomic forced microscopy (AFM). Furthermore, AFM images of CT doped co-crystals showed the same sheet terrace morphology like the host crystals (**Figure 3-7**). Therefore, the XRD and AFM image so far point out the crystal structure of host crystal remained intact by the doping of the isometric guest.

To further study the molecular arrangements in CT doped co-crystals, the light phase of CT emission was investigated by rotating the polarizer under UV irradiation condition through OM. The CT emissions in the same crystalline domain changed all together (**Figure 3-8**), and this indicates CT emitting species aligned in the crystalline domain. Therefore, the guest molecules are grown in-phase in the plate co-crystals with the majority of host molecules. At this moment, the guest molecules possibly can be thought to take the interstitial position or the substitutional position in the host crystal. In fact, the possibility on interstitial doping can be excluded because there is not enough space to interstitial doping of guest due to the tight stacking of host molecules (**Scheme 3-1a**) [26], and there is no sign of crystal structural change at host crystal from the XRD results (*vide supra*). Therefore, the results so far highly indicate the CT doped co-crystals are molecular substitutional CT doped co-crystals (**Scheme 3-1a**) as expected from the isometric structure of guest and host at the beginning (**Figure 3-1a-b**).

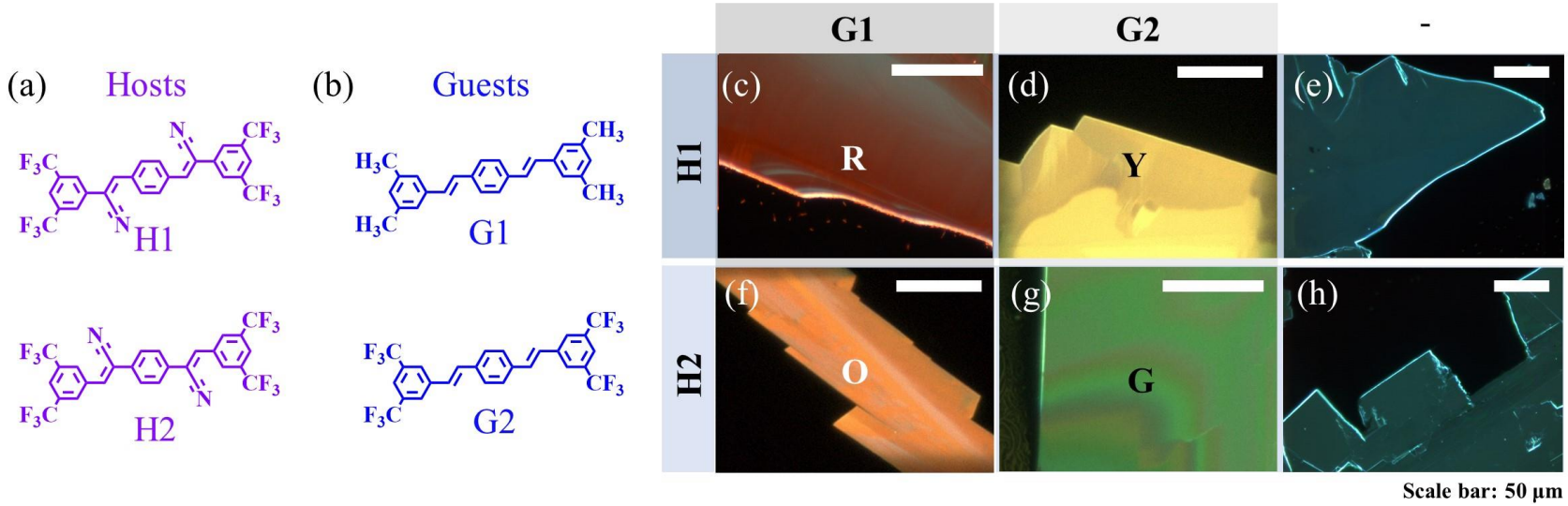

Figure 3-1. Isometric molecular structure of host/guest and their molecular substituted CT doped crystals. (a) Molecular structure of hosts (H1, H2) and (b) guests (G1, G2), (c-e) optical microscopy images of H1 host based plate crystals; (c) red (R) CT doped plate crystal G1:H1 (10:90), (d) yellow (Y) CT doped plate crystal G2:H1 (1:99), (e) H1 crystal without doping. (f-h) optical microscopy images of H2 host based plate crystals; (f) orange (O) CT doped plate crystal G1:H2 (1:99), (g) green (G) CT doped plate crystal G2:H2 (1:99), (h) H2 crystal without doping. (Scale bar = 50 µm)

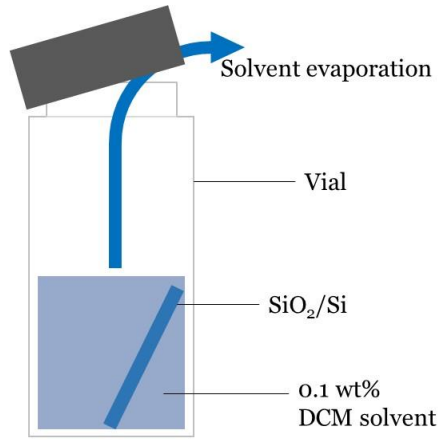

Figure 3-2. Plate crystal growth method

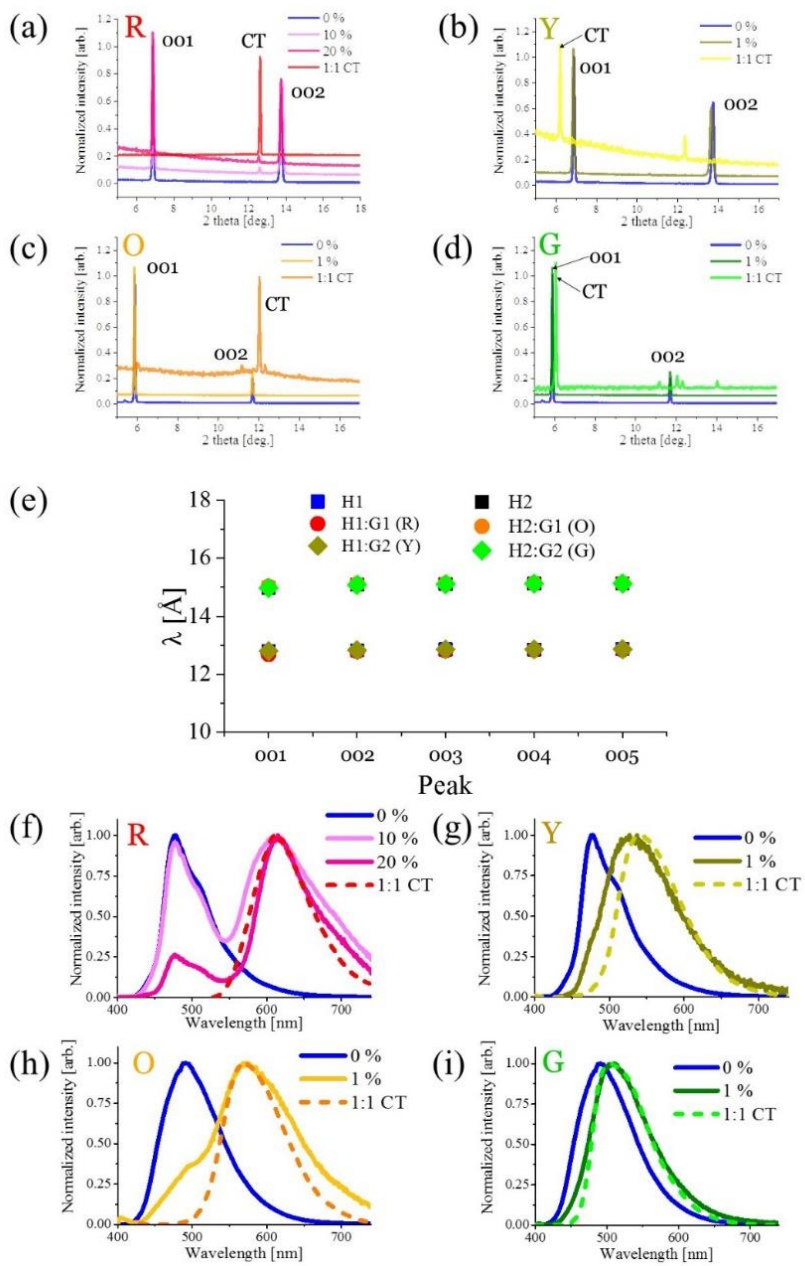

Figure 3-3. X-ray diffraction (XRD) and Photo-luminescence (PL) of molecular substituted CT doped co-crystals. Out-of-plane XRD of (a) H1, G1 doped H1 co-crystals, G1:H1=1:1 CT co-crystals, (b) H1, G2 doped H1 co-crystals, G2:H1=1:1 CT co-crystals, (c) H2, G1 doped H2 co-crystals, G1:H2=1:1 CT co-crystals, (d) H2, G1 doped H1 co-crystals, and G2:H2=1:1 CT co-crystals. (e) d-spacing of each (co-)crystals. PL spectra of (f) H1, G1 doped H1 co-crystals, G1:H1=1:1 CT co-crystals, (g) H1, G2 doped H1 co-crystals, G2:H1=1:1 CT co-crystals, (h) H2, G1 doped H2 co-crystals, G1:H2=1:1 CT co-crystals, (f) H2, G1 doped H1 co-crystals, and G2:H2=1:1 CT co-crystals.

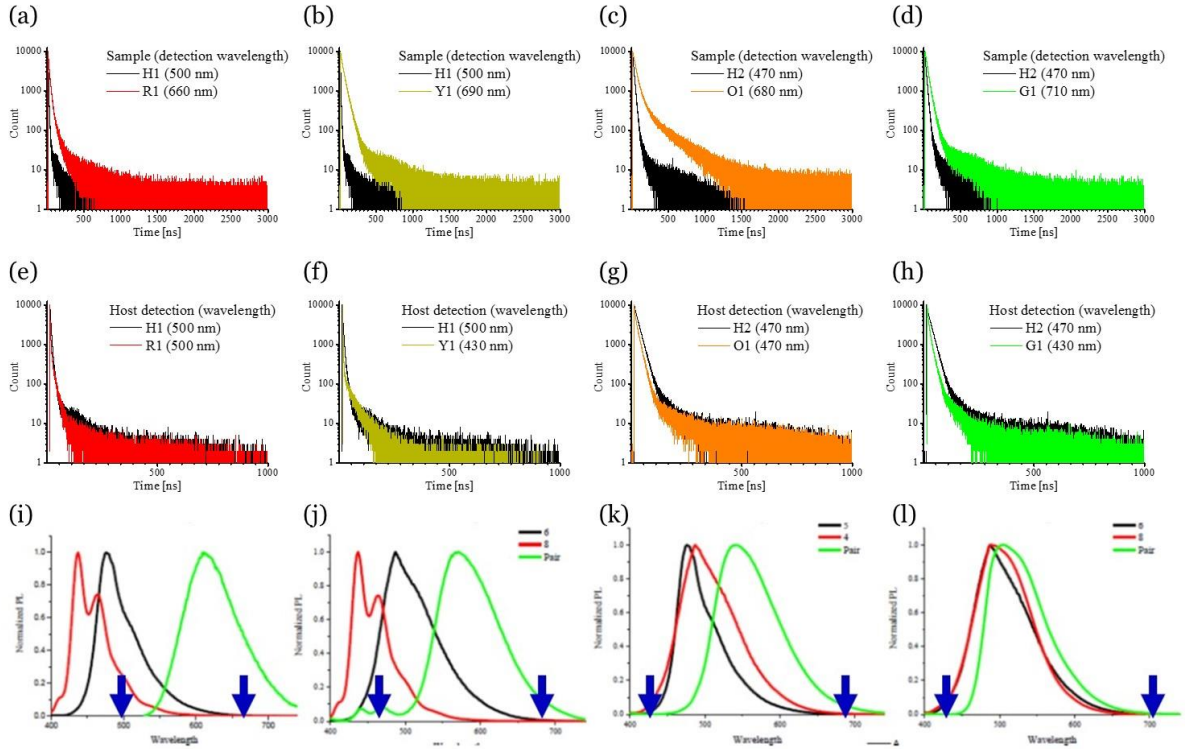

Figure 3-4. Emission and lifetime decay profiles. (a-d) Lifetime decay of CT doped (1%) co-crystals (colored) detected at CT only region and corresponding host crystals (black) detected at emission maximum, (e-h) Lifetime decay of CT doped co-crystals detected at host only region (colored) and corresponding host crystals detected at emission maximum (black), and (i-l) Photo-luminescent (PL) spectrum of corresponding guest (red), host (black), and their 1:1 CT complex (green). The left arrows mean host only detection wavelength, and right arrows mean CT only detection wavelength

R						
Dopant %		001	002	003	004	005
0	2theta [deg.]	6.9	13.8	20.7	27.7	34.8
	λ [Å]	12.8	12.8	12.9	12.9	12.9
1	2theta [deg.]	6.9	13.8	20.7	27.8	34.8
	λ [Å]	12.8	12.8	12.8	12.8	12.9
5	2theta [deg.]	7.0	13.9	20.8	27.8	34.8
	λ [Å]	12.7	12.8	12.8	12.8	12.9
10	2theta [deg.]	7.0	13.8	20.8	27.8	34.9
	λ [Å]	12.7	12.8	12.8	12.8	12.8
20	2theta [deg.]	7.0	13.8	20.8		
	λ [Å]	12.7	12.8	12.8		

Y						
Dopant %		001	002	003	004	005
0	2theta [deg.]	6.9	13.8	20.7	27.7	34.8
	λ [Å]	12.8	12.8	12.9	12.9	12.9
0.5	2theta [deg.]	6.9	13.8	20.7	27.7	34.8
	λ [Å]	12.8	12.8	12.9	12.9	12.9
1	2theta [deg.]	6.9	13.7	20.5	27.5	34.5
	λ [Å]	12.8	12.9	13.0	13.0	13.0
5	2theta [deg.]	6.9	13.7	20.6		
	λ [Å]	12.8	12.9	12.9		

O						
Dopant %		001	002	003	004	005
0	2theta [deg.]	5.9	11.7	17.6	23.5	29.5
	λ [Å]	15.0	15.1	15.1	15.1	15.1
0.5	2theta [deg.]	5.9	11.7	17.6	23.5	29.5
	λ [Å]	14.9	15.1	15.1	15.1	15.1
1	2theta [deg.]	5.9	11.7	17.6	23.5	29.5
	λ [Å]	15.0	15.1	15.1	15.1	15.1
5	2theta [deg.]	5.9	11.7	17.6	23.5	29.5
	λ [Å]	14.9	15.1	15.1	15.1	15.1

G						
Dopant %		001	002	003	004	005
0	2theta [deg.]	5.9	11.7	17.6	23.5	29.5
	λ [Å]	15.0	15.1	15.1	15.1	15.1
0.5	2theta [deg.]	5.9	11.7	17.6	23.5	29.4
	λ [Å]	15.0	15.1	15.1	15.2	15.2
1	2theta [deg.]	5.9	11.7	17.6	23.5	29.5
	λ [Å]	15.0	15.1	15.1	15.1	15.1
5	2theta [deg.]	5.9	11.7	17.6	23.5	29.5
	λ [Å]	14.9	15.1	15.1	15.1	15.1

Table 3-1. Out-of-plane XRD of doped plate co-crystals and their d-spacing

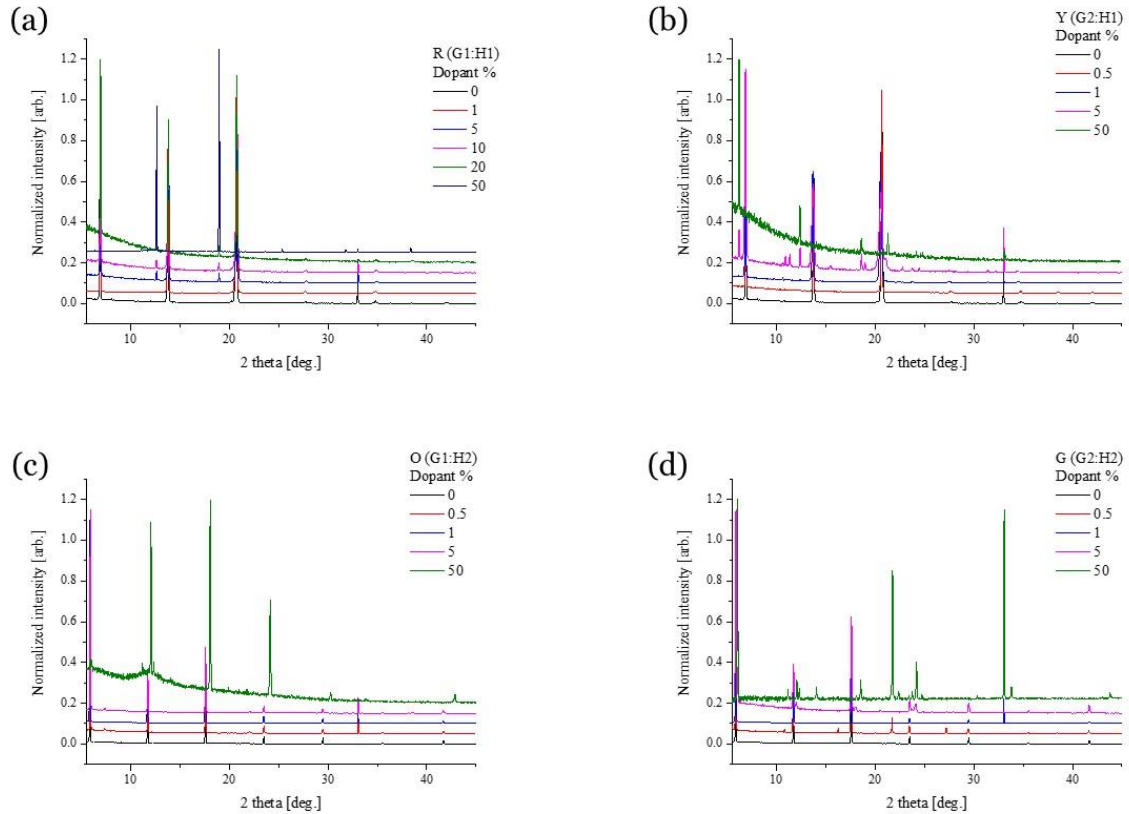

Figure 3-5. Full scaled out-of-plane XRD of doped plate co-crystals. XRD image in various doping ratio of (a) R(G1:H1), (b) Y(G2:H1), (c) O(G1:H2), and (d) G(G2:H2)

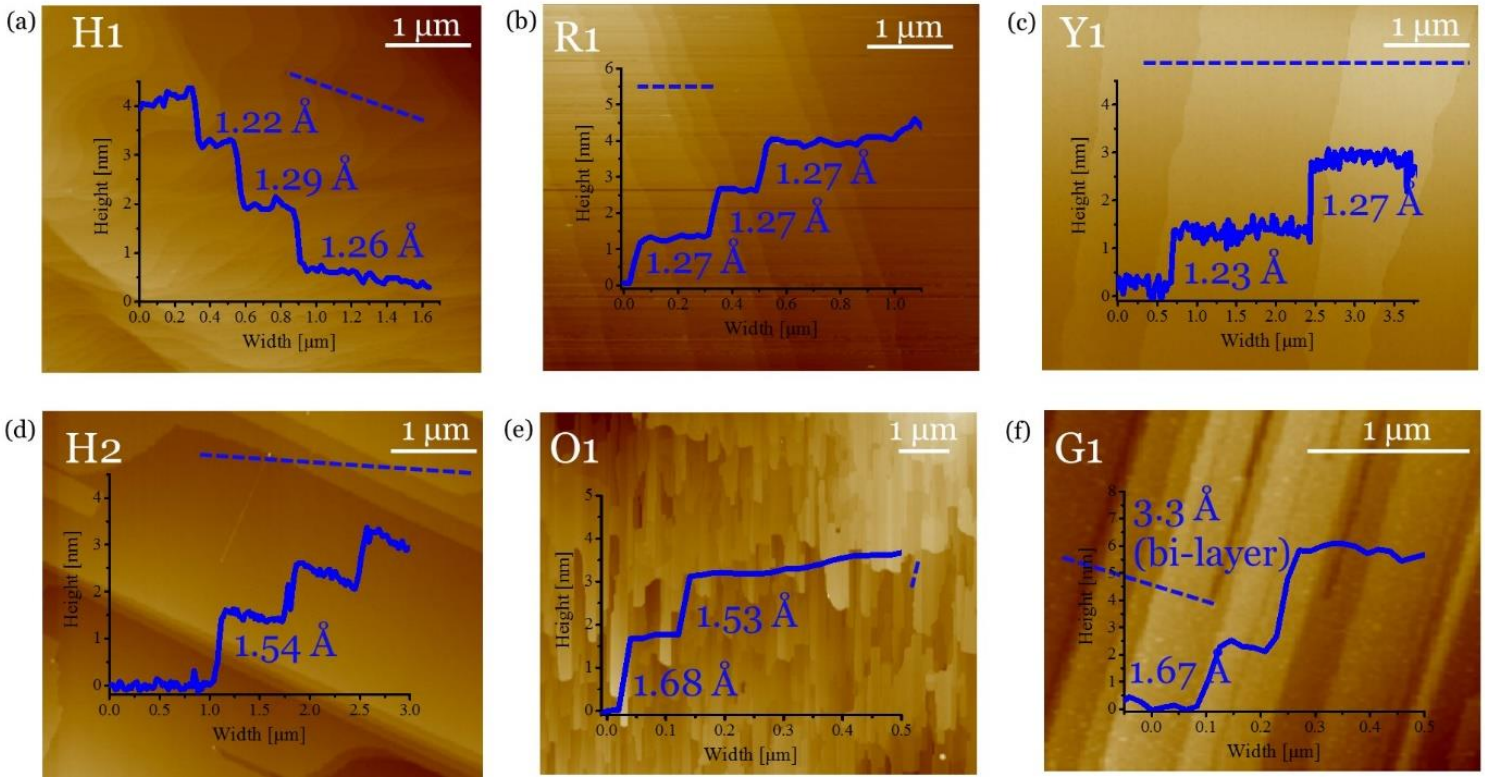

Figure 3-6. AFM images of doped plate co-crystals and host crystals. AFM image and steps of (a) H1, (b) R(G1:H1 = 1:99), (c) Y (G2:H1 = 1:99), (d) H2, (e) O(G1:H2 = 1:99), G(G2:H2 = 1:99) (co-)crystals.

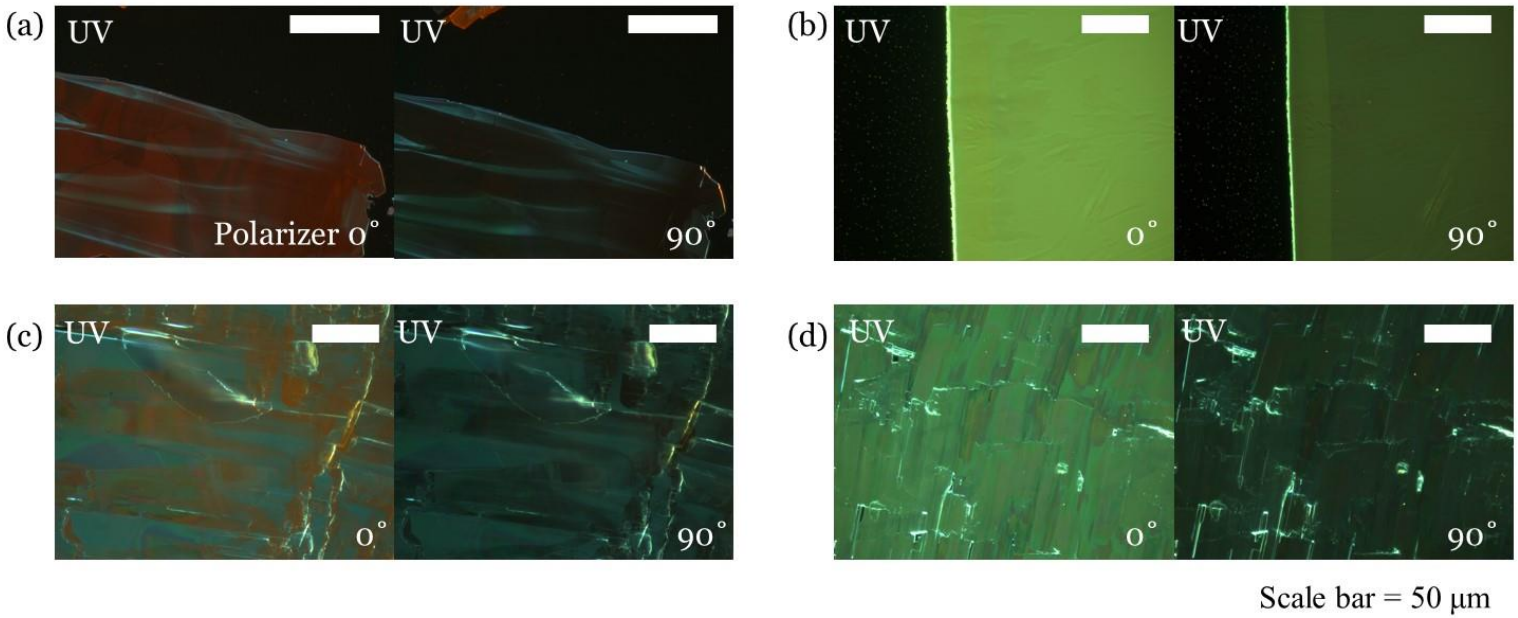

Figure 3-7. OM images of doped plate co-crystals under UV with polarizer
(a) R(G1:H1), (b) Y(G2:H1), (c) O(G1:H2), and (d) G(G2:H2)

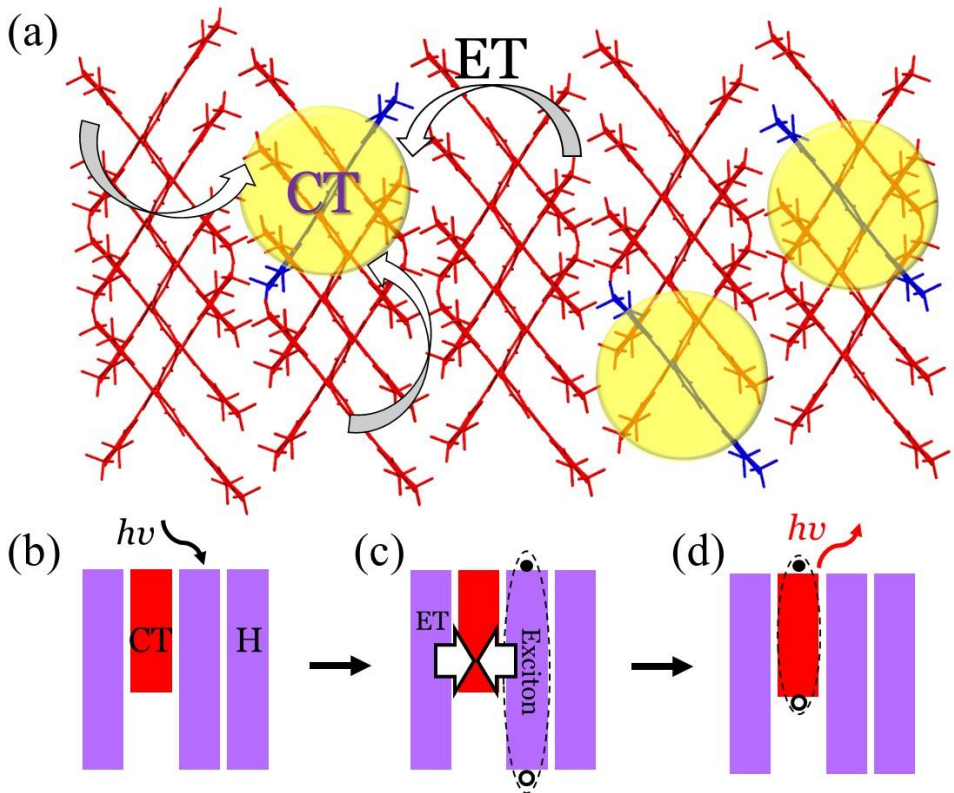

Scheme 3-1. Schematic of molecular substituted CT doped co-crystals which shows molecularly isolated CT and energy transfer. (a) Schematic of molecular substituted CT doped co-crystals (b-d) ET process of molecular substituted CT doped co-crystals: optical excitation (b) – Exciton formation and energy transfer to molecular CT (c) – Radiative decay of excitons at molecular CT (d)

3.3.2. Ratio dependent optical properties of CT doped crystals

The DSB guests and DCS hosts can form crystalline solid solution in various composition by virtue of their molecular isometric structure, and their morphological/ photophysical properties are variated depending on the stoichiometry of compositions (*vide infra*).

The morphology of the crystalline solid solutions was variated depending on the stoichiometry (dopant %) between isometric constituents (**Figure 3-9**). Interestingly, original plate type morphology of hosts became continuously less contributable with the higher dopant %: crystalline domain size became smaller and the aspect ratio became higher. To the end, needle type 1:1 cocrystals are formed at the 50 % of dopant %. This kind of gradual morphological tuning by composition changes often found with the solid solution systems where crystal structural parameters also linearly changes by composition [27, 28]. In fact, over the certain dopant % (around 1~5 % of dopant %), cotton-like structures as well as plate crystals was observed in the both case of G2:H1 (yellow) and G2:H2 (green) compositions, and this cotton-like structure can be assigned as bundle of needle type CT cocrystals which didn't participate in solid solution. Meanwhile, red and orange cases maintained their plate like morphology without cotton-like structure at rather heavily doped conditions; 20 % and 5 % of dopant % for red and orange respectively. This discrepancy depending on stoichiometry between isostructural crystalline solid solutions can be understood through the thermo-dynamics in the crystalline solid solution (*vide infra*).

Figure 3-10 shows differential scanning calorimetry (DSC) results of the guests,

hosts, and their 1:1 cocrystals. Each melting points represents overall intermolecular interactions presence in crystals which includes interactions at intra-stack as well as inter-stack directions. As discussed earlier (**Chapter 2**), intermolecular distance along the π-stack (intra-stack) became smaller with the stronger CT interaction (3.31, 3.38, 3.40, 3.46 Å for CT-R, O, Y, G respectively). However, overall intermolecular interaction regarding also the inter-stack direction gives different story: For the 1:1 cocrystal cases, melting temperature (T_M) and freezing temperature (T_F) are increasing in the order of CT-R, O, Y, G; *e.g.*, 211, 238, 264, 281 ˚C for the second T_M respectively. Indeed, the intermolecular interactions at π-stack direction is most prominent than the others regarding the needle-type morphology of the crystals, however, the summation of intermolecular interaction in 3-D directions was different as indicated from the DSC results. In fact, interaction between π-stacks of CT-R seems to be rather small which indicated from the perpendicular π-stacks along the inter-plane direction, while the intra-stacks of the others aligned in parallel (**Chapter 2**). Furthermore, additional secondary interactions by the CF_3 groups of G2 (D2) was observed at the CT-Y, G cases, *e.g.*, Ar-H− F interaction.

In the situation in the crystalline solid solution, in fact, it is hard to predict the intermolecular interactions between guest and host in the crystalline solid solution because the exact molecular conformation is hard to be expected due to the CT pairs are randomly distributed at crystalline solid solution. However, stoichiometry dependent morphology can be correlated with the DSC results of CT 1:1 cocrystals and host crystals: the T_M and T_F of CT-R and CT-O were similar and/or smaller than corresponding acceptor while those of CT-Y and CT-G were larger than corresponding acceptor, for example, second sweep T_M of CT-R and A1 were 211

and 247 ˚C while that of CT-G and A2 were 281 and 233 ˚C (**Figure 3-11**). Therefore, CT-Y and CT-G have thermodynamically larger chance to form 1:1 CT cocrystals at the certain critical dopant % than CT-R and CT-O cases. Indeed, at the lower dopant %, CT-Y and CT-G participated into solid solution, but the larger dopant % statistically increases the possibility to make 1:1 cocrystals, so cotton-like CT 1:1 cocrystals are observed from the certain condition of dopant %. In addition, crystalline solid solution in reverse composition of majority of donor also seem to be affected by the estimated intermolecular interaction by DSC result. T_M and T_F of D1 were much smaller than corresponding CT and those of D2 were similar with corresponding CT (**Figure 3-10**), and therefore, plate type D1 crystal and corresponding needle type CT (CT-R, CT-O) showed clearly segregated fashion, meanwhile, D2 and corresponding CT (CT-Y, CT-G) were hard to be distinguished each other (**Figure 3-11**). In fact, electrostatic force is negligible intermolecular interactions at the organic solids[29], therefore, electrostatic interactions promoted by cyano groups (−C≡N) and CF_3 groups of acceptor can stabilize the lattice energy of crystalline solid solution, while especially the D1 host was not suitable to generate crystalline solid solution.

By virtue of the dispersed CT in the mixed crystals, crystalline solution showed rather high energy transfer (ET) efficiency, and it can be also correlated with the stoichiometry dependent morphology: ET efficiency (η) of R(G1:H1) and O(G1:H2) were increased with higher dopant %, while η of Y(G2:H1) and G(G2:H2) were increased in certain range of dopant % and decreased when the cotton-like CT cocrystals generated at higher dopant % (**Table 3-2**). The PL spectra depending on dopant % follows the trends of η: portion of CT emission became stronger with higher dopant % at R(G1:H1) and O(G1:H2) case, while

portion of CT emission became stronger at low dopant % range and decreased when cotton-like CT crystal formed at higher dopant % (**Figure 3-12**). The CT emission of crystalline solid solution also showed bi-component decay like 1:1 CT cocrystals (**Chapter 2**) of which lifetime was longer than that of corresponding donor and acceptors (**Table 3-3**). The η trend depending on stoichiometry is straight forward because the higher CT concentration in solid solution will show higher η. Regarding the thermodynamic investigation above, Y(G2:H1) and G(G2:H2) were cannot afford more CT in the solid solution from certain dopant % but CT cocrystals started to be generated rather than included into solid solution, and thus result in lesser amount of CT and lower η.

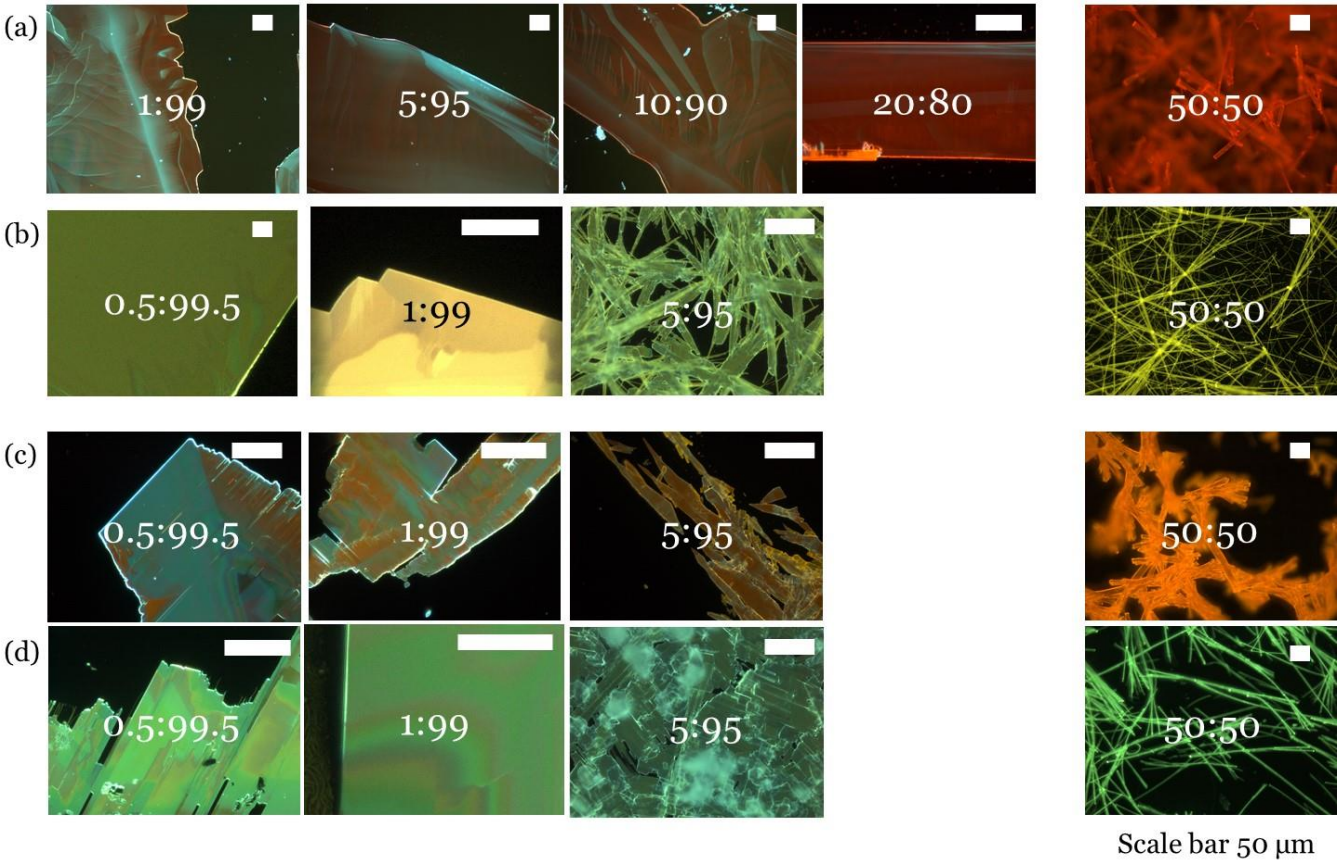

Figure 3-9. Ratio dependent morphology. OM image under UV light in various dopant concentration of (a) R(G1:H1), (b) Y(G2:H1), (c) O(G1:H2), and (d) G(G2:H2)

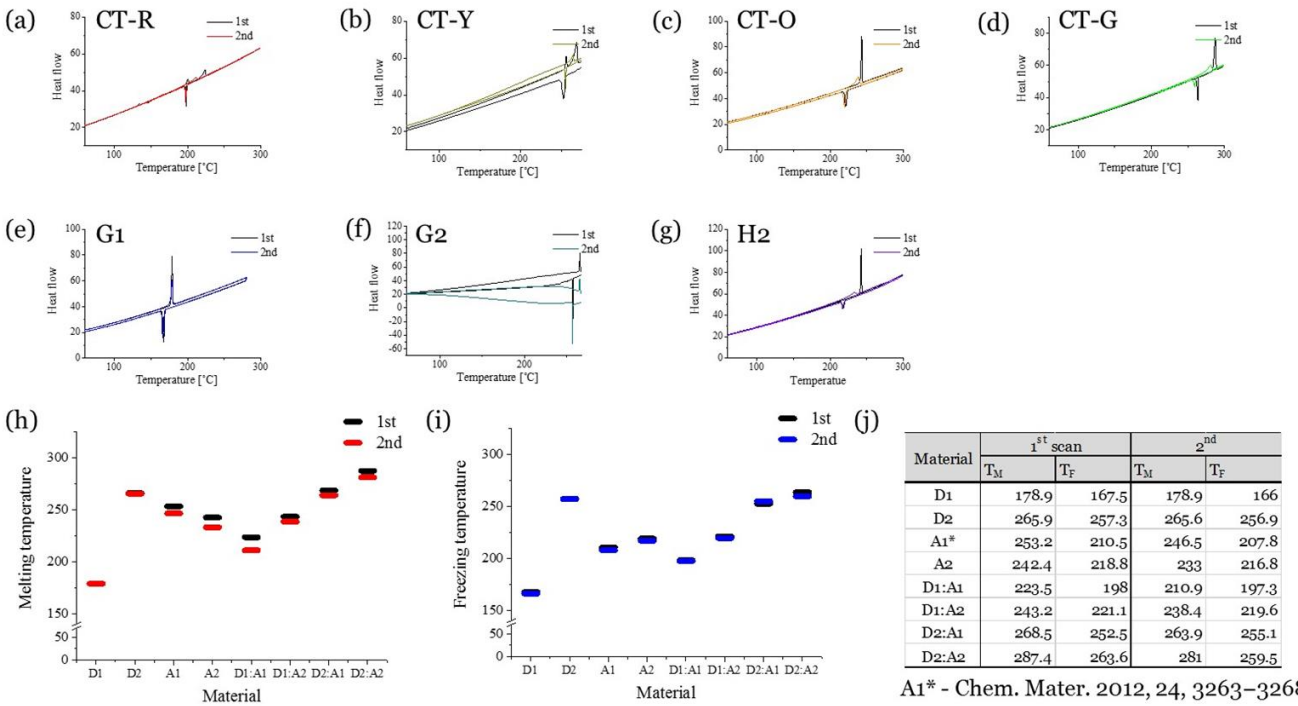

Material	1st scan		2nd	
	T_M	T_F	T_M	T_F
D1	178.9	167.5	178.9	166
D2	265.9	257.3	265.6	256.9
A1*	253.2	210.5	246.5	207.8
A2	242.4	218.8	233	216.8
D1:A1	223.5	198	210.9	197.3
D1:A2	243.2	221.1	238.4	219.6
D2:A1	268.5	252.5	263.9	255.1
D2:A2	287.4	263.6	281	259.5

A1* - Chem. Mater. 2012, 24, 3263−3268

Figure 3-10. DSC data of guest crystals, host crystals, and D:A (1:1) CT complex. DSC data of (a) G1:H1 (1:1) co-crystal, (b) G2:H1 (1:1) co-crystal, (c) G1:H2 (1:1) co-crystal, (d) G2:H2 (1:1) co-crystal, (e) G1 crystal, (f) G2 crystal, and (g) H2 crystal. (h) Summary of melting temperature (MT) of each (co-)crystals in first/second cycle, and freezing temperature (FT) of each (co-)crystals in first/second cycle. (j) Table of MT and FT of each (co-)crystals in first/second cycle.

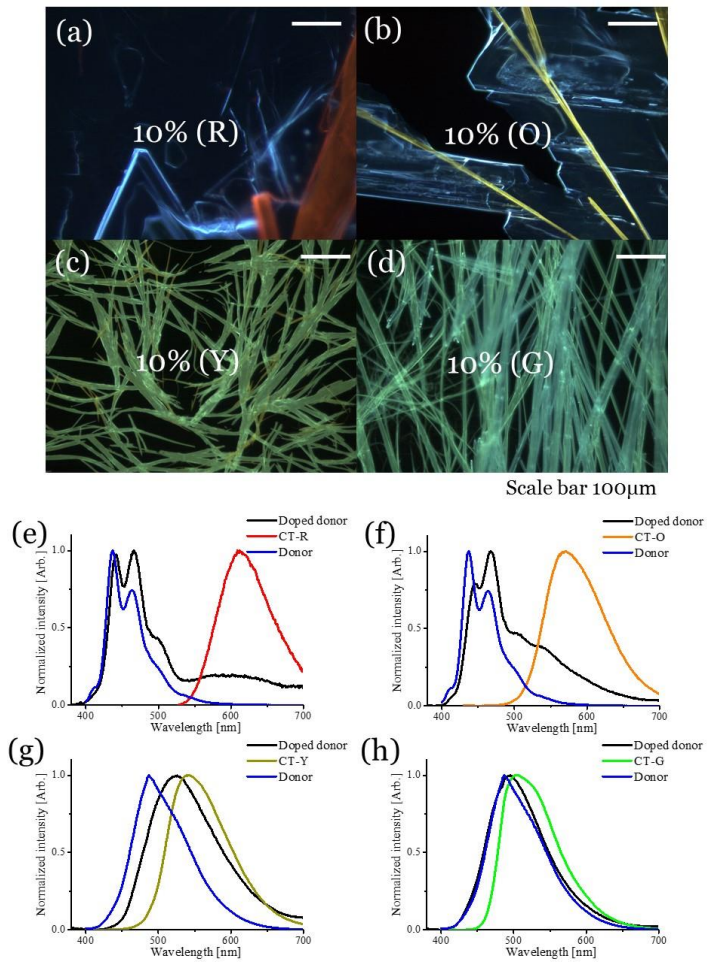

Figure 3-11. OM images and PL spectra of crystals fabricated by slowing evaporation of solution containing trace of acceptor (10 %) and donor.
OM images under UV light of (a) H1 (10%) with G1 as host, (b) H2 (10%) with G1 as host, (c) H2 (10%) with G1 as host, and (d) H2 (10%) with G2 as host. PL spectra of (a) H1 (10%) with G1 as host, (b) H2 (10%) with G1 as host, (c) H2 (10%) with G1 as host, and (d) H2 (10%) with G2 as host.

CT (dopant %)	H1(0)	R (1)	R (10)	R (20)	Y (0.5)	Y (1)	Y (5)	H2	O (0.5)	O (1)	O (5)	G (0.5)	G (1)	G (5)
$\tau_{F,CT}$ [ns]	-	23.7	12.6	11.7	52.0	47.5	46.6	-	55.0	55.9	46.8	39.8	39.0	38.3
$\tau_{F,Host}$ [ns]	6.5	2.7	1.4	1.3	1.7	1.3	1.8	22.3	18.5	15.9	12.8	11.3	13.0	15.1
η	-	0.59	0.79	0.80	0.74	0.80	0.71	-	0.17	0.29	0.43	0.49	0.42	0.32

Table 3-2. Lifetime and energy transfer (CT)efficiency of CT and host of the CT doped crystals. Dopant % : number in the parenthesis, $\tau_{F,CT}$: amplitude weighted lifetime detected from pure CT emissive region, $\tau_{F,Host}$: amplitude weighted lifetime detected from pure host emissive region, η: energy transfer efficiency of CT doped crystals (1- $\tau_{F,CT}/\tau_{F,Host}$)

Detection (nm)			D:A	t_F [ns]	$t_{1,h}$	$I_{1,h}$	$t_{2,h}$	$I_{2,h}$	$t_{1,CT}$	$I_{1,CT}$	$t_{2,CT}$	$I_{2,CT}$	η	Morphology
A1	Host	506	0:100	6.5	5.2	76.9	41.6	23.1	-	-	-	-	-	Plate
A2	Host	491	0:100	22.3	21.4	95.0	136.3	5.0	-	-	-	-	-	Plate
R (D1:A1)	Host	500	1:99	2.7	2.0	69.5	13.8	30.5	-	-	-	-	0.59	Plate
	CT	670	1:99	23.7	-	-	-	-	20.7	84.7	127.2	15.3		
	Host	500	5:95	1.6	1.0	48.7	4.1	51.3	-	-	-	-	0.75	Plate
	CT	670	5:95	16.0	-	-	-	-	14.8	91.3	90.9	8.7		
	Host	500	10:90	1.4	1.0	66.6	5.2	33.4	-	-	-	-	0.79	Plate
	CT	670	10:90	12.6	-	-	-	-	10.9	84.1	72.9	15.9		
	Host	500	20:80	1.3	1.0	72.7	7.9	27.3	-	-	-	-	0.80	Plate
	CT	670	20:80	11.7	-	-	-	-	9.9	82.3	70.6	17.7		
	CT	620	50:50	12.6	-	-	-	-	10.4	79.2	68.3	20.8	-	Needle
O (D1:A2)	Host	470	0.5:99.5	18.5	17.5	93.5	83.5	6.5	-	-	-	-	0.17	Plate
	CT	680	0.5:99.5	55.0					40.8	70.2	307.9	29.8		
	Host	470	1:99	15.9	15.0	93.0	79.0	7.0	-	-	-	-	0.29	Plate
	CT	680	1:99	55.9	-	-	-	-	43.8	74.3	276.2	25.7		
	Host	470	5:95	12.8	11.9	91.2	67.7	8.8	-	-	-	-	0.43	Plate
	CT	680	5:95	46.8	-	-	-	-	38.3	78.5	247.4	21.5		
	CT	580	50:50	30.4	-	-	-	-	26.6	85.3	171.2	14.7	-	Needle
Y (D2:A1)	Host	430	0.5:99.5	1.7	0.3	17.4	46.9	82.6					0.74	Plate
	CT	690	0.5:99.5	52.0					49.6	94.8	380.7	5.2		
	Host	430	1:99	1.3	1.0	81.3	28.6	18.7	-	-	-	-	0.80	Plate
	CT	690	1:99	47.5	-	-	-	-	45.2	94.3	301.2	5.7		
	Host	430	5:95	1.8	1.5	78.7	26.5	21.3	-	-	-	-	0.71	Broken plate
	CT	690	5:95	46.6	-	-	-	-	43.8	92.7	253.2	7.3		
	CT	540	50:50	62.0	-	-	-	-	41.7	60.7	249.6	39.3	-	Needle
G (D2:A2)	Host	430	0.5:99.5	11.3	9.0	74.0	44.7	26.0					0.49	Plate
	CT	710	0.5:99.5	39.8					37.8	94.5	367.0	5.5		
	Host	430	1:99	13.0	11.3	82.7	51.1	17.3	-	-	-	-	0.42	Plate
	CT	710	1:99	39.0					37.2	94.6	323.1	5.4		
	Host	430	5:95	15.1	14.0	90.8	76.1	9.2	-	-	-	-	0.32	Broken plate
	CT	710	5:95	38.3					35.6	92.1	304.1	7.9		
	CT	500	50:50	71.7	-	-	-	-	46.7	59.1	318.4	40.9	-	Needle

Table 3-3. Lifetime decay of host and CT doped plate co-crystals depending on dopant %

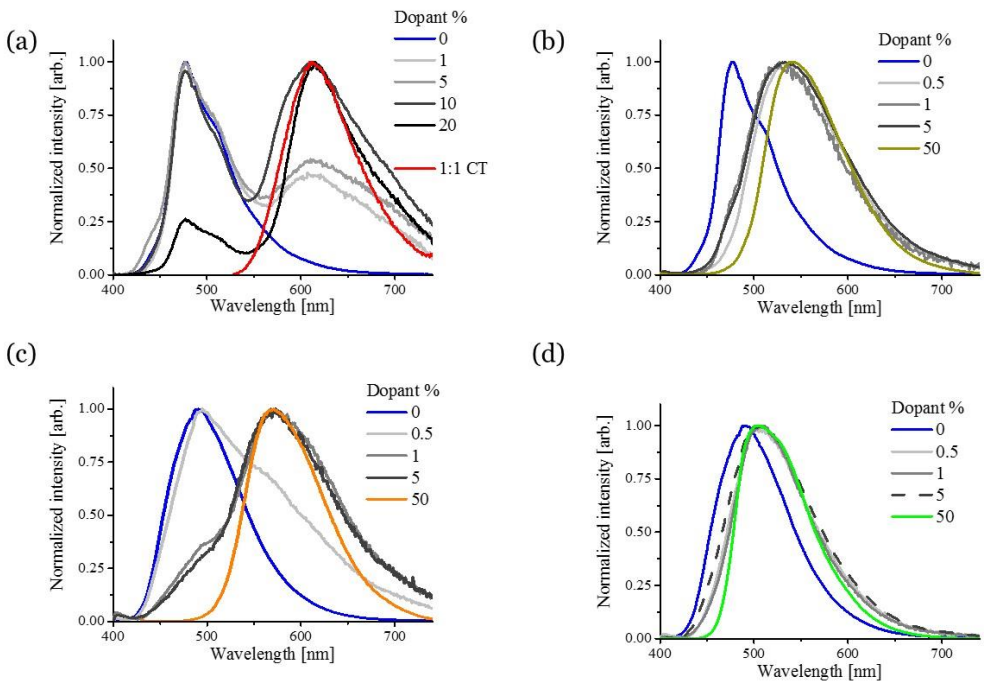

Figure 3-12. PL spectra of doped plate crystal depending on dopant %. PL spectra in various dopant concentration of (a) R(G1:H1), (b) Y(G2:H1), (c) O(G1:H2), and (d) G(G2:H2)

3.3.3. Structure-organic phototransistor relationship by controlled crystal structure

It should be noted that CT doped co-crystals and the corresponding host crystals shares the same crystal structure between them due to substitutional doped structures (**Scheme 3-1**); R(G1:H1), Y(G2:H1) co-crystals and H1 crystal, and also O(G1:H2), G(G2:H2) co-crystals and H2 crystal. This novel crystallographic feature of the (co-)crystals is important in terms of revealing the structure-property relationships of organic crystals because we can exclude the effect of crystal structure on optical/electrical properties of organic crystals [29, 30, 31, 32] and can only regard the parameters derived from the different molecular constitution of the (co-)crystals.

Based on the above mentioned systemic merit, optoelectrical properties of the CT doped co-crystals were extensively investigated through the photo-response of the organic field-effect transistor (OFET) device (**Figure 3-13**). All of the CT doped co-crystal OFETs showed photo-response without introducing any supplementary layer (**Figure 3-13a**). For the equal comparison, the dopant % was fixed to 1 %, and OFETs of non-doped crystal (H1, H2 crystal) were also fabricated as the control device. Every device showed n-type transistor behavior (**Figure 3-13c-h**, Black line). Under the halogen lamp illumination, all CT doped co-crystal OFETs showed photo-response against the dark condition (**Figure 3-13c-d, f-g**), *i.e.*, ΔV_{TH} and drain current (I_D) increment. Also, all of the CT doped OPT showed dynamic photocurrent response to UV light illumination (**Figure 3-13i-l**), and the responsivity depending on UV light intensity showed linear relation in log-log plot (**Figure 3-13m**). However, non-doped control devices were hardly shown the

photo-response (**Figure 3-13e, h**). Therefore, CT complexes generated the photo-response at the OFET devices.

The CT complexes in the co-crystal can play a role to activate the photo-response due to the energy gap between highest occupied molecular orbital (HOMO) of CT and HOMO of host (**Figure 3-13b**), *e.g.*, the roughly estimated corresponding energy gap in R(G1:H1) was *ca.*, 1.6 eV [25] (**Figure 3-14**). This energy gap can provide the built-in-potential which can dissociate excitons [23, 33, 34], and also the minor carriers (holes) from dissociated excitons can be trapped at the CT HOMO by the surrounded host HOMO (**Figure 3-13b**) [23, 34]. In fact, the built-in-potential of CT doped co-crystals affects the performance of OPT which will be discussed soon. In case of the trapping of the hole, it was found CT doped OPT devices in light illuminated condition showed memory window (V_{TH} shift by hysteresis) by gate voltage (V_G) sweep like memristors [35, 36, 37] while memory window was hardly found in the dark condition (**Figure 3-15**). This means that the optical input signal (optically excited excitons) is mainly responsible to memory window rather than electrical input signals. While in case of the non-doped control devices, they hardly showed the memristor behavior in both with/ without light illumination conditions (**Figure 3-15**). Regarding the negative (positive) V_{TH} shift in memristor known to be come from hole (electron) trapping [35, 38], memristor behavior of OPTs in illuminated condition highly indicates the existence of trapped holes which are stemmed from the optically excited excitons. By the way, the electrons dissociated from optically excited excitons can flow by the external bias due to rather small energy barrier [14] between lowest unoccupied molecular orbital (LUMO) of CT and LUMO of host. Therefore, the investigation so far can well-define the operation mechanism of OPT as follows (**Scheme 3-2**): 1. Light illumination → 2. Exciton

migration from host to CT → 3. Exciton dissociation into hole and electron via built-in-potential → 4. Hole trapping and electron flows by external bias → 5. ΔV_{TH} shift and following current increment.

Based on the well-defined OPT operation mechanism, structure-property relationship between OPT devices of equivalent crystal structured (co-)crystals can be systemically investigated (*vide infra*). The stronger CT (higher energetical offset, see **Figure 3-14**), ΔV_{TH} was larger; R(G1:H1) co-crystals (ΔV_{TH} = 72.2 V) > Y(G2:H1) co-crystals (13.0 V) for H1 based co-crystals and O(G1:H2) co-crystals (10.9 V) > G(G2:H2) co-crystals (7.7 V) for H2 based co-crystals (**Figure 3-13**, **Table 3-4**). The result is obvious because stronger CT complexes has larger built-in-potential and large energetical barrier for holes (*vide supra*). In the same context, co-crystals with stronger CT also showed larger memory window (**Figure 3-15**) because the more holes can be trapped by the larger energetical offset between CT HOMO and host HOMO.

Therefore, by taking into account the built-in-potential, energetic barrier, the performance order of OPT can be understood. With the apparent trends of ΔV_{TH}, R also followed the same trend, *i.e.*, R(G1:H1) co-crystals (R= 14.3 $A \cdot W^{-1}$) > Y(G2:H1) co-crystals (3.0 $A \cdot W^{-1}$) and O(G1:H2) co-crystals (0.6 $A \cdot W^{-1}$) > G(G2:H2) co-crystals (0.5 $A \cdot W^{-1}$) respectively (**Table 3-4**). The same trend is observed at the various light intensity as shown at **Figure 3-13m**, and the more detailed electrical, optoelectrical properties of OPT can be found at **Table 3-5**.

Other than the equivalent crystal structures among the (co-)crystals, one of the CT doped co-crystal showed the crystalline polymorphs which can also provide almost ideal platform to investigate the structure-property relationships because they have identical molecular structure with different crystal structure[39]. So far, we

considered the only one crystalline polymorph of H1 (G-phase), but it also showed other crystalline polymorph (B-phase), and the optical/ electrical properties H1 crystalline polymorphs are extensively discussed elsewhere [26, 39]. Through the slow solvent evaporation method (**Figure 3-2**) like in the G-phase H1 (G-H1) crystal cases at **Figure 3-1c**, G1 can be doped into B-phase H1 (B-H1) crystal and made red emissive co-crystals (**Figure 3-17**). The R(G1:B-H1) co-crystals also showed molecular substitutional doped behavior like the other CT doped co-crystals (**Figure 3-18**), and therefore R(G1:G-H1) and R(G1:B-H1) co-crystals themselves are also crystalline polymorph like G-H1 and B-H1 crystal case. The both co-crystals showed CT-R emission (**Figure 3-17**), and ET efficiency of R(G1:B-H1) co-crystals (0.41) was rather smaller than that of R(G1:G-H1) co-crystal (0.59) as in **Figure 3-17**.

Similar with the previous observation, OFET devices of the non-doped B-H1 crystals (**Figure 3-18a-c**) showed one order higher averaged electron mobility (μ_e = 1.6×10^{-2} $cm^2V^{-1}s^{-1}$, **Table 3-6**) than that of non-doped G-H1 crystals (7.9×10^{-4} $cm^2V^{-1}s^{-1}$ for doped and non-doped G-H1 crystals, **Table 3-4**). Also the corresponding R(G1:B-H1) co-crystal showed one order higher averaged mobility (3.0×10^{-2} $cm^2V^{-1}s^{-1}$, **Table 3-6**) than that of R(G1:G-H1) co-crystal (7.7×10^{-3} $cm^2V^{-1}s^{-1}$, **Table 3-4**). R(G1:B-H1) co-crystal OFET also showed photo-response (**Figure 3-18a**) without supplementary layer, while non-doped B-H1 crystal showed relatively small photo-response (**Figure 3-18c**): The average ΔV_{TH} and R (**Table 3-6**) of R(G1:B-H1) co-crystal OPT (20.3 V and 496.7 AW^{-1}, respectively) was larger than that of non-doped (B-H1) OPT (8.6 V and 33.7 AW^{-1}, respectively). R(G1:B-H1) co-crystal OPT also showed dynamic photo-response (**Figure 3-18d**) and linear log-log plot of light intensity and R (**Figure 3-19**) like other CT doped

co-crystal OPT devices (*vide supra*), and therefore, CT complex played a central role in OPT also in the case of R(G1:B-H1).

The difference on OPT performances of two crystalline polymorphs was dramatic: The average ΔV_{TH} of R(G1:B-H1) co-crystals was much smaller (20.3 V) than that of R(G1:G-H1) co-crystals (72.2 V), while the average R of R(G1:B-H1) co-crystals (496.7 AW^{-1}) was much higher than that of R(G1:G-H1) co-crystals (26.0 AW^{-1}). The different ET efficiency seem to be contributed to ΔV_{TH} difference between CT doped crystalline polymorphs. Regarding the much more higher R of the R(G1:B-H1) co-crystal OPT devices, the higher electrical mobility seem to have surpassed the effect of ΔV_{TH} in this case: The current maximum ($I_{D, Max}$) was much higher than that of R(G1:G-H1) co-crystals (1.0×10^{-6}A, 5.5×10^{-8}A for CT-R doped B-phase, G-phase H1 crystal respectively, **Table 3-7**).

In this context, electrically non-destructive doping is crucially important to secure photo-response of OPT devices. The molecular substitutional doped crystals we have discussed so far showed crystal structurally non-destructive (**Figure 3-4a-e**, **Figure 3-18**), and also they were electrically non-destructive: all of them showed slight mobility increments compared to their corresponding non-doped crystals (**Table 3-6**), *e.g.*, R(G1:B-H1) co-crystals ($\mu_e = 3.0 \times 10^{-2}\,cm^2V^{-1}s^{-1}$) > non-doped B-H1 crystals ($1.6 \times 10^{-2}\,cm^2V^{-1}s^{-1}$). Furthermore, even the 20 % doped R(G1:G-H1) co-crystals also showed electrically non-destructive behavior (**Figure 3-20**). This is because of the compatible morphology of guest and host molecules in solid-state by isometric molecular structure, and therefore, the isometric molecular design can be the novel solution for the trade-off issue between dopant concentration and host crystallinity. [13, 14]

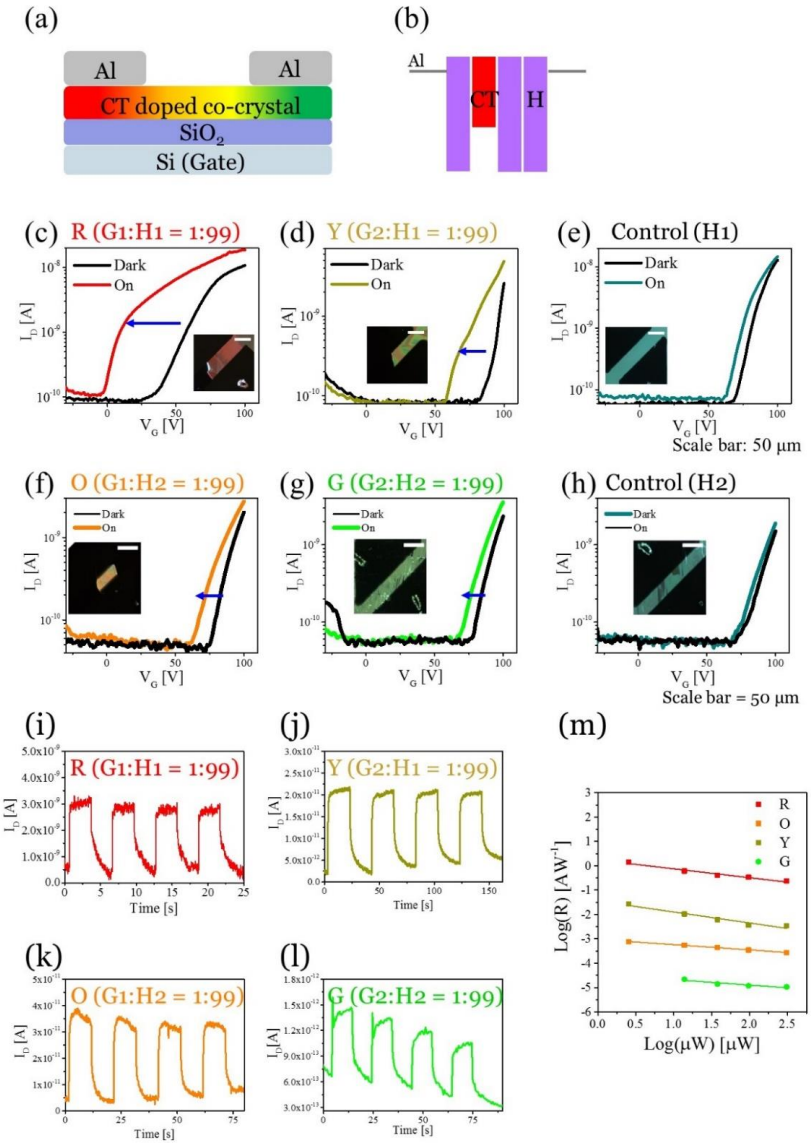

Figure 3-13. Organic photo-transistor of CT doped crystals (dopant % = 1 %) (a) Schematic of device structure, (b) Brief energy diagram of the devices, transfer curves under dark (black) and illuminated (colored) condition of (c) R (G1:H1 =1:99) co-crystal, (d) Y (G2:H1 =1:99) co-crystal, (e) H1 crystal, (f) O (G1:H2 =1:99) co-crystal, (g) G (G2:H2 =1:99) co-crystal, and (h) H1 crystal (inset: optical microscopy image of corresponding devices, scale bar = 50 μm). Dynamic response of (i) R (G1:H1 =1:99) co-crystal, (j) Y (G2:H1 =1:99) co-crystal, (k) O (G1:H2 =1:99) co-crystal, and (l) G (G2:H2 =1:99) co-crystal, (m) Log-log plot between responsivity (R) and light intensity of CT doped co-crystals.

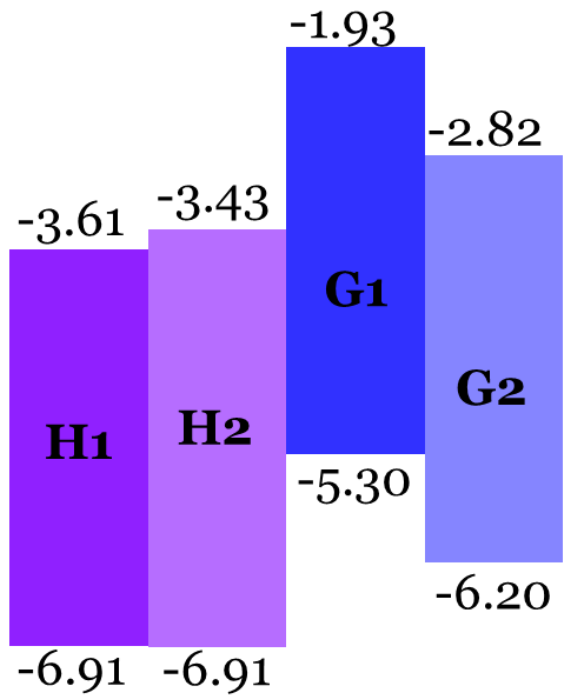

Figure 3-14. Energy levels of guests and hosts

Sample	μ_e ($cm^2V^{-1}s^{-1}$)		ΔV_{TH} (V)	R (AW^{-1})
Light	**Off**	**On**	**-**	**-**
R(G1:H1)	7.7.E-03	7.9.E-04	71.7	26.0
(SD)	3.4.E-03	4.5.E-04	14.0	12.1
Y1(G2:H1)	1.1.E-03	6.3.E-04	13.0	3.0
(SD)	1.1.E-03	6.9.E-04	3.8	1.1
H1	7.9.E-04	6.7.E-04	7.4	0.5
(SD)	3.2.E-04	3.6.E-04	2.1	0.2
O1(G1:H2)	2.5.E-04	1.5.E-04	10.9	0.6
(SD)	1.1.E-04	8.9.E-05	2.1	0.3
G1(G2:H2)	4.2.E-04	3.2.E-04	7.7	0.5
(SD)	3.5.E-04	2.5.E-04	2.6	0.4
H2	1.4.E-04	2.1.E-04	4.6	0.3
(SD)	9.0.E-05	2.7.E-04	2.3	0.3

Table 3-4. Summary of organic photo-transistor properties of CT doped co-crystals (1% dopant) and non-doped crystals. Every values are averaged and corresponding standard deviation (SD) values are provided in gray color.

Host phase	Sample	μ_e ($cm^2V^{-1}s^{-1}$)		I_{on} (A)		I_{OFF} (A)		$I_{ON/OFF}$		V_{TH} (V)		ΔV_{TH} (V)	R (AW^{-1})
	Light	**Off**	**On**	**Off**	**On**	**Off**	**On**	**Off**	**On**	**Off**	**On**	-	-
G	R1	**7.7.E-03**	7.9.E-04	**5.5.E-08**	1.1.E-07	7.3.E-12	9.3.E-11	1.2.E+04	1.3.E+03	81.0	9.4	**71.7**	**26.0**
	(SD)	3.4.E-03	4.5.E-04	2.9.E-08	5.2.E-08	4.5.E-12	4.3.E-11	8.1.E+03	4.9.E+02	7.5	8.0	14.0	12.1
G	Y1	**1.1.E-03**	6.3.E-04	**1.0.E-08**	1.3.E-08	8.7.E-11	9.1.E-11	1.0.E+02	1.4.E+02	70.1	57.1	**13.0**	**3.0**
	(SD)	1.1.E-03	6.9.E-04	6.8.E-09	6.8.E-09	6.8.E-12	5.8.E-12	7.9.E+01	8.3.E+01	15.3	13.5	3.8	1.1
G	A1	**7.9.E-04**	6.7.E-04	**1.8.E-08**	1.9.E-08	6.8.E-11	7.6.E-11	2.2.E+02	4.5.E+02	70.7	63.3	**7.4**	**0.5**
	(SD)	3.2.E-04	3.6.E-04	7.7.E-09	7.4.E-09	5.9.E-12	1.1.E-11	9.7.E+01	3.5.E+02	4.1	5.1	2.1	0.2
G	O1	**2.5.E-04**	1.5.E-04	**8.0.E-10**	1.1.E-09	5.5.E-11	6.2.E-11	1.2.E+01	1.7.E+01	78.4	68.0	**10.9**	**0.6**
	(SD)	1.1.E-04	8.9.E-05	5.4.E-10	7.7.E-10	3.6.E-12	2.9.E-12	9.0.E+00	1.2.E+01	1.8	3.4	2.1	0.3
G	G1	**4.2.E-04**	3.2.E-04	**7.7.E-09**	8.9.E-09	5.9.E-11	6.3.E-11	1.2.E+02	1.3.E+02	77.4	69.7	**7.7**	**0.5**
	(SD)	3.5.E-04	2.5.E-04	8.4.E-09	8.7.E-09	6.5.E-12	5.7.E-12	1.3.E+02	1.4.E+02	4.2	3.4	2.6	0.4
G	A2	**1.4.E-04**	2.1.E-04	**3.8.E-09**	4.3.E-09	5.3.E-11	5.5.E-11	5.6.E+01	6.7.E+01	78.2	72.8	**4.6**	**0.3**
	(SD)	9.0.E-05	2.7.E-04	6.3.E-09	6.7.E-09	8.4.E-12	9.0.E-12	9.7.E+01	1.1.E+02	3.7	6.4	2.3	0.3

Table 3-5. Summary of electrical properties of OPT devices

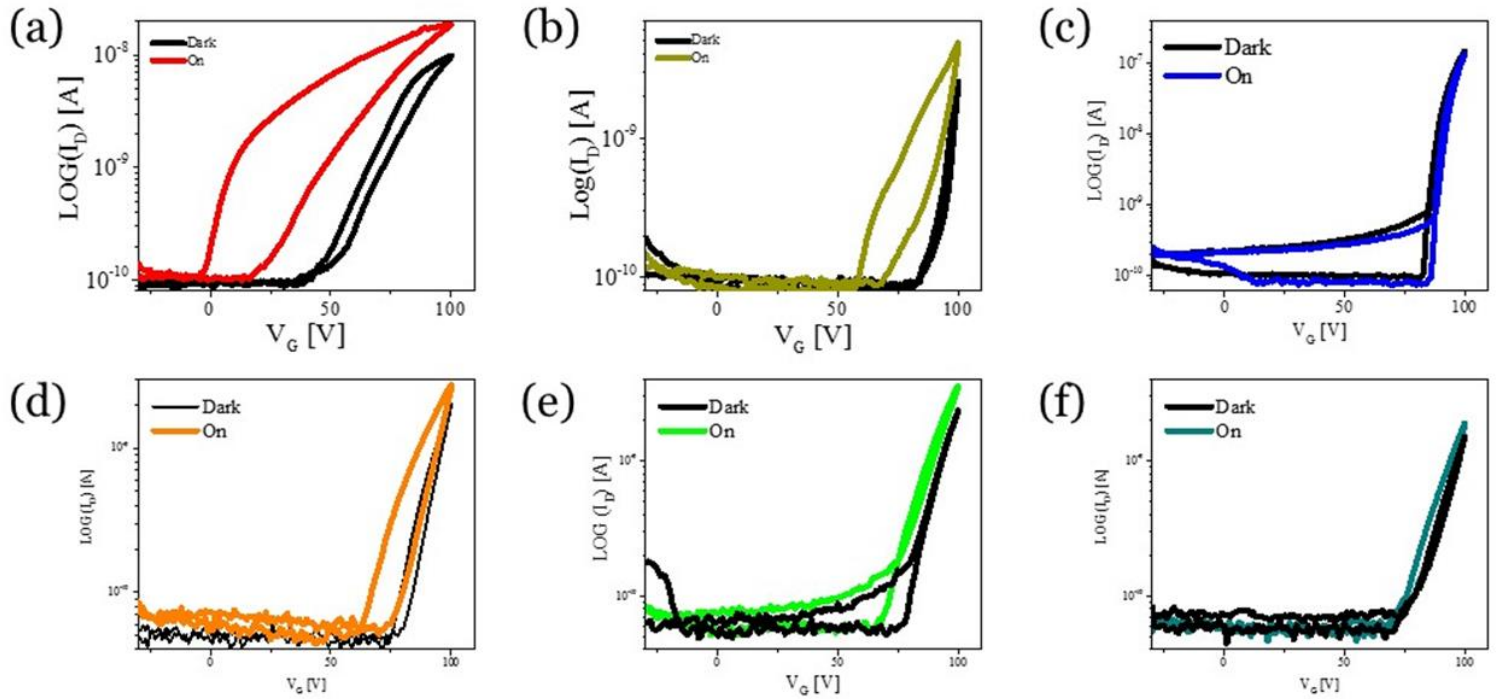

Figure 3-15. Memristor behavior of OPT devices. Transfer curves with gate voltage (V_G) dual sweep condition under light (colored) and dark (black) of (a) R(G1:H1) crystal, (b) Y(G2:H1) crystal, (c) H1 crystal, (d) O(G1:H2) crystal, (e) G(G2:H2) crystal, and (f) H2 crystal

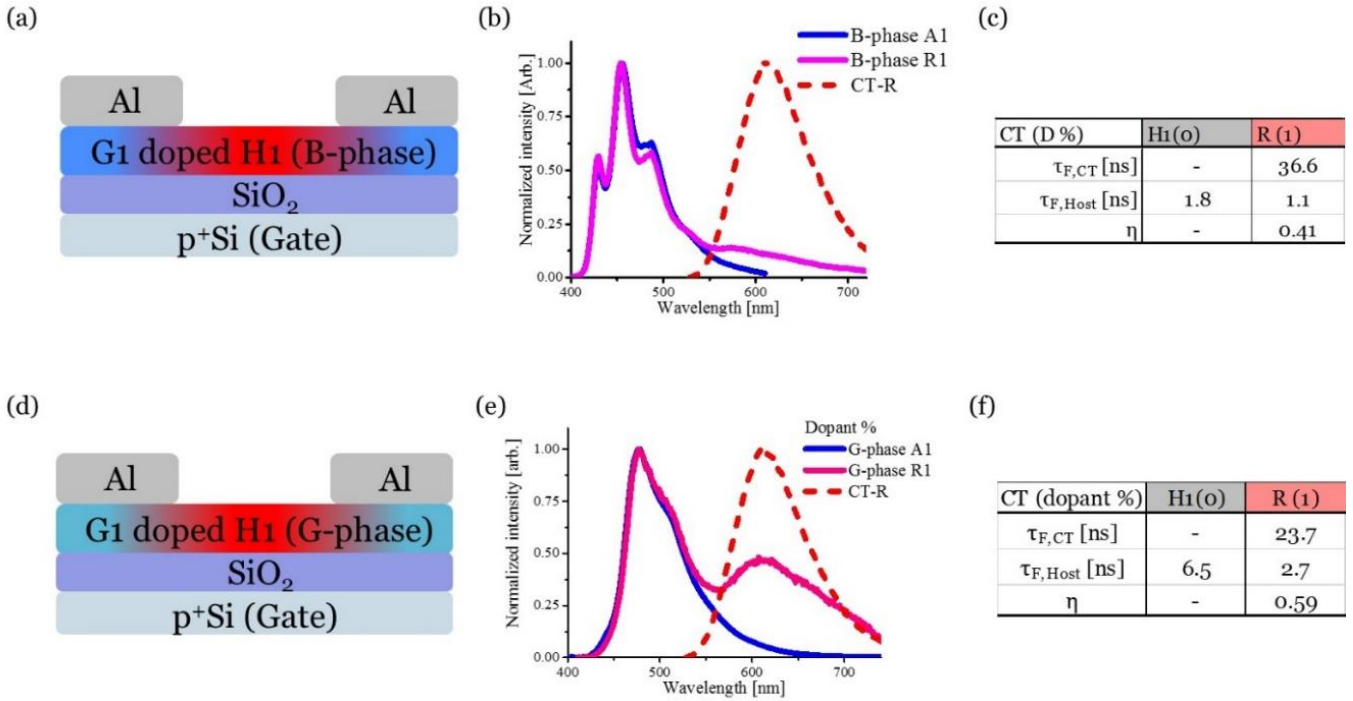

CT (D %)	H1(0)	R (1)
$\tau_{F,CT}$ [ns]	-	36.6
$\tau_{F,Host}$ [ns]	1.8	1.1
η	-	0.41

CT (dopant %)	H1(0)	R (1)
$\tau_{F,CT}$ [ns]	-	23.7
$\tau_{F,Host}$ [ns]	6.5	2.7
η	-	0.59

Figure 3-16. Optical properties of CT-R doped B-phase H1 crystal. (a) Device structure of R(G1:B-H1) co-crystal OPT, (b) PL spectra of R(G1:B-H1) co-crystal (magenta), CT-R (red dash), and B-H1 (blue), and energy transfer efficiency of R(G1:B-H1) co-crystal. (d) Device structure of R(G1:G-H1) co-crystal OPT, (e) PL spectra of R(G1:G-H1) co-crystal (magenta), CT-R (red dash), and G-H1 (blue), and energy transfer efficiency of R(G1:G-H1) co-crystal.

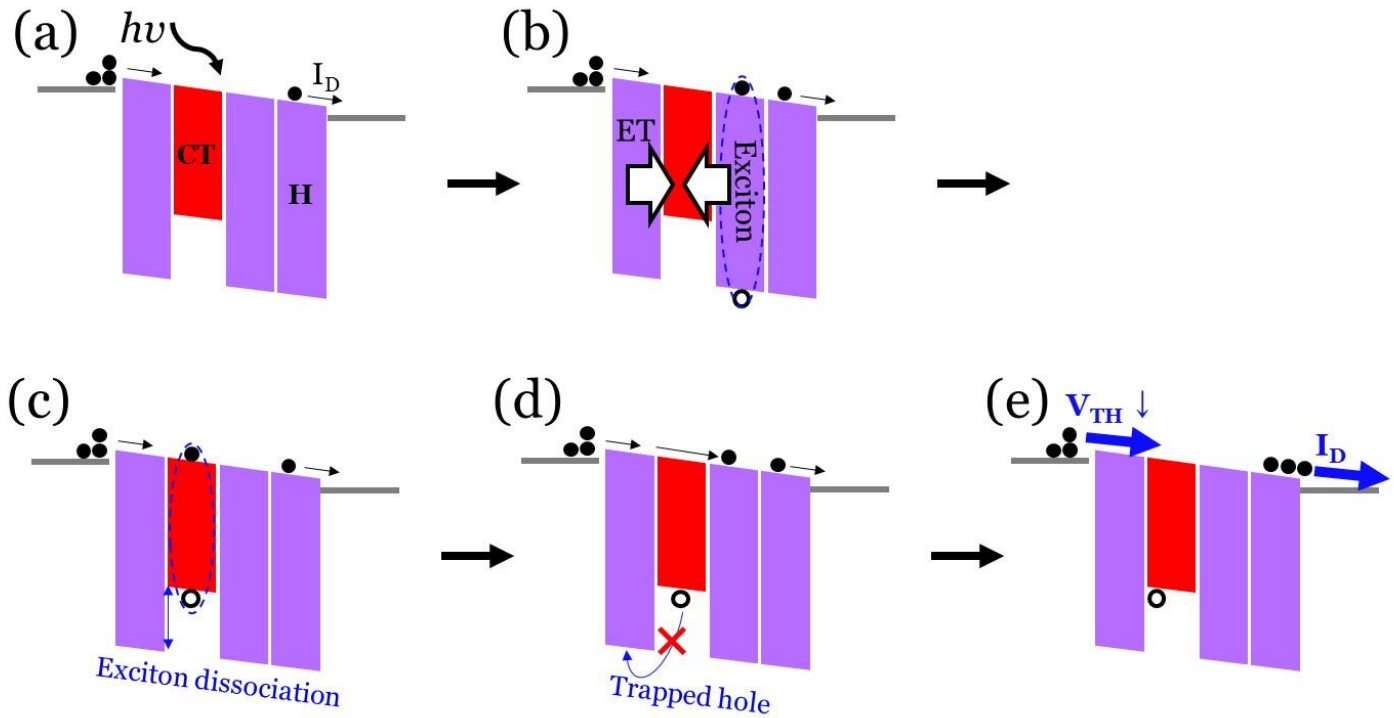

Scheme 3-2. Schematic of photo-transistor operation in order. (a) Optical excitation in biased condition (V_G, V_D > 0), (b) Exciton migration to molecular CT by ET process, (c) Exciton dissociation by built-in potential of CT, (d) destiny of separated charges: holes trapped in the energetic well and electrons driven by external bias, (e) trapped holes induced threshold shift (ΔV_{TH}) and consequent electrical signal gain

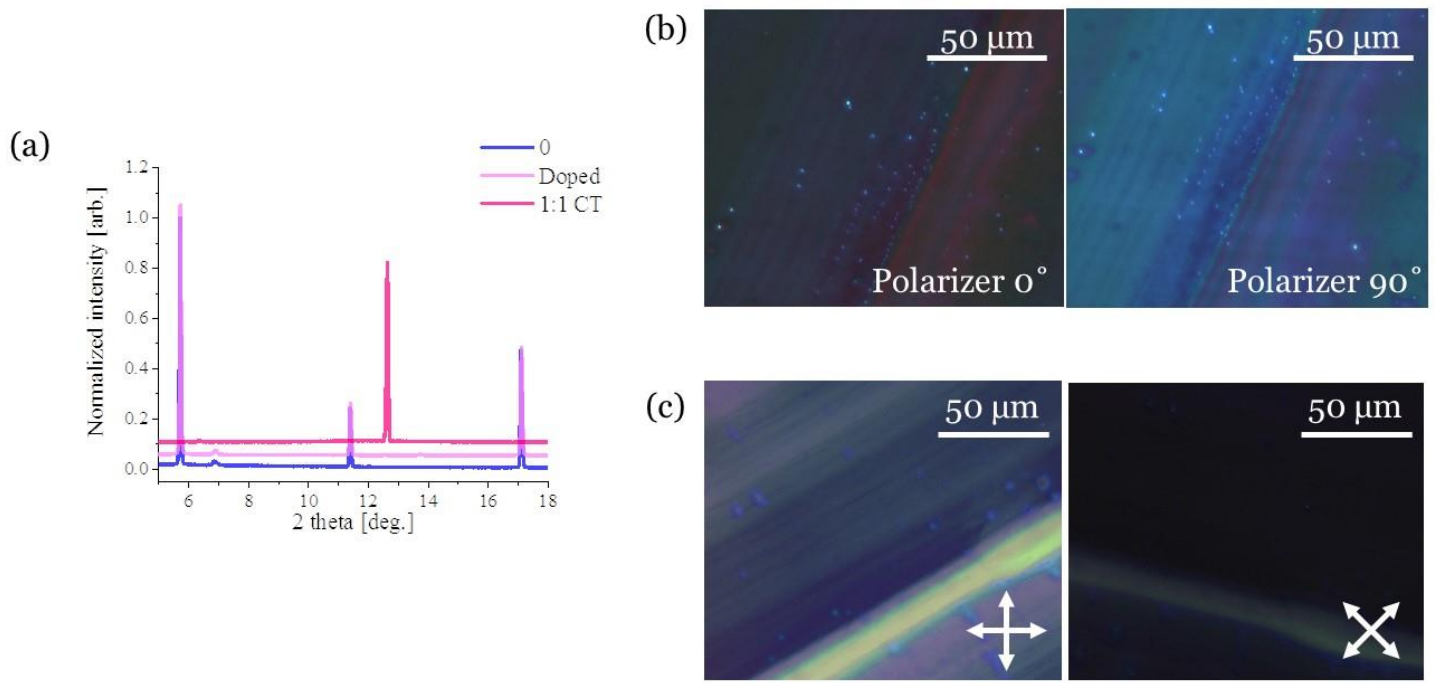

Figure 3-17. Molecular substitutional CT-R doped B-phase H1 crystal. (a) Out-of-plane XRD result of CT-R doped B-phase H1 crystal (pink), B-phase H1 crystal (blue), and CT-R (red). OM image of CT-R doped B-phase H1 crystal under (b) UV and (c) under room light with polarizer/analyzer.

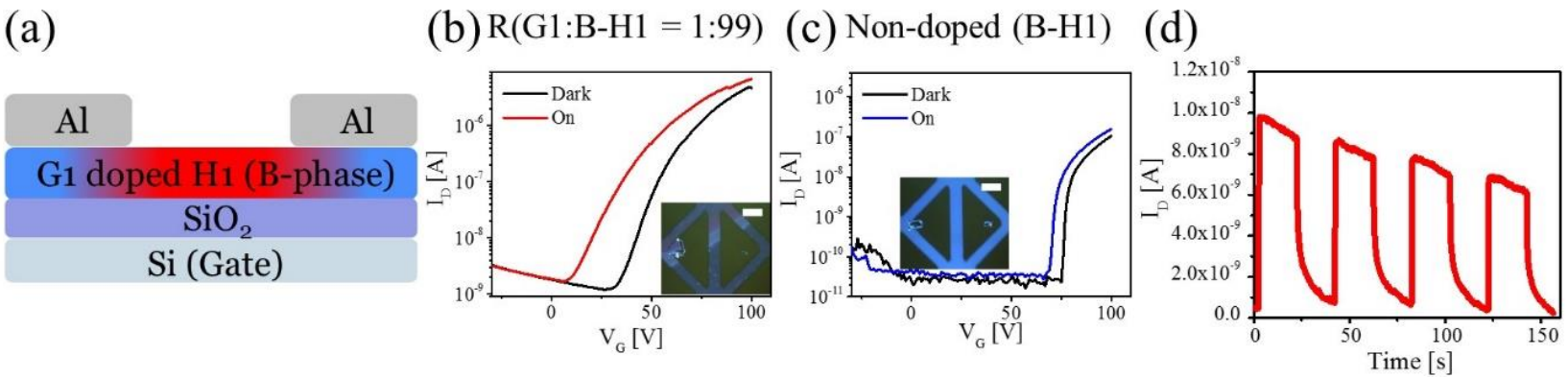

Figure 3-18. Organic photo-transistor of B-phase H1 (B-H1) based CT-R doped crystals (dopant % = 1%). (a) Schematic of device structure, transfer curves under dark (black) and illuminated (colored) condition of (b) R(G1:B-H1 = 1:99) and (c) B-H1 crystal (inset: inset: optical microscopy image of corresponding devices, scale bar = 50 μm), and (d) Dynamic response of R(G1:B-H1 = 1:99).

Sample	μ_e ($cm^2V^{-1}s^{-1}$)		ΔV_{TH} (V)	R (AW^{-1})
Light	**Off**	**On**	**-**	**-**
R(G1:B-H1)	3.0.E-02	2.5.E-02	20.3	496.7
(SD)	2.1.E-02	1.7.E-02	6.7	269.8
B-H1	1.6.E-02	1.2.E-02	8.6	33.7
(SD)	5.2.E-03	5.5.E-03	4.2	16.2

Table 3-6. Summary of organic photo-transistor properties of B-phase H1 (B-H1) based CT-R doped crystals (dopant % = 1%) and non-doped B-H1 crystals. Every values are averaged and corresponding standard deviation (SD) values are provided in gray color.

Host phase	Sample	μ_e ($cm^2V^{-1}s^{-1}$)		I_{on}		I_{OFF} (A)		$I_{ON/OFF}$		V_{TH} (V)		ΔV_{TH}	R (AW^{-1})
	Light	**Off**	**On**	**Off**	**On**	**Off**	**On**	**Off**	**On**	**Off**	**On**	-	-
B	R1	**3.0.E-02**	2.5.E-02	**1.0.E-06**	2.1.E-06	2.5.E-10	3.5.E-10	8.2.E+03	1.4.E+04	67.6	47.3	**20.3**	**496.7**
	(SD)	2.1.E-02	1.7.E-02	1.4.E-06	1.8.E-06	4.9.E-10	6.7.E-10	4.4.E+03	9.0.E+03	6.2	7.3	6.7	269.8
B	A1	**1.6.E-02**	1.2.E-02	**2.4.E-07**	3.1.E-07	1.8.E-10	2.3.E-10	1.3.E+03	1.3.E+03	76.4	67.8	**8.6**	**33.7**
	(SD)	5.2.E-03	5.5.E-03	1.9.E-07	2.0.E-07	4.9.E-11	9.9.E-11	9.7.E+02	5.8.E+02	12.6	14.5	4.2	16.2

Table 3-7. Summary of electrical properties of B-phase H1 based OPT devices

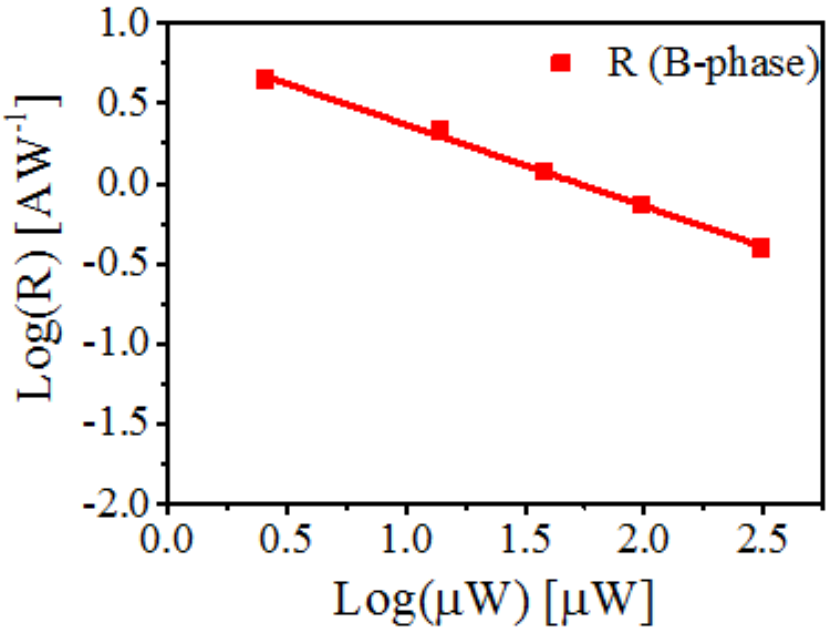

Figure 3-19. Log-log plot between responsivity (R) and light intensity of R(G1:B-H1 = 1:99) co-crystals.

	μ_e ($cm^2V^{-1}s^{-1}$)		I_{OFF} (A)		V_{TH} (V)		ΔV_{TH} (V)	R (AW^{-1})
Dopant %	Dark	Bright	Dark	Bright	Dark	Bright	-	-
0	7.9.E-04	6.7.E-04	6.8.E-11	7.6.E-11	70.7	63.3	7.4	0.5
(SD)	3.2.E-04	3.6.E-04	5.9.E-12	1.1.E-11	4.1	5.1	2.1	0.2
1	7.7.E-03	7.9.E-04	7.3.E-12	9.3.E-11	81.0	9.4	71.7	26.0
(SD)	3.4.E-03	4.5.E-04	4.5.E-12	4.3.E-11	7.5	8.0	14.0	12.1
5	6.3.E-03	6.5.E-04	1.8.E-11	5.6.E-11	84.5	20.2	64.3	17.4
(SD)	3.0.E-03	1.2.E-04	1.7.E-11	2.1.E-11	2.6	7.6	10.0	7.9
10	5.0.E-03	2.8.E-04	1.4.E-11	4.5.E-11	89.8	13.1	76.7	13.7
(SD)	7.7.E-04	8.5.E-05	7.5.E-12	8.5.E-12	0.7	4.2	6.8	4.7
20	2.7.E-03	3.1.E-04	4.9.E-12	4.8.E-11	73.6	19.6	54.0	4.2
(SD)	9.3.E-04	7.2.E-05	4.2.E-12	1.6.E-11	3.6	11.7	8.9	1.5

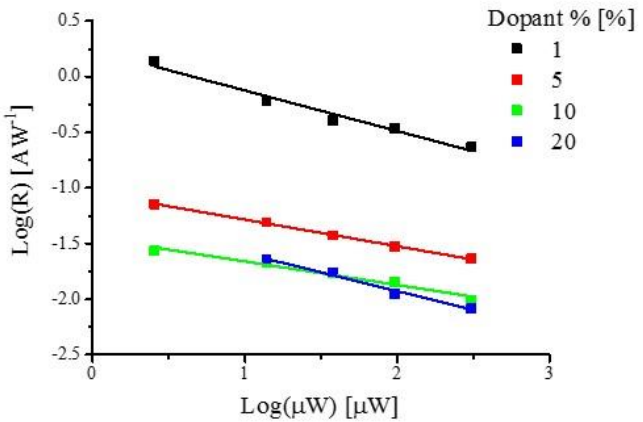

Figure 3-20. Dopant % dependent OPT behavior of CT-R doped plate co-crystal

3.4. Conclusion

In conclusion, we developed the first molecular substitutional doped co-crystals with apparent D:A interactions by introducing molecular isometric two guests and two hosts. The molecular substitutional doped co-crystals showed the novel features than the other bimolecular systems: (i) Dispersed CT in the host matrix which maximizes the exciton dissociation with efficient energy transfer (ET), (ii) Electrically non-destructive feature even in the very high doping concentration (20 %) due to high morphological compatibility between guests and hosts. Especially, molecular substitutional doped co-crystals provided novel platform to unveil the structure-property relationships of the organic functional crystals, because our crystal system includes (co-)crystal with equivalent crystal structures and also crystalline polymorphs. Therefore, relationship between OPT performance (*e.g.*, ΔV_{TH} and R) and built-in-potential, energy levels, ET efficiency, and mobility of the co-crystals can be extensively investigated and revealed in this work.

3.5. References

1. Lee H.; Park C.; Sin D. H.; Park J. H., Cho K. *Adv. Mater.,* **2018**, *30*, 1800453.

2. Naveed H. B.; Zhou K., Ma W. *Acc. Chem. Res.,* **2019**, *52*, 2904-2915.

3. Wang G.; Melkonyan F. S.; Facchetti A., Marks T. J. *Angew. Chem. Int. Ed.,* **2019**, *58*, 4129-4142.

4. Colella M.; Danos A., Monkman A. P. *J. Phys. Chem. Lett.,* **2019**, *10*, 793-798.

5. Kim K. H.; Yoo S. J., Kim J. J. *Chemistry of Materials,* **2016**, *28*, 1936-1941.

6. Goushi K.; Yoshida K.; Sato K., Adachi C. *Nat Photonics,* **2012**, *6*, 253.

7. Salzmann I.; Heimel G.; Oehzelt M.; Winkler S., Koch N. *Acc. Chem. Res.,* **2016**, *49*, 370-378.

8. Kim J. H.; Yun S. W.; An B. K.; Han Y. D.; Yoon S. J.; Joo J., Park S. Y. *Adv. Mater.,* **2013**, *25*, 719-724.

9. Soeda J.; Hirose Y.; Yamagishi M.; Nakao A.; Uemura T.; Nakayama K.; Uno M.; Nakazawa Y.; Takimiya K., Takeya J. *Adv. Mater.,* **2011**, *23*, 3309-3314.

10. Baeg K. J.; Binda M.; Natali D.; Caironi M., Noh Y. Y. *Adv. Mater.,* **2013**, *25*, 4267-4295.

11. Yang Y.; Mielczarek K.; Zakhidov A., Hu W. *ACS Appl. Mater. Interfaces,* **2014**, *6*, 19282-19287.

12. Yang Y.; Mielczarek K.; Zakhidov A., Hu W. *ACS Appl. Mater. Interfaces,* **2016**, *8*, 7300-7307.

13. Salzmann I.; Heimel G.; Oehzelt M.; Winkler S., Koch N. *Acc. Chem. Res.,* **2016**, *49*, 370-378.

14. Salzmann I.; Heimel G.; Duhm S.; Oehzelt M.; Pingel P.; George B. M.; Schnegg A.; Lips K.; Blum R. P.; Vollmer A., Koch N. *Phys. Rev. Lett.*, **2012**, *108*, 035502.

15. Kleemann H.; Schuenemann C.; Zakhidov A. A.; Riede M.; Lussem B., Leo K. *Org. Electron.*, **2012**, *13*, 58-65.

16. Kufer D., Konstantatos G. *acs photonics*, **2016**, *3*, 2197-2210.

17. García de Arquer F. P.; Armin A.; Meredith P., Sargent E. H. *Nat. Rev. Mater.*, **2017**, *2*.

18. Kim J. H.; Oh S.; Park S. K., Park S. Y. *Adv. Electron. Mater.*, **2019**, *0*, 1900478.

19. Jansen-van Vuuren R. D.; Armin A.; Pandey A. K.; Burn P. L., Meredith P. *Adv. Mater.*, **2016**, *28*, 4766-4802.

20. Jansen-van Vuuren R. D.; Armin A.; Pandey A. K.; Burn P. L., Meredith P. *Adv. Mater.*, **2016**, *28*, 4766-4802.

21. Chow P. C. Y.; Matsuhisa N.; Zalar P.; Koizumi M.; Yokota T., Someya T. *Nat. Commun.*, **2018**, *9*, 4546.

22. Han T.; Shou M.; Liu L.; Xie Z.; Ying L.; Jiang C.; Wang H.; Yao M.; Deng H.; Jin G.; Chen J., Ma Y. *J. mater. chem. c*, **2019**, *7*, 4725-4732.

23. Zukawa T.; Naka S.; Okada H., Onnagawa H. *J. Appl. Phys*, **2002**, *91*, 1171-1174.

24. Baeg K.-J.; Binda M.; Natali D.; Caironi M., Noh Y.-Y. *Adv. Mater.*, **2013**, *25*, 4267-4295.

25. Oh S.; Park S. K.; Gierschner J.; Park S. Y., (unpublished). **2020**.

26. Park S. K.; Kim J. H.; Yoon S.-J.; Kwon O. K.; An B.-K., Park S. Y. *Chem. Mater.*, **2012**, *24*, 3263-3268.

27. Lusi M. *Cryst Growth Des*, **2018**, *18*, 3704-3712.

28. Lusi M. *Crystengcomm*, **2018**, *20*, 7042-7052.

29. Park S. K.; Kim J. H., Park S. Y. *Advanced Materials*, **2018**, *30*, 1704759.

30. Gierschner J.; Varghese S., Park S. Y. *Adv. Opt. Mater.*, **2016**, *4*, 348-364.

31. Gierschner J., Park S. Y. *J. Mater. Chem. C*, **2013**, *1*, 5818-5832.

32. Coropceanu V.; Cornil J.; da Silva Filho D. A.; Olivier Y.; Silbey R., Bredas J. L. *Chem Rev*, **2007**, *107*, 926-952.

33. Zhong J.; Wu X.; Lan S.; Fang Y.; Chen H., Guo T. *ACS Photonics*, **2018**, *5*, 3712-3722.

34. Yan F.; Li J. H., Mok S. M. *J. Appl. Phys.*, **2009**, *106*.

35. Shao Z.; Jiang T.; Zhang X.; Zhang X.; Wu X.; Xia F.; Xiong S.; Lee S. T., Jie J. *Nat. Commun.*, **2019**, *10*, 1294.

36. Gao X.; Liu C.-H.; She X.-J.; Li Q.-L.; Liu J., Wang S.-D. *Org. Electron.*, **2014**, *15*, 2486-2491.

37. Zhou L.; Mao J.; Ren Y.; Han S.-T.; Roy V. A. L., Zhou Y. *Small*, **2018**, *14*, 1703126.

38. Baeg K.-J.; Noh Y.-Y.; Sirringhaus H., Kim D.-Y. *Adv. Funct. Mater.*, **2010**, *20*, 224-230.

39. Aliaga-Gosalvez M. J.; Demitri N.; Dohr M.; Roldao J. C.; Park S. K.; Oh S.; Varghese S.; Park S. Y.; Olivier Y.; Milián-Medina B.; Resel R., Gierschner J. *Adv. Opt. Mater.*, **2019**, *7*, 1900749.

Chapter 4. Micro-Patterned Templated Grown Luminescent Charge-Transfer (CT) Cocrystals via Patterned Taping: A Universal Thin Film Patterning Soft Lithographic Method

4.1. Introduction

Micro-scale or nano-scale pattern fabrication using lithographic techniques is widely studied on the practical applications of electronic/ optoelectronic devices[1, 2, 3, 4] such as commercially affordable light-emitting diodes (LEDs), smartphones, and personal computers (PCs). Similarly, the patterning of active layers and/or electrodes is indispensable to the construction of flexible electronic devices based on organic materials, such as organic light-emitting diodes (OLEDs)[5-6], organic field-effect transistors (OFETs)[7-8], and organic photovoltaic (OPV) cells[9- 10]. Optical lithography is commonly used to pattern commercial inorganic electronic devices through high-energy beam irradiation and chemical etching. These harsh processing conditions for optical lithography compromise the functionality of materials (e.g., organic materials). In this sense, as an alternative to conventional optical lithography, simpler and more cost-effective technique called soft lithography technique has been extensively researched[11, 12, 13, 14, 15, 16]. Of the soft lithographic techniques, dry transfer printing methods, such as micro-contact printing[17] (μCP), hot lift off[3, 18], and others[19-20] have been widely used to pattern optoelectronic devices. These transfer printing approaches have opened new avenues for device application, high-speed processing, scalability, and the prevention of lateral diffusion or the swelling of mold by liquid. However, a large number of soft lithographic printing techniques act as a potential destructive influence on the materials because they directly apply external stimuli such as heat,

pressure, or a combination of these to the functional layer.[18, 21, 22] These outer stimuli can lead to oxidation by heat[23-24] as well as pressure deformation[19]. These commonly used processes prevent the use of certain methods owing to deterioration in functionality or a shortening of the lifetime of the relevant device in case the target material is sensitive to external stimuli. In this regard, the non-evasive characteristic of patterning method is advantageous for highly efficient micro device fabrication.[25, 26, 27] Further, soft lithographic printing has practical limitations related to efficiency in one or more of the following ways: (1) it is a time-consuming process, i.e., the application of heat or pressure is often required for a long time (over several minutes)[18, 28], and diffusion-dependent patterning[19] is sometimes needed; (2) it requires additional steps such as modification of the surface of the substrate[22] and the introduction of a sacrificial layer[21, 29]; (3) it is difficult to apply to a wide range of materials, e.g., organic materials[20, 30]. These limitations result in a loss of time and expenditure on patterning methods. The above drawbacks are potential obstacles to the implementation of practical organic devices. Hence, it is important to develop practical approaches for lithography that can solve the problems afflicting conventional techniques.

In this context, I propose a soft lithographic printing technique for “patterned taping” that operates in two modes: selective removal of pattern from substrate (subtractive), and/or subsequent transfer of the pattern to the other substrate (additive). Patterned taping has short processing time (it is time efficient) and low processing cost (it is cost efficient) because of the simplicity/convenience of its procedures, and does not involve any invasive treatment of the target materials (it is damage free). Commercial adhesive tape has been widely utilized in a variety of methods for micro structured device fabrication,[29, 31, 32, 33, 34] because of fine

adhesion ability and flexibility of adhesive tapes. Originally, our printing process employs soft lithographically patterned adhesive tape, which forms a thin film pattern over a large area (~cm^2 scale) with a virtually perfect yield of patterning (yield of picking and/or transferring patterns), and can construct patterns on a wide variety of substrates: flat, curved, uneven, and flexible. Through the property of universal adhesion in pressure-sensitive tapes, this method can be applied to various kinds of materials, including layers of organic, polymeric, metallic, inorganic materials.

In addition, as well as organic thin film (layer) patterning, organic crystal patterning has been researched by virtue of the promising optoelectrical features of organic crystals [17, 35, 36]. However, To assemble the organic molecules into the crystals, usually solvent drying wet process[36, 37, 38] and physical vapor transport[17, 39] have been widely introduced, however, it is still a challenge to place the crystal in a targeted position (nucleation control) and align the crystals in one direction (directional growth) in reproducible manner.

In this context, as the possible scenario to pattern the isometric D-A CT crystals, I tried to pattern the CT crystals on the host (donor or acceptor) crystals via sequent process of top-down and bottom-up process: Patterned taping as top-down method and cocrystal formation through vapor-driven self-assembly (VDSA) [40, 41] as bottom-up process. The similar term of vapor-driven self-assembly (VDSA) is solvent vapor annealing (SVA) [42] which is one of the following works of originally reported VDSA process. The top-down process is expected to determine the nucleation position of the CT crystals, and molecularly aligned host crystal surface can provide the template while on the growing process of nucleated crystal mediated by bottom-up process, *c.f.,* micro-structured substrate which can control

crystal growth direction, for example like concept of liquid crystal (LC) case on the rubbed substrate [43] and epitaxial growth between distinct crystalline material [44].

Therefore, in this section, I report the generation of extensively designed patterns of organic semiconductor film, thin metal film, micro-pixels, and lines of luminescent organic RGB films that emit white luminescence through patterned taping. Furthermore, the CT patterns on the host crystals were demonstrated, and their following peculiar morphological/ optical properties derived from isometric molecular structure of D, A are investigated in this section.

4.2. Experimental

Master mold fabrication. The patterned Si wafer was photo-lithographically fabricated with a photomask. The polydimethylsiloxane (PDMS) master mold was fabricated by pouring PDMS Sylgard 184 as a pre-polymer onto the patterned Si wafer, and was cured for six hours at 80˚C in an oven.[45] The polyurethane acrylate (PUA) master mold was fabricated by using PUA 311RM as a pre-polymer over the patterned Si wafer. Ultraviolet light (λ = ~250-400 nm) with a UV dose of ~100 mJ/cm^2 was illuminated to cure the PUA pre-polymer.[46]

Patterned taping. Patterned taping processes have been described in detail above. Nitrogen blowing was done at every step of the pattern transfer for patterning yield and purity. Commercial adhesive tape was used which was listed as follows; Tapex OPP tape (Cat. KST 1046), 3M scotch package tape (Cat. 3615c), 3M scotch tape (Cat. 581) 3M scotch magic tape (Cat. 104), Printec package tape (Cat. P4840br) and Niceday OPP tape (Cat. 312930).

Device fabrication. For substrate preparation, SiO_2/Si substrates (p-doped,

SiO_2 thickness: 300 nm) were rinsed with acetone and isopropyl alcohol, respectively, for 10 min under an ultrasonicator, and then a 20-min UV (360 nm) O_3 treatment was applied. Hexamethyldisilazane (HMDS) or octadecyl trichloro silane (ODTS) was introduced onto the substrates as a self-assembled monolayer (SAM) in vapor phase in a vacuum oven. Subtractive patterned taping was carried out in the nitrogen-filled glove box. Organic and source-drain electrodes were thermally evaporated sequentially onto the SAM-treated substrates. The I-V characteristics of all OFETs were measured in a nitrogen (N_2)-filled glove box using a Keithley 4200 SCS instrument connected with probe stations. The mobility and threshold voltage were calculated from the saturation region of the transfer curve, and the width and length of the pentacene pattern within the source-drain channel were checked using an optical microscope to calculate charge carrier mobility.

CT grown crystal characterization. The optical microscope (OM) images were taken by Leica DMLP polarizing optical microscope. For the atomic force microscopy (AFM) images, Bruker Nanoscope III multimode SPM was used through tapping mode using RTESP cantilever. The photoluminescence (PL) spectra was measured by QM-40. Luminescence lifetime decay of each compound was measured by Fluo Time 200. Efficiency of energy transfer (η) was obtained through the lifetime according to following equation: $1-(\tau_{F,\,CT}/\tau_{F,\,Host})$. $\tau_{F,\,CT}$ is the amplitude weighted lifetime detected from pure CT emissive region, and $\tau_{F,\,Host}$ is the amplitude weighted lifetime detected from pure host emissive region.

4.3. Result and discussion

4.3.1. Patterned taping

Figure 4-1. a-g shows the procedure involved in patterned taping for thin films. The pressure-sensitive tape is laid onto the pre-patterned side of a master mold (**Fig. 4-1a**), following which mild pressure (~100 g/cm^2) and heat (ca. 60 ˚C) are applied to the tape, which is adhesively attached to the master mold, for a few seconds (**Fig. 4-1b**). This operation replicates the structures of the master mold (**Fig. 4-1h**) onto the surface of the adhesive tape (**Fig. 4-1i**). The application of mild heat lowers the viscosity of the adhesive polymer, and pressure induces the adhesives to fill the recessed areas of the stamp through viscous flow of the adhesive polymer. By the viscoelasticity of the adhesive element, the patterns on the structured master mold can be finely replicated onto the pressure-sensitive tape. This aspect of pattern replication onto the adhesive tape is analogous to capillary force lithography (CFL)[47]. Many kinds of materials can be chosen as master mold for the adhesive tape without a restriction on the surface energy of the stamp, e.g., polydimethylsiloxane (PDMS, surface energy ~25 mJ m^{-2}), polyurethane acrylate (PUA, ~20 mJ m^{-2}), and photo-lithographically fabricated silicone (Si) master mold (~1500 mJ m^{-2}). Having been cooled at room temperature for a few seconds, the adhesive recovers its elasticity, and the structure is replicated onto the adhesive tape as it is peeled off the stamp. (**Fig. 4-1c, i**) This patterned tape can be disposable after a single use or limited number of cycles (durable more than 16 cycles, see **Figure 4-2**). By repeating the procedure shown in **Figure 4-1** with new adhesive tape, however, the completely identical patterned tape can be regenerated and reused. Therefore, it should be mentioned that the reusability of patterned

taping is principally non-restricted.

The soft lithographically patterned pressure-sensitive tape is then used to cover the substrate on which the target thin film is deposited such that only protruding parts of the patterned tape make contact with the target layer (**Fig. 4-1d**). Without applying physical or chemical stimuli to the thin film at room temperature (RT), the subsequent delamination of the patterned tape from the substrate yields a subtractive patterned thin film. (**Fig. 4-1e**) While direct pressure and/or heat application onto target film (used in the conventional soft lithography like 'hot lift off' method) often deforms the patterns of target, our patterned taping method does not induce any deformation to accurately replicate the master mold structures. (**Fig. 4-3**) Due to the high capacity for adhesion of the pressure-sensitive tape[48], clear patterns without residues between lines (**Figure 4-4**) are attainable. To achieve such a structure, a higher delamination speed for the patterned tape is recommended for greater adhesion. The kinetic control of adhesion by regulating the peeling speed of the viscoelastic stamp is a well-known technique[49, 50, 51]. Viscoelastic, polymer-based, pressure-sensitive tapes show large magnitudes of adhesion energy at higher peeling rates (> 10 cm/s along the direction of peeling).

Following subtractive patterned taping, the thin film of the target material was dressed only on the protruding part of the patterned tape (**Fig. 4-1e**). Softly covering an empty substrate with tape and sequent exfoliation transferred the pattern structure to the other (or the other types of) substrates owing to the adhesion interaction between the material and the substrate (**Fig. 4-1f-g**). Moreover, the lamination and delamination of the additive patterned taping was carried out in conditions similar to those used for subtractive patterning (i.e., at room temperature, and so on). The material attached to the adhesive stamp was also reusable, and

yielded daughter patterns onto other substrates. The principle of additive patterned taping is consistent with graphene transfer onto a substrate studied in related research[49, 50, 51]. Because thin adhesive tape is flexible, conformal contact with the target can be effected. In terms of time/cost efficiency, all processes were manually handled within 1–2 min, and the minimum expenditure per patterning process was the same as or less than one sheet of adhesive tape owing to the reusability of the master mold and the adhesive stamp.

Subtractive patterned taping

Patterns of organic semiconductors occupying large areas were generated through subtractive patterned taping (**Fig. 4-13-5a-c**). **Figure 4-14-5a-b** show subtractive patterned large-area organic micro parallel line patterns using optical microscopy and SEM, respectively. According to the visible light interference effect of this micro parallel line patterns, clear structural color is seen in the 1.2 cm × 1.2 cm whole size substrate image (**Fig. 4-13-5c**). The patterning yield of subtractive patterned taping was close to perfection due to the accurately replicated structure of the master mold on the adhesive tape (**Fig. 4-1i**) and the flexible nature of the thin tape (usually at the sub-millimeter scale). Patterned taping is also compatible with various shape of patterns such as micro letters as shown in **Figure 4-14-5d-f**. Thousands of (~ 3600) micro-squares (length: 10 μm, spacing between squares: 6 μm) were fabricated within a 1 mm × 1 mm area by repeating subtractive lift off in the vertical and the horizontal directions (**Fig. 4-6a**, **Fig. 4-7**). Micro-square arrays of an organic semiconductor (2E, 2′E)-3, 3′-(2, 5-bis(hexyloxy)-1, 4-phenylene)bis(2-(5-(4-(trifluoromethyl)phenyl)thiophen-2-yl)acrylonitrile) (Hex-4-TFPTA)[52] (**Fig. 4-6a**) led to the massive patterning yield of the subtractive

patterned taping method due to conformal contact of the patterned tape to targeted thin films.

With the PDMS master mold of the adhesive tape, a micro-level pattern of various organic materials was constructed on different substrates: a hydrophobic octadecyltrichlorosilane (ODTS)-treated SiO_2 substrate (static water contact angle ~98°, **Figs. 3a-c**), and a hexamethyldisilazane (HMDS)-treated SiO_2 substrate (static water contact angle ~84°, Fig. 4-6d). There were some leftovers between the lines on the bare hydrophilic SiO_2 (static water contact angle ~0°, **Fig. 4-6e**) because adhesion between the bare SiO_2 substrate and the target material (DBDCS, (2Z,2′Z)-2,2′-(1,4-phenylene)bis(3-(4-butoxyphenyl) acrylonitrile[53]) was not sufficiently trivial to yield a clear pattern. A micro-line pattern of a gold electrode (**Fig. 4-6f**) was generated through subtractive patterned taping. The metallic bonds of the thin gold film along the in-plane direction were broken due to the universal adhesion of the pressure-sensitive tape. Nanometer-level patterns of TIPS-pentacene (TIPS-PEN) were built at a ~350-nm scale (**Fig. 4-6b**), and a structured Si wafer was used as the master mold for the adhesive tape. As master molds of patterned tape, PUA and Si wafer can be utilized in order to construct the nano/ sub-micro structures on the patterned tape. Because the physical properties of PUA (Young's modulus: ~40 MPa) and the Si wafer (~200 GPa) are superior to that of PDMS (roughly 1–9 MPa), sub-micro/ nano structure can be constructed on PUA and Si wafer. Even if the master molds can fabricate nano scale structure, indeed, there are resolution limit depends on the target films. By adjusting deposition temperature of substrates, pentacene with different grain sized (T_{sub}= RT, 80℃) films were fabricated. With the more small sized grain, more small patterns were achievable. (See **Figure 4-8**) Furthermore, in order to discover the resolution limit

of patterned taping method itself, smallest patterns on the patterned tape was investigated with SEM. As a result, observed thinnest line pattern width was thin as ~210nm, and this value would be the estimated theoretical uppermost resolution limit of patterned taping (**Figure 4-8c**).

Regardless of the slight curvature of substrates along the contact area, the patterned tape (**Fig. 4-1i**) can also effect the removal of materials in the inner part of the curvature. (**Fig. 4-9**) For instance, bottom-gate bottom-contact (BGBC) organic field-effect transistor (OFET) devices have a patterned active organic layer. The uneven surface was fabricated by thermally depositing an interdigitate-type pattern of a gold thin film (thickness: 30 nm, line width: 5 μm) with a shadow mask on the substrate, and an organic semiconductor pattern was fabricated onto the uneven substrate with virtually perfect patterning yield. (**Figure 4-9**)

Device fabrication via subtractive patterned taping

In order to better understand the non-destructive character of the method, the electrical properties of patterned and non-patterned devices were measured and compared because electrical contact[54, 55] between the semiconducting films, and the dielectric and electrode layers, as well as the orderedness[56] of the molecules were strongly correlated with the properties of transistor devices. Patterned top-contact, bottom-gate (TCBG) OFET devices of pentacene showed a clear transfer curve and an output curve typical of hole-transporting OFET devices (**Fig. 4-10**). The calculated electrical properties of patterned and non-patterned channel devices showed comparable levels of performance: the average FET mobility of the non-patterned device was 0.496 $cm^2/V \cdot S$, whereas that of the patterned device was 0.525 $cm^2/V \cdot S$, as the threshold voltage (V_{TH}) and the on/off current ratio ($I_{ON/OFF}$) remained constant (**Fig. 4-10**). Moreover, as shown in other studies[3, 29], the output

curve of the patterned device showed no leakage current (crosstalk or parasitic leakage current) between neighboring devices at V_G = 0, whereas that of non-patterned devices recorded leakage current flow at V_G=0 (**Fig. 4-10**).

Furthermore, with the patterned taping approach (**Figure 4a**), microstrip lines (60 μm width) of n-type semiconductor Hex-4-TFPTA[57] ((2E,2′E)-3,3′-(2,5-bis(hexyloxy)-1,4-phenylene) bis(2-(5-(4-(trifluoromethyl)phenyl) thiophen-2-yl)acrylonitrile) could be patterned perpendicular to the transistor channel (**Figure 4-11b**). For the injection of both charge carrier, source-drain electrode composed of asymmetrically designed molybdenum oxide/ aluminum (MoO_3/Al) was fabricated via angled deposition. For the areal emission, semitransparent electrodes (Al: 8 nm and MoO_3: 10 nm) were introduced [58, 59]. The transmittance of the semitransparent Al/MoO_3 was found to be 43.5%, which was simply obtained from **Equation 1**. The equation includes the EL and transmittance spectra (**Figure 4-11c**) in the 550~780 nm wavelength range due to the wavelength detection limit of the EL spectrometer.

$$\frac{\int_{550}^{780} EL(\lambda) \times Transmittance(\lambda)\, d\lambda}{\int_{550}^{780} EL(\lambda)\, d\lambda} \quad (1)$$

The DR-emitting pixels showed gate-controlled FET behavior and EL brightness. In **Figure 4-11d-e**, the emission zone gradually expanded with the gate bias increment (V_G = 0 ~ 100 V) for an EQE of 1.82×10^{-2}%. The device presented a pixelated areal emission zone of *ca.* 45 μm × 60 μm in width and length, respectively (**Figure 4-11d**, inset). The pixel resolution of this result is already higher than the subpixels of a 4K UHD (3840 × 2160) 40 inch flat-panel display (subpixel size: 75 μm × 75 μm) [5]. Furthermore, *ca.* 13 μm × 15 μm OLET pixels

could be fabricated via patterned taping (**Figure 4-12)**, in which the pattern size was higher than the resolution limit of the FMM technique (~20 μm) [60, 61]. These pixel dimensions are comparable with the subpixel size of a 20K UHD 40 inch flat-panel display (subpixel size: 15 μm × 15 μm) [5].

In addition, multi-functional devices can be fabricated through introducing micro-structure to multi-component devices, *e.g.*, laterally aligned (patterned) n-/p-micro channels bridging source/ drain electrode showed ambipolar transport (**Figure 4-13**). The laterally aligned architecture fabricated via simple few steps based on the patterned taping process (**Figure 4-13a-d**): (1) first layer deposition onto a substrate (**Figure 4-13a-b**), and (2) the first layer are selectively delaminated via subtractive patterned taping (**Figure 4-13b-c**), and sequent (3) second layer deposition on the patterned first layer and exposed dielectric surface finally makes laterally aligned architecture (**Figure 4-13c-d**). By virtue of organic compatibility of patterned taping, ambipolar devices were successfully demonstrated of which mobilities are comparable with the original organic semiconductors: the ambipolar devices showed 0.54/ 0.35 $cm^2V^{-1}s^{-1}$ of averaged e/h mobility and the unit devices of corresponding n-type, p-type semiconductors showed 0.56 and 0.29 $cm^2V^{-1}s^{-1}$ respectively (**Figure 4-13**).

Additive patterned taping

The basic principle underlying additive patterned taping is analogous to that used in graphene layer transferral[49, 50, 51]. Following subtractive patterned taping, the patterned tape is inked with a thin film of the target material on the protruding regions of the tape. Tape attachment and the following detachment transfer the target material to other substrates (receiver substrates). Because the van der Waals

force acts between materials and substrates, the pattern is fixed onto the receiver substrate. Thinner features than on the film of the donor substrate are transferred because the layer or domains directly in contact with the adhesive persist on the adhesive surface due to the significant attraction between the adhesive and the materials.

Through additive transfer, the thin film of the source material was transferred onto various classes of substrates: the curved surface (**Fig. 4-13a**, **Figure 4-15**) of a capillary tube (radius of curvature: 355 μm), a transparent flexible substrate composed of polyethylene naphthalene (PEN, **Fig. 4-13b**), and a flat, bare SiO_2 substrate (**Fig. 4-13c**, **Fig. 4-15**).

A more complex structure was constructed by repeating the transfer, such as by multi-stack or parallel alignment. Regular micro-2D lattice arrays of homogeneously integrated organic semiconductor (2Z,2′Z)-3,3′-(1,4-phenylene)-bis-(2-(3,5-bis(trifluoromethyl)phenyl)-acrylonitrile) (CN-TFPA)[62] are fabricated by twice applying additive patterned taping in perpendicular directions (**Fig. 4-15**). As with subtractive taping, additive patterned taping exhibited scalability and high patterning yield. Furthermore, a heterogeneous assembly (Fig. 4-13c) was fabricated using micro-scale layouts of organic materials. A line pattern of red luminescent material (DBADCS[63], (2Z,2′Z)-2,2′-(1,4-phenylene)bis(3-(4-(dibutylamino)phenyl)acrylonitrile)) was first transferred, followed by that of a green emitting material (λ_{max}= 495 nm) onto a red one (λ_{max}= 598 nm). At the intersection of the two layers, red emission was observed due to energy transfer to the material emitting light of longer wavelength. Due to ultra-flexibility nature of adhesive tape, heterogeneous multi stacked pattern is fabricated even on capillary tube (radius curvature: 355 μm) by additive patterned taping. (**Figure 4-15**) In

commercial display devices, RGB sub pixels prevent energy transfer to low band gap materials by spatially separating each emitter. Similar to this, our white light-emitting substrate independently fabricated micro-sub pixels (sub pixel size: 10 μm × 10 μm) and the micro-line (line width: 10 μm) configuration of luminophores (Fig. 4-16e), and evaded energy transfer to light-emitting material that generates longer wavelengths (green and blue, to red or green to red). **Figure 4-17** shows the white light-emitting substrate with three systemically arranged luminescent micro-lines fabricated through the additive transfer of the micro-lines of each component. The line pattern of the red emitting film (λ_{max}= 598 nm) was first additive transferred onto the bare SiO_2 substrate, and the alternating parallel lines of green (λ_{max}= 495 nm) and blue (λ_{max}= 445 nm) were deposited by additive transfer in different directions from the red line (**Fig. 4-16a, b, e**). Arrows of **Fig. 4-16a, b** (↑, ↑, ↑) indicate line directions of R, G, and B, respectively. The differences in brightness among the three colors were balanced by the thickness regulation of each RGB component. Macroscopically, as shown in photoluminescence spectrum (**Fig. 4-16c**) covering whole visible range (400 nm~ 700 nm), heterogeneously integrated RGB layers on substrate emitted white light (**Fig. 4-16b**) at the Commission Internationale de I'Eclairage (CIE) chromaticity coordinate of (0.342, 0.367) (**Fig. 4-16d**).

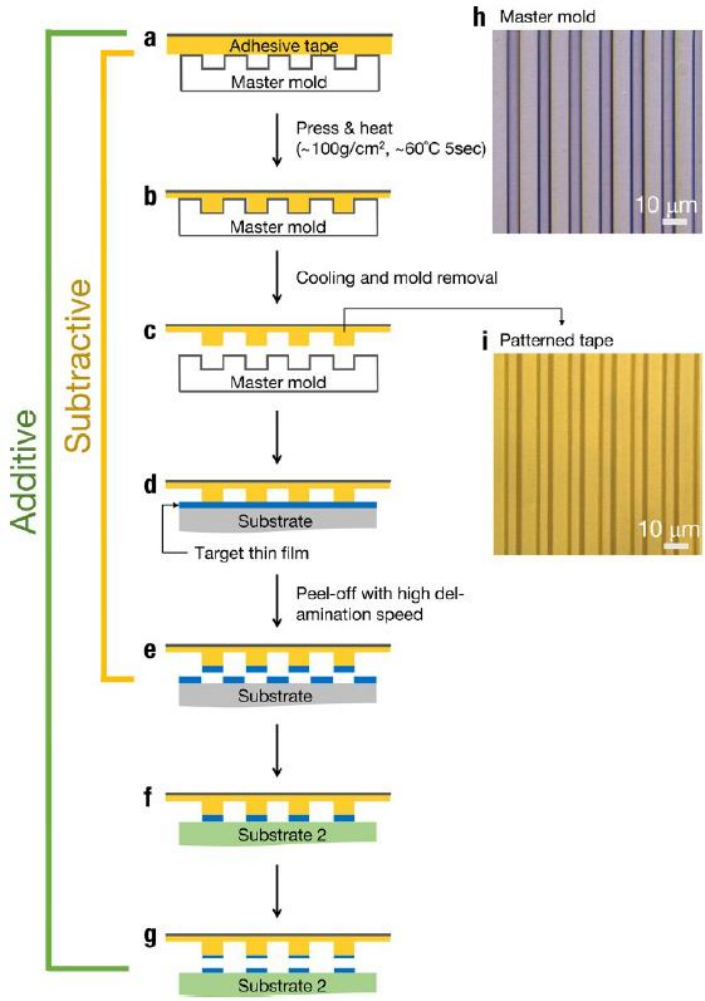

Figure 4-1. Patterned taping. a-g) Schematic illustration of patterned taping. The yellow and green brackets represent subtractive patterned taping (Fig. 4-1a-e) and additive patterned taping (Fig. 4-1a-g), respectively. h) Pre-patterned PDMS master mold. The darker area is recessed. i) Patterned tape from the master mold in Fig. 4-1h. The recessed area of the master mold protruded in the patterned tape.

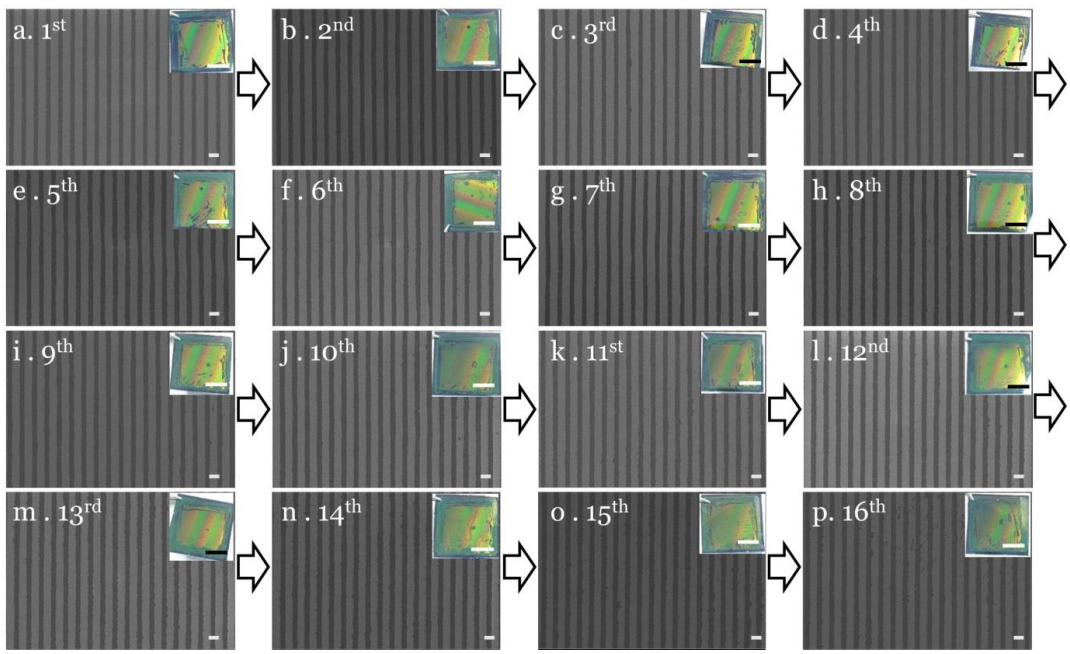

Figure 4-2. Reusability experiment of Subtractive patterned taping. SEM images of micro line pattern with the same adhesive tape by repeating subtractive patterned taping 16 times. (Inset: camera images of patterned target thin films, scale bar: 10 μm, inset scale bar: 50 mm)

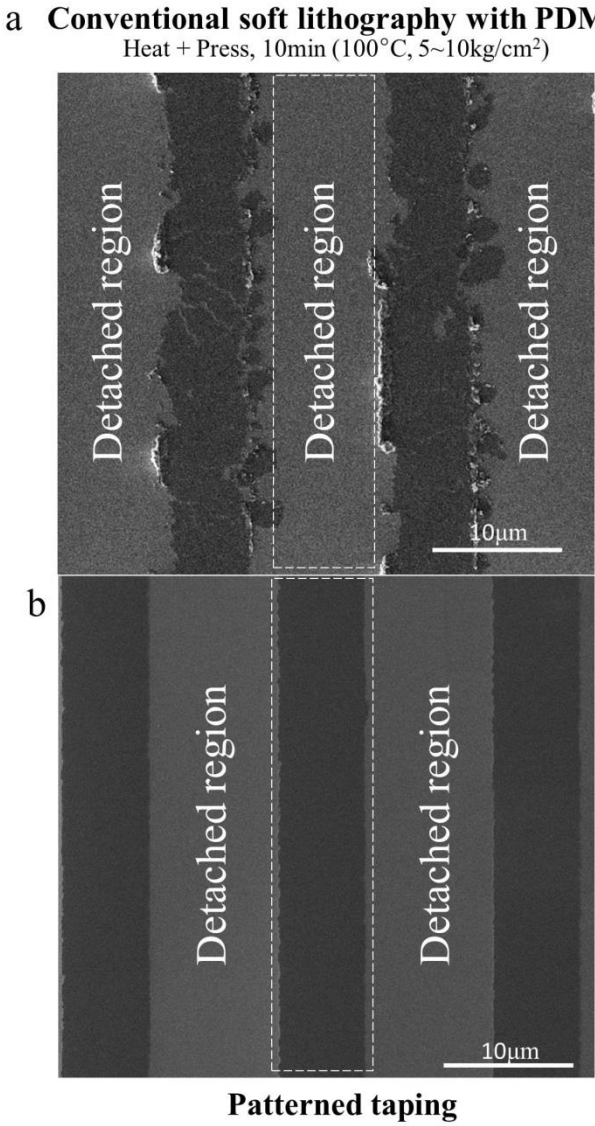

Figure 4-3. Parallel comparison between Patterned taping and other conventional soft lithography method with PDMS Figure 4-3a show SEM image of organic thin films (Hex-4-TFPTA) patterns via subtractive patterned taping. Figure 4-3b show SEM image organic thin films (Hex-4-TFPTA) patterns via conventional subtractive patterning method: 100°C heat and 5~10kg/cm^2 pressure was applied for 10 min in order to endow sufficient adhesion energy between PDMS and target films.[18]

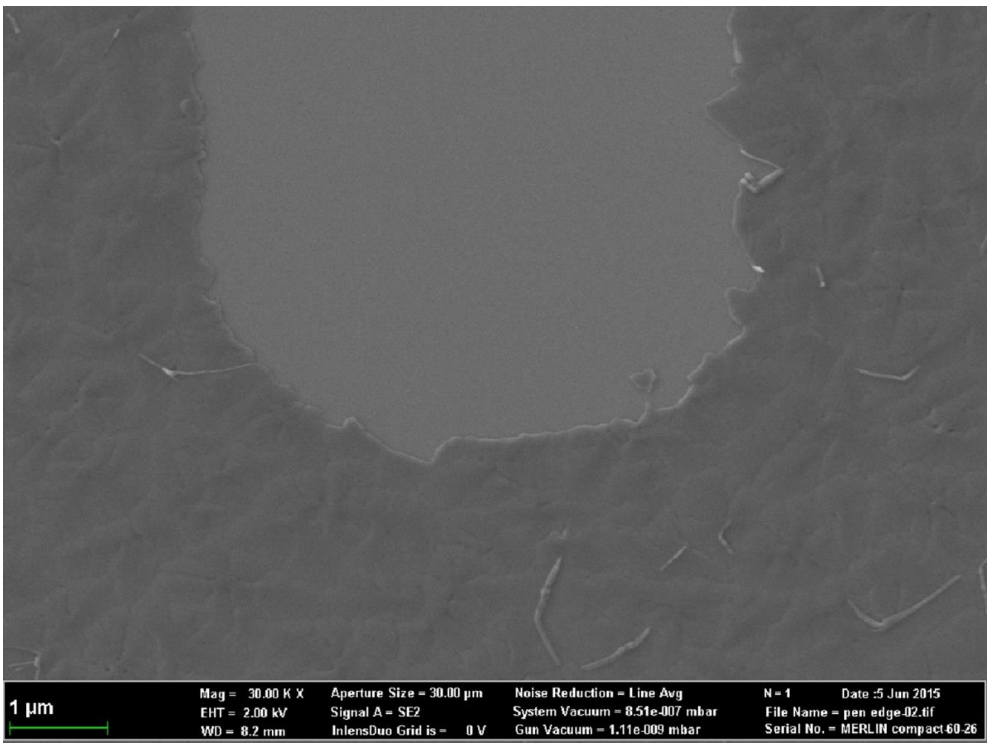

Figure 4-4. SEM image of subtractive patterned pentacene (Fig. 4-6e) thin film on HMDS-treated SiO_2 surface. A clear pattern was attainable without residual of pentacene or adhesive tape because of fine adhesion, conformal contact of flexible adhesive tapes, and reduced substrate–material interaction by proper surface modification.

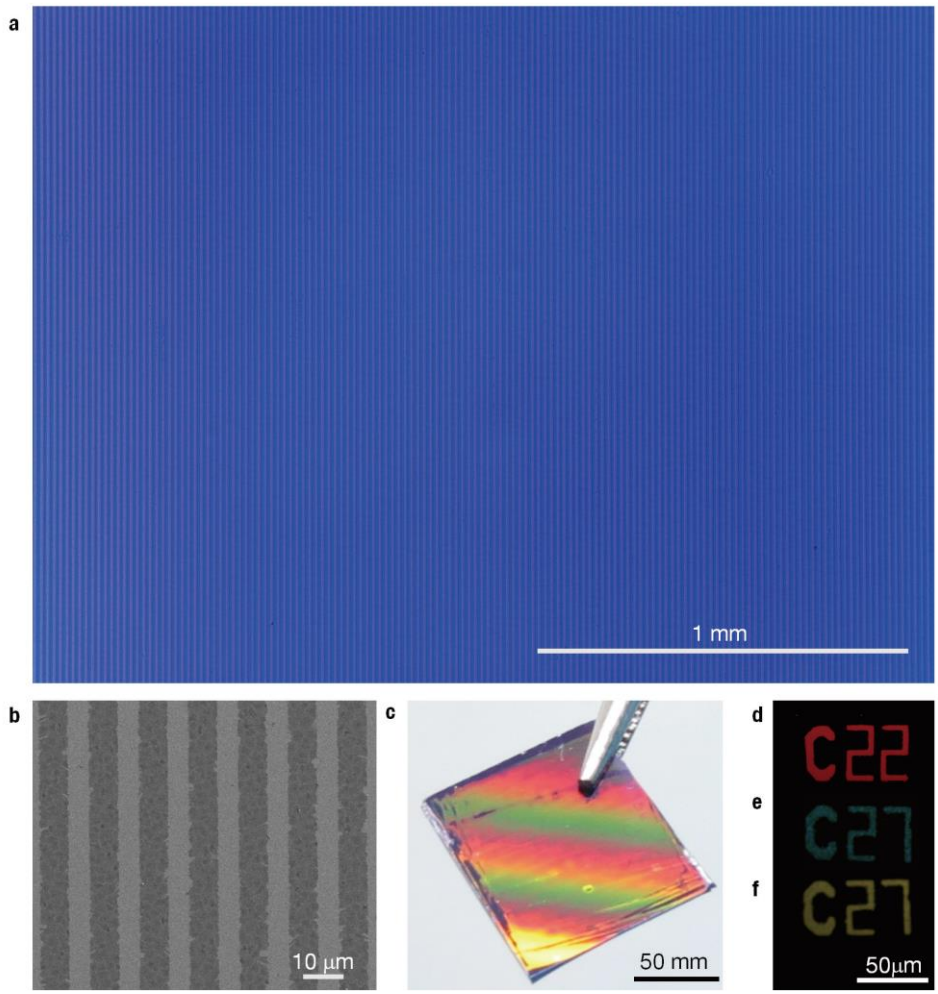

Figure 4-5. Subtractive pattern of thin organic film. a) Line-patterned thin organic film of semiconductor Hex-4-TFPTA. The patterning yield of subtractive patterned taping was close to unity. b) SEM image of Fig. 4-13-5a. c) 1.2 cmx1.2 cm patterned wafer of Hex-4-TFPTA with structural color d-f. Micro-scale letter by optical microscopy image under UV light. d) Hex-4-TFPTA on ODTS-treated SiO2 substrate. e) DBDCS on bare SiO2 substrate. f) Phase-transitioned thermally annealed DBDCS. The same micro-letter as that in Fig. 4-13-5e.

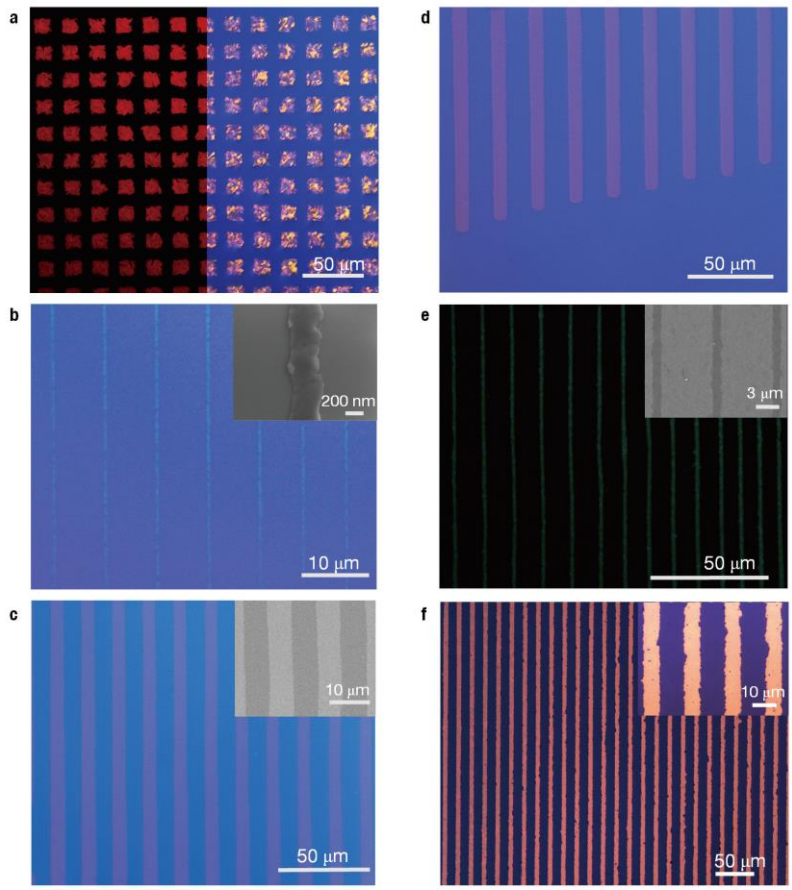

Figure 4-6. Optical microscopy image and SEM images of subtractive patterned of thermally deposited materials on various substrates. a) Square (■) array pattern on ODTS-treated SiO2 under UV light (patterned taping occurring twice in perpendicular directions) of Hex-4-TFPTA. b) Sub-micro line-patterned TIPS-pentacene on ODTS-treated SiO2 (inset: SEM image of ~350 nm-wide line pattern). c) CuPC line pattern on ODTS-treated SiO2 surface. d) Line pattern edge of thin pentacene film on HMDS-treated SiO2 surface. e) DBDCS line pattern image under UV light on bare SiO2 surface. f) Line pattern of gold thin film on bare SiO2 substrate. (SEM images in Fig. 4-6a, d are at Fig. 4-7, 2, respectively).

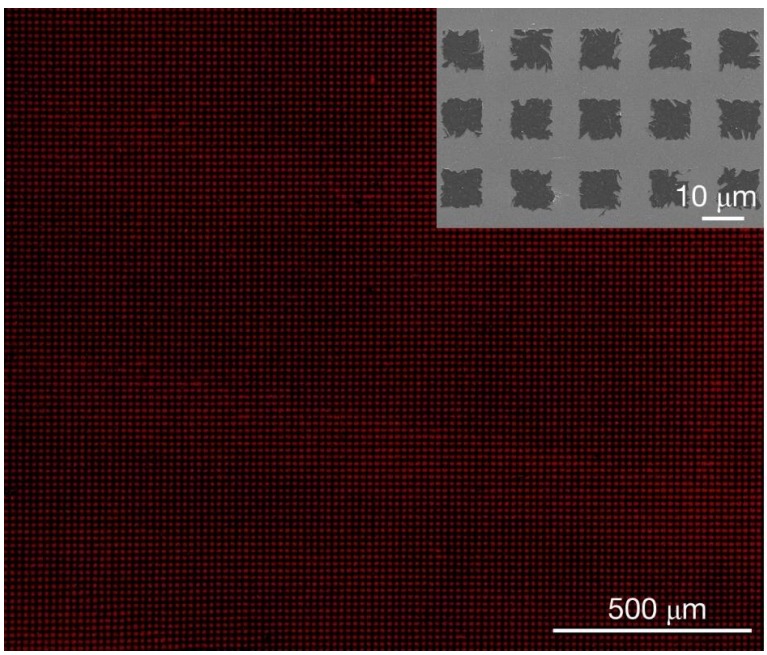

Figure 4-7: Organic semiconductor Hex-4-TFPTA micro-square (■) array. Optical microscopy image under UV light of subtractive-patterned organic semiconductor Hex-4-TFPTA micro-square array. ~3600 micro-square (10 μm x 10 μm micro-square area and 6 μm spacing between squares) were placed within 1 mm^2, which indicates a high degree of integration in the organic transistor device. The thin organic film was lifted off twice in perpendicular directions. Scale bar: 0.5 mm (inset: SEM image of micro-square array).

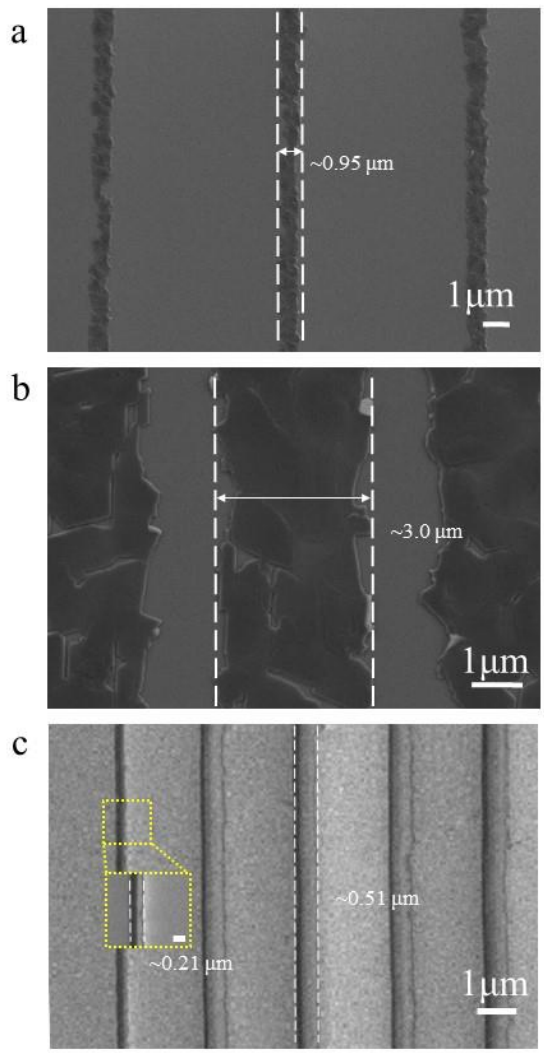

Figure 4-8. Resolution limit study of various thin films. SEM image of vacuum deposited organic semiconductors of small grain pentacene (Fig. 4-15a, T_{sub} = RT) and large grain pentacene (Fig. 4-15b, T_{sub} = 80℃). Fig. 4-8c shows sub-micro structures on patterned tape of which master mold is micro-/ nano structured Si wafer. (Inset scale bar: 200 nm)

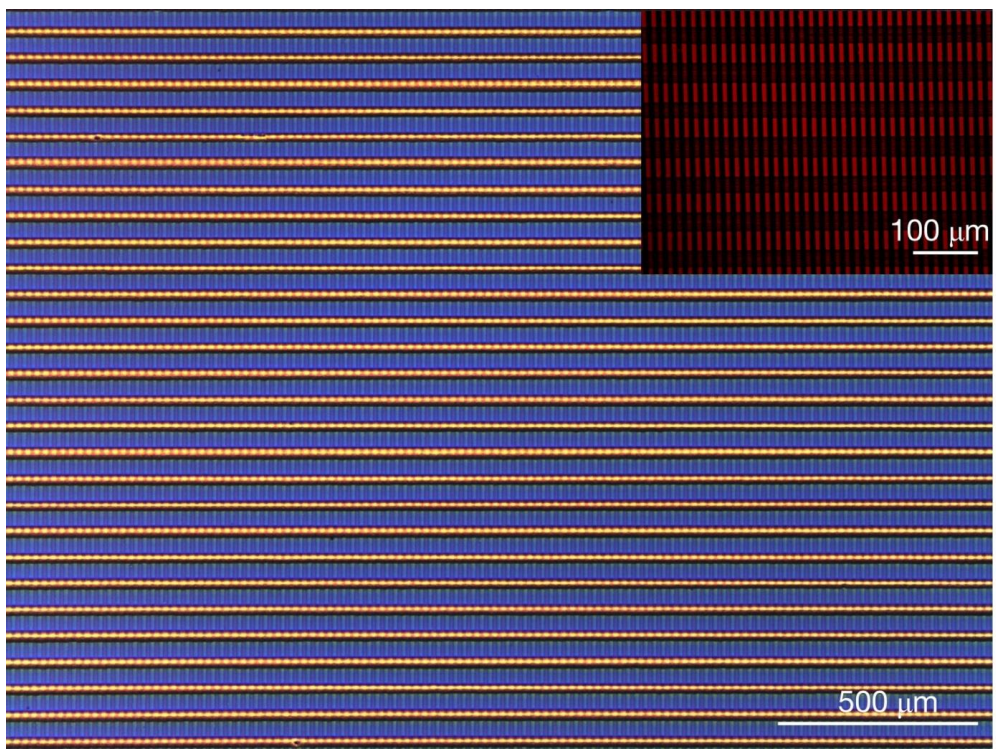

Figure 4-9. Subtractive patterned bottom-contact OFET device. Optical microscopy image of subtractive patterned bottom-contact OFET device Hex-4-TFPTA under room light. An interdigitated-type pattern of gold thin film (thickness: 30 nm, line width 5 μm) was thermally evaporated (inset: OM image under UV light with higher power objective lens).

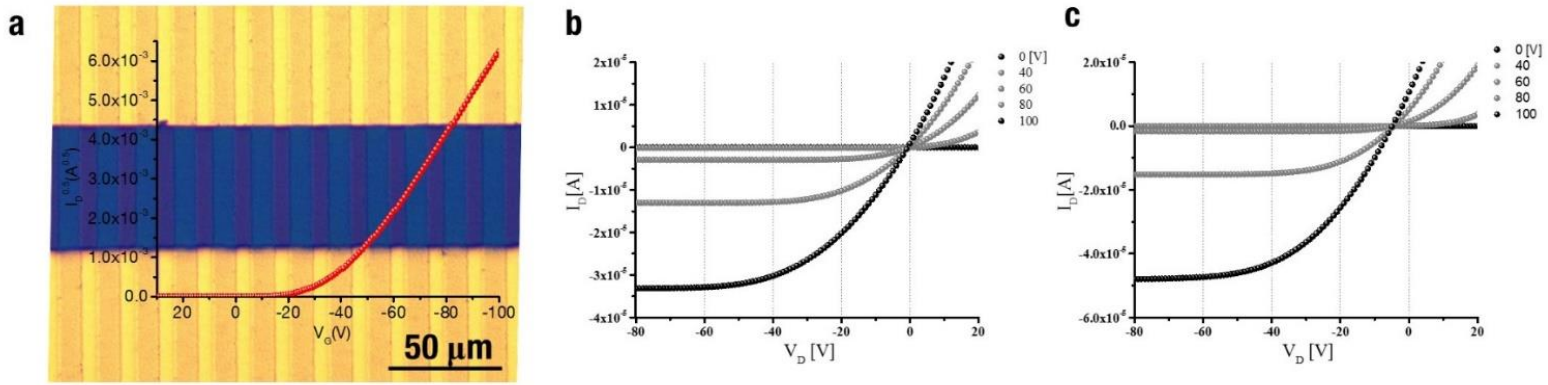

d

Sample	μ_p [$cm^2V^{-1}s^{-1}$]	V_{TH} [V]	I_{ON}/I_{OFF}	N
Patterned	5.25×10^{-1}	-42.6	10^7	3
Non patterned	4.96×10^{-1}	-52.0	10^7	3

Figure 4-10. OFET device characterization with pentacene semiconductor thin film on HMDS-treated SiO_2 substrate. a) Optical microscopy image of OFET channel of micro-line patterned pentacene and its p-type transfer curve. b) Output curve of micro-line patterned pentacene. c) Output curve of micro-line non-patterned pentacene, which shows parasitic leakage current at zero gate voltage. d) Comparison of OFET properties between patterned pentacene OFET and non-patterned pentacene OFET devices. All values were averaged. The properties remained intact following patterned taping, which is a damage-free method for sensitive organic materials.

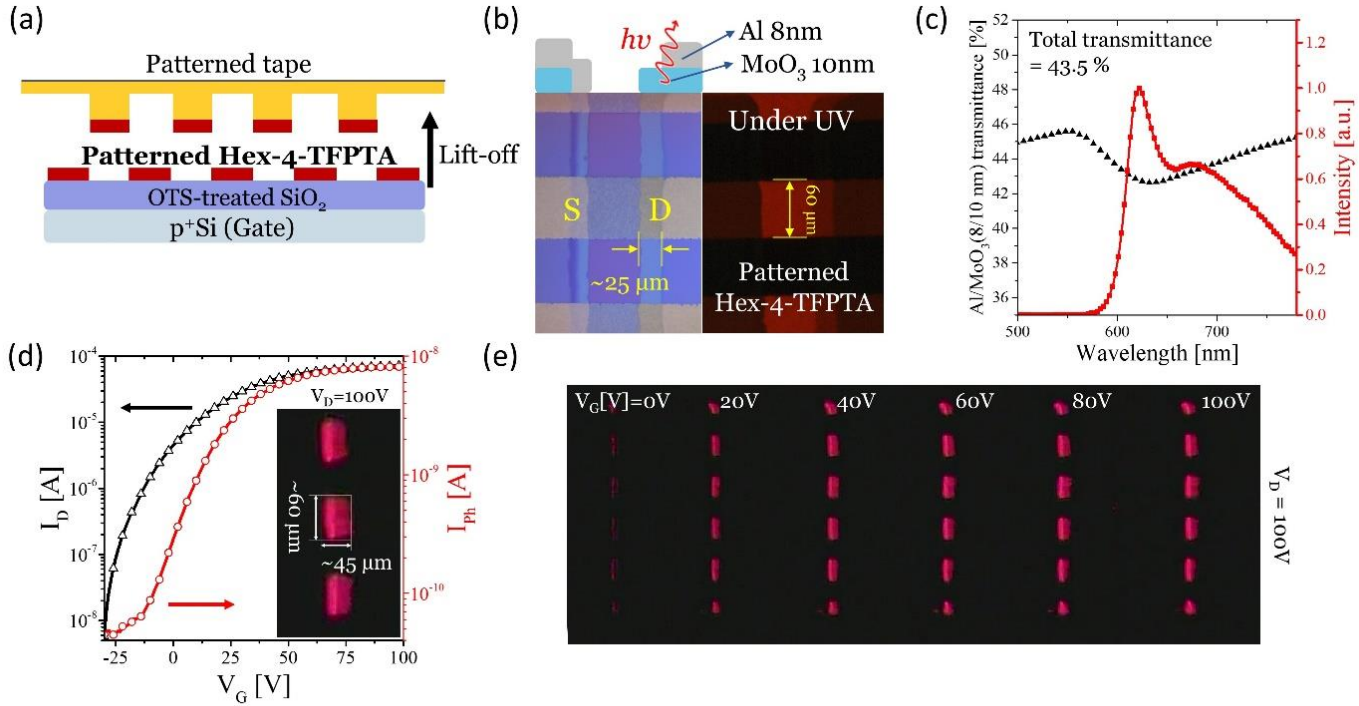

Figure 4-11. Pixel emission of the Hex-4-TFPTA OLET (a) An illustration of the soft-lithographic technique: subtractive 'patterned taping'. (b) An optical microscopy image of the pixelated OLET under visible light (left) and under UV light (right). (c) The transmittance and total transmittance of the thin metal electrode with respect to the EL spectrum. (d) The transfer characteristics and photodiode response of the pixelated OLET (inset: the dimensions of the emission area). (e) EL emission depends on the voltage conditions.

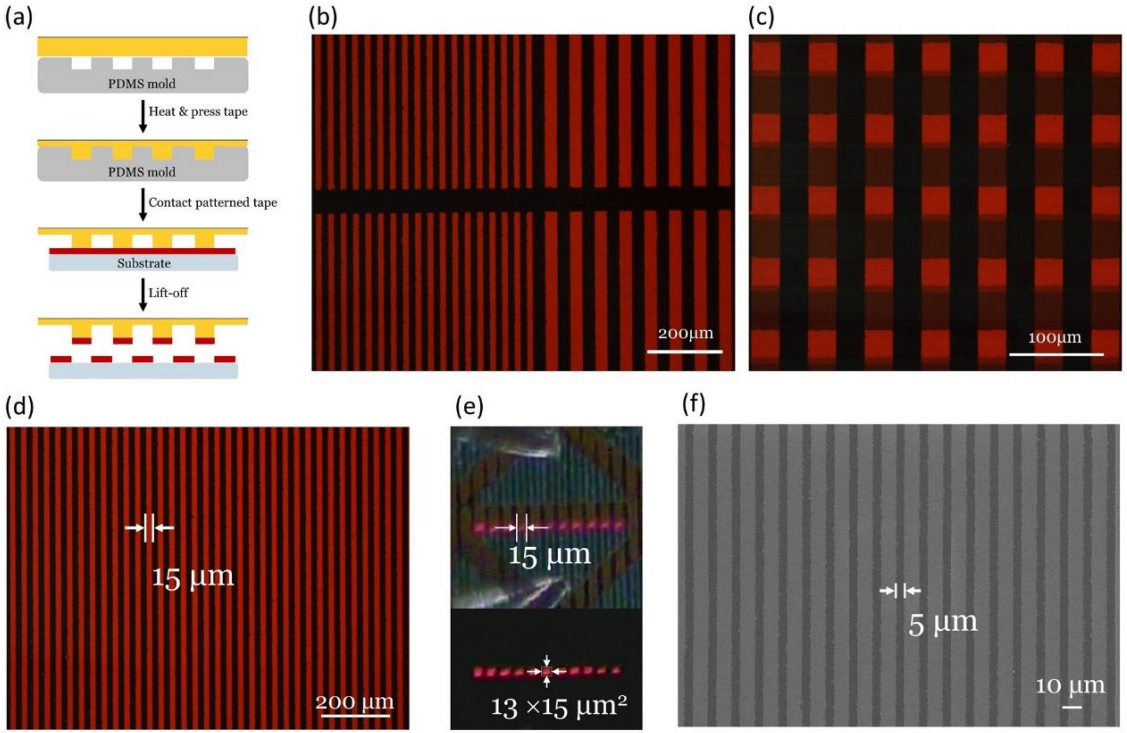

Figure 4-12. Patterned Hex-4-TFPTA thin film by subtractive Patterned taping. (a) Illustration of subtractive Patterned taping (b) Patterned Hex-4-TFPTA thin film (Line/Space : 30/30 μm, 60/60 μm) (c) 30/30 μm (L/S) patterned Hex-4-TFPTA thin film (vertical) and 30/30 μm (L/S) patterned Al 8 nm/ MoO_3 10nm metal through shadow mask (horizontal) (d) Higher resolution line pattern (15 μm) than FMM patterning resolution (20 μm) (e) Electroluminescence of 15 μm patterned OLET, and the pixel size (13 × 15 μm) is comparable with the sub-pixel size of 20K UHD 40-inch flat panel display (15 × 15 μm) (f) Higher resolution line pattern (5 μm) than FMM patterning resolution (20 μm)

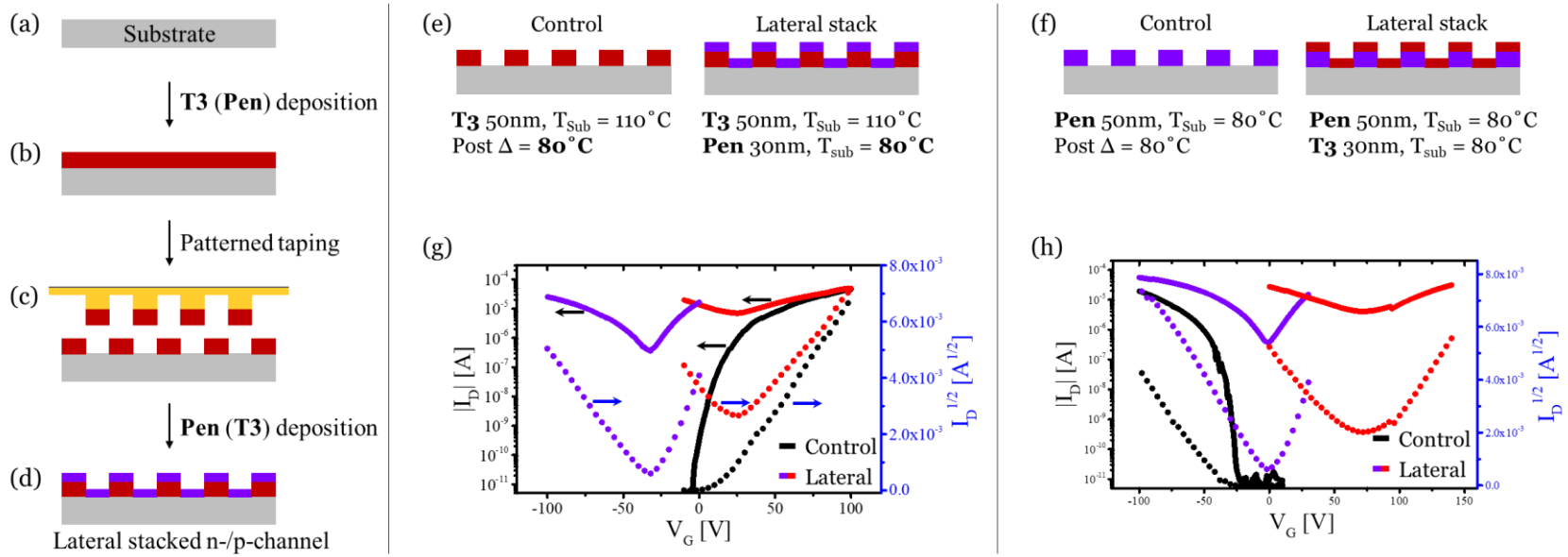

Figure 4-13. Fabrication of laterally aligned n-/p-channel ambipolar transistor via patterned taping. n-type material is Hex-4-TFPTA (T3) and p-type material is pentacene (Pen). (a-b) T3 (Pen) deposition on substrate, (b-c) subtractive patterning via patterned taping, and then (c-d) deposition of Pen (T3) generates laterally stacked ambipolar transistor channel. (e) Device structure of first comparison group; control device and laterally aligned device, (b) Device structure of second comparison group; control device and laterally aligned device. T_{Sub} while on the second layer deposition of each layer was indicated, and for the equal comparison, control devices were also additionally annealed. (c-d) Transfer curves of first and second comparison group respectively. Black lines are transfer curve of control device, and red and violet lines are n-/p-type transfer curve of laterally aligned devices respectively. Solid lines and dot lines are $|I_D|$ at log-scale and $|I_D|^{1/2}$ respectively.

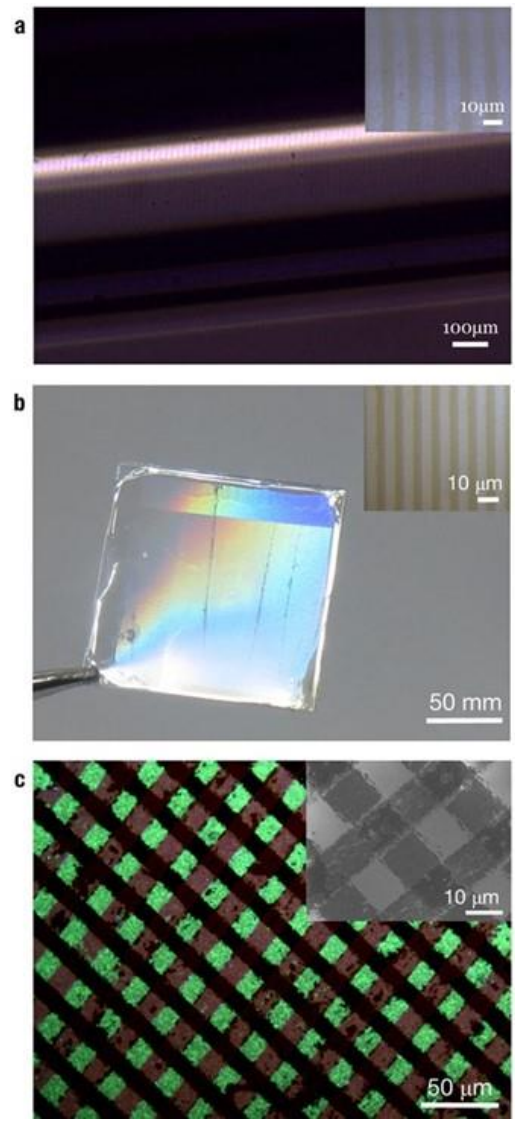

Figure 4-14. Micro-pattern images of additive patterned taping process. a) Additive patterned organic film on capillary tube (Radius of curvature: 355 μm, inset: high powered optical microscopy image of micro patterns on capillary tube. Slight blur occurred because out of focusing due to the curved surface). b) Patterned organic film on flexible polyethylene naphthalene (PEN) substrate (inset: optical microscopy image). c) Optical microscopy image of heterogeneous stacked layout of DBADCS and CN-TFPA luminescent organic materials under UV light (inset: SEM image).

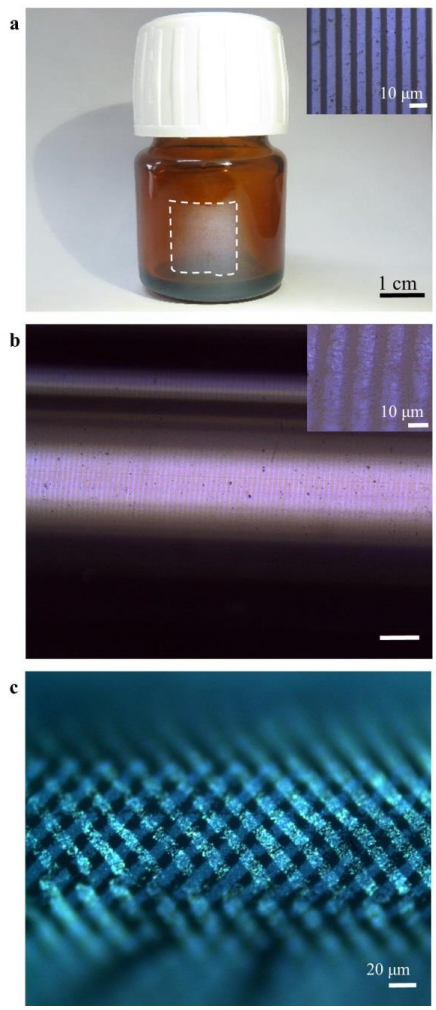

Figure 4-15. Micro-pattern images of additively patterned taping on curved surfaces with various radius of curvature. Patterns are transfer on a) round glass vial. (Radius of curvature: 1.6 cm, inset: high powered OM image), b) capillary tube (Radius of curvature: 720 μm, inset: high powered OM image), and c) thinner capillary tube (radius of curvature: 355 μm).

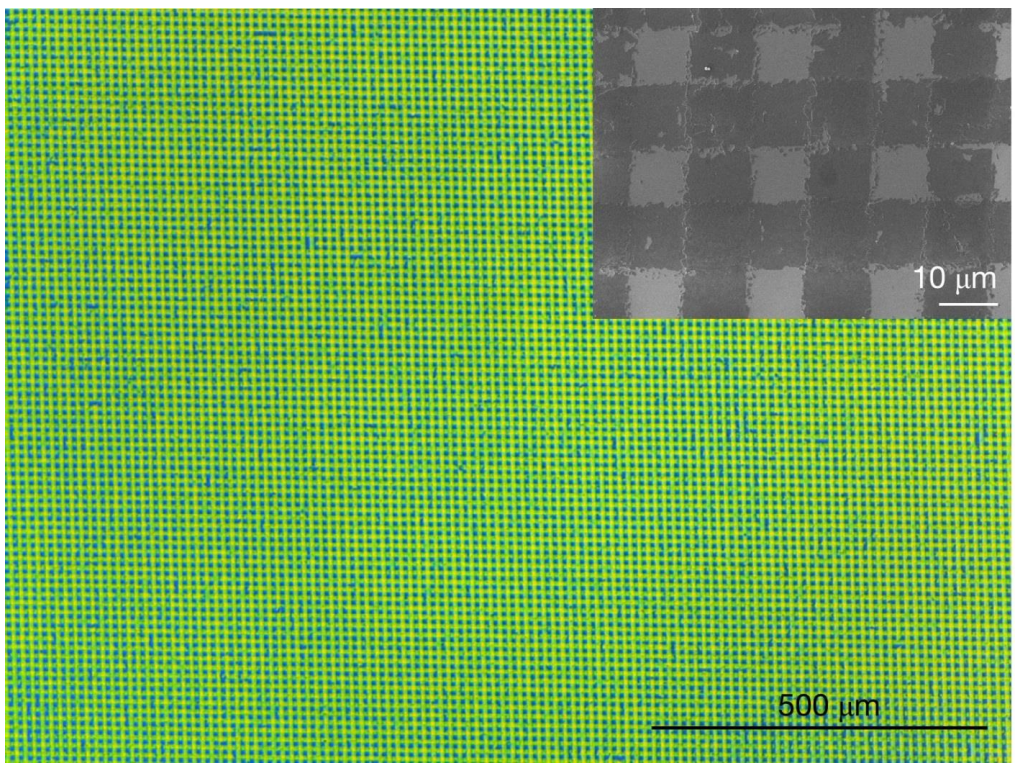

Figure 4-16. Micro-lattice array of organic material via additive transfer. Optical microscopy image of CN-TFPA micro-lattice array (green color) by multi-stack layout additive patterned over a large area on a bare SiO_2 substrate (blue color). The additive transfer occurred twice in perpendicular directions, and the image shows the high patterned yield and scalability of additive patterned taping (inset: SEM image of micro-lattice).

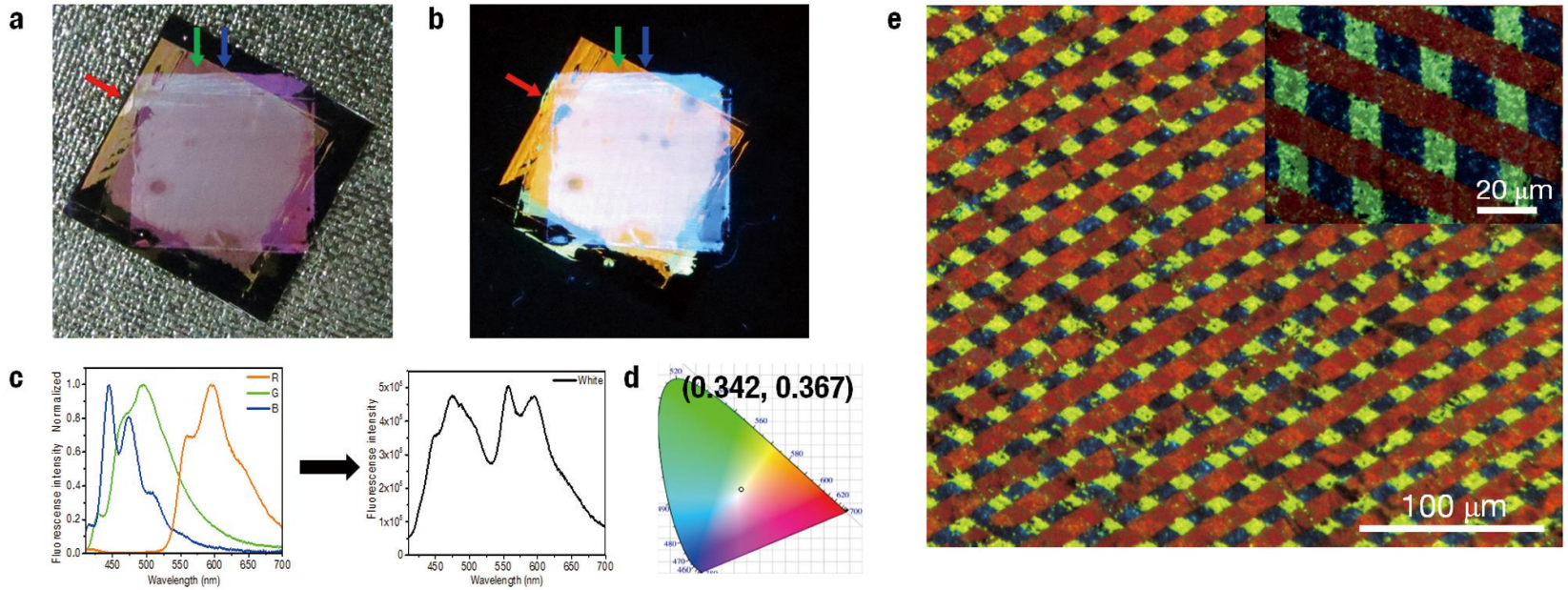

Figure 4-17. White luminescence-emitting substrate via additive patterned taping. a) Substrate under room light of additive transferred DBADCS (R, line pattern direction: ↑), CN-TFPA (G, ↑), DSB (B, ↑) for white luminescence-patterned organic materials. b) Image of Fig. 4-16a under 365 nm hand-held UV light. Arrows (↑, ↑, ↑) indicate line directions of R, G, and B, respectively. c) Photo luminescence spectrum of components of red, green, blue organic materials and photo luminescence spectrum of Fig. 4-16b. d) CIE chromaticity coordinate of (0.342, 0.367) derived by the photo luminescence spectrum of Fig. 4-16b. e) Optical microscopy image of spatially well-arranged R, G, B for white luminescence similar to the subpixels of commercial displays (inset: zoomed-in optical microscopy image).

4.3.2. CT patterning procedure

Based on this versatile/ novel patterned taping method, procedure for patterning CT crystals onto host crystal was devised (**Fig. 4-17**): On the host crystal of donor (acceptor), guest thin film of acceptor (donor) is thermally deposited (**Fig. 4-17c-d**), then the guest thin film on host are subtractive patterned by patterned taping process (**Fig. 4-17e**), and sequent exposure to organic solvent vapor (dichloromethane: DCM) generates CT crystal on the host crystals (**Fig. 4-17f**). For the proof of this procedure, A2 thin film (30 nm) was deposited onto D1 crystal, and sequent patterning and solvent vapor treatment, orange color emitting micro-line patterns are successfully generated on to D1 host crystal which will be now called CT-O_D1 (**Figure 4-19**). Through the suggested procedure, micro-line patterns which emits corresponding CT emission can be found at the other additional possible 7 pairs depending on the CT and the host (**Figure 4-20**); CT-R_D1, CT-Y_D2, CT-G_D2, CT-R_A1, CT-O_A2, CT-Y_A1, and CT-G_A2.

In order to verify the CT crystal generation by the solvent exposure, optical properties of each pair were investigated. From the OM images of pristine guest deposited host crystals (**Figure 4-21**) only showed host emission. After DCM vapor exposure, different color of emission is observed of which each color corresponds to CT emission of D-A pair without change of overall host crystal morphology (**Figure 4-22**). In some cases, small CT color emitting crystalline domains can be observed by the OM image at the surface of host crystal (**Figure 4-22**). The same aspect is found with the PL spectra of each pairs (**Figure 4-23**). Before vapor exposure, emission intensity of vacuum deposited (VD) film was hardly found and only the emission of host crystal is observed (**Figure 4-23,** blue

lines). This is no surprise because the very small grain size of VD film will result in small PL quantum yield by large surface/volume ratio while the bulk crystals has minimized surface/volume ratio and higher crystallinity which can effectively suppress the non-radiative process [64, 65]. Meanwhile, after vapor exposure, the red-shift emission is arisen which can be correlated with CT emission of corresponding D-A pair. It is apparent new red-shift peak by vapor exposure is originated from D-A interaction because the lifetime decay of red-shift spectrum is longer than that of host emission spectrum (**Figure 4-24**) which were measured from host only region and red-shift spectrum only region at each spectrum respectively. The emission spectra of vapor exposed crystals were collected from excitation of UV light where host can be excited. However, emission spectrum can be taken even at the red-shifted excitation wavelength condition where the host do not absorb (**Figure 4-25**), e.g., absorption spectra of D1 nano-crystal onset is around 410 nm and vapor exposed CT-R_D1 are excited at 500nm, it emits light (**Figure 4-25a**). This means the new absorption band is arisen by vapor exposure for each sample, and regarding the emission spectra excited from this new absorption band is coincided with the red-shift emission spectrum, I could assign the vapor exposure generated CT crystal on the host crystal: guest molecules at the VD film coupled with host molecules in the crystal by vapor exposure. This is indeed the evidence of strong D-A intermolecular interaction, and this is induced by the rod-type and isometric molecular design of D and A molecules. Therefore, CT crystals generation can be regarded as vapor-driven self-assembly (VDSA).

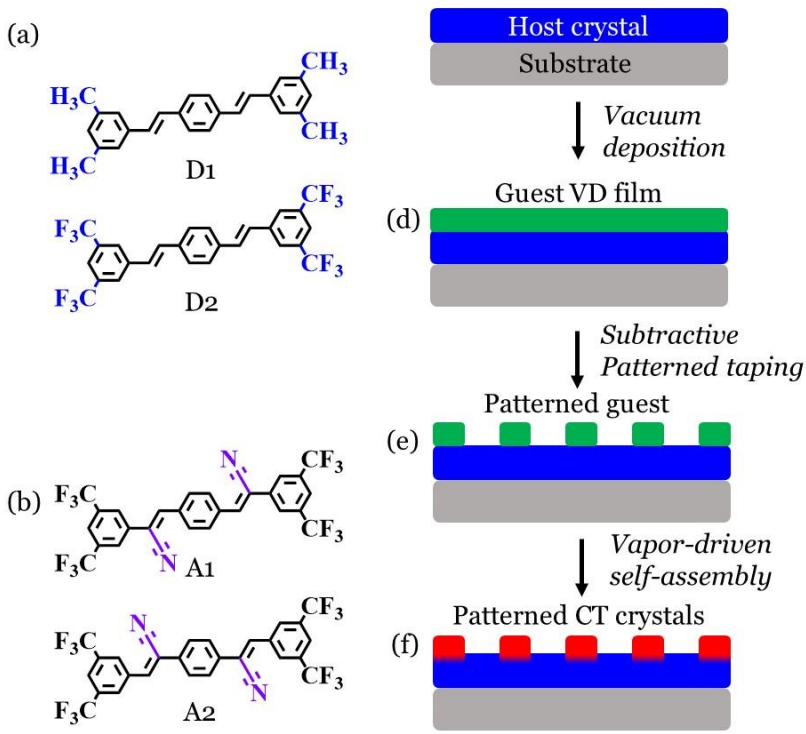

Figure 4-18. Molecular structure of isometric donors and acceptors and procedure of patterned templated grown CT cocrystal fabrication. Molecular structure of (a) donor 1 (D1) , donor 2 (D2), (b) acceptor 1 (A1), and acceptor 2 (A2). Procedure of templated grown CT cocrystal fabrication: (c) Host crystal on substrate, (d) deposited guest film on host, (e) patterned guest film by patterned taping, and (f) patterned CT crystal generation by solvent vapor treatment.

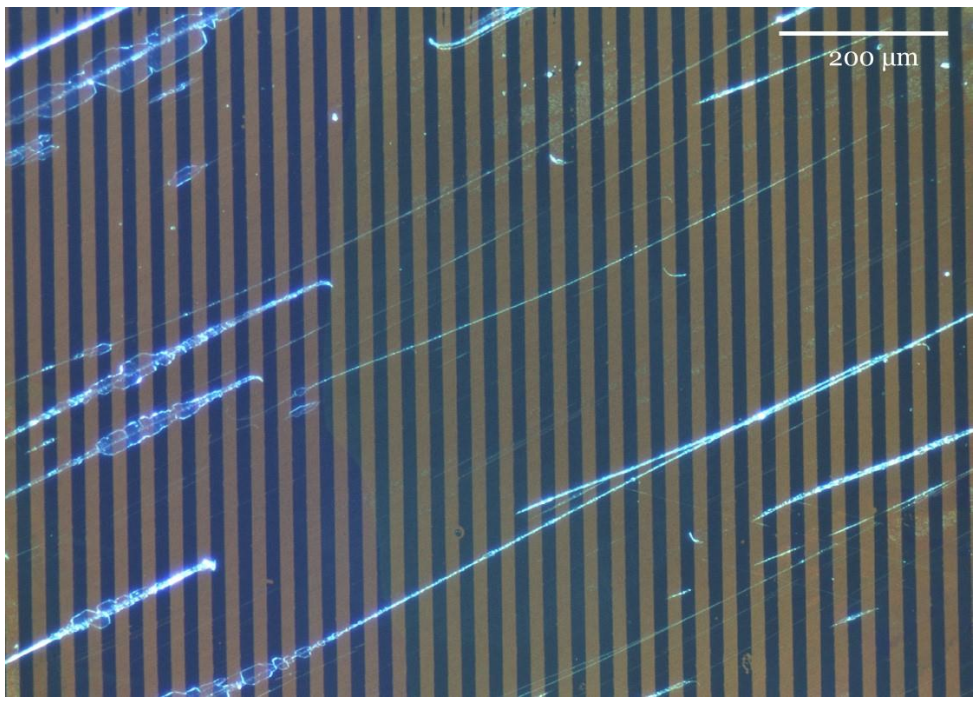

Figure 4-19. Large-scaled optical microscopy (OM) image under ultra-violet (UV) light of patterned CT-O on D1 crystal. (Scale bar: 200 μm)

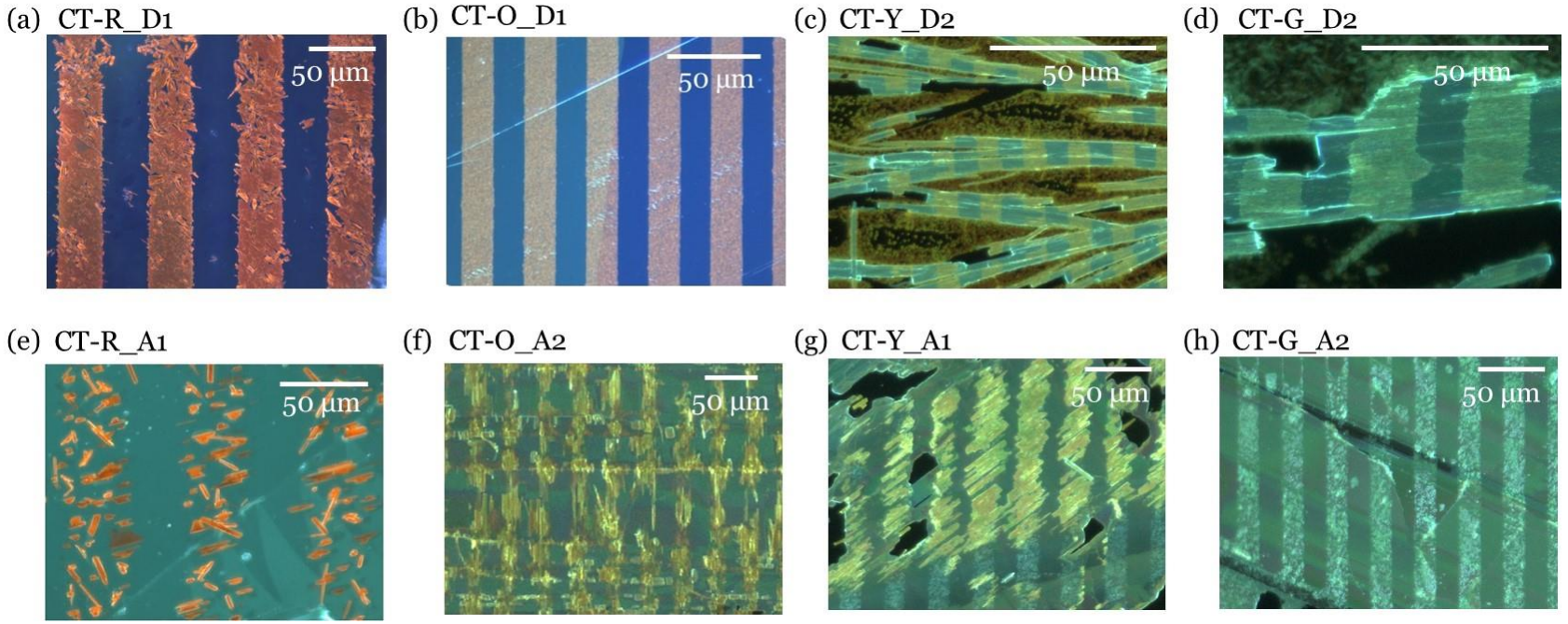

Figure 4-20. Optical microscopy (OM) images under ultra-violet (UV) light of micro-patterned templated grown CT cocrystal for each pair of combination. OM image of (a) micro-patterned CT-R grown D1 host crystal (CT-R_D1), (b) micro-patterned CT-O grown D1 host crystal (CT-O_D1), (c) micro-patterned CT-Y grown D2 host crystal (CT-Y_D2), (d) micro-patterned CT-G grown D2 host crystal (CT-G_D2), (e) micro-patterned CT-R grown A1 host crystal (CT-R_A1), (f) micro-patterned CT-O grown A2 host crystal (CT-O_A2), (g) micro-patterned CT-Y grown A1 host crystal (CT-Y_A1), and (h) micro-patterned CT-G grown A2 host crystal (CT-G_A2) respectively. (Scale bar: 50 μm)

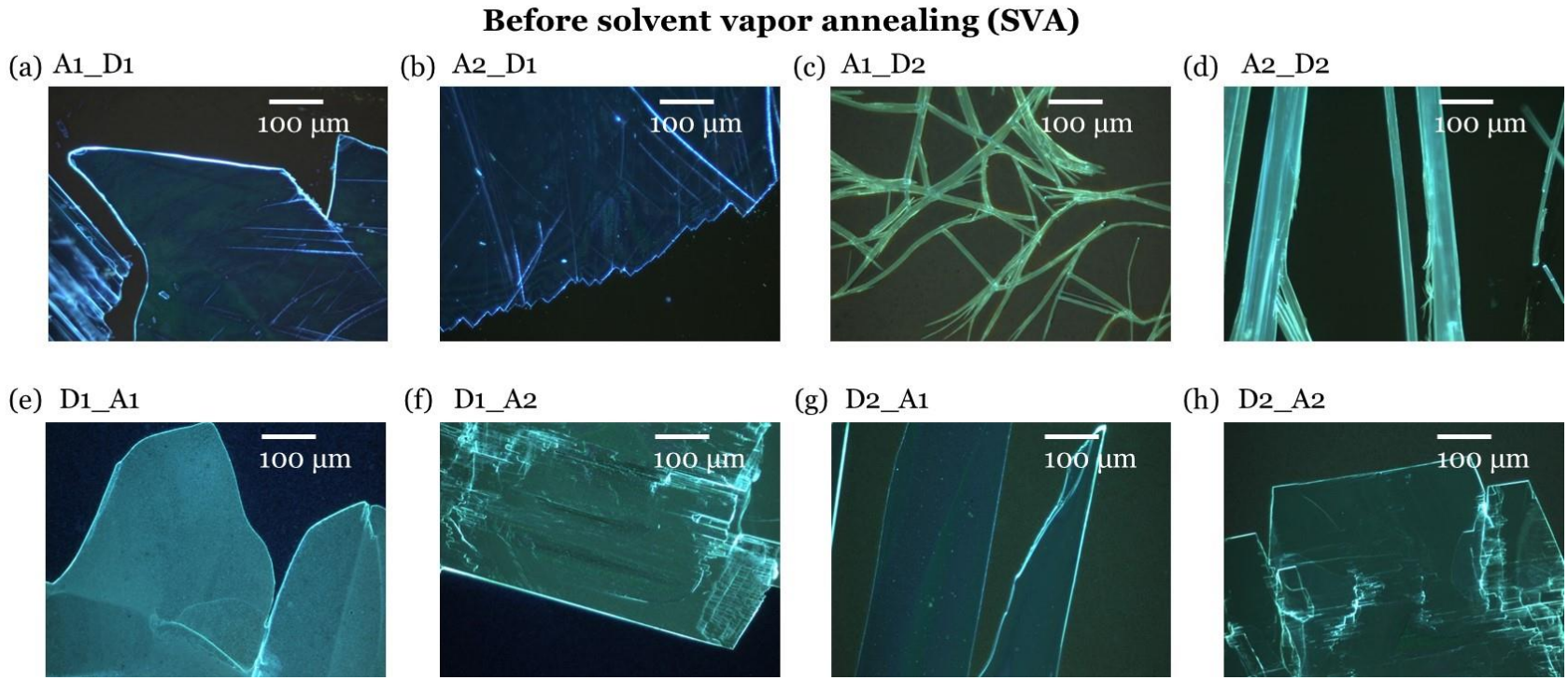

Figure 4-21. Optical microscopy (OM) images under UV light of vacuum deposited guest thin film on host crystal for each pair of combination. OM image of (a) A1 deposited D1 host crystal (A1_D1), (b) A2 deposited D1 host crystal (A2_D1), (c) A1 deposited D2 host crystal (A1_D2), (d) A2 deposited D2 host crystal (A2_D2), (e) D1 deposited A1 host crystal (D1_A1), (f) D1 deposited A2 host crystal (D1_A2), (g) D2 deposited A1 host crystal (D2_A1), and (h) D2 deposited A2 host crystal (D2_A2) respectively. (Scale bar: 100 μm)

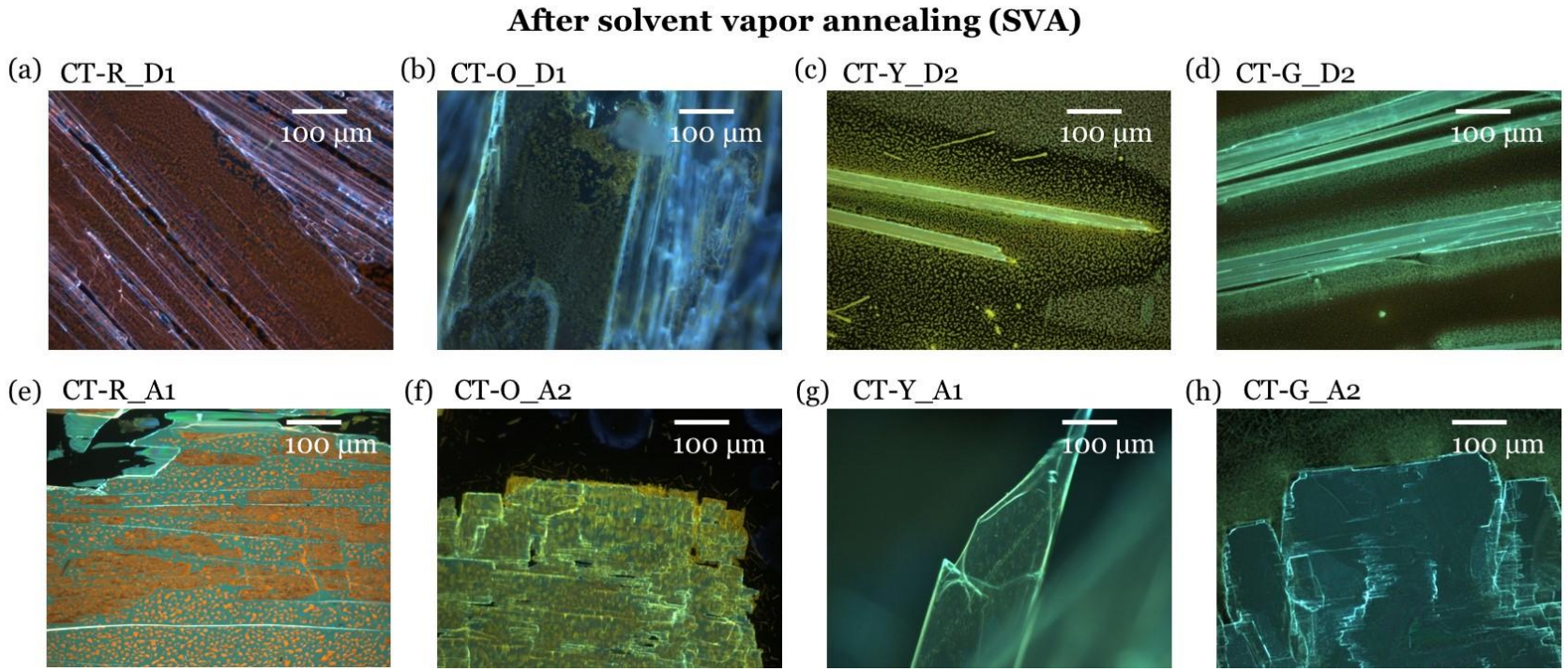

Figure 4-22. Optical microscopy (OM) images under UV light of CT grown host crystal after solvent vapor exposure for each pair of combination. OM image of (a) CT-R grown D1 host crystal (CT-R_D1), (b) CT-O grown D1 host crystal (CT-O_D1), (c) CT-Y grown D2 host crystal (CT-Y_D2), (d) CT-G grown D2 host crystal (CT-G_D2), (e) CT-R grown A1 host crystal (CT-R_A1), (f) CT-O grown A2 host crystal (CT-O_A2), (g) CT-Y grown A1 host crystal (CT-Y_A1), and (h) CT-G grown A2 host crystal (CT-G_A2) respectively. (Scale bar: 100 µm)

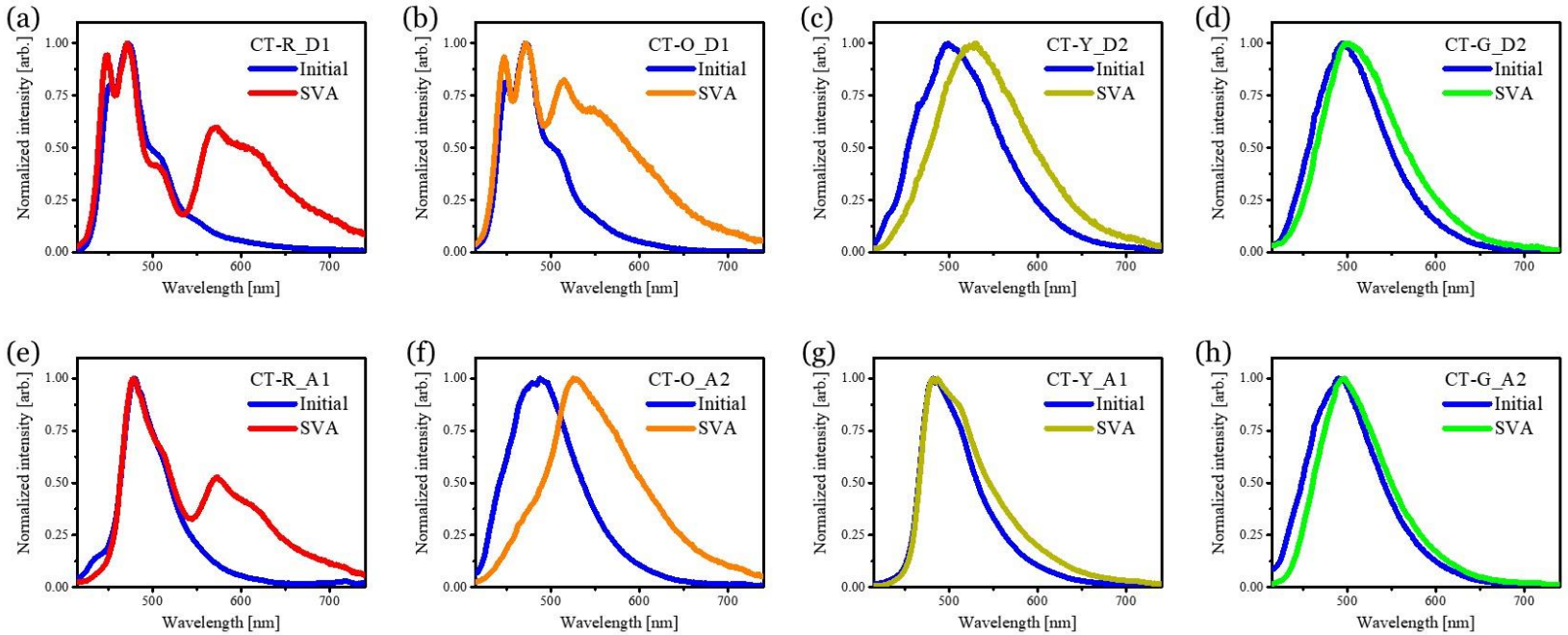

Figure 4-23. Photo-luminescence (PL) spectra of guest deposited host crystal (Before solvent vapor exposure) and CT grown host crystal (After solvent vapor exposure). PL spectrum of guest deposited host crystal (Blue) and CT grown host crystal (CT colored) of corresponding combination pair of (a) CT-R_D1, (b) CT-O_D1, (c) CT-Y_D2, (d) CT-G_D2, (e) CT-R_A1, (f) CT-O_A2, (g) CT-Y_A1, and (h) CT-G_A2 respectively

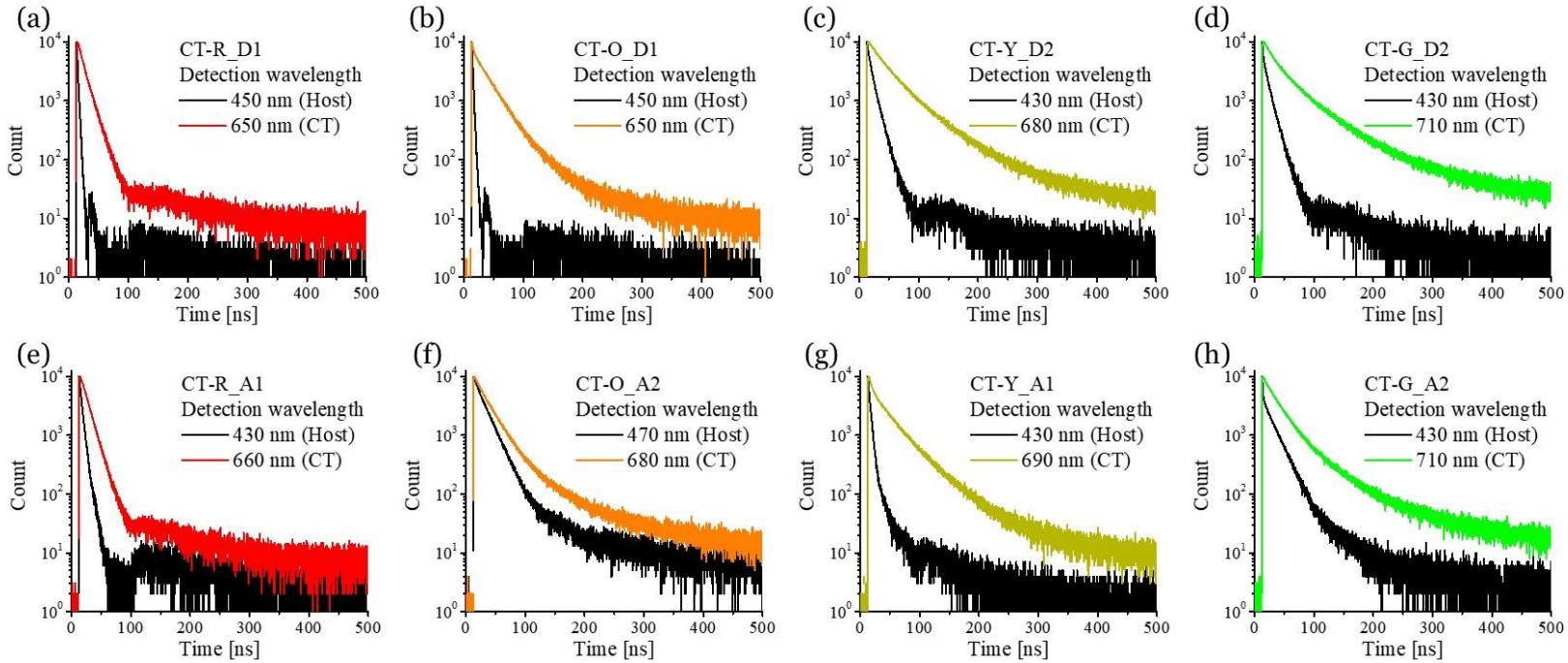

Figure 4-24. Lifetime decay of CT grown host crystal

Lifetime decay of CT grown host crystal at CT only wavelength detection(CT colored) and host only wavelength detection (blue) of (a) CT-R_D1, (b) CT-O_D1, (c) CT-Y_D2, (d) CT-G_D2, (e) CT-R_A1, (f) CT-O_A2, (g) CT-Y_A1, and (h) CT-G_A2 respectively.

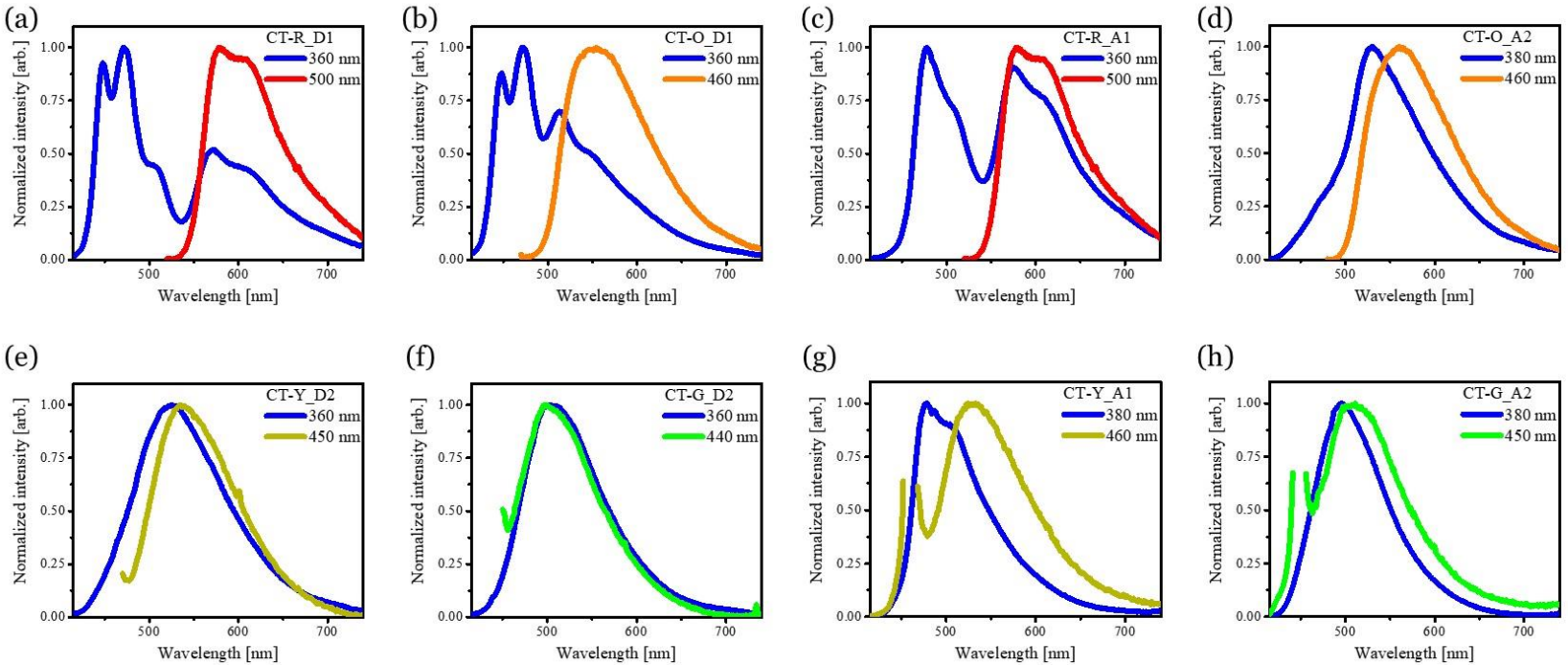

Figure 4-25. Photo-luminescence (PL) spectra of CT grown host crystal.
PL spectrum of CT grown host crystal under 360 nm excitation (Blue) and CT grown host crystal under CT only excitation (CT colored) of (a) CT-R_D1, (b) CT-O_D1, (c) CT-Y_D2, (d) CT-G_D2, (e) CT-R_A1, (f) CT-O_A2, (g) CT-Y_A1, and (h) CT-G_A2 respectively.

4.3.3. Morphological/ optical investigation

While on the optical investigation on CT grown host crystals, I have found that CT crystalline domains are quiet well-aligned in one direction as can be found at **Figure 4-20**. Based on this observation, emission from CT domains would have same light phase each other, and therefore, polarizer was rotated as to see the phase of light; CT emission cannot be detected at a specific angle, while 90˚ of rotation against that angle makes CT emission brightest than the other angle (**Figure 4-26**). Interestingly, at the part of the CT grown host crystals, orthogonal light phase was observed between CT and host emission (**Figure 4-26 a-d**) while others only CT emission responded to rotation of polarizer (**Figure 4-26 e-h**). In order to deeply understand this novel observation, morphology of CT grown crystals was investigated (*vide infra*).

Indeed, the CT crystals would mainly be grown from the surface of host crystals, and it can be checked with cross-sectional scanning electron microscopy (SEM) as can be found at **Figure 4-27**. It should be noted that for the better understand on the finding, CT grown crystals with hosts with known crystal structure (A1[66] and D1[67]) were mainly focused in this section, *i.e.*, CT-R_D1, CT-O_D1, CT-R_A1, CT-Y_A1. The lifetime of the host only region of CT grown crystals were measured and compared with that of original host lifetime (**Figure 4-28, Table 4-1**). Due to the rather small interfacial area between CT crystal and the host, energy transfer (ET) efficiency between them was much smaller than that of CT doped 2D-like crystals at Chapter 3: Compared with ET efficiency (η) four type of CT doped 2D-like crystals with same composition, the η value of CT grown crystals is dropped into around one-third level for every four pair, *e.g.*, CT-Y_A1 (CT grown crystal)

showed 0.24 of η while CT-Y doped A1 crystal showed 0.80 of η. The other four pairs of CT grown crystals also showed (very) small inefficient ET under 0.15, *e.g.*, CT-R_D1 showed only 0.03 of η.

To study nucleation process of CT on the host crystal depending on solvent vapor exposure time, very thin guest film (2~5 nm) was deposited on host crystal and atomic forced microscopy (AFM) was taken (**Figure 4-29**). As reported at the previous researches[66, 67], A1 and D1 host crystal before guest thin film deposition showed terrace like morphology (**Figure 4-29**). Through the AFM, Micro-domain thin guest film (2~5 nm) was found before VDSA, and most the guest domains hardly showed aligned behavior. The vapor exposure started to make some nucleus-like small CT crystals, and further vapor exposure made more grown crystals on the host surface. The nucleated and/or slightly grown micro-CT crystals by solvent vapor are aligned in one direction which highly indicates the growth direction of CT crystals are templated by underlying the host crystals. Depending on the CT and host combination, solvent exposure time required for nucleation were different each other, *i.e.,* CT-R_D1 ~ CT-O_D1 < CT-R_A1 < CT-Y_A1. In fact, melting temperature (MT) of each guest and host roughly follows the trend of this exposure time order; MT of A1 (253 ˚C) was higher than that of D1 (179 ˚C), and MT of D2 (266 ˚C) was higher than that of A1 (253 ˚C) and A2 (242 ˚C). To nucleate/ growth the CT crystal, mobile host and guest is required, and therefore, the order of exposure time can be influenced by the intermolecular interaction of constituting guest and host and thus solubility which can be represented by melting temperature (MT) (**Figure 4-30a**). Furthermore, the aspect ratio of CT crystals was different depending on combination (**Figure 4-29**); CT crystals on A1 host showed needle type morphology with high aspect ratio while CT crystals on D1 host are

rather more widely spread on the host. In the case of CT crystal on D1 (CT-R_D1, CT-O_D1), guest and host are rather easily co-assembled by solvent vapor in a short time period, and thus CT crystal on D1 can be rather easily grown along the interface of the guest and host layer thereby laterally grown CT crystals (**Figure 4-29a-b**). Meanwhile, in the CT crystal on A1 case (CT-R_A1, CT-Y_A1) (**Figure 4-29c-d**), because of longer solvent vapor exposure period can give more possibility to recrystallize the generated CT micro-crystals which can be dissolved easily than the bulk crystals, and thus CT crystal on the A1 can resemble the needle type morphology of 1:1 bulk CT crystals (**Chapter 2**). Indeed, CT micro-crystals of CT-R_D1 and CT-O_D1 can be easily dissolved, however, regarding the wide spread morphology of CT micro-crystals, it seems the assembly between guest and host is faster than the recrystallization of CT crystal by rather lower MT of D1 (179 ˚C) than that of CT-R (224 ˚C) and CT-O (243 ˚C).

Through the thicker guest film (30 nm), growth process of CT crystal can be roughly investigated via morphological study. After the nucleation, the growing CT crystals are surrounded by unreacted guest thin film in the in-plane direction and out-of-plane direction, and there is unreacted host crystal under the growing CT crystals, and the preferred CT crystal growth direction can be different depending on the constitution. However, in the growth process, large volume of templated grown crystal is involved different from nucleation process here, and thus it seems MT of CT crystal and host crystal is major factor which influences the final morphology, *vide infra* (**Scheme 4-1**). In fact, only CT-R_A1 case, the host has larger MT than that of CT as can be found at the relative difference between MT of CT and host, and otherwise CT shows larger MT than that of the host (**Figure 4-30b**). In the latter cases, the host molecules are more mobile than the molecules in

the CT crystals, and thus most preferred direction for crystal growing is in-plane direction as can be found at cross-sectional SEM image (**Figure 4-27a, c-d**). Meanwhile, the former case indeed CT crystal can be grown to in-plane direction, but also the guest molecules can possibly meet the host under the CT crystal by the dissolved/ mobile CT crystals. If this kind of aspect happens CT crystals of CT-R_A1 case will grow in both direction; in-plane and downward direction. At least it seems obvious the relative extent of MT between CT and host result in different aspect of CT crystal growth direction, regarding the fact the only host crystal of CT-R_A1 showed somewhat sunken morphology by CT crystals (**Figure 4-27b**) different from the other cases.

To understand the light phase of templated grown CT emission and host emission (**Figure 4-26**), the transient dipole moments (TDM) of emissive state based on the crystal structure of host were taken into account (**Figure 4-31**). From the known crystal structural solution of D1 and A1, TDM between S_1 and S_0 states were calculated elsewhere[66, 67], and the TDM direction was lying along the long axis of D1 and A1 molecules (**Figure 4-31a**). Also previous literature showed CT-R cocrystal' TDM between S_1 and S_0 states [68] of which direction is crossing between D and A molecules due to their CT character (**Figure 4-31b,** left). Like in the CT-R case, the calculated TDM of other CT cocrystals were directed between D and A molecules respectively (**Figure 4-31b**). From the crystal structure of D1 crystal (**Figure 4-32a-b**), all TDM (blue arrow) is oriented in the D1 crystal at the above view against out-of-plane direction (**Figure 4-32b**), and therefore, the birefringence occurs by polarizer rotation (**Figure 4-26a-b**). Meanwhile, TDM of A1 (**Figure 4-32c-d,** blue arrow) has two different directions at the above view (**Figure 4-32d**). Due to the angle between two kinds of TDM is 78˚ the birefringence was hardly

found at the A1 crystals (**Figure 4-26e-f**). At this moment, it should be noted that the most prominent force between D and A molecules is dispersion force (Chapter 1) like other organic molecules [69], which can roughly guide the rod-type DSB donor and DCS acceptor stacking in parallel. Due to the strong intermolecular interaction between DSB donor and DCS acceptor, templated grown CT are well-generated (*vide supra*), and therefore, with high probability, guest and host molecule can be aligned parallel with the original molecular orientation of host crystals. In fact, the light phase of CT and the host can be well explain through this assumption as following two cases. If the guest molecules of templated grown CT crystal is aligned in parallel with original D1 molecules of D1 crystal, TDM of CT will be close to orthogonal direction with TDM of D1 (**Figure 4-32b**, red arrow). Like in the former case, the possible TDM direction of templated growth CT on A1 is indicated with red arrow (**Figure 4-32d**), and they have different direction with A1 TDM but parallel each other. The described both cases coincided with the optical behavior of four CT grown crystals, and therefore, the rough molecular orientation of templated grown CT can be understood based on morphological investigation and crystallography.

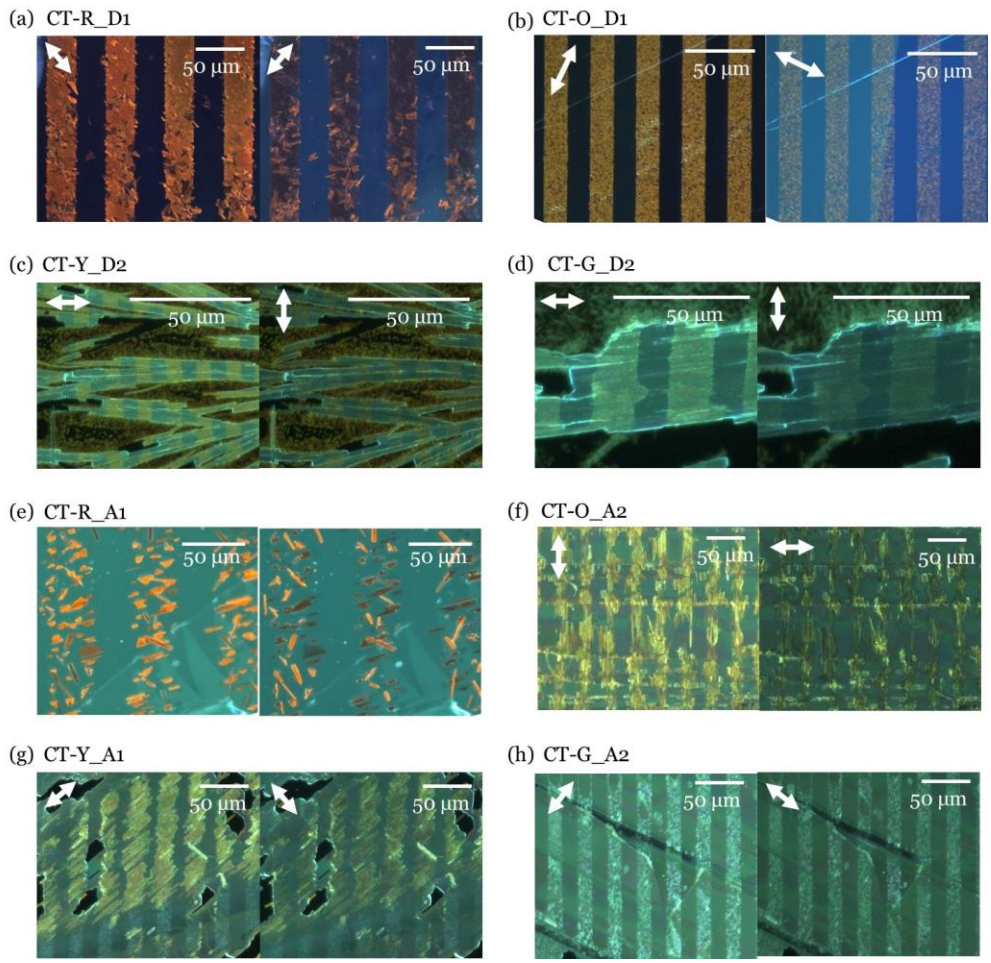

Figure 4-26. Polarized optical microscopy (POM) image of CT patterned host crystals. Polarized OM image of (a) CT-R_D1, (b) CT-O_D1, (c) CT-Y_D2, (d) CT-G_D2, (e) CT-R_A1, (f) CT-O_A2, (g) CT-Y_A1, and (h) CT-G_A2 respectively. The brightest CT emission is observed at the specific angle of polarizer as left images, and from that specific angle, the polarizer rotated orthogonally like at the right images (Scale bar: 50 μm)

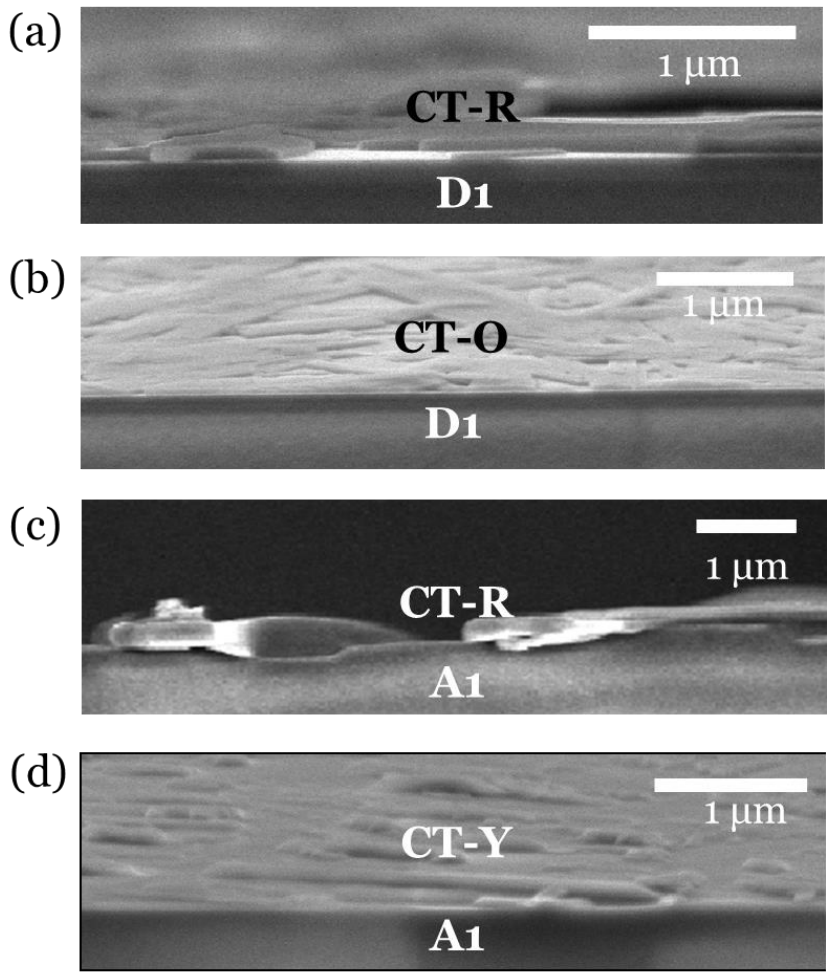

Figure 4-27. Cross-sectional scanning electron microscope (SEM) images of CT grown host crystals. CT grown host crystal of (a) CT-R_D1, (b) CT-O_D1, (c) CT-R_A1, and (d) CT-Y_A1 respectively.

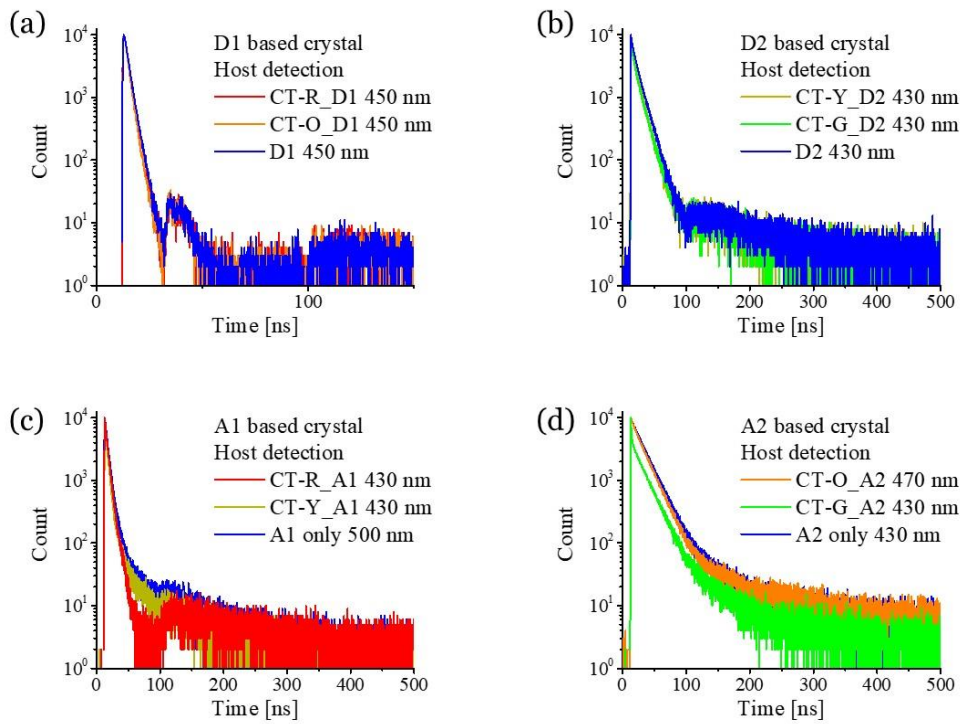

Figure 4-28. Host lifetime decay at the presence of CT and the host only condition. (a) Lifetime decay of D1 based crystals (CT-R_D1, CT-O_D1, D1) detected from host only emission wavelength (450 nm), (b) Lifetime decay of D2 based crystals (CT-Y_D2, CT-G_D2, D2) detected from host only emission wavelength (430 nm), (c) Lifetime decay of A1 based crystals (CT-R_A1, CT-Y_A1, A1) detected from host only emission wavelength (430 nm), and (d) Lifetime decay of A2 based crystals (CT-O_A2, CT-G_A2, A2) detected from host only emission wavelength (430 nm)

Sample	t_F [ns]	$t_{1,h}$	$I_{1,h}$	$t_{2,h}$	$I_{2,h}$	η	η_{disp}*
D1	2.1	2.1	100.0	-	-	-	-
D2	12.1	11.3	93.0	147.2	7.0	-	-
A1	6.5	5.2	76.9	41.6	23.1	-	-
A2	22.3	21.4	95.0	136.3	5.0	-	-
CT-R_D1	2.0	2.0	100.0	-	-	**0.03**	-
CT-O_D1	1.8	1.8	100.0	-	-	**0.13**	-
CT-Y_D2	19.6	10.0	91.4	121.4	8.6	**0.10**	-
CT-G_D2	12.0	10.7	88.2	93.8	11.8	**0.01**	-
CT-R_A1	4.6	4.1	82.2	11.1	17.8	**0.30**	0.80
CT-O_A2	19.6	18.6	94.5	203.3	5.5	**0.12**	0.43
CT-Y_A1	4.9	4.1	81.8	33.8	18.2	**0.24**	0.80
CT-G_A2	19.4	18.4	92.9	73.1	7.1	**0.13**	0.49

η_{disp}*: ET efficiency of dispersed CT at Chapter 3.

Table 4-1. ET efficiency of CT grown crystals and CT doped crystals (Chapter 3) based on lifetime of host crystals

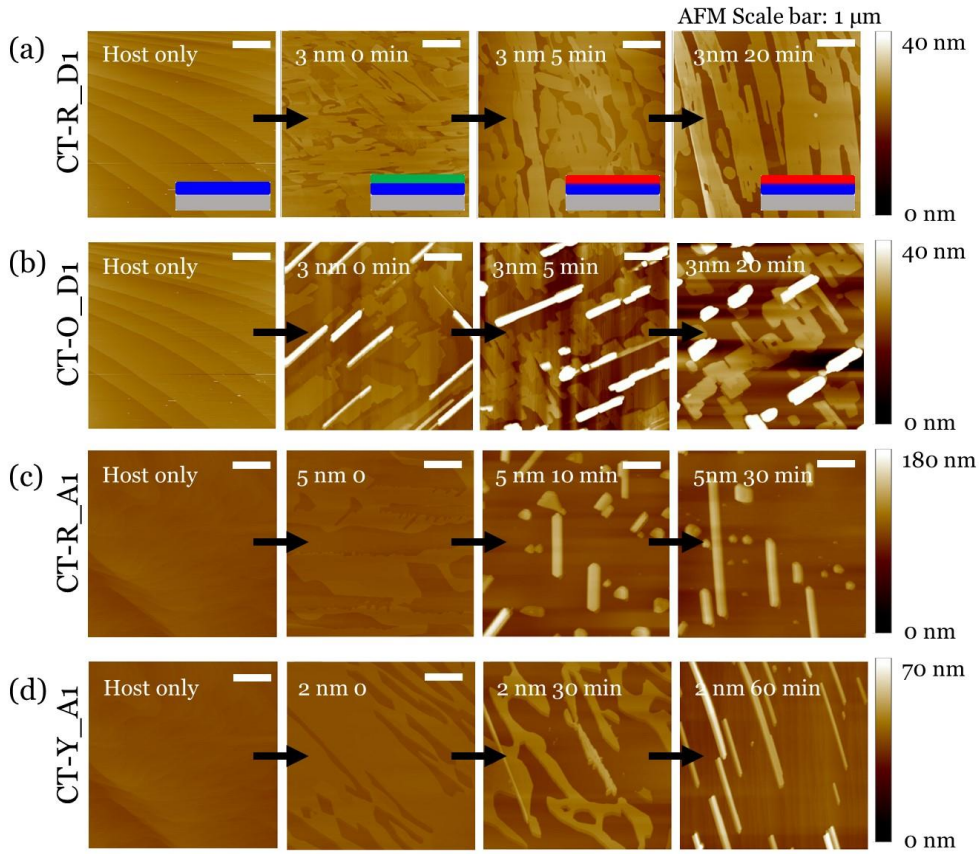

Figure 4-29. Atomic forced microscopy (AFM) images showing nucleation and growth of each CT grown crystal. From left to the right, morphology of host only crystals, guest deposited (3 nm) host crystals, shortly solvent vapor annealed sample, fully grown CT on host crystals investigated by AFM is displayed. Each images show (a) CT-R_D1 (inset: corresponding stage in Figure X1), (b) CT-O_D1, (c) CT-R_A1, and (d) CT-Y_A1 respectively (Scale bar: 1 μm).

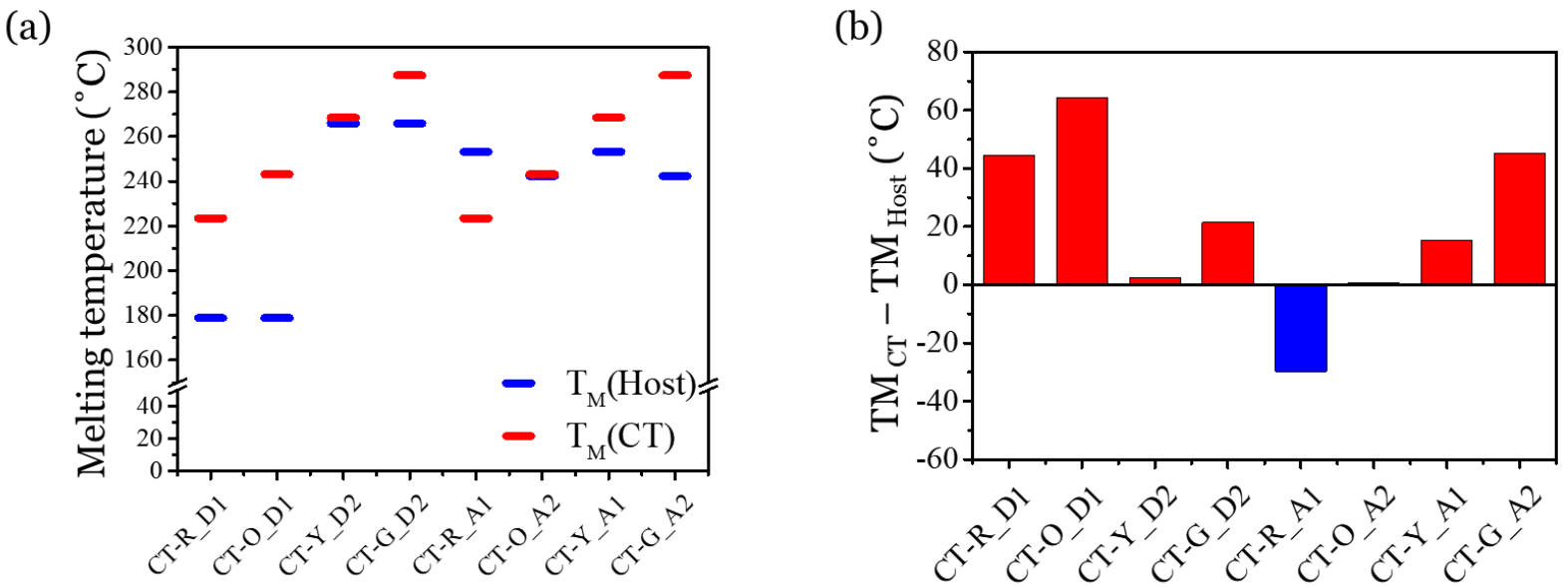

Figure 4-30. Relative melting temperatures (MT) of CT and hosts. (a) Melting temperature of CT (TM_{CT}) and host (TM_{host}) of each 8 pair extracted from the first scanned DSC data, (b) Relative melting temperature of CT against that of host (TM_{CT}-TM_{HOST}) of each 8 pair (the value below zero marked with blue).

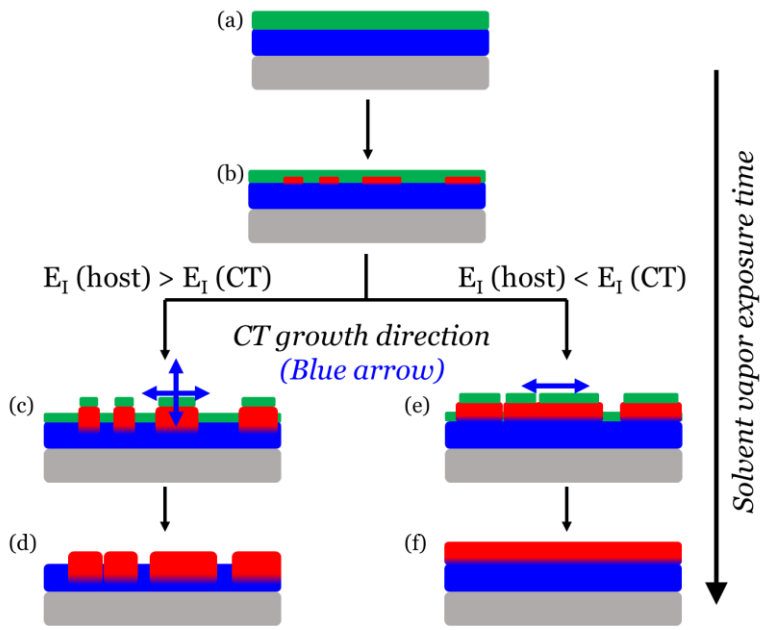

Scheme 4-1. Estimated CT growth direction depending on interaction energy (E_I) relation of CT and host. Schematic of (a) Guest deposited host crystal, and (b) Nucleation of CT by solvent vapor. Growth of CT seed by solvent vapor exposure at E_I (Host) > E_I (CT) condition in the (c) lateral and vertical directions (Blue arrow), and (d) fully grown CT by solvent vapor. Growth of CT seed by solvent vapor at E_I (Host) < E_I (CT) condition in the lateral direction (Blue arrow), and (f) fully grown CT by solvent vapor.

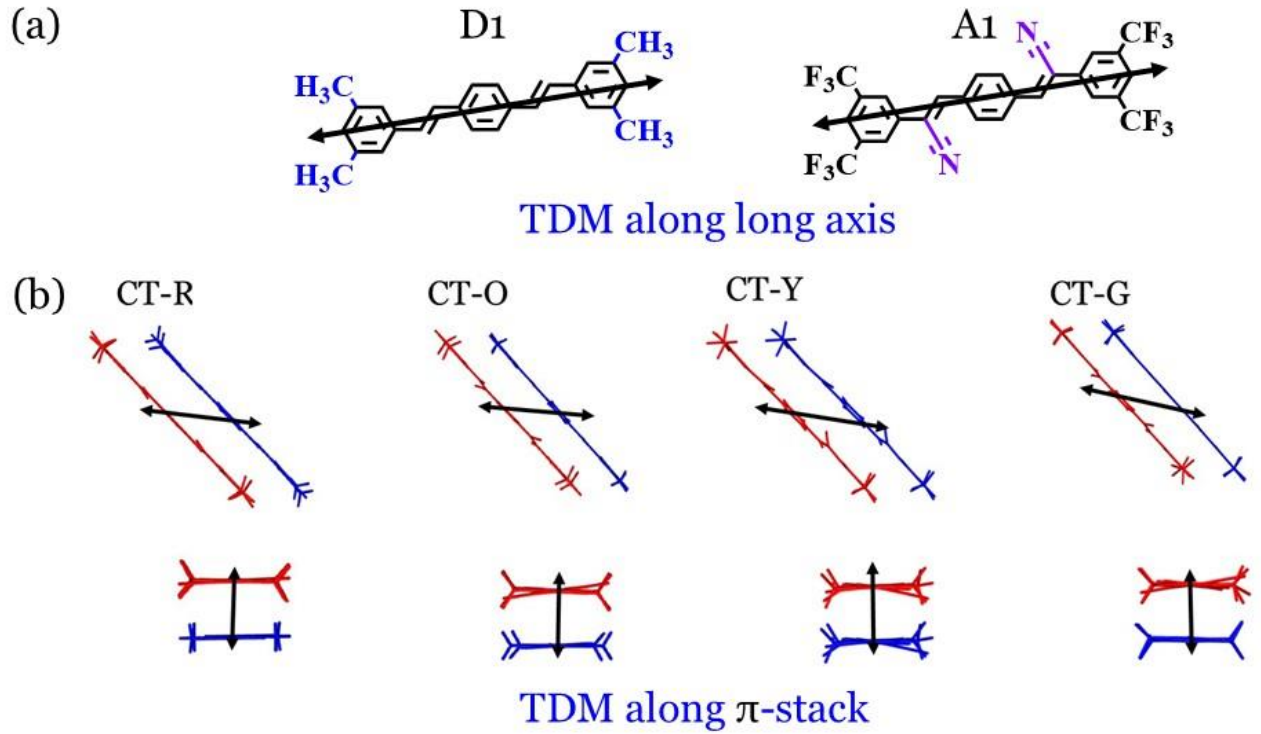

Figure 4-31. Transient dipole moment (TDM) direction between S_0 and S_1 of D1, A1, and CT crystal. (a) TDM lying along long axis of D1 and A1 molecules, (b) TDM lying along π-stack of CT pairs

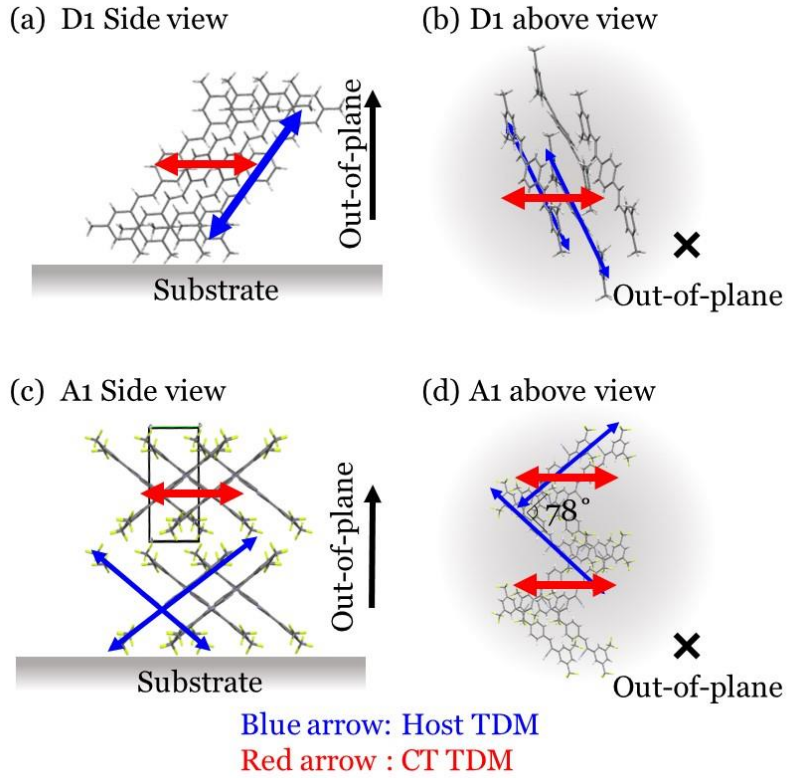

Figure 4-32. Transient dipole moment (TDM) direction of templated grown CT on D1 or A1 crystal. TDM direction of D1 (Blue) and expected TDM direction (Red) of templated grown CT at the (a) side view of D1 crystal structure and (b) above view of D1 crystal structure (Out-of-plane direction was marked). TDM direction of A1 (Blue) and expected TDM direction of templated grown CT (Red) at the (a) side view of A1 crystal structure and (b) above view of A1 crystal structure (Out-of-plane direction was marked).

4.4. Conclusion

In conclusion, I proposed and verified the effectiveness of a strategically novel and universal micro-scale/nano-scale soft lithographic method of patterned taping that uniquely exploits patterned pressure-sensitive tape as stamp material. Subtractive and/or additive patterning of various thin films, including organic semiconductors, luminescent chromophores, and metals, was implemented to fabricate complicated and high-performance optoelectronic devices. It was shown that the patterned taping process draws its usefulness from an industrial perspective in terms of its time/cost efficiency, supreme patterning yield, scalability (commercial adhesive tape-size scale), and truly non-destructive characteristics.

Based on the patterned taping, micro-patterned CT crystals on the surface of host crystal was successfully demonstrated the with the aid of vapor-driven self-assembly (VDSA) process. Due to the strong self-assembling character of isometric donor and acceptor, CT crystals were templated grown following the orientation of host molecules. Based on this morphological information and crystallographic information of the host and CT crystals, novel optical behavior of CT grown crystals under polarizer was thoroughly investigated in this chapter.

4.5. References

1. Wen Y.; Liu Y.; Guo Y.; Yu G., Hu W. *Chem Rev,* **2011**, *111*, 3358-3406.

2. Persano L.; Camposeo A., Pisignano D. *Journal of Materials Chemistry C,* **2013**, *1*, 7663-7680.

3. Lee H. M.; Kim J. J.; Choi J. H., Cho S. O. *ACS Nano,* **2011**, *5*, 8352-8356.

4. Min S. Y.; Kim T. S.; Kim B. J.; Cho H.; Noh Y. Y.; Yang H.; Cho J. H., Lee T. W. *Nat Commun,* **2013**, *4*, 1773.

5. Choi M. K.; Yang J.; Kang K.; Kim D. C.; Choi C.; Park C.; Kim S. J.; Chae S. I.; Kim T. H.; Kim J. H.; Hyeon T., Kim D. H. *Nat Commun,* **2015**, *6*, 7149.

6. Muller C. D.; Falcou A.; Reckefuss N.; Rojahn M.; Wiederhirn V.; Rudati P.; Frohne H.; Nuyken O.; Becker H., Meerholz K. *Nature,* **2003**, *421*, 829-833.

7. Liu W.; Jackson B. L.; Zhu J.; Miao C. Q.; Chung C. H.; Park Y. J.; Sun K.; Woo J., Xie Y. H. *ACS Nano,* **2010**, *4*, 3927-3932.

8. Hwang J. K.; Cho S.; Dang J. M.; Kwak E. B.; Song K.; Moon J., Sung M. M. *Nat Nanotechnol,* **2010**, *5*, 742-748.

9. Angmo D.; Larsen-Olsen T. T.; Jorgensen M.; Sondergaard R. R., Krebs F. C. *Advanced Energy Materials,* **2013**, *3*, 172-175.

10. Tipnis R.; Bernkopf J.; Jia S.; Krieg J.; Li S.; Storch M., Laird D. *Solar Energy Materials and Solar Cells,* **2009**, *93*, 442-446.

11. Gates B. D.; Xu Q.; Stewart M.; Ryan D.; Willson C. G., Whitesides G. M. *Chem Rev,* **2005**, *105*, 1171-1196.

12. Seo S.; Lee J.; Kim K. S.; Ko K. H.; Lee J. H., Lee J. *ACS Appl. Mater. Interfaces,* **2014**, *6*, 1345-1350.

13. Yoo B.; Cho S.; Seo S., Lee J. *ACS Appl. Mater. Interfaces,* **2014**, *6*,

19247-19253.

14. Lee T. W.; Jeon S.; Maria J.; Zaumseil J.; Hsu J. W. P., Rogers J. A. *Advanced Functional Materials*, **2005**, *15*, 1435-1439.

15. Loo Y. L.; Someya T.; Baldwin K. W.; Bao Z.; Ho P.; Dodabalapur A.; Katz H. E., Rogers J. A. *Proc Natl Acad Sci U S A*, **2002**, *99*, 10252-10256.

16. Kim S.; Wu J.; Carlson A.; Jin S. H.; Kovalsky A.; Glass P.; Liu Z.; Ahmed N.; Elgan S. L.; Chen W.; Ferreira P. M.; Sitti M.; Huang Y., Rogers J. A. *Proc Natl Acad Sci U S A*, **2010**, *107*, 17095-17100.

17. Briseno A. L.; Mannsfeld S. C.; Ling M. M.; Liu S.; Tseng R. J.; Reese C.; Roberts M. E.; Yang Y.; Wudl F., Bao Z. *Nature*, **2006**, *444*, 913-917.

18. Wang Z.; Zhang J.; Xing R.; Yuan J.; Yan D., Han Y. *J Am Chem Soc*, **2003**, *125*, 15278-15279.

19. Packard C. E.; Aidala K. E.; Ramanan S., Bulovic V. *Langmuir*, **2011**, *27*, 9073-9076.

20. Meitl M. A.; Zhu Z. T.; Kumar V.; Lee K. J.; Feng X.; Huang Y. Y.; Adesida I.; Nuzzo R. G., Rogers J. A. *Nature Materials*, **2006**, *5*, 33-38.

21. Park S. Y.; Kwon T., Lee H. H. *Advanced Materials*, **2006**, *18*, 1861-1864.

22. Kim K. H.; Bong K. W., Lee H. H. *Applied Physics Letters*, **2007**, *90*, 093505.

23. Katz H. E.; Lovinger A. J.; Johnson J.; Kloc C.; Siegrist T.; Li W.; Lin Y. Y., Dodabalapur A. *Nature*, **2000**, *404*, 478-481.

24. Jung Y.; Baeg K. J.; Kim D. Y.; Someya T., Park S. Y. *Synthetic Metals*, **2009**, *159*, 2117-2121.

25. Lee T. W.; Zaumseil J.; Kim S. H., Hsu J. W. P. *Advanced Materials*, **2004**, *16*, 2040-2045.

26. Jeong J.; Kim J.; Song K.; Autumn K., Lee J. *J R Soc Interface*, **2014**, *11*, 20140627.

27. *Proceedings of the National Academy of Sciences,* **2004**, *101*, 429-433.

28. Choi J. H.; Kim D.; Yoo P. J., Lee H. H. *Advanced Materials,* **2005**, *17*, 166-171.

29. Liu S. H.; Becerril H. A.; LeMieux M. C.; Wang W. C. M.; Oh J. H., Bao Z. N. *Advanced Materials,* **2009**, *21*, 1266-1270.

30. Yu J., Bulovic V. *Applied Physics Letters,* **2007**, *91*, 043102.

31. Kim B. J.; Lee D.; Lee J., Yang S. *Journal of Micromechanics and Microengineering,* **2015**, *25*, 017003.

32. Beesley D. J.; Semple J.; Krishnan Jagadamma L.; Amassian A.; McLachlan M. A.; Anthopoulos T. D., deMello J. C. *Nat Commun,* **2014**, *5*, 3933.

33. Chou H. H.; Nguyen A.; Chortos A.; To J. W.; Lu C.; Mei J.; Kurosawa T.; Bae W. G.; Tok J. B., Bao Z. *Nat Commun,* **2015**, *6*, 8011.

34. Fujita K.; Yasuda T., Tsutsui T. *Applied Physics Letters,* **2003**, *82*, 4373-4375.

35. Fan C.; Zoombelt A. P.; Jiang H.; Fu W.; Wu J.; Yuan W.; Wang Y.; Li H.; Chen H., Bao Z. *Adv Mater,* **2013**, *25*, 5762-5766.

36. Zhang X.; Mao J.; Deng W.; Xu X.; Huang L.; Zhang X.; Lee S. T., Jie J. *Adv Mater,* **2018**, e1800187.

37. Zhao X.; Liu T.; Liu H.; Wang S.; Li X.; Zhang Y.; Hou X.; Liu Z.; Shi W., Dennis T. J. S. *ACS Appl Mater Interfaces,* **2018**, *10*, 42715-42722.

38. Tarsoly G.; Park S., Pyo S. *Journal of Materials Chemistry C,* **2019**, *7*, 11465-11472.

39. Park S. K.; Kim J. H.; Ohto T.; Yamada R.; Jones A. O. F.; Whang D. R.; Cho I.; Oh S.; Hong S. H.; Kwon J. E.; Kim J. H.; Olivier Y.; Fischer R.; Resel R.; Gierschner J.; Tada H., Park S. Y. *Adv. Mater.,* **2017**, *29*, 1701346.

40. An B. K.; Kwon S. K., Park S. Y. *Angew. Chem. Int. Ed.,* **2007**, *46*, 1978-

1982.

41. An B.-K.; Gierschner J., Park S. Y. *Acc. Chem. Res.*, **2012**, *45*, 544-554.

42. De Luca G.; Liscio A.; Maccagnani P.; Nolde F.; Palermo V.; Müllen K., Samorì P. *Adv. Funct. Mater.*, **2007**, *17*, 3791-3798.

43. Tong X.; Zhao Y.; An B. K., Park S. Y. *Adv Funct Mater*, **2006**, *16*, 1799-1804.

44. Kim J. H.; Ribierre J. C.; Yang Y. S.; Adachi C.; Kawai M.; Jung J.; Fukushima T., Kim Y. *Nat. Commun.*, **2016**, *7*, 10653.

45. Qin D.; Xia Y., Whitesides G. M. *Nat Protoc*, **2010**, *5*, 491-502.

46. Choi S. J.; Yoo P. J.; Baek S. J.; Kim T. W., Lee H. H. *J Am Chem Soc*, **2004**, *126*, 7744-7745.

47. Ho D.; Zou J.; Zdyrko B.; Iyer K. S., Luzinov I. *Nanoscale*, **2015**, *7*, 401-414.

48. Benedek I., Heymans L. J. *Adhesives Technology*. Marcel Dekker: New York, 1997.

49. Carlson A.; Bowen A. M.; Huang Y.; Nuzzo R. G., Rogers J. A. *Adv. Mater*, **2012**, *24*, 5284-5318.

50. Zhou Y., Loh K. P. *Adv. Mater*, **2010**, *22*, 3615-3620.

51. Liang X.; Fu Z., Chou S. Y. *Nano Lett*, **2007**, *7*, 3840-3844.

52. Yun S. W.; Kim J. H.; Shin S.; Yang H.; An B. K.; Yang L., Park S. Y. *Adv. Mater*

2012, *24*, 911-915.

53. Yoon S. J.; Chung J. W.; Gierschner J.; Kim K. S.; Choi M. G.; Kim D., Park S. Y. *J Am Chem Soc*, **2010**, *132*, 13675-13683.

54. Chang J. F., Sirringhaus H. *Advanced Materials*, **2009**, *21*, 2530-2535.

55. Kobayashi S.; Nishikawa T.; Takenobu T.; Mori S.; Shimoda T.; Mitani T.; Shimotani H.; Yoshimoto N.; Ogawa S., Iwasa Y. *Nat Mater,* **2004**, *3*, 317-322.

56. Coropceanu V.; Cornil J.; da Silva Filho D. A.; Olivier Y.; Silbey R., Bredas J. L. *Chem Rev,* **2007**, *107*, 926-952.

57. Yun S. W.; Kim J. H.; Shin S.; Yang H.; An B. K.; Yang L., Park S. Y. *Adv. Mater.,* **2012**, *24*, 911-915.

58. Sobus J.; Bencheikh F.; Mamada M.; Wawrzinek R.; Ribierre J.-C.; Adachi C.; Lo S.-C., Namdas E. B. *Adv. Funct. Mater.,* **2018**, *28*, 1800340.

59. Ullah M.; Armin A.; Tandy K.; Yambem S. D.; Burn P. L.; Meredith P., Namdas E. B. *Sci. Rep.,* **2015**, *5*, 8818.

60. Kwon J. H., Lampande R. *OLED Manufacturing Process for Mobile Application*, 2018.

61. Cantatore E. *Applications of Organic and Printed Electronics: A Technology-Enabled Revolution*, 2013.

62. Park S. K.; Kim J. H.; Yoon S. J.; Kwon O. K.; An B. K., Park S. Y. *Chemistry of Materials,* **2012**, *24*, 3263-3268.

63. Varghese S.; Yoon S. J.; Calzado E. M.; Casado S.; Boj P. G.; Diaz-Garcia M. A.; Resel R.; Fischer R.; Milian-Medina B.; Wannemacher R.; Park S. Y., Gierschner J. *Adv. Mater,* **2012**, *24*, 6473-6478.

64. Gierschner J., Park S. Y. *J. Mater. Chem. C,* **2013**, *1*, 5818-5832.

65. Gierschner J.; Lüer L.; Milián-Medina B.; Oelkrug D., Egelhaaf H.-J. *J. Phys. Chem. Lett.,* **2013**, *4*, 2686-2697.

66. Park S. K.; Kim J. H.; Yoon S.-J.; Kwon O. K.; An B.-K., Park S. Y. *Chem. Mater.,* **2012**, *24*, 3263-3268.

67. Varghese S.; Park S. K.; Casado S.; Fischer R. C.; Resel R.; Milian-Medina B.; Wannemacher R.; Park S. Y., Gierschner J. *J. Phys. Chem. Lett.,* **2013**, *4*, 1597-1602.

68. Park S. K.; Varghese S.; Kim J. H.; Yoon S. J.; Kwon O. K.; An B. K.; Gierschner J., Park S. Y. *J. Am. Chem. Soc.*, **2013**, *135*, 4757-4764.

69. Park S. K.; Kim J. H., Park S. Y. *Advanced Materials*, **2018**, *30*, 1704759.

Abstract in Korean

지난 수십년 간 파이 공액 분자 기반 유기 결정은 그의 광전자적 기능성 및 소자로의 적용 가능성으로 인해 각광을 받아왔다. 여기서 원하는 기능성을 가진 물질을 설계하기 위해서 구조-물성 상관관계에 대한 체계적인 이해는 매우 중요하다. 그러나 유기 결정의 다양한 광전자적 특성을 예측하는 것은 아직 도전과제로 남아 있으며, 그 이유는 이들의 특성이 분자 구조에 영향을 받을 뿐 아니라 분자간 쌓임 구조와도 밀접히 관계되어 있기 때문이다. 따라서 본 관점에서 결정 구조적 유사성을 지닌 결정 시스템은 (등구조형 결정계) 분자간 쌓임 구조를 상수로 설정함으로서 분자 구조 변화에 따른 광전자적 특성 변화를 면밀하게 살펴볼 수 있도록 할 것이다. 한편, 파이 공액 유기 결정 중 전자 주개 (electron donor)와 전자 받개 (electron acceptor)의 쌍으로 구성된 전하 전이 (charge-transfer) 결정에 대한 관심이 집중되고 있는데, 이는 전하 전이 결정이 전자 주개와 전자 받개와는 차별화된 독특한 전하 이동 특성과 발광 특성을 보이기 때문이다. 그러나 전하 전이 복합체를 위한 분자 설계 지침이 아직 마련되지 못한 실정으로 인해 전하 전이 결정에 대한 광전자특성-구조 상관관계에 대한 연구는 제한 점이 많은 상황에 머물러 있다.

본 연구는 등적 (isometric) 분자 구조를 공유하는 두개의 다이스티릴벤젠 (distyrylbenzene) 타입 전자 받개와 두개의 다이사이아노다이스티릴벤젠 (dicyano-distyrylbenzene) 타입 전자 주개 분자에 집중하였다. 해당 분자들의 강한 자기 조립 능력으로 인해, 전자 받개 및 전자 주개의 가능한 네 가지 쌍에서 모두 1:1 비율 공결정이 형성 된다는 것을 확인 할 수 있었고, 공결정들은 경계 분자 궤도들의 (frontier molecular orbitals) 준위 차이를 따라 적색 부터 녹색까지의 강한 고상 발광성을 보이는 주목할 만한 결과를 보였다. 번갈아 쌓인 (mixed-stack) 전자 주개-받개 공 결정 구조의 빗겨 쌓인 구조 (slipped stack)에서 적합한 배치간 상호작용으로 (configuration interaction) 인해 증진된 진동자 힘 (oscillator strength)이 발견되었고 이 뿐 아니라 효과적으로 억제된 비방사 과정 (non-radiative process) 및 역항간 교차 (reverse intersystem crossing)으로 인한 삼중항 활용이 일어남을 확인하였다. 본 저자가 제시한 번갈아 쌓인 전하 이동 결정은 앞서 언급한 효과들의 시너지로 인해 83 %의 발광 효율 최고기록을 갱신하였다. 특히 설계된 전자 주개와 전자 받개 분자들은 등적 분자 구조를 공유하고 있기 때문에 파이 쌓임 방향에서 모두 등정형 (isomorphic) 및 유사 등구조형 결정계를 구성하였으며, 본 시스템을 통해 광물리적 특성에 대한 복잡한 형태학적 변수를

제거할 수 있었으며, 이에 전하 이동 복합체의 광물리적 특성에 대한 전하 이동 상호작용과 관련된 전자적 특성이 미치는 순수한 영향에 대한 연구를 할 수 있었다.

본 등적 분자 구조를 가진 분자들의 결정안에서의 높은 혼화성 (miscibility) 덕분에, 모든 전자 주개-받게 쌍은 결정질 고용체 (crystalline solid solution)상에서도 열역학 적으로 안정한 모습을 보여주었다. 1:1 공결정과 유사하게 네가지의 결정질 고용체는 (전자 주개: 전자 받개 비율 = 1:99~10:90) 등적 분자구조를 가진 분자들로 인해 유사 등구조를 보였다. 한편 1:1 공결정과 다르게 결정질 고용체는 전자 주개 (호스트) 결정의 형태를 따라 2D 형태의 결정을 형성하였다. 등적 구조의 전자 주개-받개로 인해 밀집된 분자 쌓임 형태에서 전자 이동 복합체가 호스트 결정 내에서 치환 도핑된(substitutional doped) 형태로 존재하였으며, 동시에 모든 결정질 고용체는 높은 에너지 전달 효율로 (80 %) 인해 결정 전영역에서 전하 이동 복합체의 발광 특성을 보였다. 심지어 20 %의 고농도 도핑된 조건에서 조차 전자 이동 복합체가 호스트 결정의 구조적, 전기적 특성에 대한 영향은 비파괴적이었다. 흥미롭게도 호스트 결정 내부의 전하 이동 복합체는 유기 광트랜지스터 특성을 활성화 시켰으며, 해당 소자는 보통의 응답 특성과 (~500 AW^{-1}) 수십 수준의 문턱 전압 이동 (ΔV_{TH}) 특성을 보였

다. 이에 따라 유기 광트랜지스터 특성과 등구조의 결정질 고용체의 다양한 물리적 특성과의 (에너지 전달 효율, 전자 주개-받개 에너지 준위 차이, 전기적 이동 특성) 상호관계에 대한 체계적인 연구가 진행되었다.

한편 리소그래피 기술을 통한 마이크로 구조 형성은 상용 유기 소자 개발에 있어 필수적인 요소라고 할 수 있다. 그러나 유기물의 약한 물리적 특성으로 인해 유기물에 완전히 적합한 패터닝 기술은 매우 드문 상황이다. 따라서 본 저자는 유기물에 매우 적합한 '패턴드 테이핑'이라는 소프트 리소그래피 신기술을 개발하였고, 이를 활용해 전자 주개 혹은 전자 받개 결정 위에 마이크로 패턴된 전하 전이 결정을 제작할 수 있었다. 구체적으로는 탑-다운 및 바텀-업 방식의 조합으로서 패턴드 테이핑과 용매 증기로 인한 자기 조립의 방식으로 패터닝 하였다. 패턴드 테이핑은 상용 압감 접착제 (pressure-sensitive tape)를 패터닝 하여 테이프의 강한 접착력만을 활용하여 서브트랙티브 (substractive) 및 어디티브 (additive) 방식의 패터닝이 가능한 기술이다. 본 기술은 다양한 박막에 대해 적용이 가능하며, 유기 물질에 대한 어떤 형태학적, 전기적 특성에 악영향도 발견되지 않았다. 더욱이 패턴드 테이핑은 고 효율의 패터닝 방식으로서 여러 강점을 보여주었는데, 마이크로 이하 패터닝 가능, 낮은 공정 비용, 간단한 공정, 넓은 영역

에 적용 가능하다는 장점이 있다. 본 방법을 활용하여 마이크로 패터닝된 전자 주개 혹은 받개 필름을 전자 받개 혹은 주개 결정 위에 형성 할 수 있었고, 이어지는 용매 노출을 통해 형판을 따라 자란 (templated grown) 전하 전이 결정을 제작할 수 있었다. 본 구조체는 편광 필터 회전에 의한 독특한 광학적 특성을 보여주었으며, 이 현상의 원리를 결정 구조적 방법, 광학적 접근, 양자 화학적 계산을 통해 명확하게 밝힐 수 있었다. 또한 형판을 따라 자라는 전하 전이 결정의 핵형성 및 성장 메커니즘을 형태학적, 열역학적 관점에서 면밀히 고찰하였다.

본 학위 논문에서는 등구조형 (isostructural) 전하 전이 결정 시스템 개발을 통해 형태학적 조건을 고정하고, 전하 전이 복합체의 전자 주개 및 받개 분자에 따른 구조-물성 상관관계를 밝히고자 하였다. 이를 위해 등적 분자 구조를 가지는 전자 주개 두개와 전자 받개 두개를 통해 유사 등구조형 1:1 전자전이 공결정 및 유사 등구조형 결정질 고용체를 만들 수 있었다. 이에 본 등구조형 결정 시스템 덕분에 다양한 물리적 변수들이 전자전이 결정의 광전자적 특성에 미치는 순수한 영향에 대해 광물리학적 접근과 결정학적 고찰 그리고 양자 화학적 계산 방법을 통하여 폭 넓은 고찰이 가능하게 되었다. 더 나아가 전자 전이 결정의 강한 자기 조립 능력과 더불어 유기물에 적합한 소프트 리소그래피 방식을 활

용하여 상용 소자 응용 가능성을 염두에 두고 마이크로 패터닝 된 형판을 따라 자라는 전자 전이 결정을 제작하는 데에 성공하였다.

주요어: 전하 전이 결정, 등적 분자구조를 가지는 전자 주개와 전자 받개, 구조-특성 상관관계, 등구조의 1:1 전하 전이 공결정, 등구조의 결정질 고용체, 소프트 리소그래피 신기술

학번: 2013-20609

List of Publications

Original Papers

1. Jinfeng Bai, Yucun Liu, **Sangyoon Oh**, Wenwei Lei, Bingzhu Yin, Soo Young Park, Yuhe Kan, "*A high-performance ambipolar organic field-effect transistor based on a bidirectional π-extended diketopyrrolopyrrole under ambient conditions*", *RSC advances*, **2015**, 5, 53412-53418.

2. **Sangyoon Oh**, Sang Kyu Park, Jin Hong Kim, Illhun Cho, Hyeong-Ju Kim, Soo Young Park, *"Patterned Taping: A High-Efficiency Soft Lithographic Method for Universal Thin Film Patterning", ACS Nano*, **2016**, 10, 3478-3485.

3. Sang Kyu Park, Jin Hong Kim, Tatsuhiko Ohto, Ryo Yamada, Andrew Jones, Dong Ryeol Whang, Illhun Cho, **Sangyoon Oh**, Jeffrey Hong, Ji Eon Kwon, Jong H. Kim, Yoann Olivier, Roland Fischer, Roland Resel, Johannes Gierschner, Hirokazu Tada, Soo Young Park, *"Highly Luminescent 2D-type Slab Crystals Based on a Molecular Charge-Transfer Complex as Promising Organic Light-Emitting Transistor Materials", Adv. Mater.*, **2017**, 29, 1701346.

4. Jin Hong Kim,† Min-Woo Choi,† Won Sik Yoon, **Sangyoon Oh**, Seung Hwa Hong, Soo Young Park († equal contribution), *"Structural and Electronic Origin of Bis-Lactam Based High Performance Organic Thin Film Transistors", ACS Applied Materials & Interfaces*, **2019**, 11, 8301−8309.

5. Junqing Shi, Maria Izquierdo, **Sangyoon Oh**, Soo Young Park, Begoña Milián-Medina, Daniel Roca-Sanjuán, Johannes Gierschner, *"Inverted Energy Gap Law for the Nonradiative Decay in Fluorescent Floppy Molecules: Larger Fluorescence Quantum Yields for Smaller Energy Gaps", Org. Chem. Front.*, **2019**, 6, 1948.

6. Jin Hong Kim, **Sangyoon Oh**, Sang Kyu Park, Soo Young Park, *"Green Sensitive Phototransistor Based on Solution Processed Two-Dimensional n-type*

Organic Single Crystal", Advanced Electronic Materials, **2019**, 5, 1900478

7. María José Aliaga Gosalvez, Nicola Demitri, Michael Dohr, Juan Carlos Roldao, Sang Kyu Park, **Sangyoon Oh**, Shinto Varghese, Soo Young Park, Yoann Olivier, Begoña Milián Medina, Roland Resel, Johannes Gierschner, *"Crossed 2D versus Slipped 1D π-Stacking in Polymorphs of Crystalline Organic Thin Films: Impact on the Electronic and Optical Response", Adv. Opt. Mater.*, **2019**, 7, 1900749.

8. **Sangyoon Oh**, Jin Hong Kim, Sang Kyu Park, Chi Hyun Ryoo, and Soo Young Park, *"Fabrication of Pixelated Organic Light-emitting Transistor (OLET) with a Pure Red-emitting Organic Semiconductor", Adv. Opt. Mater.*, **2019**, 7, 1901274.

9. Marı´a A. Izquierdo, Junqing Shi, **Sangyoon Oh**, Soo Young Park, Begon˜a Milia´n-Medina, Johannes Gierschner and Daniel Roca-Sanjuan, *"Excited-state non-radiative decay in stilbenoid compounds: an ab initio quantum-chemistry study on size and substituent effects", Phys. Chem. Chem. Phys.*, **2019**, 21, 22429.

10. Diptiman Dinda, Hyunho Park, Hyun-Jun Lee, **Sangyoon Oh**, Soo Young Park, *"Graphene quantum dot with covalently linked Rhodamine dye: a high efficiency photocatalyst for hydrogen evolution", Carbon.*, **2020**, *accepted*

List of Presentations

International

1. (Poster) SangYoon Oh, Sang Kyu Park, Illhun Cho, Soo Young Park "*Stimuli-Responsive Photoluminescent Properties of Diaryl Substituted Fumaronitrile Derivatives*" KJF-ICOMEP 2014, Japan, 2014-09-21.

2. (Poster) YoungJoo Park, Won Sik Yoon, **Sangyoon Oh**, Soo Young Park, *"Synthesis and Characterization of Isoindigo and Thienoisoindigo Derivatives for Organic Field Effect Transistor Application"*, KJF 2014, Japan, 2014-09-21

3. (Poster) Sangyoon Oh, Sang Kyu Park, Jin Hong Kim, Illhun Cho, Soo Young Park, *"Patterned taping: A novel and high-efficiency soft lithographic method for organic thin films"*, Pacifichem, USA, 2015-12-15

List of Patents

Domestic

1. 박수영, **오상윤**, 박상규, *"패턴된 접착 테이프를 이용한 소프트 리소그래피 방법(Soft lithography method with patterned adhesive tape)"*, 대한민국, 등록번호 10-1721071-0000, 2017-03-23 등록